EPFL

Ion and Trap Induced Dynamic Phenomena in Salt Semiconductor Devices

Matthias DIETHELM

■ École
polytechnique
fédérale
de Lausanne

2021

Acknowledgements

Out of endless gratitude, I dedicate this thesis to Vincy who has been supportively accompanying me along this scientific path and continues to do so which is anything but a given, and to my parents for their unconditional encouragement and support especially during my studies at ETH.

Abstract

State-of-the-art organic light-emitting diodes (OLEDs) used in commercial display technology are complex multilayer structures. In contrast, the light-emitting electrochemical cell (LEC) can be built from a single emissive layer sandwiched between two electrodes. Due to the presence of mobile ions - intermixed with the active material - the single layer can perform all the tasks that take place in an OLED, i.e., electrical charge injection, transport, exciton formation, and radiative recombination. Therefore, LECs have the potential to be fabricated by low-cost solution coating and printing processes. While the structure is simple, the simultaneous occurrence of electronic and mobile ionic charge introduces a complex device functionality. Basic operation principles have been discussed for years in the field and consensus has been reached on the electrochemical doping model. For nonlimited injection, formation of electronic double layers by ionic charges at the electrodes facilitate the injection of electric charges. Subsequently, the injected charges lead to the formation of n- and p-doped regions at the cathode and anode, which are locally compensated by ions. This electrochemical doping process increases the electronic conductivity of the active material. The doped regions grow and an intrinsic region between them gets narrower, where electronic charge carriers recombine by emissive Langevin recombination. Next to polymers as used in this thesis, ionic transition metal complexes, small molecules and organic salts have been used as active LEC materials.

The focus of this thesis is to unravel the interplay of electronic and ionic charges in LECs and to highlight the boundaries and gaps of the firmly established electrochemical doping model. Used methods and conclusions are not restricted to the polymer-based LECs and can be applied to various systems with combined electronic and ionic conduction, as demonstrated for perovskite LEDs.

First, effects of ion concentration and active layer thickness variation in the super yellow (SY) polymer LEC (PLEC) are investigated, which play a critical role on the performance. Their optimization leads to a current efficacy of 11.6 cd A^{-1}, on a par with SY OLEDs. The optimized salt content can be explained according to the electrochemical doping model, as at low concentrations carrier injection and conduction is reduced, whereas at high concentrations exciton quenching reduces the efficiency. The dependence on the layer thickness reveals the often-overlooked microcavity/Purcell effect, which leads to a strong dependence of the optical outcoupling efficiency on the emitter position (EP) within the active layer. A comprehensive optical modelling study includes the doping-induced changes of the refractive indices and self-absorption losses. For thicker PLECs, a continuous change of the emission colour during operation provides a direct visual indication of a moving EP. Results from an optical and electrical analysis indicate that the intrinsic zone narrows at early times, but starts to widen subsequently, notably well before the electrical device optimum is reached. This finding seems to be in contrast to the electrochemical doping model. Drift-diffusion simulation of the electrical measurements pinpoints the EP shift to ion dynamics and demonstrates that the only precondition for this event to occur is unequal cation and anion mobilities. Quantitative ion profiles reveal that the movement of ions stops when the intrinsic zone stabilizes, confirming the relation between ion movement and EZ shift.

The unresolved origin of device degradation after the ionic steady state has been reached leads to the study of the SY polymer LED (PLED) with the idea to isolate the electronic from ionic effects. In SY PLEDs, it is firmly established that electron transport is seriously hindered by the presence of an universal electron trap, and that hole trap formation governs the long term device stability. Response of PLEDs to electrical driving and breaks covering the timescale from microseconds to (a few) hours reveals a characteristic response of electron traps. Surprisingly, the electron trap filling dynamics takes minutes to hours, at odds with the common notion that charge trapping is complete after a few hundred microseconds. This unusual phenomenon is not reported so far and is explained with trap deactivation upon de-trapping and slow trap reactivation. The results provide useful insight to pinpoint the chemical nature of the universal electron traps in semiconducting polymers. Subsequently, the characteristic response of the electron traps to electrical breaks is identified in the PLEC as well. Further investigation by electroabsorption measurement finds that hole trap formation limits the device lifetime, in the exact same manner as for PLEDs. Therefore, charge traps present an important, but so far overlooked intrinsic degradation mechanism for PLECs.

The methodology to unravel dynamic processes due to mobile ions, electronic charges and trap development is applied to perovskite light-emitting diodes (PeLEDs). PeLEDs reached more than 20% external quantum efficiency, but ionic point defects - mobilised by high temperature, irradiation and external electric fields - contribute to the intrinsic device instability. Due to the mobility of trapping defects, many more processes compared to an organic LED/LEC system are identified. The application of the optical model based on the microcavity effect to the PeLED is discussed. Experimental thickness variation of the TPBi transport layer of a $CsPbBr_3$ based PeLED indicates the validity of the optical model. A transient voltage pulse reveals an emission feature within the time range of ionic mobility. Transient drift-diffusion simulation is able to describe the observed emission increase as a result of ionic movement. The subsequent emission drop is not reproduced by the simulation, and the missing elements of the model are discussed.

Zusammenfassung

Moderne organische Leuchtdioden (OLEDs), die in der kommerziellen Displaytechnologie eingesetzt werden, sind komplexe Mehrschichtstrukturen. Im Gegensatz dazu kann die lichtemittierende elektrochemische Zelle (LEC) aus einer einzigen emittierenden Schicht aufgebaut werden, die zwischen zwei Elektroden eingebettet ist. Aufgrund des Vorhandenseins von mobilen Ionen - vermischt mit dem aktiven Material - kann die einzelne Schicht alle Aufgaben erfüllen, die in einer OLED stattfinden, d.h. elektrische Ladungsinjektion, Transport, Exzitonenbildung und strahlende Rekombination. Daher haben LECs das Potenzial, durch kostengünstige Lösungsbeschichtungs- und Druckprozesse hergestellt zu werden. Während die Struktur einfach ist, führt das gleichzeitige Auftreten von elektronischer und mobiler ionischer Ladung zu einer komplexen Funktionalität. Die grundlegenden Funktionsprinzipien werden seit Jahren auf dem Gebiet diskutiert und es wurde ein Konsens über das elektrochemische Dotierungsmodell erreicht. Bei nicht begrenzter Injektion erleichtert die Bildung von elektronischen Doppelschichten durch ionische Ladungen an den Elektroden die Injektion von elektrischen Ladungen. In der Folge führen die injizierten Ladungen zur Bildung von n- und p-dotierten Bereichen an der Kathode und Anode, die lokal durch Ionen kompensiert werden. Dieser elektrochemische Dotierungsprozess erhöht die elektronische Leitfähigkeit des aktiven Materials. Die dotierten Bereiche wachsen und ein intrinsischer Bereich zwischen ihnen wird schmaler, in dem elektronische Ladungsträger durch emittierende Langevin-Rekombination rekombinieren. Neben Polymeren, wie sie in dieser Arbeit verwendet werden, sind auch ionische Übergangsmetallkomplexe, kleine Moleküle und organische Salze als aktive LEC-Materialien eingesetzt worden.

Der Schwerpunkt dieser Arbeit liegt darin, das Zusammenspiel von elektronischen und ionischen Ladungen in LECs zu entschlüsseln und die Grenzen und Lücken des fest etablierten elektrochemischen Dotierungsmodells aufzuzeigen. Die verwendeten Methoden und Schlussfolgerungen sind nicht auf die polymerbasierten LECs beschränkt und können auf verschiedene Systeme mit kombinierter elektronischer und ionischer Leitung angewendet werden, wie für Perowskit-LEDs demonstriert.

Zunächst werden Effekte der Ionenkonzentration und der Variation der aktiven Schichtdicke in der super yellow (SY) Polymer-LEC (PLEC) untersucht, die eine kritische Rolle für die Leistung spielen. Ihre Optimierung führt zu einer Stromausbeute von 11.6 cd A^{-1}, die auf einem Niveau mit SY-OLEDs liegt. Der optimierte Salzgehalt kann nach dem elektrochemischen Dotierungsmodell erklärt werden, da bei niedrigen Konzentrationen die Ladungsträgerinjektion und -leitung reduziert wird, während bei hohen Konzentrationen das Exzitonen-Quenchen die Effizienz verringert. Die Abhängigkeit von der Schichtdicke offenbart den oft übersehenen Mikrokavitäten-/Purcell-Effekt, der zu einer starken Abhängigkeit der optischen Auskopplungseffizienz von der Emitterposition (EP) innerhalb der aktiven Schicht führt. Eine umfassende optische Modellierungsstudie beinhaltet die Dotierungs-induzierten Änderungen der Brechungsindizes und Selbstabsorptionsverluste. Bei dickeren PLECs liefert eine kontinuierliche Änderung der Emissionsfarbe während des Betriebs einen direkten visuellen Hinweis auf eine bewegte EP. Die Ergebnisse einer optischen und elektrischen Analyse deuten darauf hin, dass sich die intrinsische Zone zu frühen Zeiten verengt,

sich dann aber zu verbreitern beginnt, insbesondere lange vor Erreichen des elektrischen Optimums. Dieser Befund scheint im Gegensatz zum elektrochemischen Dotierungsmodell zu stehen. Die Drift-Diffusions-Simulation der elektrischen Messungen führt die EP-Verschiebung auf die Ionendynamik zurück und zeigt, dass die einzige Voraussetzung für das Auftreten dieses Ereignisses ungleiche Kationen- und Anionenmobilitäten sind. Quantitative Ionenprofile zeigen, dass die Bewegung der Ionen aufhört, wenn sich die intrinsische Zone stabilisiert, was den Zusammenhang zwischen Ionenbewegung und EZ-Verschiebung bestätigt.

Der ungelöste Ursprung der Degradation nach Erreichen des ionischen Steady-States führt zur Untersuchung der SY-Polymer-LED (PLED) mit der Idee, die elektronischen von den ionischen Effekten zu isolieren. In SY-PLEDs ist es fest etabliert, dass der Elektronentransport durch das Vorhandensein einer universellen Elektronenfalle ernsthaft behindert wird und dass die Bildung von Löcherfallen die Langzeitstabilität bestimmt. Die Reaktion von PLEDs auf elektrische Ansteuerung und Unterbrechungen, die die Zeitskala von Mikrosekunden bis zu (einigen) Stunden abdecken, zeigt eine charakteristische Reaktion der Elektronenfallen. Überraschenderweise dauert die Dynamik des Füllens der Elektronenfallen Minuten bis Stunden, was im Widerspruch zu der üblichen Vorstellung steht, dass das Einfangen der Ladungen nach einigen hundert Mikrosekunden abgeschlossen ist. Dieses ungewöhnliche Phänomen wurde bisher nicht berichtet und wird mit der Deaktivierung der Fallen beim Entfallen und der langsamen Reaktivierung der Fallen erklärt. Die Ergebnisse liefern nützliche Erkenntnisse, um die chemische Natur der universellen Elektronenfallen in halbleitenden Polymeren zu bestimmen. Anschließend wird die charakteristische Reaktion der Elektronenfallen auf elektrische Unterbrechungen auch in PLECs identifiziert. Weitere Untersuchungen durch Elektroabsorptionsmessungen zeigen, dass die Bildung von Ladungsfallen die Lebensdauer begrenzt, und zwar in genau der gleichen Weise wie bei PLEDs. Daher stellen Ladungsfallen einen wichtigen, aber bisher übersehenen intrinsischen Degradationsmechanismus für PLECs dar.

Die Methodik zur Entschlüsselung der dynamischen Prozesse aufgrund mobiler Ionen, elektronischer Ladungen und der Entwicklung von Fallen wird auf Perowskit-Leuchtdioden (PeLEDs) angewendet. PeLEDs erreichen mehr als 20% externe Quanteneffizienz, aber ionische Punktdefekte - mobilisiert durch hohe Temperatur, Bestrahlung und externe elektrische Felder - tragen zur intrinsischen Instabilität bei. Aufgrund der Mobilität der Punktdefekte werden viel mehr Prozesse im Vergleich zu einem organischen LED/LEC-System identifiziert. Die Anwendung des optischen Modells basierend auf dem Mikrokavitätseffekt auf die PeLED wird diskutiert. Die experimentelle Dickenvariation der TPBi-Transportschicht einer CsPbBr3-basierten PeLED deutet auf die Gültigkeit des optischen Modells hin. Ein transienter Spannungspuls zeigt ein Emissionsmerkmal im Zeitbereich der ionischen Mobilität. Die transiente Drift-Diffusions-Simulation ist in der Lage, den beobachteten Emissionsanstieg als Folge der Ionenbewegung zu beschreiben. Der anschließende Emissionsabfall wird von der Simulation nicht reproduziert, und die fehlenden Elemente des Modells werden diskutiert.

Stichworte: lichtemittierende elektrochemische Zelle, optisches Modell, super yellow, mobiles Ion, Dotierung, Elektrolyt, Drift-Diffusions-Modell, Emitterposition, Polymer-Leuchtdiode, Elektronenfalle, Ladungsfallendynamik, Degradation, Perowskit

Résumé

Les diodes électroluminescentes organiques (OLED) de pointe utilisées dans la technologie d'affichage commerciale sont des structures multicouches complexes. En revanche, la cellule électrochimique émettrice de lumière (LEC) peut être construite à partir d'une seule couche émettrice prise en sandwich entre deux électrodes. En raison de la présence d'ions mobiles - mélangés au matériau actif - la couche unique peut effectuer toutes les tâches qui ont lieu dans une OLED, c'est-à-dire l'injection et le transport de charges électriques, la formation d'excitons et la recombinaison radiative. Par conséquent, les LEC peuvent être fabriquées par des procédés de revêtement et d'impression en solution à faible coût. Bien que la structure soit simple, l'apparition simultanée d'une charge électronique et d'une charge ionique mobile introduit une fonctionnalité complexe. Les principes de fonctionnement de base ont été discutés pendant des années dans le domaine et un consensus a été atteint sur le modèle de dopage électrochimique. Pour une injection non limitée, la formation de doubles couches électroniques par les charges ioniques aux électrodes facilite l'injection de charges électriques. Par la suite, les charges injectées conduisent à la formation de régions dopées n et p à la cathode et à l'anode, qui sont compensées localement par des ions. Ce processus de dopage électrochimique augmente la conductivité électronique du matériau actif. Les régions dopées croissent et une région intrinsèque entre elles se rétrécit, où les porteurs de charge électronique se recombinent par recombinaison de Langevin émissive. Outre les polymères utilisés dans cette thèse, des complexes ioniques de métaux de transition, des petites molécules et des sels organiques ont été utilisés comme matériaux actifs LEC.

L'objectif de cette thèse est d'élucider l'interaction des charges électroniques et ioniques dans les LEC et de mettre en évidence les limites et les lacunes du modèle de dopage électrochimique fermement établi. Les méthodes et conclusions utilisées ne se limitent pas aux LECs à base de polymères et peuvent être appliquées à divers systèmes avec une conduction électronique et ionique combinée, comme cela a été démontré pour les LEDs en pérovskite.

Tout d'abord, les effets de la concentration d'ions et de la variation de l'épaisseur de la couche active dans la LEC polymère super yellow (SY), qui jouent un rôle critique sur les performances, sont étudiés. Leur optimisation conduit à une efficacité de courant de 11.6 cd A^{-1}, à égalité avec les OLEDs SY. La teneur en sel optimisée peut être expliquée selon le modèle de dopage électrochimique, car à de faibles concentrations, l'injection et la conduction des porteurs sont réduites, tandis qu'à des concentrations élevées, l'extinction des excitons réduit l'efficacité. La dépendance de l'épaisseur de la couche révèle l'effet microcavité/Purcell, souvent négligé, qui conduit à une forte dépendance de l'efficacité du découplage optique sur la position de l'émetteur (EP) dans la couche active. Une étude de modélisation optique complète inclut les changements des indices de réfraction et des pertes par auto-absorption induits par le dopage. Pour les PLEC plus épais, un changement continu de la couleur d'émission pendant le fonctionnement fournit une indication visuelle directe d'un EP mobile. Les résultats d'une analyse optique et électrique indiquent que la zone intrinsèque se rétrécit au début, mais commence à s'élargir par la suite, notamment bien avant que l'optimum électrique ne soit atteint. Cette constatation semble être en contradiction avec le modèle de dopage électrochimique. La simulation de la dérive-diffusion des mesures électriques attribue le déplacement du PE à la dynamique des ions et démontre que

la seule condition préalable à l'apparition de cet événement est l'inégalité des mobilités des cations et des anions. Les profils ioniques quantitatifs révèlent que le mouvement des ions s'arrête lorsque la zone intrinsèque se stabilise, confirmant la relation entre le mouvement des ions et le décalage EP.

L'origine non résolue de la dégradation après que l'état d'équilibre ionique ait été atteint conduit à l'étude de la LED polymère SY (PLED) avec l'idée d'isoler les effets électroniques des effets ioniques. Dans les PLEDs SY, il est fermement établi que le transport des électrons est sérieusement entravé par la présence d'un piège à électrons universel, et que la formation de pièges à trous régit la stabilité à long terme. La réponse des PLEDs au pilotage électrique et aux ruptures couvrant une échelle de temps allant de quelques microsecondes à (quelques) heures révèle une réponse caractéristique des pièges à électrons. De manière surprenante, la dynamique de remplissage des pièges à électrons prend des minutes à des heures, contrairement à la notion commune selon laquelle le piégeage des charges est complet après quelques centaines de microsecondes. Ce phénomène inhabituel n'a pas été rapporté jusqu'à présent et s'explique par la désactivation du piège lors de son retrait et sa réactivation lente. Les résultats fournissent un aperçu utile pour identifier la nature chimique des pièges à électrons universels dans les polymères semi-conducteurs. Par la suite, la réponse caractéristique des pièges à électrons aux coupures électriques est également identifiée dans le PLEC. Une étude plus poussée par mesure d'électroabsorption révèle que la formation de pièges à trous limite la durée de vie, exactement de la même manière que pour les PLEC. Par conséquent, les pièges de charge représentent un mécanisme de dégradation intrinsèque important, mais jusqu'à présent négligé, pour les PLEC.

La méthodologie permettant de démêler les processus dynamiques dus aux ions mobiles, aux charges électroniques et à la formation de pièges est appliquée aux diodes électroluminescentes en pérovskite (PeLED). Les PeLEDs ont atteint une efficacité quantique externe de plus de 20%, mais les défauts ponctuels ioniques - mobilisés par la haute température, l'irradiation et les champs électriques externes - contribuent à l'instabilité intrinsèque. En raison de la mobilité des défauts de piégeage, de nombreux processus supplémentaires par rapport à un système LED/LEC organique sont identifiés. L'application du modèle optique basé sur l'effet de microcavité à la PeLED est discutée. La variation expérimentale de l'épaisseur de la couche de transport TPBi d'une PeLED à base de $CsPbBr_3$ indique la validité du modèle optique. Une impulsion de tension transitoire révèle une caractéristique d'émission dans la gamme de temps de la mobilité ionique. La simulation transitoire de dérive-diffusion est capable de décrire l'augmentation d'émission observée en raison du mouvement ionique. La chute d'émission ultérieure n'est pas reproduite par la simulation, et les éléments manquants du modèle sont discutés.

Contents

List of Figures

List of Tables

List of Abbreviations

The commonly used unit is indicated.

a	Anion density [cm^{-3}]
A	Peak amplitudes [eV], Admittance [1/Ω]
AC	Alternating current
c	Cation density [cm^{-3}], speed of light 2.997*10^8 m/s
C	Oscillator damping factors (broadening) [eV]
C_p	Hole capture coefficient [cm^3/s]
C_n	Electron capture coefficient [cm^3/s]
CIE	Commission Internationale de l'Éclairage
D	Diffusion coefficient
DFT	Density functional theory
DMSO	Dimethyl sulfoxide anhydrous
DOS	Density of states
η_{out}	Out-coupling factor
$\eta_{s,t}$	Singlet/triplet factor
ε_0	Vacuum permittivity 8.854*10^{-12} F/m
ε_r	Relative permittivity
ϵ_∞	Limit of the dielectric function
E_0	Peak transition energy [eV]
E_e	Irradiance, radiant flux density [W/m^2]
E_g	Bandgap [eV]
e_n	Emission coefficient [1/s]
E_v	Illuminance [lx]
EA	electron affinity, electroabsorption
ECD	Electrochemical doping model
ED	Electrodynamic model
EDL	Electronic double layer
EIL	Electron injection layer
EL	Electroluminescence
EP	Emitter position
EQE	External quantum efficiency
ETL	Electron transport layer
EZ	Emission zone
f	Frequency [Hz]
FWHM	Full width at half maximum
F	Purcell factor
γ	Charge carrier balance factor
G	Generation rate
HIL	Hole injection layer
HOMO	Highest occupied molecular orbital
HTL	Hole transport layer
i	Intrinsic region
I_e	Radiant intensity [W/sr]
I_v	Luminous intensity [cd]
IS	impedance spectroscopy
iTMC	Ionic transition metal complexes

ITO	Indium tin oxide
J	Current density [mA/cm^2]
JV	Current (density)-voltage (measurement)
h	Planck constant 6.626*10^{-34} J s
k	Extinction coefficient
k_B	Boltzmann constant 8.617*10^{-5} eV/K
KPFM	Kelvin probe force microscopy
L_e	Radiance [W/(m^2 sr)]
L_v	Luminance [cd/m^2]
LEC	Light-emitting electrochemical cell
LED	Light-emitting diode
LUMO	Lowest unoccupied molecular orbital
μ	Charge mobility [cm^2/Vs]
MA	Methylammonium
n	Electron density [cm^{-3}], refractive index
$N_{0,N}$	Density of free electron states
n_t	Trapped electron density
ω	Angular frequency [Hz]
∇	Gradient operator
OLED	Organic light-emitting diode
p	Hole density [cm^{-3}]
Φ_e	Radiant flux $[W]$
Φ_v	Luminous flux $[lm]$
PeLED	Perovskite LED
PEDOT:PSS	Poly(3,4-ethylenedioxythiophene):poly(styrenesulfonate)
PL	Photoluminescence
PLED	Polymer light-emitting diode
q	Electric charge (absolute value) 1.602*10^{-19} C
q_0, q_{eff}	Internal quantum efficiency
q_{app}	Apparent internal quantum efficiency
R	Recombination rate [cm^{-3}s^{-1}]
SRH	Shockley-Read-Hall (recombination)
SY	Super yellow (polymer)
T	Temperature [K]
T$_g$	Glass transition temperature
THF	Tetrahydrofuran
TMPE	Trimethylolpropane ethoxylate
ToF-SIMS	Time-of-flight secondary ion mass spectrometry
TPBi	2,2',2''-(1,3,5-Benzinetriyl)-tris(1-phenyl-1-H-benzimidazole)
v	Drift velocity [cm/s]
V$_{OC}$	Open circuit voltage
Z	Impedance [Ω]

Aim and structure of the thesis

The research on ion motion in optoelectronic devices is a strongly emerging field. There are a number of applications where mobile ions control the device functionality, which is referred to as iontronics.[1,2] Memristors[3,4], ionic transistors, sensing devices as well as electrochromic or electromechanic devices[1,2] are interesting developments which may become relevant in the future. Essentially, this definition applies to batteries as well; however, in this case the ion conduction within the liquid or solid electrolyte and electronic conduction at the electrodes are spatially separated. The polymer light-emitting electrochemical cell (PLEC) is an example where the electrolyte is intermixed with the conducting polymer. The combination of ionic and electronic conduction brings about a high complexity because the ionic and electronic charges influence each other through their charge. Moreover, the study of their interaction becomes also relevant for the field of perovskite devices, where the ionic motion is undesired and results from defects in the crystal structure.

This thesis aims at unravelling the interplay of ionic and electronic charges relevant for the device performance of the super yellow PLEC beyond the established electrochemical doping model. **Chapter 1** introduces the relevant techniques to do so which are used in this work. On one hand, these include measurements that shed light on the dynamic behaviour of ions and electrical charges. On the other hand, drift-diffusion simulation of those measurements enables further insight into the relevant processes. **Chapter 2** investigates effects of ion concentration and active layer thickness on the performance of PLECs. The discussion of the layer thickness introduces the important microcavity effect in light-emitting devices by an optical modelling study, which is an interference effect due to the metal electrode. This effect is often overlooked in discussions of light-emitting device performance during operation, especially in the PLEC field. Its relevance is then shown in **chapter 3**, where the optical model explains a continuous change of the emission colour for thick PLECs as a result of a moving emissive region over time. A combination of impedance spectroscopy and its electrical model reveals that the only precondition for this event to occur is that the mobilities of cations and anions are not equal. As a result, the faster cations move first to the cathode, and the subsequent process of colour change over hours is observed during the movement of the anions. While the optoelectronic behaviour is dominated by the ionic movement until the steady state is reached, the subsequent change in performance, denoted as degradation, must have a different origin. Furthermore, short breaks at 0 V during the ionic movement indicate a secondary slow effect next to to the dynamics of the ions, which I identify as electron trap filling. The investigation of charge traps leads to **chapter 4**, where a polymer LED (PLED) is investigated, which isolates the ionic effect. It is firmly established that hole trap formation governs the long-term degradation of PLEDs. The study of electron traps, again with short breaks at 0 V, reveals that filling of deep traps takes minutes to hours, which we explain with trap deactivation upon de-trapping and slow trap reactivation. **Chapter 5** unifies the former chapters by identifying the presence of electron traps in the intrinsic region of PLECs, and hole trap formation as a so far overlooked long-term degradation mechanism of these devices. Finally, **chapter 6** discusses the transfer of the methodology to investigate trap and ionic induced effects in SY PLEDs and PLECs to perovskite systems.

Chapter 1 Introduction

1.1 Salt semiconductors and devices

The term salt semiconductor in general describes semiconducting material systems that are composed of cations and anions. This work specifically investigates systems with mobile ionic species that alter the performance of the operated optoelectronic device in an applied electric field. Salt semiconductors are therefore classified in materials with immobile or mobile ions during operation.

A prominent example of an immobile salt semiconductor is PEDOT:PSS consisting of the cationic ionomer poly(3,4-ethylenedioxythiophene) (PEDOT) and the anionic ionomer polystyrene sulfonate (PSS), which has been used as hole transporter for many years in light-emitting devices[5] and solar cells[6,7]. It is still actively researched[8], especially to reduce the degrading nature due to the acidic PSS chain.[9] The electronic conductivity is a result of the connected p-orbitals and thus delocalized electrons, leading to the conjugated system.[10]

The next class of materials consists of a large immobile ionic chromophores with a small counterion used as active material in optoelectronic devices. In this case, the counterion has a high enough mobility when an electric field is applied. One example of the many organic dyes that fall into this category[11] are the cyanine dye as for e.g. Cy3-P shown in **Figure 1.1**. These dyes are used as absorbing layer in solar cells[12,13], photodiodes[14] , upconverters [15], or light-emitting devices, specifically LECs due to the mobile ionic nature[16,17]. Another example are ionic transition-metal complexes often used in LECs. They consist of a metal core like iridium or ruthenium surrounded by ligands and outer conjugated molecular parts. The positively charged complex is then again neutralized by a small anion, often also PF_6^-.[18,19] A big advantage is their triplet exciton emission, i.e. phosphorescence, as singlet emitters such as polymers loose already 75% of the energy in triplet excitons that cannot recombine radiatively.[20]

Cy3-P
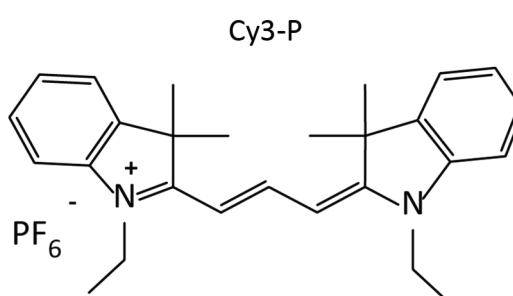
Figure 1.1. Trimethine cyanine cationic dye with the anion PF_6^-

The next two material classes contain both cationic and anionic mobile species within an electric field. The first class used for LECs is a polymer intermixed with a salt, such that the active component and the ionic part are separated. In this thesis the phenyl-substituted poly(para-phenylenevinylene) copolymer called super yellow (SY, see **Figure 1.2**) is intermixed with lithium trifluoromethanesulfonate ($Li^+CF_3SO_3^-$). To ensure perfect intermixing and conductivity of the ions

a third component (named "ion transporter"[21]) is blended, such as polyethylene oxide[22,23] or hydroxyl-capped oligoethers, for example trimethylolpropane ethoxylate (TMPE) as in this work.
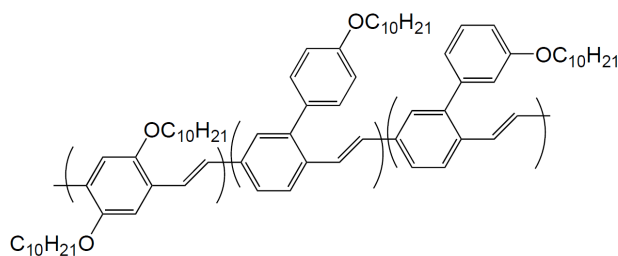
Figure 1.2. Super yellow, a phenyl-substituted poly(para-phenylenevinylene) copolymer

A completely different material class containing ionic species are crystalline perovskite structures used in a variety of optoelectronic devices ranging from LEDs[24], LECs[25] and solar cells[26] up to lasers, photodiodes and transistors[27]. The interest in perovskite materials is explained by their excellent optical and electronic properties, such as high internal quantum efficiency, long diffusion length and high charge carrier mobility.[28,29] The A-site cation of the ABX_3 structure is typically methylammonium (MA), formamidinium (FA), or caesium (Cs), B is a lead or tin cation, and X is a halogen anion such as bromide, iodide or chloride. As the activation energy of charged crystal defects such as vacancies or interstitials is low [30,31], similar effects as in LECs have been identified as the ionic defects are mobilised in an applied electric field.[32,33] A fundamental difference to the polymer LEC system is that the ions in the perovskite layer are part of the crystal structure, and their movement therefore can also lead to phase separation.[34]

1.2   Organic light-emitting diode and electrochemical cell

Before diving into the functioning of an LEC, the working principle of an organic LED is explained at the example of a SY polymer LED (PLED). In this case, the active layer consists solely of the polymer, spin coated typically from toluene or tetrahydrofuran. The latter solvent leads to more coiling of the polymer in the film and thus weaker interchain interactions.[35] This decreases the conductivity, but increases the internal quantum efficiency as quenching is reduced. Due to the general coiling of the polymer in the film, there are breaks in the conjugation leading to disordered states. Therefore, the electronic charge transport is described as hopping from localized state to state, where the energy difference is overcome by absorption and emission of phonons.[36] The mobility is thus much lower than in a crystalline system with band conduction as in a perovskite layer.

To ensure proper injection of the charge carriers into the active layer, additional layers are introduced next to the two electrodes. The hole transport in the highest occupied molecular orbital (HOMO) of the SY polymer is matched with the PEDOT:PSS HOMO next to the indium doped tin oxide electrode. The lowest unoccupied molecular orbital of the SY is matched with the work function of a thin calcium layer next to the aluminium electrode. **Figure 1.3**a shows the energy levels of all mentioned layers. In inorganic semiconductor devices n- and p-doping introduces a pn-junction, which leads to a built-in field as a result of static charges close to the junction.[37]

While the term built-in field also exists in organic semiconductors, it has a different physical origin. The situation shown in Figure 1.3a shows the device in open-circuit condition, i.e. when the device is at rest and unconnected. There is obviously no current flowing for the situation of the unconnected device. When the two electrodes are connected to a voltage source, there is a voltage where the open circuit situation is reproduced, which is the in theory the difference between the anode and cathode work function. Note that the resulting work function of the Ca/Al layers will be closer to the Ca work function, as it is pinned to the lowest unoccupied molecular orbital (LUMO) of the SY[38], and the two metals will equilibrate[39,40]. For an assumed resulting work function of 3 eV for the Ca/Al layer, the necessary voltage would here be 1.8 V to reach open circuit condition. This value of 1.8 V is the built-in field. If the applied voltage is below, e.g. short circuit at 0 V, there is an electric field within the layers in the opposite direction since the bands get bent. The biggest part of this built-in field will drop across the SY layer as it has the lowest conductivity. When a voltage higher than 1.8 V is applied, the electric field points in the direction where charges can be injected from both electrodes, which then form excitons in the centre of the SY layer which recombine radiatively. Note that in a real measurement the current will also be positive below 1.8 V (> 0 V) due to the shunt resistance within the device.
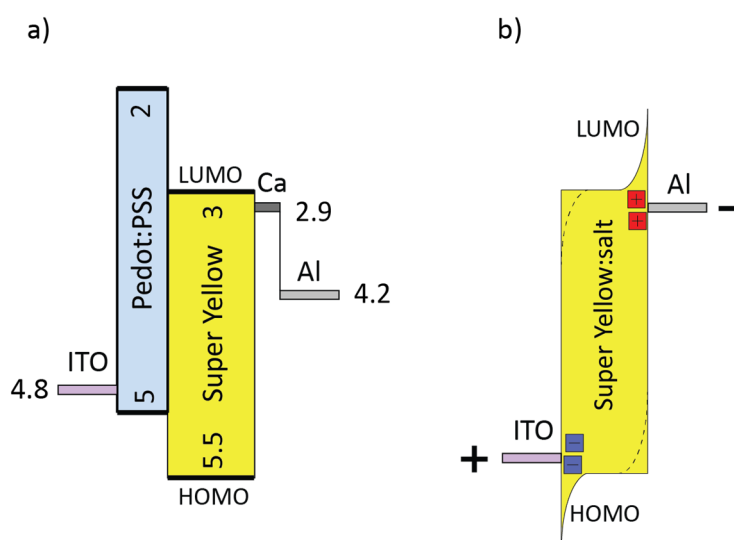
Figure 1.3. SY PLED and LEC energy diagram.

To fabricate an LEC as in Figure 1.3b, the PEDOT:PSS and Ca layer are omitted, which leads to high injection barrier on both sides. This is overcome by the addition of a salt as described in section 1.1, which splits up into ions under an applied electric field. The first of two processes the ions introduce is the formation of an electronic double layer (EDL) at both interfaces as the ions move to their respective interface. The EDL consists of an ionic charge on the SY layer side, countered by electronic charge on the electrode side. This introduces a very high capacitance and thus a strong electric field in a very small region at the interface of a few nm. The resulting potential drop bends the HOMO and LUMO at the interface as illustrated in Figure 1.3b, such that charge tunnelling from the electrode into the SY layer gets possible. This leads to a strong increase of

current and luminance when a constant voltage is applied, or a strong decrease of voltage and increase of luminance as shown in **Figure 1.4**a in the first hour (segment ①).

The second ion-induced process is the formation of doped zones. With the starting injection, electronic charges travel inwards as polarons on the SY backbone and are attracted by counterions, thus forming a static, uncharged doping element as shown in Figure 1.4b, segment ①. Due to the charge neutrality, a high doping density is possible, resulting in a considerably increase of the conductivity in the regions close to the electrodes. With progressing time, these doped regions grow inwards, which leads to a shrinking of the intrinsic region and thus further (slower) increase of luminance and decrease of voltage over several hours (segment ②). The steady-state situation when the doped zones do not grow anymore and the ionic motion has stopped can be compared again to a PLED structure with electrode, EDLs as injection layer, doped regions as transport layers and the intrinsic region as the active layer. The subsequent increase of voltage is commonly attributed to degradation[19,41], while a decrease in luminance is often explained by increased exciton quenching as the intrinsic region gets thinner (segment ③ in Figure 1.4a).[42,43] The explanation up to this point follows the firmly established electrochemical doping model (ECD), in contrast to the injection-limited electrodynamic model (ED) without doped zone formation and without potential drop in the intrinsic region.[44,45] As explained in chapter 3, movement of the intrinsic region due to ion dynamics introduces changes in the current/voltage and luminance characteristics and is the dominating process in this system until the ions are in steady state. The subsequent degradation is pinpointed to hole trap formation as explained in chapter 4.
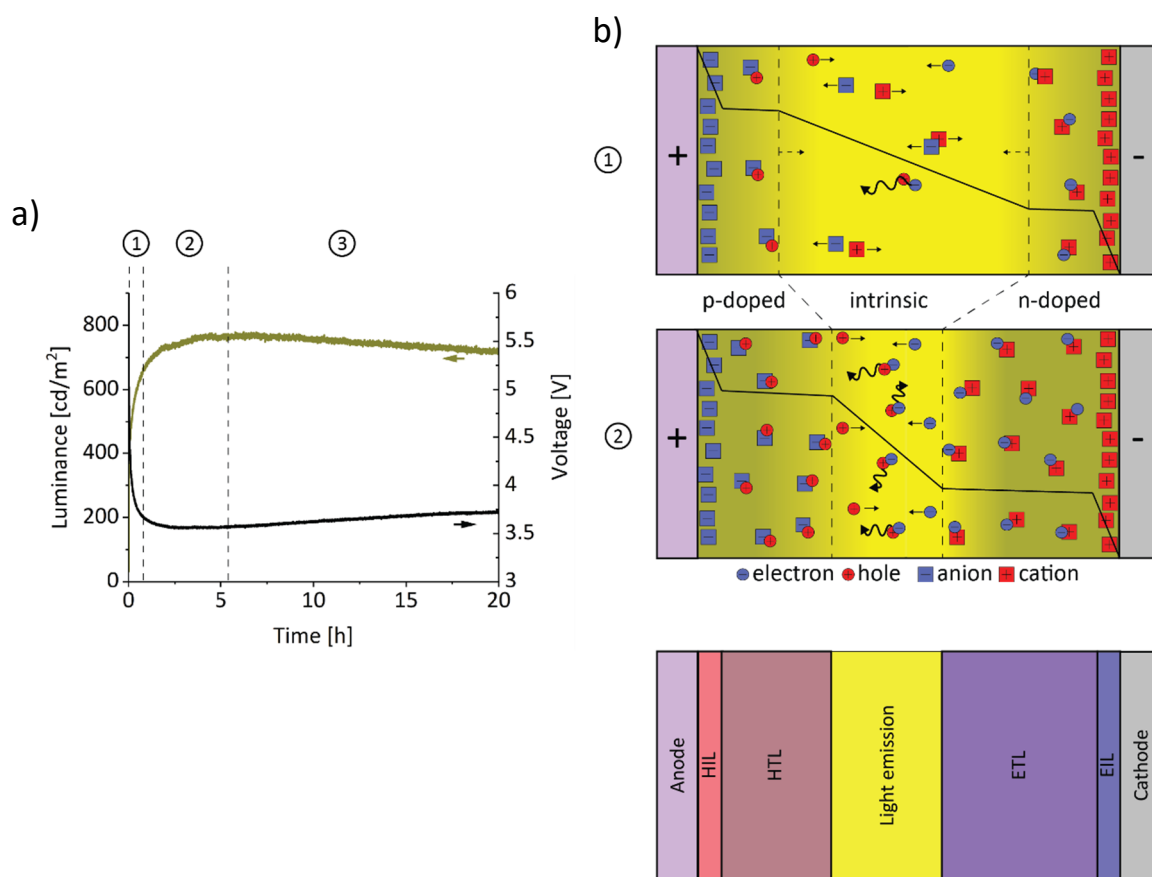
Figure 1.4. a) Measurement of a thin LEC with a SY thickness of 70 nm. b) LEC working principle. The black line is the qualitative drop of the potential within the EDL and the intrinsic region.

1.3   Characterization

1.3.1   Emission Characterization

While the optical part of the solar cell characterization is rather simple as the relevant spectrum is defined by the sun, it is much more complex for LEDs. This is because a comparison of efficiency between LEDs with different emission spectra needs to take into account the energy of the emitted photons. In addition, we have to introduce a quantity that describes the efficiency in terms of how humans perceive light, as this is mostly the ultimate application. For LEDs, light is characterized with radiometric or photometric quantities, as shown in Table 1.1. Photometric quantities describe how a human eye perceives the emitted light from a LED as an integral over all wavelengths of the spectral power in watts multiplied by the photopic luminosity function shown in **Figure 1.5**. The luminosity function was defined by the Commission Internationale de l'Éclairage (CIE) in 1924 and is still a standard, despite its inaccuracies in the short wavelength region, where the function is an underestimation[46]. For this reason it was further improved.[47,48] Note that there is also a definition of the CIE in 1951 for the human vision in the dark called scotopic luminosity function.[46] All radiometric quantities can be shown spectrally resolved or integrated as in **Table 1.1**, while photometric quantities are usually integrated. The power units (radiant and luminous flux) describe the power of a light source across several or all angles, as for example measured by a photodiode or a spectrometer with an integrating sphere, respectively. There are several definitions to describe a light intensity, their usage depends on the situation. If for example the source is far away as for the sun where the light rays are parallel, it is useful to divide the power by the detector area, i.e. watts per square meter here on earth (irradiance). This quantity is also applied for angular emission measurements of a light source with a fibre, where the incoming power per fibre area is measured. For a close light source where the light rays are not parallel the intensity is described as power per steridian. Within the photometric quantities this is called candela (lumen per steridian). If these quantities are divided additionally by the source area, we end up with radiance and luminance. The latter is measured for example with a Konica Minolta camera, which measures like a fibre from a specific angle, but with the lens optics in front the camera is additionally focused on a specific spot on the light source such that it is able to measure the luminous intensity per source area. Note that this camera, in contrast to a photodiode, has a built in optical filter that matches the photopic luminous function in order to measure photometric quantities.

Table 1.1. Radiometric vs. photometric measurements (modified from [49])

	Radiometry *e*: energetic		Photometry *v*: visual	
Power	Radiant flux	$\Phi_e = \dfrac{dE}{dt}\ [W]$	Luminous flux	$\Phi_v\ [lm]$
Power per steridian	Radiant intensity	$I_e = \dfrac{d\Phi_e}{d\Omega}\ [\dfrac{W}{sr}]$	Luminous intensity	$I_v\ [cd = \dfrac{lm}{sr}]$
Power per detector area	Irradiance, radiant flux density	$E_e = \dfrac{d\Phi_e}{dA_t}\ [\dfrac{W}{m^2}]$	Illuminance	$E_v\ [lx = \dfrac{lm}{m^2}]$
Intensity per source area	Radiance	$L_e = \dfrac{dI_e}{dA_e}\ [\dfrac{W}{m^2 sr}]$	Luminance	$L_v\ [\dfrac{cd}{m^2}]$
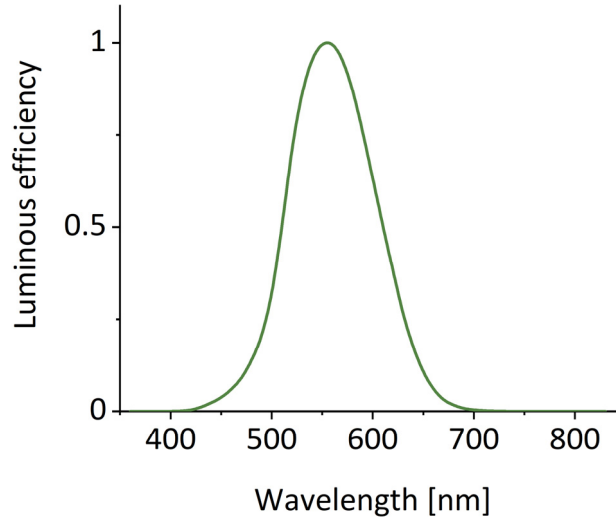
Figure 1.5. Photopic luminosity function.[46] The maximum of the function is 683 lm/W.

Table 1.2 shows further relevant quantities for the measurement and calculations in the field. From the luminance measurement $L_v\ [cd/m^2]$ at a given current density $J\ [A/m^2]$ and voltage, the current efficacy (also called current efficiency) is calculated as $L_v/J\ [cd/A]$. The change to radiance $L_e\ [W/m^2 sr]$ is calculated by using the above mention integral such that

$$L_e = \frac{L_v}{\int \Phi_{e,normed}(\lambda) * V(\lambda) * 683\ \text{lm/W}} \tag{1.1}$$

where $\Phi_{e,normed}(\lambda)$ is the electroluminescence spectra measured by a spectrometer and integrating sphere which is normed to an integrated area 1. $V(\lambda)$ is the photopic luminosity function in Figure 1.5. Note that the integral is therefore zero below 400 nm and above 700 nm. To calculate the luminous flux $\Phi_v\ [lm]$ from the luminance or radiant flux $\Phi_e\ [W]$ from the radiance, one has to know in principle the emission characteristics $L_e(\theta, \phi)$ of the whole

semisphere to be able to calculate the power emitted from the hole device from the radiance at one angle. The normalized emission characteristics times the maximum L_e is then integrated across the semisphere

$$\Phi_e = \int L_{e,norm}(\theta, \phi) * L_e \, d\theta d\phi \stackrel{Lamb.}{\hat=} \pi * L_e \tag{1.2}$$

where $L_{e,norm}(\theta, \phi)$ is typically assumed to be a Lambertian emitter, such that this integral results in simply a factor π. It has been shown by angular emission measurements that this assumption is valid for SY LECs below 100 nm active layer thickness, but is not true for thicker devices due to interference effects.[50] From the luminous flux, the power conversion efficiency is calculated by dividing with the electrical power, i.e. the current $I = J * A$ (area) times the voltage.

Table 1.2. Measured and calculated quantities as done in this thesis

Quantity	Unit	Measurement / calculation
Luminance L_v	$\dfrac{cd}{m^2}$	Konica Minolta measurement
Current efficacy	$\dfrac{cd}{A}$	Luminance / current density
Radiant flux Φ_e	W	Spectrometer with integrating sphere
Radiance L_e	$\dfrac{W}{m^2 sr}$	Equation (1.1)
Luminous flux Φ_v	lm	$\Phi_v = L_v * \pi$, see Equation (1.2)
Power conversion efficacy	lm/W	Lumen / Current * Voltage

In chapter 3, the measured angular spectral irradiance $E_e \, [W/m^2/nm]$ is fitted by simulated radiance spectra L_e at different angles. While these different quantities cannot be compared absolutely, their conversion is essentially only a factor, hence the relative changes in the spectra can be compared. The conversion factor would be the solid angle A_f/L^2 defined by the fibre area A_f and the optical path length from fiber to emitter L such that

$$L_e = \frac{\Phi_e}{A_f/L^2} = \frac{E_e * A_f}{A_f/L^2} = \frac{E_e}{L^2} \tag{1.3}$$

where the relation was used that the spectral irradiance E_e is the radiant flux Φ_e divided by the detector area, in the case of the measurement setup the fiber area A_f.

1.3.2 Impedance Spectroscopy

Impedance spectroscopy is a very useful measurement technique especially for devices with both electronic and ionic conduction. This is because the frequency sweep over many orders of magnitude allows tracking simultaneously those two charge carrier types with mobility differences of 10^6 or higher. As an introduction to impedance spectroscopy and capacitance measurement

used in the thesis, measurements of electronic circuit board elements with two adjacent capacitors each with a parallel resistor are shown. In **Figure 1.6**a, the real and imaginary part of the impedance is shown, while in Figure 1.6b the y-axis is the imaginary part of the admittance divided by the angular frequency $\omega = 2 * \pi * f$. It is named capacitance because in the case of an equivalent circuit network of a resistor with impedance $Z_R = R$ and a capacitor with impedance $Z_C = \frac{1}{i*\omega*C}$ in parallel described by the impedance Z and admittance A

$$Z = Z_R // Z_C = \cfrac{1}{\cfrac{1}{R} + \cfrac{1}{\cfrac{1}{i*\omega*C}}} = \cfrac{1}{\cfrac{1}{R} + i*\omega*C} \quad \rightarrow \quad A = \frac{1}{Z} = \frac{1}{R} + i*\omega*C \tag{1.4}$$

the above-described definition of the y-axis indeed results in the capacitance, as $\frac{Im(A)}{\omega} = C$. The measurement in beween A and B can indeed solely be described by the parallel connection of the 1 nF capacitor and the 200 Ω resistor, therefore the capacitance measurement shows a flat line at 1 nF. For the parallel connection in between B-C the series resistance of the cables of 2 Ω must be taken into account to describe the reduction at high frequencies. This is the RC effect, i.e. the frequency gets too fast to charge the capacitor. The cutoff frequency is calculated as $\frac{1}{2*\pi*R*C} = \frac{1}{2*\pi*2\Omega*5nF} = 1.7 * 10^7\ Hz$ in this case, which matches the measurement. As the smaller capacitor between A-B has a cut of frequency of $8 * 10^7\ Hz$, we do not see the decrease in the capacitance measurement. Unless the parallel resistance is not too small such that the capacitor partially discharges, the capacitance value can be directly read from the plot in Figure 1.6b for the individual networks A-B or B-C. This is apparently not true anymore for the series connection of the two capacitor parallel connections in between A-C. Furthermore, variation of the parallel resistor also influences the individual capacitance level even for higher values. It is therefore already necessary for this simple series connection to extract the individual physical parameters with equivalent circuit modelling.
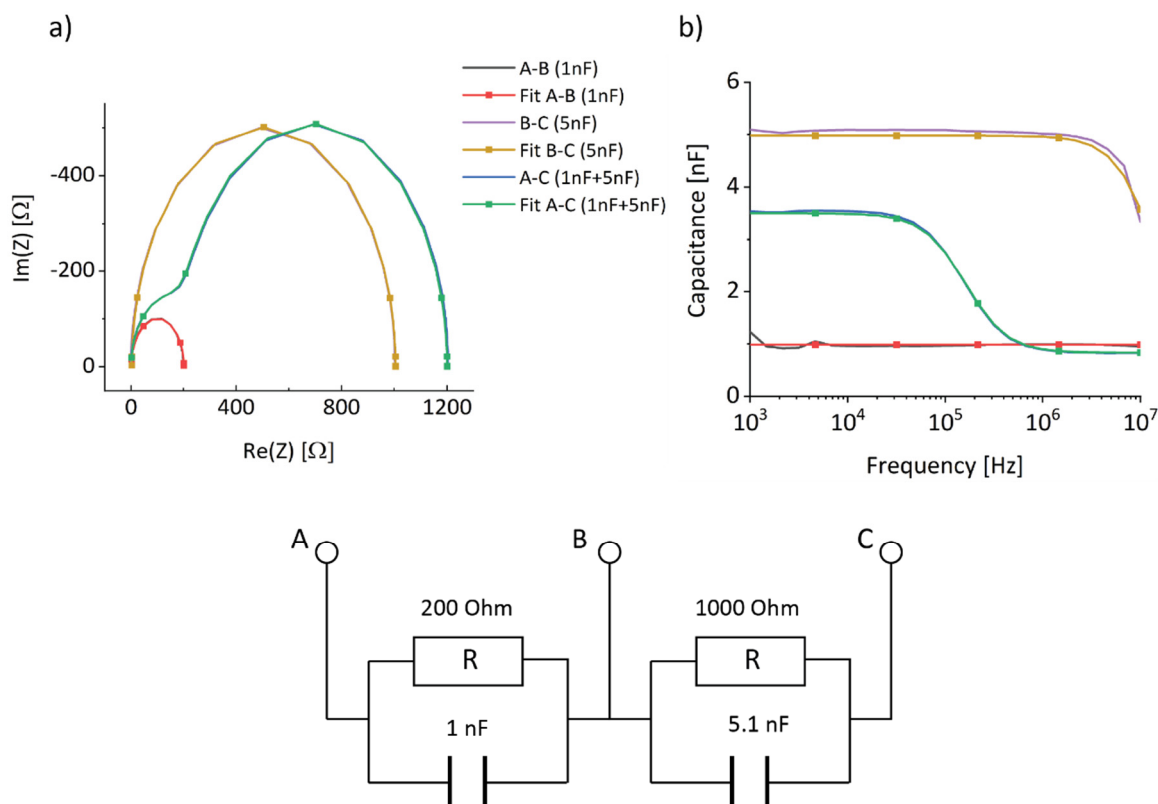
Figure 1.6. a) Real and imaginary part of the impedance of the parallel connection in between A-B and B-C, as well as the series connection in between A-C. The components are inorganic electronic circuit elements. b) Capacitance vs. the frequency f calculated from the impedance measurement. All measurements are fitted with the equivalent circuit as shown in the schematic. Note that the fitted value for the higher capacitance was 5 nF, the other parameters matched the datasheet values. To simulate the decrease of capacitance of the B-C circuit at high frequency, the cable series resistance of 2 Ω had to be introduced.

In the following, impedance measurement of LECs and PLEDs are discussed where it becomes evident that the SY LEC behaves like a single parallel connection of a capacitor and a resistor with a series resistance in front[51,52], such that direct read out of the geometric capacitance is possible. This is not the case for the PLED, as equivalent circuits often use series connection of capacitors.[53–56] The capacitance measurement of pristine thin and thick LECs (ITO/SY/Al) are shown in **Figure 1.7**a (black). As shown in chapter 3, the thickness of the SY layer calculated from the capacitance level ($C = \varepsilon_r \varepsilon_0 * \frac{A}{d}$) agrees with the thickness obtained from profilometer measurement. The red curves show the measurements after the LECs were biased for several hours such that doped regions developed. For low enough frequencies, the AC charges are then able to penetrate into the SY layer across the doped zones, where they pile up at the intrinsic region as simulated in Figure 1.7b. The integration of one simulated charge peak is $1.24 * 10^9\ cm^{-2}$, which leads to a capacitance of $C = \frac{Q}{U} = \frac{1.24*10^9\ cm^{-2}*q}{10mV} = 20\ nF/cm^2$. This capacitance corresponds to the measured capacitance in Figure 1.7a at 10 Hz. Since the charges pile up at the edge of the intrinsic

region and the thickness can be calculated from this capacitance, here $d = \varepsilon_r \varepsilon_0 * \frac{A}{C} = 2.8 * \varepsilon_0 * \frac{1}{20\frac{nF}{cm^2}} = 124\ nm$, the thickness of the intrinsic region can be tracked with the capacitance measurement at low frequencies.
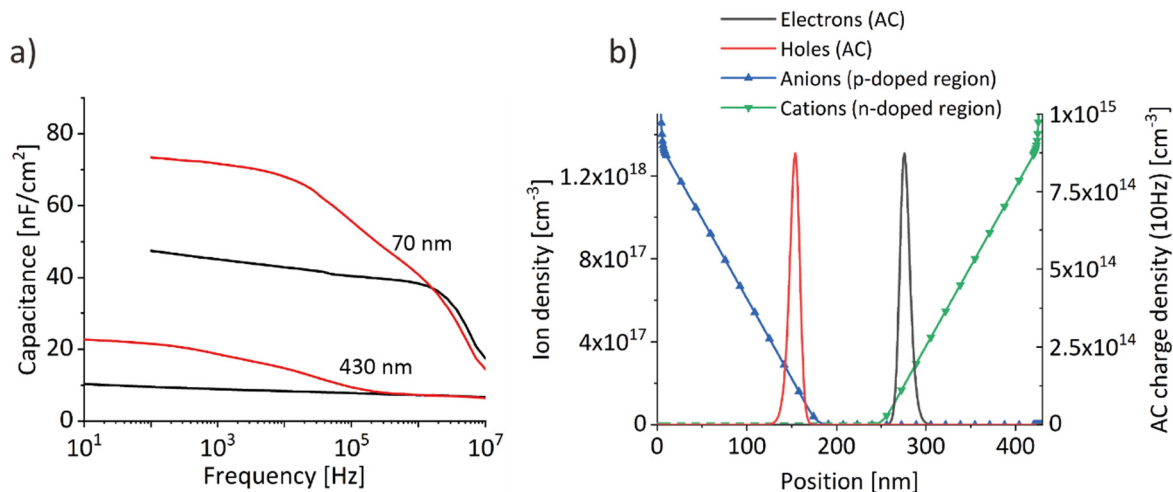
Figure 1.7. a) Capacitance measurement of thin (70 nm) and thick (430 nm) SY LECs after fabrication (black) and after a several hours of biasing at 7.7 mA/cm^2 (red). b) Simulation of a sinusoidal voltage with a frequency of 10 Hz and an amplitude of 10 mV, leading to a pile up of electric charges at the intrinsic region. Shown is the charge during the positive peak of the sinusoidal voltage, when the full 10 mV is applied to the ITO electrode.

If we now look at capacitance measurements of a PLED in **Figure 1.8**a, the features look similar to a biased LEC as there is a second capacitance plateau emerging at low frequencies. Here, however, it is not because of an intrinsic region that gets thinner, but the result of two capacitances in series, one for the SY layer and one for the PEDOT:PSS layer.[53–56] A direct interpretation of the capacitance level as geometric capacitance is therefore critical as explained above.

As explained in section 1.2, the EDL introduces a high capacitance and as such can be measured with impedance spectroscopy. Because ionic movement to the interface forms this capacitance, it arises only at very low frequencies. Figure 1.8b shows the measurement of a CsPbBr$_3$ perovskite LED, where a strong increase of the capacitance below 0.1 Hz is observed. For even lower frequencies, a plateau would be reached where the EDL capacitance could be read from.[57] Note that in the perovskite literature the EDL is sometimes called Helmholtz layer, as he was the first to study the effect of the EDL.[58] As the ionic mobility is much lower in the SY LEC system, the EDL capacitance could not be measured.

A rise in capacitance to a secondary plateau was also interpreted as a result of traps that are "stored" and that are only released below a certain frequency.[59–61] In the SY PLED, the capacitance measurement at 0 V does not change over several hours of biasing while at early times electron and later hole traps develop, therefore an interpretation of the capacitance rise as a result of traps is unlikely. Capacitance-voltage measurements, where the offset voltage was varied for a fixed frequency, has been used to quantify hole trap site densities of SY PLEDs by fitting a characteristic

negative capacitance contribution due to a recombination current at voltages close to the bandgap.[62] Note also that in perovskite devices a negative capacitance at voltages close to the bandgap was identified, however this was the result of ionic movement that modifies electronic charge injection and transport.[63]
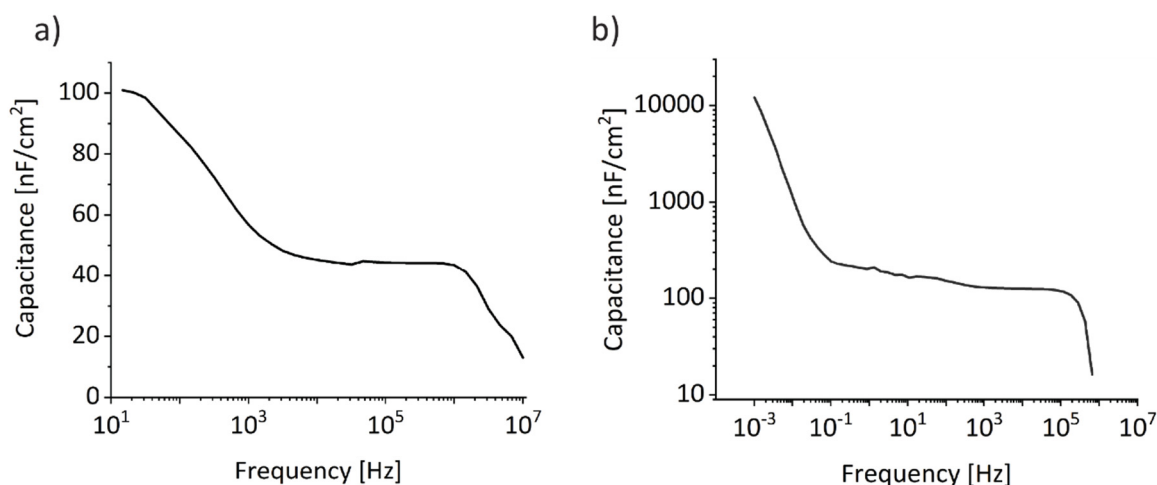
Figure 1.8. a) Measurement of an 85 nm thick PLED which does not change during biasing. b) Impedance spectroscopy to very low frequencies of a perovskite LED (ITO/PEDOT:PSS/CsPbBr$_3$/TPBi/LiF/Al)

1.3.3 Transient optoelectronic measurements

Even a simple constant voltage pulse is able to reveal many different dynamic processes within an optoelectronic device. The interpretation, however, is not straightforward and requires an overview of the many possible origins over several orders of magnitude in timescale. **Figure 1.9** shows examples of such dynamic effects in a SY PLED and LEC system. There are many electronic processes faster than ns which are not mentioned here, for example intersystem crossings or phonon interactions.[10] Photoluminescence decay in SY is in the order of a few ns and is a measure for the exciton lifetime.[64,65] Electroluminescence decay on the other hand takes a few µs as the free charges first have to form excitons (see chapter 4).[65] The charging of the capacitance with the characteristic RC time (when it is charged to 63%) is for a typical capacitance of 50 nF/cm^2 and a series resistance of 10 Ohm $\tau_{RC} = 2 * \pi * 50 \frac{nF}{cm^2} * 0.03 \; cm^2 * 10 \; \Omega = 94 \; ns$ and can get above µs for larger areas and capacitances. It is important to keep this charging and decharging time in mind as it can distort fast transient measurements. Another distortion for fast measurements is the displacement current as a result of fast changes in the electric field. It is typically visible in transient measurement when the bias is switched on as in **Figure 1.10**a (segment ①). It also gets relevant for hysteresis measurement, as a ramp rate of 10 V/s as shown in chapter 4 introduces a displacement current of about 3*10^{-3} mA/cm^2, and a rate of 1000 V/s already 0.15 mA/cm^2, such that low current behaviour cannot be observed. The measurement agrees with the displacement current law[66] $J_D = \frac{d}{dt} \varepsilon_0 \varepsilon_r * E = \varepsilon_0 \varepsilon_r * \frac{dV}{dt} * \frac{1}{d}$. For $\varepsilon_r = 2.8$, the layer thickness d of 100 nm

where the voltage drops and generates on average the electric field $E = \frac{V}{d}$, the resulting displacement current is $2.5 * 10^{-3} \frac{mA}{cm^2}$ for the rate $\frac{dV}{dt} = 10\frac{V}{s}$ and $0.25 \frac{mA}{cm^2}$ for the rate $1000\frac{V}{s}$.

Displacement current

e⁻/h⁺ movement   Ion movement ─────────

PL decay   EL decay   Joule heating

RC time   Trap filling   Trap emptying (0V) ─────────

ns   μs   ms   s
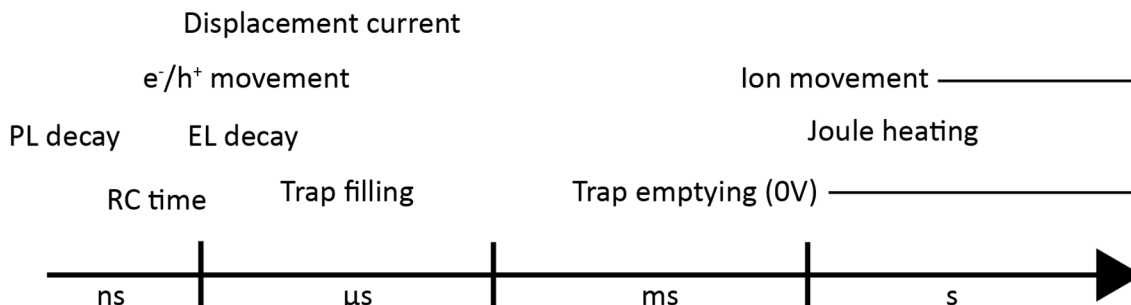
Figure 1.9. Time range of different dynamic effects for the example of the SY PLED and LEC system

For typical organic mobilities in the order of 10^{-6}-10^{-5} cm²/Vs space charge takes several μs to build up when a bias is applied. For an average field of 200 kV/cm (see chapter 4) the drift velocity $is\ v\ = \mu * E = 10^{-5} \frac{cm^2}{Vs} * 200 \frac{kV}{cm} = 2 \frac{cm}{s}$ such that it takes 5 μs for the electronic charge carriers to travel 100 nm. This time scale can be observed in Figure 1.10a (segment ②) as the time it takes for the emission to peak, here about 10 μs, as the Langevin recombination is proportional to the product of the electron and hole space charge. In the SY PLED system, the trap filling is slower and leads therefore to the drop of the emission as shown in segment ③ until an electronic steady state is reached, and the emission is stable for some time. In segment ④, the emission and current decrease again and show a slow effect. As explained in chapter 4, we attribute this effect to the slow formation of trap sites. Trap emptying at 0 V by thermal emission across the trap depth barrier is an effect that is spread from ms up to days, as the de-trapping rate drastically changes over many orders of magnitude for trap depths from 0.4 eV to 0.7 eV. Ion dynamics occurs within seconds for perovskite systems[67] and also TMC based LECs[68], and can go up to hours as shown in chapter 2 and chapter 3. A very important effect to keep in mind is Joule heating or self-heating as soon as the device is switched on. The time until an equilibrated temperature is reached takes seconds to minutes[69] and can influence several processes within a device. Note that a different effect of Joule heating is the coupling of temperature increase and voltage drift, where the temperature is responsible for the voltage increase, which in turn leads to more Joule heating. This spiralling effect has been documented in MEH-PPV LECs.[70]
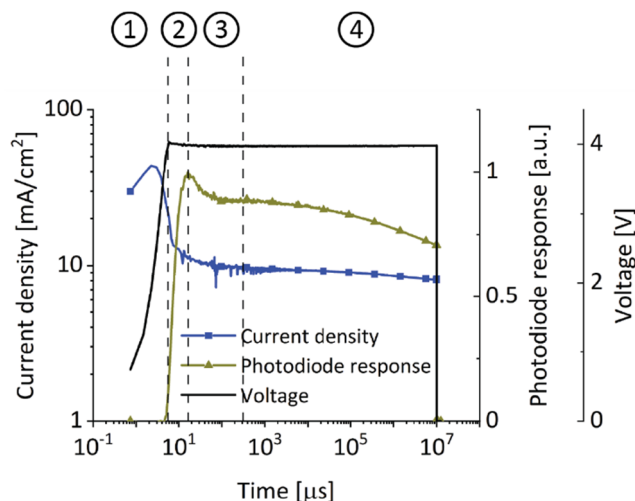
Figure 1.10. Current and emission response to a 4 V pulse applied to a SY PLED

The complexity of dynamic response interpretation results from the relation of the different processes. Arguably, the most critical parameter is the temperature, as nearly all processes within an optoelectronic device are temperature dependent. It is therefore mandatory to investigate the role of temperature early on. This can be done by intentionally heating and cooling the device to understand its effect on transient measurements as shown in chapter 4. Infrared camera measurements also help to pinpoint the actual temperature increase and equilibration time for a given applied electric power, such that Joule heating can be excluded as reason for transient effect of shorter or longer duration (see chapter 5). Trapping of charges has - besides the introduction of a further recombination channel (SRH) - a large effect on the whole system when the trap site density was neutral and gets charged with the trapped species as in the polymer systems of Figure 1.10. In this case, the trapped charge leads to a decrease of electronic space charge which in turn reduces the current and the Langevin recombination ([71], see chapter 4). The relation of space charge and trap dynamics is a good example for how the relative speed of the two processes matters. The only reason why we see a peak in the emission (Figure 1.10) is because charge trapping as slightly slower than the build-up of space charge. If the trapping would be faster (i.e. higher capture coefficient, see chapter 4), then we would have a completely different situation. In this case, trapping would happen during the build-up of the space charge, i.e. as soon as the space charge grows, the amount of trapped charge adjust immediately. In this case, there would be no emission peak visible, the plateau at the end of segment ③ would be directly reached. Ionic movement is an example of how a slow process changes the device situation, such that in turn all fast processes adapt. At the interface, for example, ions lead to increased injection due to the formation of an EDL (in perovskite devices[33] and polymer LECs in this thesis) or decrease of interface recombination in perovskite devices.[72] While the ions move and pile up at the interface, all faster processes like changes in space charge and therefore also bulk trap densities adapt instantaneously. For the sake of completeness, a fast process can also invoke the change of a slow process. As an example, a change of the applied potential leads to a fast change of the electric fields within the device, which in turn invokes the change of essentially all other processes. A more intriguing example her is the irradiation of a device with light. The resulting photocarriers in a

perovskite solar cell alter the electric field distribution, which then in principle leads to a redistribution of ions on a slower timescale. Slow changes of the trap distribution upon irradiation of light are shown in chapter 4 and 5.

1.4   Device Simulation

Simulating and modelling are often used as synonyms, also throughout this thesis. However, a distinction of these two terms is possible.[73] Modelling, i.e. the building of a model is the process of approximating a real system, in the context of this work by mathematical equations. Simulating, i.e. creating a simulation is then the usage of the model to study a behaviour by changing a parameter, here this parameter is mostly time for a transient simulation or infinite time for a steady state simulation. Optoelectronic device behaviour can be simulated on many levels. Density functional theory (DFT) is modelling on a deepest, quantum mechanical level such that e.g. band structures or molecular orbitals can be calculated.[74,75] On an arguably higher level to compute dynamics of molecular or atomic systems, there is Monte Carlo or Molecular Dynamics simulation. Thereby, thermodynamic properties and evolution of systems can be computed.[76,77] With the jump to drift-diffusion simulation used in this work, we change from microscopic to macroscopic quantities. Many quantum mechanical quantities are then summarized in one parameter, for example the mobility of a charge carrier. Optoelectronic behaviour of one device can be simulated. On a slightly higher level, equivalent circuit modelling is also able to simulate electronic measurement of devices by modelling physical processes with building blocks such as capacitors and resistors.[51,78] This also enables simulation of more complex structures, e.g. monolithically interconnected solar cells or crosstalk in LED display pixels.[79,80] Since with this method large electronic circuits can be simulated, this method is considered as the highest level of optoelectronic device simulation. On a similar, narrower level is finite element simulation which can be as well used to simulate solar modules and LED displays.[80,81]

The application of drift-diffusion simulation is separated in three categories. Fitting studies aim at reproduce a certain measurement, often a current-voltage measurement, in order to identify a relevant process. For example, constant current measurements of a SY PLED were fitted to show the relevance of increasing hole traps and to quantitatively determine their density[71], or temperature dependent current-voltage measurement of perovskite films were fitted to extract information on the relation of hole, electron and ion transport.[82] The second category are parameter studies where the goal is to explore the model behaviour. The studies are especially robust if it follows from a fitting study.[83] A third group uses simulation on a qualitative level to compare with measurements, with the goal to identify dominating processes and elucidate their origin. The use of drift-diffusion in this work varies in between these three groups, the goal however is in line with the third group.

1.4.1   Electrical Simulation

The very heart of the electrical model are the drift currents of charged particles due to an electric field (marked in blue for electrons n, holes p, anions a and cations c) and diffusion currents due to statistical diffusion of randomly moving particles in a gradient profile (marked in green) leading to the total currents

$$\vec{J_n} = q * n * \mu_n * \vec{E} + q * D_n * \nabla n(\vec{r}) \tag{1.5}$$

$$\vec{J_p} = q * p * \mu_p * \vec{E} - q * D_p * \nabla p(\vec{r}) \tag{1.6}$$

$$\vec{J_a} = q * a * \mu_a * \vec{E} + q * D_a * \nabla a(\vec{r}) \tag{1.7}$$

$$\vec{J_c} = q * c * \mu_c * \vec{E} - q * D_c * \nabla c(\vec{r}) \tag{1.8}$$

where the charge q is the absolute elementary charge, the mobililty μ describes the relation of electric field to the drift velocity $\vec{v} = \mu * \vec{E}$. The notation is generalized with respect to the dimension, typically the implementation is one-dimensional, i.e. $\nabla n(\vec{r}) \to \frac{dn(x)}{dx}$. This is because the lateral scale of mm-cm is much larger than the thickness of a device below μm, such that border effects at the edge of the device can be neglected. All potential and particle profiles along the two lateral axes are therefore constant such that there is neither a flow of particles due to drift nor diffusion, as there is no potential drop (i.e. $\vec{E}_{lateral} = 0$) or particle gradient (i.e. $\nabla n(\vec{r}_{lateral}) = 0$), respectively. The diffusion coefficient from the Einstein relation is $D = \frac{\mu k_B T}{q}$, k_B the Boltzmann constant and T the temperature.

If at any position within the device a particle density changes with time, there is an imbalance of several processes, such as a change in current density from one position to another ($\nabla \vec{J_n} \neq 0$), a generation of particles due to absorption of light at a rate G or recombination at rate R. This can be either emissive Langevin recombination or dark Shockley-Read-Hall (SRH) recombination. The balance is described by the Continuity equations

$$\frac{dn}{dt} = \frac{\nabla \vec{J_n}}{q} + G - R \tag{1.9}$$

$$\frac{dp}{dt} = -\frac{\nabla \vec{J_p}}{q} + G - R \tag{1.10}$$

$$\frac{da}{dt} = \frac{\nabla \vec{J_a}}{q} \tag{1.11}$$

$$\frac{dc}{dt} = -\frac{\nabla \vec{J_c}}{q} \tag{1.12}$$

where no additional terms were considered for the ions. A generation and reduction term can come into play when a salt binding energy is considered, such that a neutral salt molecule dissociates into free anions and cations and reforms again at a specific rate.[84] This is discussed further in chapter 3.

The connection between the different charges and the electric field comes from the Poisson equation

$$\varepsilon_r \varepsilon_0 \nabla \vec{E} = -q(p - n + c - a + p_t - n_t) \tag{1.13}$$

with the vacuum permittivity ε_0, the relative permittivity ε_r, the hole trap density p_t and the electron trap density n_t. The rate equation of traps for the example of the electron trap density is discussed in chapter 4. The Poisson equation basically states that a net charge at a certain position leads to a change in the electric field from the position to the next. Furthermore, the equation illustrates the concept of space charge. In steady state, i.e. when there is no change of a quantity with time anymore (e.g. $\frac{dn}{dt} = 0$), there must be a non-changing profile of electrons and holes as there is also a fixed electric field profile. This does not mean that the electric charges are immobile at steady state. In the example of the electrons in the centre region in **Figure 1.11**a, they move to the left due to the positive electric field. But because eventually all electrons recombine with holes due to emissive Langevin recombination, the profile does not change its shape. If no recombination is present, the resulting profiles are all flat (besides at the interface) as shown in Figure 1.11b. This situation is simpler to picture, as there is a constant electric field and electron density across the layer, which leads to a constant electron current. In this picture, one can say that the charges just flow to the opposite electrode. Note that at the electrodes when a charge density drops and thus the drift current of the specific electronic charge too, the current and continuity is maintained due to diffusion current.
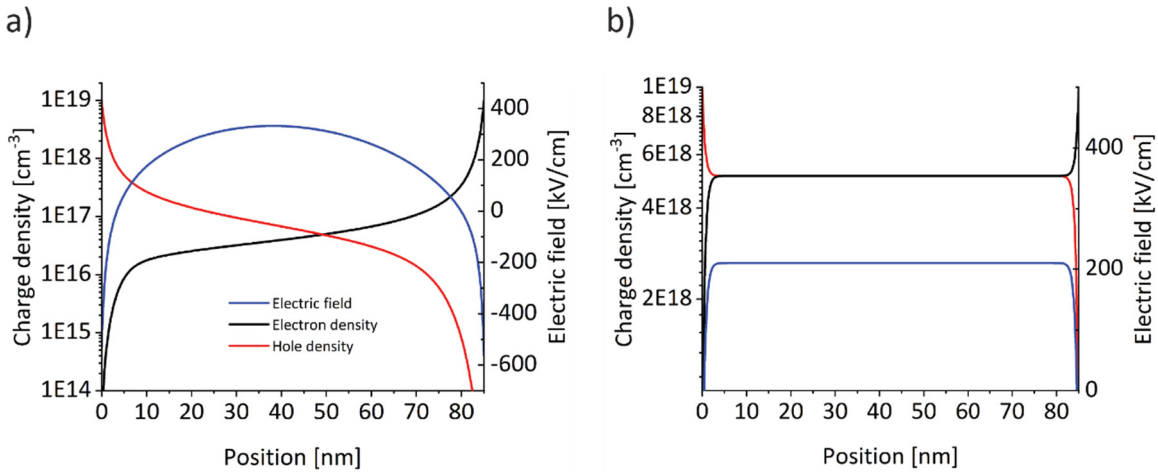
Figure 1.11. a) Steady state simulation of a SY PLED (for details see chapter 4). At the interface to the PEDOT:PSS layer on the left side and to the Ca/Al electrode on the right side, a hole and electron injection, respectively, of 10^{19} cm^{-3} are assumed. Not shown is the electron trap density, which leads to the slight asymmetry in the profiles. b) Steady state simulation of a SY PLED without Langevin or SRH recombination.

The implementation of the formalism introduces further problems as for example boundary conditions or choice of an appropriate solver. While for the steady state solution equations (1.9)-(1.12) are set to 0 and iteratively solved together with equations (1.5)-(1.8) and (1.13) until the error lies below a defined residuum, the transient simulation requires the definition of a time step Δt. A following time step $i + 1$, taking the example of the electron density, is then calculated via equation (1.9), where the right hand side is essentially a function of the electric field and the charge densities such that

$$\frac{dn}{dt} = \frac{n^{i+1} - n^i}{\Delta t} = \frac{\nabla \vec{J_n}}{q} + G - R = F_n(E, n, p)$$
$$\rightarrow n^{i+1} = n^i + \Delta t * F_n(E^{i+1}, n^{i+1}, p^{i+1}) \tag{1.14}$$

which is the implicit equation that is then again consistently solved for all parameters of the time step $i + 1$. Further details of the drift-diffusion model and implementation are given in [85].

1.4.2 Optical Simulation

The main input for the optical model is the refractive index n and the extinction coefficient k as part of the complex refractive index $n + i * k$. Data for the metals were taken from material databases. The ITO and glass substrate were determined by ellipsometry measurement by the use of a suiting oscillator model to fit the measurement. The glass substrate is nearly constant in the relevant range from 400 nm to 900 nm with $n \approx 1.5$ and $k \approx 0$. The ITO layer measurement was fitted with two Lorentz oscillators. Thereby, the limit of the dielectric function is ϵ_∞ = 1, the peak transition energies are $E_0 \approx 0$ eV and 7 eV, the oscillator damping factors (broadening) are C=0.08 eV and 0 eV, and the peak amplitudes A = 4.1 eV and 130 eV for the two oscillators. For the SY layer, a Tauc-Lorentz based oscillator model was developed previously, which also accounts for the complex refractive index change due to doping in the SY LEC.[86] The complex refractive index can be calculated from the real and imaginary part of the dielectric function as

$$n = \sqrt{\frac{\sqrt{\epsilon_{real}^2 + \epsilon_{imag}^2} + \epsilon_{real}}{2}} \tag{1.15}$$

$$k = \sqrt{\frac{\sqrt{\epsilon_{real}^2 + \epsilon_{imag}^2} - \epsilon_{real}}{2}} \tag{1.16}$$

, which follows from $\epsilon = \epsilon_{real} + i * \epsilon_{imag} = (n + i * k)^2$. Below, the formula of one Tauc-Lorentz oscillator is given which has additional to the Lorentz model also the bandgap E_g as parameter. The real part is calculated from the imaginary part

$$\epsilon_{imag} = \frac{A * E_0 * C * (E - E_g)^2}{(E^2 - E_0^2)^2 + C^2 * E^2} * \frac{1}{E} \tag{1.17}$$

by the Kramers-Kronig relation and results in

$$\begin{aligned}
\epsilon_{real} = & \frac{A * C * a_{ln}}{2 * \pi * \zeta^4 * \alpha * E_0} * \ln\left(\frac{\left(E_0^2 + E_g^2 + \alpha * E_g\right)}{\left(E_0^2 + E_g^2 - \alpha * E_g\right)}\right) - \frac{A * a_{atan}}{\pi * \zeta^4 * E_0} \\
& * \left(\pi - \tan^{-1}(\frac{2 * E_g + \alpha}{C}) + \tan^{-1}(\frac{-2 * E_g + \alpha}{C})\right) + \frac{2 * A * E_0}{\pi * \zeta^4 * \alpha} \\
& * E_g * (E^2 - \gamma^2) * \left(\pi + 2 * \tan^{-1}\left(\frac{2 * (\gamma^2 - E_g^2)}{\alpha * C}\right)\right) \\
& - \frac{A * E_0 * C * \left(E^2 + E_g^2\right)}{\pi * \zeta^4 * E} * \ln\left(\frac{|E - Eg|}{\left(E + E_g\right)}\right) + \frac{2 * A * E_0 * C}{\pi * \zeta^4} \\
& * E_g * \ln\left(\frac{|E - Eg| * \left(E + E_g\right)}{\sqrt{\left(E_0^2 - E_g^2\right)^2 + E_g^2 * C^2}}\right)
\end{aligned}$$
(1.18)

with

$$\gamma = \sqrt{E_0^2 - \frac{C^2}{2}} \qquad \alpha = \sqrt{4 * E_0^2 - C^2} \qquad \zeta^4 = (E^2 - \gamma^2)^2 + \frac{\alpha^2 * C^2}{4}$$

$$a_{atan} = (E^2 - E_0^2) * (E_0^2 + E_g^2) + E_g^2 * C^2$$

$$a_{ln} = \left(E_g^2 - E_0^2\right) * E^2 + E_g^2 * C^2 - E_0^2 * (E_0^2 + 3 * E_g^2)$$

The complex refractive index of SY can be described using a Tauc-Lorentz dispersion model for the SY and one for the polaron transition. In addition, the polaron transitions for the p- and n-doping types are located at different energies, therefore there are separate parameter sets 1 and 2 for A, C, E_0 and E_g as shown in references.[86,87] For each wavelength λ with the energy $E = \frac{h * c}{\lambda}$ (Planck-Einstein relation with the Planck constant h and the speed of light c), the contributions of the oscillators are summed up. The final real part of the dielectric function is then $\epsilon_{real}(E) = \epsilon_\infty + \epsilon_{real,set1}(E) + \epsilon_{real,set2}(E)$, and the final imaginary part is $\epsilon_{imag}(E) = \epsilon_{imag,set1}(E) + \epsilon_{imag,set2}(E)$. Note that the imaginary part is 0 below the bandgap E_g.

Excitons couple the electrical to the optical model. Essentially, when a free hole and electron meet they form an exciton that emits light via Langevin recombination. The exciton in the model does not alter the electrical model anymore because it is neutral and it is assumed that excitons do not split up anymore and only recombine by emission of a photon. Note in the simulation of an organic solar cell the exciton very much influences to electrical model as the photogenerated exciton have to split up into free holes and electrons at the donor acceptor interface.[88] The radiative recombination profile of the excitons, called emission zone, is then the input to the optical simulation. The emission of the molecule is modelled as a driven damped harmonic dipole oscillator[89] with the oscillating dipole moment $\vec{p}$ described as

$$\frac{d^2\vec{p}}{dt^2} + \omega^2\vec{p} = -b_0 * \frac{d\vec{p}}{dt} + \frac{q^2}{m}\overrightarrow{E_R}$$
(1.19)

where the left hand side equated to zero is a simple harmonic oscillator with the oscillator frequency ω in the absence of damping. The intrinsic power of the dipole b_0 introduces damping,

and the reflected field at the dipole position $\overrightarrow{E_R}$ with the effective mass of the dipole m is the external force leading to the driven damped harmonic oscillator model. In a typical device structure, the reflected field is mainly a result of the reflection at the metal electrode. **Figure 1.12**a shows the outcoupled luminance for an assumed constant current of 7.7mA/cm^2 (see chapter 3). On the x-axis a Gaussian shaped emission zone with a full width at half maximum of 50 nm is swept across the SY active layer in between the ITO at a position of 0 and Al at 1. This is done for several SY thicknesses on the y-axis. The resulting pattern seems unintuitive, but if the same data is plotted on the x-axis in absolute distance from the Al electrode in Figure 1.12b, it is apparent that the distance of the emission zone to the metal electrode determines the interference pattern. This effect is often referred to as microcavity or Purcell effect[50,90] and can be mathematically described as Purcell factor F, which leads to the apparent internal quantum efficiency

$$q_{app} = \frac{q_0 * F}{q_0 * F + 1 - q_0} \tag{1.20}$$

from the internal quantum efficiency q_0.[91] Losses due to the microcavity or Purcell effect are therefore reflected in changes of the nonradiative part $1 - q_{app}$.[87] The propagation of electromagnetic field of the radiated part q_{app} into other layers and outcoupled into air is then calculated by transfer matrix formalism.[92,93]
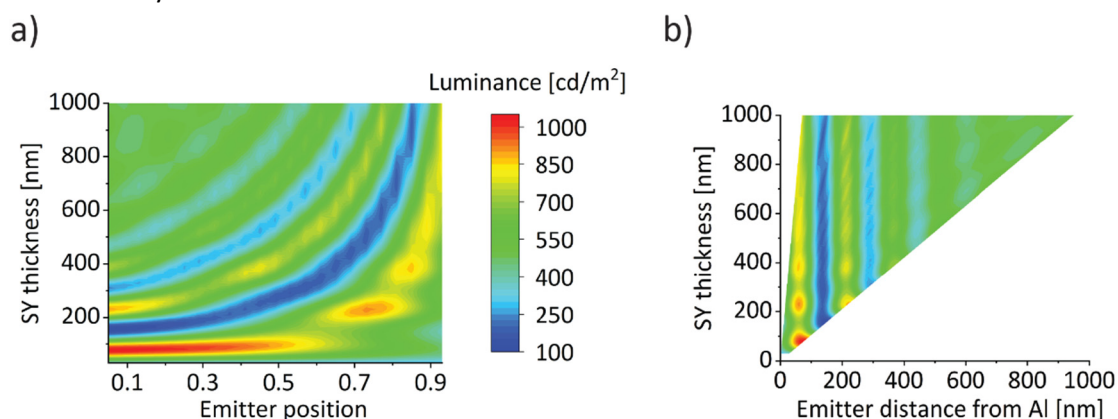
Figure 1.12. Optical simulations of the luminance for several SY layer thicknesses, plotted as relative position from the ITO electrode in a) and absolute distance from the Al electrode in b)

References

[1]   S. Z. Bisri, S. Shimizu, M. Nakano, Y. Iwasa, *Adv. Mater.* **2017**, *29*, 1607054.

[2]   J. Leger, M. Berggren, S. Carter, *Iontronics*; Leger, J.; Berggren, M.; Carter, S., Eds.; CRC Press, 2011; Vol. 8.

[3]   D. Liu, H. Cheng, X. Zhu, G. Wang, N. Wang, *ACS Appl. Mater. Interfaces* **2013**, *5*, 11258.

[4]   W. Qian, X. Cheng, Y. Zhao, J. Zhou, J. He, H. Li, Q. Xu, N. Li, D. Chen, J. Lu, *Adv. Mater.* **2019**, *31*, 1806424.

[5]   S.-H. Jeong, S. Ahn, T.-W. Lee, *Macromol. Res.* **2019**, *27*, 2.

[6]   L. Hu, J. Song, X. Yin, Z. Su, Z. Li, *Polymers (Basel).* **2020**, *12*, 145.

[7]   Y. Xia, S. Dai, *J. Mater. Sci. Mater. Electron.* **2021**, *32*, 12746.

[8]   Z. Fan, J. Ouyang, *Adv. Electron. Mater.* **2019**, *5*, 1800769.

[9]   J. Cameron, P. J. Skabara, *Mater. Horizons* **2020**, *7*, 1759.

[10]   A. Köhler, H. Bässler, *Electronic Processes in Organic Semiconductors*; Wiley-VCH Verlag, 2015.

[11]   F. A. Nüesch, In *Advanced Photonics 2018 (BGPP, IPR, NP, NOMA, Sensors, Networks, SPPCom, SOF)*; OSA: Washington, D.C., 2018; Vol. Part F107-, p. NoTh1D.1.

[12]   A. Devižis, A. Gelzinis, J. Chmeliov, M. Diethelm, L. Endriukaitis, D. Padula, R. Hany, *Adv. Funct. Mater.* **2021**, *2102000*, 2102000.

[13]   H. Benmansour, F. A. Castro, M. Nagel, J. Heier, R. Hany, F. Nüesch, *Chim. Int. J. Chem.* **2007**, *61*, 787.

[14]   S. B. Anantharaman, K. Strassel, M. Diethelm, A. Gubicza, E. Hack, R. Hany, F. A. Nüesch, J. Heier, *J. Mater. Chem. C* **2019**, *7*, 14639.

[15]   R. Aderne, K. Strassel, S. Jenatsch, M. Diethelm, R. Hany, F. Nüesch, R. dos S. Carvalho, C. Legnani, M. Cremona, *Org. Electron.* **2019**, *74*, 96.

[16]   A. Devižis, S. Jenatsch, M. Diethelm, V. Gulbinas, F. Nüesch, R. Hany, *ACS Photonics* **2018**, *5*, 3124.

[17]   S. Jenatsch, M. Regnat, R. Hany, M. Diethelm, F. Nüesch, B. Ruhstaller, *ACS Photonics* **2018**, *5*, 1591.

[18]   R. D. Costa, E. Ortí, H. J. Bolink, F. Monti, G. Accorsi, N. Armaroli, *Angew. Chemie - Int. Ed.* **2012**, *51*, 8178.

[19]   K. Youssef, Y. Li, S. O'Keeffe, L. Li, Q. Pei, *Adv. Funct. Mater.* **2020**, *30*, 1909102.

[20]   M. Reufer, M. J. Walter, P. G. Lagoudakis, A. B. Hummel, J. S. Kolb, H. G. Roskos, U. Scherf, J. M. Lupton, *Nat. Mater.* **2005**, *4*, 340.

[21]   J. Mindemark, S. Tang, H. Li, L. Edman, *Adv. Funct. Mater.* **2018**, *28*, 1801295.

[22]   L. E. Cells, M. Zhu, X. Yuan, G. Ni, **2019**.

[23]   J. Fang, P. Matyba, N. D. Robinson, L. Edman, *J. Am. Chem. Soc.* **2008**, *130*, 4562.

[24]   X.-K. Liu, W. Xu, S. Bai, Y. Jin, J. Wang, R. H. Friend, F. Gao, *Nat. Mater.* **2021**, *20*, 10.

[25]   A. Mishra, M. Alahbakhshi, R. Haroldson, L. D. Bastatas, Q. Gu, A. A. Zakhidov, J. D. Slinker, *Adv. Opt. Mater.* **2020**, *8*, 2000226.

[26]   N. Li, X. Niu, Q. Chen, H. Zhou, *Chem. Soc. Rev.* **2020**, *49*, 8235.

[27]   H. Wang, M. Zhou, H. Luo, *ACS Omega* **2018**, *3*, 1445.

[28]   J. Y. Kim, J. W. Lee, H. S. Jung, H. Shin, N. G. Park, *Chem. Rev.* **2020**, *120*, 7867.

[29]   S. D. Stranks, S. D. Stranks, G. E. Eperon, G. Grancini, C. Menelaou, M. J. P. Alcocer, T. Leijtens, L. M. Herz, A. Petrozza, H. J. Snaith, *Science* **2014**, *342*, 341.

[30]   W. Zhou, J. Gu, Z. Yang, M. Wang, Q. Zhao, *J. Phys. D. Appl. Phys.* **2021**, *54*, 063001.

[31]   S. Liu, Y. Guan, Y. Sheng, Y. Hu, Y. Rong, A. Mei, H. Han, *Adv. Energy Mater.* **2020**, *10*, 1902492.

[32]   L. Fu, H. Li, L. Wang, R. Yin, B. Li, L. Yin, *Energy Environ. Sci.* **2020**, *13*, 4017.

[33]   D. Gets, M. Alahbakhshi, A. Mishra, R. Haroldson, A. Papadimitratos, A. Ishteev, D. Saranin, S. Anoshkin, A. Pushkarev, E. Danilovskiy, S. Makarov, J. D. Slinker, A. A. Zakhidov, *Adv. Opt. Mater.* **2021**, *9*, 2001715.

[34]   A. J. Knight, L. M. Herz, *Energy Environ. Sci.* **2020**, *13*, 2024.

[35]   T. Q. Nguyen, I. B. Martini, J. Liu, B. J. Schwartz, *J. Phys. Chem. B* **2000**, *104*, 237.

[36] M. Kuik, G. J. A. H. Wetzelaer, H. T. Nicolai, N. I. Craciun, D. M. De Leeuw, P. W. M. Blom, *Adv. Mater.* **2014**, *26*, 512.

[37] S. M. Sze, K. K. Ng, *Physics of Semiconductor Devices*; John Wiley & Sons, Inc.

[38] L. J. Brillson, *Surfaces and Interfaces of Electronic Materials*; Wiley-VCH Verlag, 2010.

[39] A. Yaniv, *Phys. Rev. B* **1978**, *17*, 3904.

[40] J. Rammer, *Physics of Electronic Materials: Principles and Applications*; CAMBRIDGE UNIVERSITY PRESS, 2017.

[41] R.-H. Yi, C.-L. Lo, D. Luo, C.-H. Lin, S.-W. Weng, C.-W. Lu, S.-W. Liu, C.-H. Chang, H.-C. Su, *ACS Appl. Mater. Interfaces* **2020**, *12*, 14254.

[42] S. Van Reenen, R. A. J. Janssen, M. Kemerink, *Adv. Funct. Mater.* **2015**, *25*, 3066.

[43] S. Jenatsch, L. Wang, M. Bulloni, A. C. Véron, B. Ruhstaller, S. Altazin, F. Nüesch, R. Hany, *ACS Appl. Mater. Interfaces* **2016**, *8*, 6554.

[44] K. Schlingman, Y. Chen, R. S. Carmichael, T. B. Carmichael, *Adv. Mater.* **2021**, *2006863*, 2006863.

[45] E. Fresta, R. D. Costa, *Adv. Funct. Mater.* **2020**, *30*, 1908176.

[46] G. Wyszecki, W. S. Stiles, *Color Science: concepts and methods, quantitative data and formulae*; 2nd ed.; New York: Wiley, 1982.

[47] L. T. Sharpe, A. Stockman, W. Jagla, H. Jägle, *J. Vis.* **2005**, *5*, 3.

[48] L. T. Sharpe, A. Stockman, W. Jagla, H. Jägle, *Color Res. Appl.* **2011**, *36*, 42.

[49] F. Pedrotti, L. Pedrotti, W. Bausch, H. Schmidt, *Optik für Ingenieure*; 4th ed.; Springer-Verlag Berlin Heidelberg, 2008.

[50] E. M. Lindh, P. Lundberg, T. Lanz, J. Mindemark, L. Edman, *Sci. Rep.* **2018**, *8*, 6970.

[51] A. Munar, A. Sandström, S. Tang, L. Edman, *Adv. Funct. Mater.* **2012**, *22*, 1511.

[52] L. D. Bastatas, K. Y. Lin, M. D. Moore, K. J. Suhr, M. H. Bowler, Y. Shen, B. J. Holliday, J. D. Slinker, *Langmuir* **2016**, *32*, 9468.

[53] Y. S. Lee, J.-H. Park, J. S. Choi, J. I. Han, *Jpn. J. Appl. Phys.* **2003**, *42*, 2715.

[54] Y. S. Lee, J.-H. Park, J. S. Choi, *Mol. Cryst. Liq. Cryst.* **2003**, *405*, 53.

[55] M. P. Aleksandrova, *Microelectron. Int.* **2016**, *33*, 47.

[56] C. Lungenschmied, G. Dennler, E. Ehrenfreund, H. Neugebauer, N. S. Sariciftci, In *Organic Optoelectronics and Photonics II*; Heremans, P. L.; Muccini, M.; Meulenkamp, E. A., Eds.; 2006; Vol. 6192, p. 61921W.

[57] G. Garcia-Belmonte, J. Bisquert, *ACS Energy Lett.* **2016**, *1*, 683.

[58] H. Wang, A. Guerrero, A. Bou, A. M. Al-Mayouf, J. Bisquert, *Energy Environ. Sci.* **2019**, *12*, 2054.

[59] C. Han, K. Wang, X. Zhu, H. Yu, X. Sun, Q. Yang, B. Hu, *J. Phys. D. Appl. Phys.* **2018**, *51*.

[60] L. Burtone, D. Ray, K. Leo, M. Riede, *J. Appl. Phys.* **2012**, *111*.

[61] L. Bertoluzzi, P. P. Boix, I. Mora-Sero, J. Bisquert, *J. Phys. Chem. C* **2014**, *118*, 16574.

[62] Q. Niu, G.-J. A. H. Wetzelaer, P. W. M. Blom, N. Irina Crăciun, *Appl. Phys. Lett.* **2019**, *114*, 163301.

[63] F. Ebadi, N. Taghavinia, R. Mohammadpour, A. Hagfeldt, W. Tress, *Nat. Commun.* **2019**, *10*, 1574.

[64] I. Rörich, Q. Niu, B. van der Zee, E. del Pino Rosendo, N. I. Crăciun, C. Ramanan, P. W. M. Blom, *Adv. Electron. Mater.* **2020**, *1700643*, 1.

[65]   P. Wang, Q. Huang, S. Zhao, Z. Qin, Z. Xu, D. Song, B. Qiao, *Org. Electron.* **2019**, *68*, 45.

[66]   J. C. Maxwell, *A Dynamical Theory of the Electromagnetic Field*; Publishers, W. & S., Ed.; 1996.

[67]   J. Zhang, C. Li, M. Chen, K. Huang, *J. Phys. D. Appl. Phys.* **2021**, *54*, 044002.

[68]   L. D. Bastatas, M. D. Moore, J. D. Slinker, *Chempluschem* **2018**, *83*, 266.

[69]   J. Ràfols-Ribé, N. D. Robinson, C. Larsen, S. Tang, M. Top, A. Sandström, L. Edman, *Adv. Funct. Mater.* **2020**, *30*, 1908649.

[70]   S. Hu, J. Gao, *Adv. Mater. Technol.* **2018**, *3*, 1800229.

[71]   Q. Niu, R. Rohloff, G.-J. A. H. Wetzelaer, P. W. M. Blom, N. I. Crăciun, *Nat. Mater.* **2018**, *17*, 557.

[72]   M. T. Neukom, S. Züfle, E. Knapp, M. Makha, R. Hany, B. Ruhstaller, *Sol. Energy Mater. Sol. Cells* **2017**, *169*, 159.

[73]   A. Maria, In *Proceedings of the 29th conference on winter simulation*; 1997.

[74]   H. T. Nicolai, M. Kuik, G. A. H. Wetzelaer, B. de Boer, C. Campbell, C. Risko, J. L. Brédas, P. W. M. Blom, *Nat. Mater.* **2012**, *11*, 882.

[75]   Z. Fang, W. Chen, Y. Shi, J. Zhao, S. Chu, J. Zhang, Z. Xiao, *Adv. Funct. Mater.* **2020**, *30*, 1.

[76]   S. Athanasopoulos, F. Schauer, V. Nádaždy, M. Weiß, F. J. Kahle, U. Scherf, H. Bässler, A. Köhler, *Adv. Energy Mater.* **2019**, *9*, 1.

[77]   D. Meggiolaro, F. Ambrosio, E. Mosconi, A. Mahata, F. De Angelis, *Adv. Energy Mater.* **2020**, *10*, 1902748.

[78]   S. Ravishankar, C. Aranda, S. Sanchez, J. Bisquert, M. Saliba, G. Garcia-Belmonte, *J. Phys. Chem. C* **2019**, *123*, 6444.

[79]   B. E. Pieters, *IEEE J. Photovoltaics* **2011**, *1*, 93.

[80]   M. Diethelm, L. Penninck, S. Altazin, R. Hiestand, C. Kirsch, B. Ruhstaller, *J. Inf. Disp.* **2018**, *19*, 61.

[81]   M. Diethelm, L. Penninck, M. Regnat, T. Offermans, B. Zimmermann, C. Kirsch, R. Hiestand, S. Altazin, B. Ruhstaller, *Sol. Energy* **2020**, *209*, 186.

[82]   M. Sajedi Alvar, P. W. M. Blom, G.-J. A. H. Wetzelaer, *Nat. Commun.* **2020**, *11*, 4023.

[83]   M. T. Neukom, A. Schiller, S. Züfle, E. Knapp, J. Ávila, D. Pérez-del-Rey, C. Dreessen, K. P. S. Zanoni, M. Sessolo, H. J. Bolink, B. Ruhstaller, *ACS Appl. Mater. Interfaces* **2019**, *11*, 23320.

[84]   S. Van Reenen, R. A. J. Janssen, M. Kemerink, *Adv. Funct. Mater.* **2012**, *22*, 4547.

[85]   W. Tress, *Organic Solar Cells*; 2014.

[86]   T. Lanz, E. M. Lindh, L. Edman, *J. Mater. Chem. C* **2017**, *5*, 4706.

[87]   E. M. Lindh, P. Lundberg, T. Lanz, L. Edman, *Sci. Rep.* **2019**, *9*, 10433.

[88]   R. Häusermann, E. Knapp, M. Moos, N. A. Reinke, T. Flatz, B. Ruhstaller, *J. Appl. Phys.* **2009**, *106*.

[89]   R. . Chance, A. Prock, R. Silbey, *Advances in Chemical Physics*; Prigogine, I.; Rice, S. A., Eds.; Advances in Chemical Physics; John Wiley & Sons, Inc.: Hoboken, NJ, USA, 1978; Vol. 162.

[90]   G.-R. Lin, H.-F. Chen, H.-C. Shih, J.-H. Hsu, Y. Chang, C.-H. Chiu, C.-Y. Cheng, Y.-S. Yeh, H.-C. Su, K.-T. Wong, *Phys. Chem. Chem. Phys.* **2015**, *17*, 6956.

[91]   M. Furno, R. Meerheim, S. Hofmann, B. Lüssem, K. Leo, *Phys. Rev. B* **2012**, *85*, 115205.

[92]   L. A. A. Pettersson, L. S. Roman, O. Inganäs, *J. Appl. Phys.* **1999**, *86*, 487.

[93]   P. Yeh, *Optical Waves in Layered Media*; 2005.

Chapter 2   The Relevance of the Optical Model for LECs

Optimized Electrolyte Loading and Active Film Thickness for Sandwich Polymer Light-Emitting Electrochemical Cells

Matthias Diethelm[1,2], Quirin Grossmann[1], Andreas Schiller[3,4], Evelyne Knapp[3], Sandra Jenatsch[4], Maciej Kawecki[5], Frank Nüesch[1,2], and Roland Hany[1]

[1]Empa, Swiss Federal Laboratories for Materials Science and Technology, Laboratory for Functional Polymers, CH-8600 Dübendorf, Switzerland
[2]Institute of Materials Science and Engineering, Ecole Polytechnique Fédérale de Lausanne (EPFL), Station 12, CH-1015 Lausanne, Switzerland
[3]Institute of Computational Physics, Zurich University of Applied Sciences, Technikumstrasse 9, 8401 Winterthur, Switzerland
[4]Fluxim AG, Katharina-Sulzer-Platz 2, 8400 Winterthur, Switzerland
[5]Empa, Nanoscale Materials Science, CH-8600 Dübendorf, Switzerland

Declaration of Contribution
M.D. contributed to and overviewed the device preparation and luminance characterisation, did the optical simulation including all related input data measurements, analysed the data and contributed to manuscript preparation.

Abstract

Effects of ion concentration and active layer thickness play a critical role on the performance of light-emitting electrochemical cells. Expanding on a pioneering materials system comprising the super yellow (SY) polymer and the electrolyte trimethylolpropane ethoxylate (TMPE)/$Li^+CF_3SO_3^-$, it is reported that a slightly lowered salt concentration and layer thickness result in a substantial efficiency increase, and that this increase is confined to a narrow concentration and thickness range. For a film thickness of 70 nm, a blend ratio SY:TMPE: $Li^+CF_3SO_3^-$ = 1:0.075:0.0225, and a current of 7.7 mA cm^{-2} the current efficacy is 11.6 cd A^{-1}, on a par with SY light-emitting diodes. The optimized salt content can be explained by increased exciton quenching at higher concentrations and hindered carrier injection and conduction at lower concentrations, while the optical dependence on the layer thickness is due to weak microcavity effects. A comprehensive optical modelling study is presented, which includes the doping-induced changes of the refractive indices and self-absorption losses due the emission–absorption overlap of intrinsic and doped SY.

The analysis indicates either a thickness-independent emitter position (EP) close to the anode or a thickness-dependent EP, shifted to the cathode for increased thicknesses.

2.1   Introduction

In contrast to the multiple layers required for a state-of-the-art organic light-emitting diode (OLED), light-emitting electrochemical cells (LECs) can be built from a single emissive layer that contains a salt and is sandwiched between two electrodes.[1] Due to the presence of mobile ions, the single layer can perform all the tasks that take place in an electroluminescent device, i.e., facile electrical charge injection, transport, exciton formation, and radiative recombination. LECs have the potential to be fabricated by low-cost solution processes using large-area compatible coating and printing processes.[2,3] This makes LECs a competing technology for inexpensive future light and signage sources.[4,5] Consensus has now been reached on the functionality of LECs.[6] For ohmic nonlimited injection, device operation involves the formation of electric double layers by ionic charges at the electrodes that facilitate the injection of electrical charges. The injected charges produce n- and p-doped regions at the cathode and anode which are locally compensated by ions. This electrochemical doping process increases the electronic conductivity of the active material. The doped regions grow and an intrinsic region, where electron-hole recombination and light emission take place, forms between them. In planar LECs, where the active area can be directly imaged, the p-i-n situation could be confirmed by measuring the electrostatic potential across the device and the doping-induced quenching of the photoluminescence.[6,7] For sandwich LECs, the junction formation was evidenced with impedance spectroscopy and angular emission measurements.[8–10]

In nonionic polymer-based LECs the electronic conductivity is enabled by the emitting material and the ionic conductivity is introduced by adding an electrolyte. In early work, the latter was typically a complex of polyethylene oxide and an alkali salt.[11,12] It is well established that the turn-on time, junction position, and device lifetime are highly dependent on the electrolyte selection and its concentration.[7,13–15] The cations and anions stabilize the injected electronic charges. This prevents the formation of space charge, results in enhanced carrier density and enables higher device currents and light output.

This suggests that the ion concentration should be as high as possible.[16] However, for too high ion concentrations the radiative recombination is reduced by doping-related exciton quenching, which reduces the luminescence efficiency.[9,17] On the other hand, the amount of salt must be sufficient to allow the formation of electric double layers, resulting in balanced and facile charge injection. An ideal situation is considered to be a p-i-n junction with highly doped regions, separated by a salt-free intrinsic region with a dimension of approximately the exciton diffusion length.[18,19]

The rational adjustment of the ionic concentration (c_{ion}) that results in this desired device situation, however, is not straightforward.[20] The required c_{ion} depends on the fraction of doped polymer repeating units.[19] For planar LECs, it was found that a light-emitting junction formed when $c_{ion} \geq 0.1$ ions/polymer repeat unit and that for lower c_{ion} the doped region came to a stop before making contact.[15] Concentrations of ≈ 0.1 and ≈ 0.15 dopants/polymer repeat unit for p-

and n-doping were determined.[7,21] For small molecule LECs, an n-type concentration of 0.8 dopant/molecule was found.[22]

There are several sources of uncertainty in the doping concentration determination and the choice of the optimum salt concentration.[23] Electrochemical side reactions other than the doping of the polymer falsify the calculation.[21] In addition, salts with an appreciable, but often unknown, binding energy cannot (immediately) be used for doping.[10,24] For high salt concentrations, the spatial competition between the electrolyte and the polymer can become important. A comparison between modelled and experimental LEC results showed that the effective initial mobile ion density in a real LEC is a strongly nonlinear function of the salt concentration.[16]

While the particular functionality of LECs implies that the electrical performance is insensitive to the precise thickness of the active layer, relatively few studies have considered that the optical dependence on the layer thickness is indeed distinct.[25] The active layer is sandwiched between a metal electrode and a reflecting substrate, and this structure forms a weak optical microcavity for the emitted light.[26] The luminance depends on the exact position of the emitter position (EP). In addition, re-absorption losses by the intrinsic and doped material can become substantial for thick active layers.[27] When evaluating the efficiency potential of an LEC materials system it is important to incorporate these optical effects because even a high performing material will result in a low luminance level when operated in a poorly designed optical cavity.

A breakthrough in efficiency and lifetime for polymer LECs was achieved when the ion-conductor polyethylene oxide was replaced by a hydroxyl-capped oligoether, termed trimethylolpropane ethoxylate (TMPE).[28] The commonly employed phenyl-substituted poly(para-phenylenevinylene) copolymer, termed super yellow (SY), was used as the emitting material, along with an electrolyte composed of the salt lithium trifluoromethanesulfonate ($Li^+CF_3SO_3^-$) dissolved in TMPE. The blend film, with a mass ratio of $SY:TMPE:Li^+CF_3SO_3^- = 1:0.1:0.03$ and a thickness of 100 nm, was sandwiched between an ITO (indium tin oxide):PEDOT:PSS (poly(3,4-ethylene-dioxythiophene)poly(styrene sulfonate)) anode and an Al cathode. When driven with a constant current of 1.9 mA cm^{-2}, such LECs exhibited a lifetime of 1150 h until the brightness dropped below 100 cd m^{-2}. The peak efficiency reached a value of 8.6 cd A^{-1} for the current efficacy and 8.6 lm W^{-1} for the power conversion efficacy.

Here, we demonstrate that the inherent efficiency potential of this materials system for LEC device applications has not been fully exploited so far, and that the combination of a reduced active layer thickness (to 70 nm) and a decrease of the electrolyte loading (by 25%) results in an increase of over 30% of the peak and average values for both the current efficacy and power conversion efficacy. To study the pronounced optical dependence on the active layer thickness, we introduce a comprehensive optical model that includes doping-induced changes of the complex refractive indices[29] and reabsorption losses due to the overlap between the SY electroluminescence (EL) and the absorption of intrinsic SY and the n- and p-polaron bands. Our analyses suggest that a systematic optimization of the light out-coupling efficiency and electrolyte loading can improve the performance of similar LEC material systems as well.

2.2 Results and Discussion

2.2.1 Optimized Electrolyte Loading

Figure 2.1 displays the LEC device architecture, chemical structures of SY and TMPE, and the luminance and voltage trend of an LEC. To allow a direct comparison with literature data,[28,30] devices were driven at a constant current of 7.7 mA cm^{-2} and the chosen mass ratio was SY:TMPE:Li$^+$CF$_3$SO$_3^-$ = 1:0.1:0.03. In the following we denote this as the "standard" blend with a relative salt concentration of "1" and refer other salt concentrations to this standard. Luminance and voltage trends for a larger set of standard LECs are compiled in Figure S2.1 in the Supporting Information. Although care was taken to keep the experimental device fabrication procedure constant, it is evident that the sample-to-sample variation for the turn-on time, peak luminance, and voltage was rather large. The cause for this low reproducibility is currently not known but we note that similar observations for that particular material system have been mentioned before.[28,31]
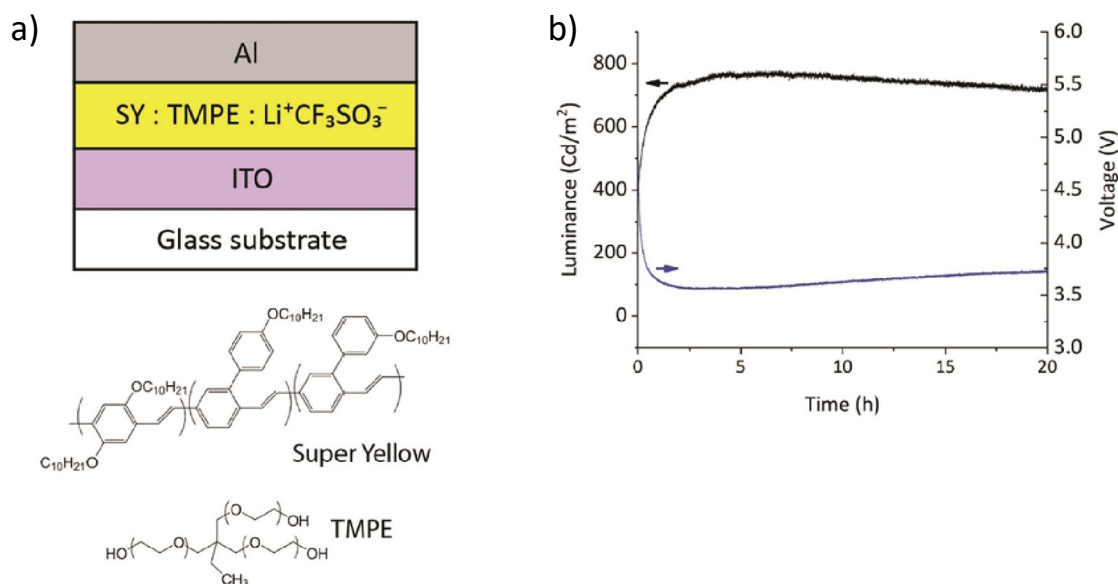
Figure 2.1. a) Sketch of the device architecture and chemical structures of the emitter super yellow and the ion conductor TMPE. b) Luminance and voltage trend of an (ITO/SY + TMPE + Li$^+$CF$_3$SO$_3^-$/Al) LEC. The mass ratio was SY:TMPE:Li$^+$CF$_3$SO$_3^-$ = 1:0.1:0.03, the active layer thickness was 70 nm and the device was driven at a constant current of 7.7 mA cm^{-2}.

Despite the observed data variability, the device performance was rather high. The peak luminance of the best device was 755 cd m^{-2} and from a set of 11 devices we determined champion (and average) values for the current efficacy of 9.8 (8.4) cd A^{-1} and for the power conversion efficacy of 8.7 (7.2) lm W^{-1}, (**Table 2.1**a). These performance values exceed reported data by over 20% for the standard device with the only difference being the active layer thickness, which was 100 nm[30,32] compared to 70 nm in our case (Table 2.1b,c). To exclude variations in experimental device fabrication procedure as a reason for the observed performance increase, we

also fabricated a set of standard devices with an increased ($\approx$110 nm) active layer thickness (Table 2.1d). Although our measured peak performances were higher, the average values agree well with reported values.[32] This suggests that indeed lowering of the active layer thickness was the main cause for the observed performance increase.

Table 2.1. Performance metrics of ITO/SY + TMPE + $Li^+CF_3SO_3^-$/Al sandwich LECs.

Entry[a]	Mass ratio SY:TMPE:$Li^+CF_3SO_3^-$	Abbr. concentration	Film thickness [nm]	Current efficacy[b] [cd A^{-1}]	Power conversion efficacy[b,c] [lm W^{-1}]	Reference
a	1:0.1:0.03	1, standard	70	9.8 (8.4)	8.7 (7.2)	This work
b	1:0.1:0.03	1	100	8.3	5.7	[30][d]
c	1:0.1:0.03	1	100	7.1 (6.4)	5.9 (5.2)	[32]
d	1:0.1:0.03	1	110	8.2 (6.7)	7.0 (5.6)	This work
e	1:0.05:0.015	0.5	70	10.7 (10.6)	7.2 (7)	This work
f	1:0.075:0.0225	0.75	70	11.6 (10.9)	9.5 (8.6)	This work
g	1:0.15:0.045	1.5	70	6.3 (5.6)	6.4 (5.8)	This work
h	1:0.2:0.06	2	70	3.8 (3.3)	4.2 (3.5)	This work
i	1:0.075:0.0225	0.75	110	10.0 (9.9)	8.1 (7.8)	This work
j	1:0.1:0.03	1	50	3.7 (3.6)	3.5 (3.4)	This work
k	1:0.1:0.03	1	160	7.4 (7.3)	5.6 (5.6)	This work

[a]Devices were driven at a constant current of 7.7 mA cm^{-2}; [b]Best result, average result is presented in parentheses; [c]Calculated by assuming the devices are Lambertian emitters; this is justified for thin active films;[26] [d]Included a PEDOT:PSS layer.

The next step was to vary the electrolyte concentration between 0.5 and 2 relative to the standard SY:TMPE:$Li^+CF_3SO_3^-$ = 1:0.1:0.03 blend, while keeping a constant active layer thickness of 70 nm. **Figure 2.2** displays the luminance and voltage trends for the champion cell of each concentration, a larger data set is compiled in Figure S2.2 in the Supporting Information. Voltage trends are consistently characterized by an initially high bias that dropped to a minimum value and after that increased steadily (but by less than 7%) over the remaining period. This progress can be ascribed to the ion displacement toward the electrodes that facilitates electrical charge injection and the effectively decreasing device resistance during the doping progress. The time for the initial voltage drop increased with decreasing salt concentration, from $\approx$0.5 to $\approx$3 h, which we attribute to a delayed electric double layer formation when the salt amount is decreased. Due to eventual ion depletion the low-conductive intrinsic region remains wider for lower salt content, consequently the driving voltage increases when the concentration is decreased.
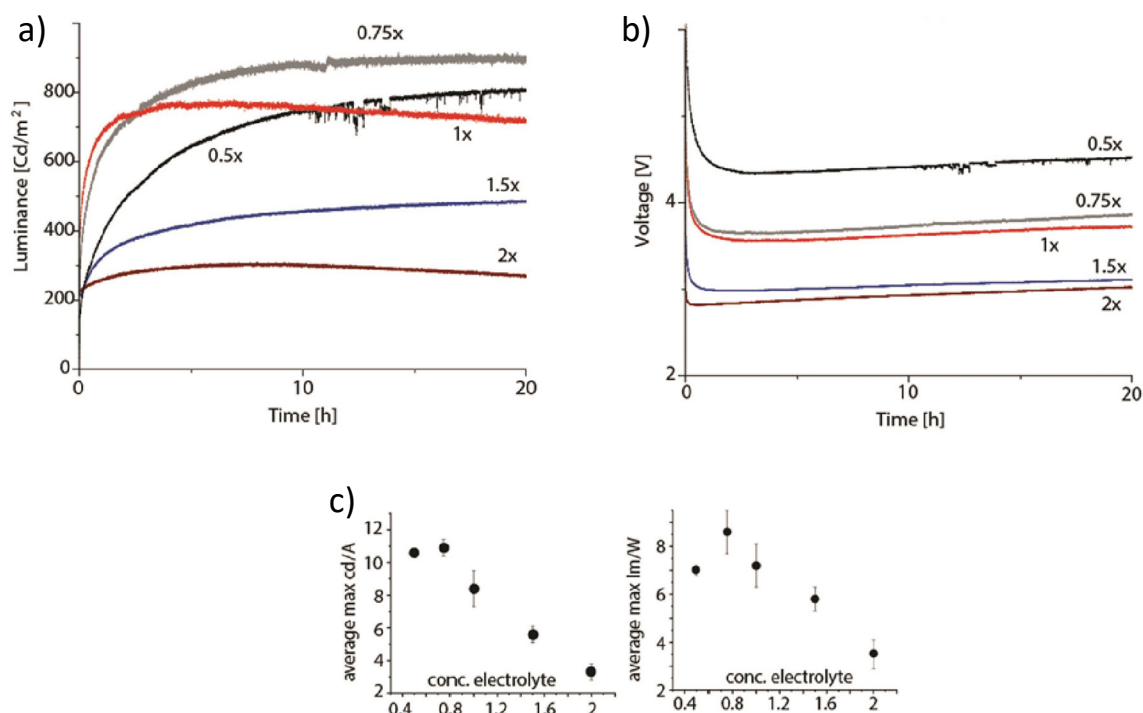
Figure 2.2. a) Luminance and b) voltage trends of champion devices for (ITO/SY + TMPE + Li$^+$CF$_3$SO$_3^-$/Al) LECs with different electrolyte concentrations, relative to the standard (=1) mass ratio SY:TMPE:Li$^+$CF$_3$SO$_3^-$ = 1:0.1:0.03. The active layer thickness was 70 nm and devices were driven at a constant current of 7.7 mA cm^{-2}. c) Average and standard deviation of maximum current efficacy and maximum power conversion efficacy values as function of electrolyte concentration.

We mention, however, that in the general case the transient device kinetics for varying salt concentrations must not necessarily follow the expected trend. Recently,[33] we quantitatively mapped the CF$_3$SO$_3^-$ distribution in SY LECs that were driven inside a time-of-flight secondary ion mass spectrometer and that were cooled to liquid nitrogen temperature before depth profiling. We found that the initial salt distribution is strongly inhomogeneous and further observed that the distribution changes when the salt concentration is changed. It is clear that an inhomogeneous salt distribution can have a large influence on the transient device kinetics: for example, a fast turn-on can be imagined when the salt accumulates preferentially at one film interface in such a way that the ion with the lower mobility is already at "the right electrode," whereas a slower turn-on is expected for the reversed situation.

The luminance curves (Figure 2.2a) show a peak luminance (895 cd m^{-2}) for a salt concentration of 0.75 as well as a strong and slight decrease for higher and lower salt concentrations, respectively. This trend is more clearly visible in Figure 2.2c where the average maximum current efficacy and power conversion efficacy values are displayed from a larger data set. The corresponding numerical values are summarized in Table 2.1, and the best-performing device (Table 2.1f) showed a current efficacy of 11.6 cd A^{-1} and a power conversion efficacy of 9.5 lm W^{-1}. These values are in good agreement with the performance of state-of-the art SY OLEDs, for

which a maximum (and average) current efficacy of 11.9 (10.14) cd A^{-1} (at 1000 cd m^{-2}) was reported.[34]

It is quite possible that a fine adjustment of the active layer thickness and electrolyte concentration can improve the device efficiency further, but we believe that the experimental conditions found for our champion device (Table 2.1f) are close to the optimum. First, we decreased the standard electrolyte concentration by 25% for 110 nm thick devices and measured an average performance increase of close to 40% (cf. Table 2.1i with Table 2.1d). This is in agreement with findings for 70 nm thick devices and suggests that a lowered electrolyte concentration improves the efficiency independent of the active layer thickness. We also observed that the performance drops for thinner (50 nm) and thicker (160 nm) active layers (Table 2.1j,k), supporting an optimized layer thickness in the range of 70 nm.

Here, we used a constant current density of 7.7 mA cm^{-2} to allow a direct comparison with literature data, but as well-known from OLEDs[34,35] the exact current value had a strong influence on the performance. For 70 nm thick devices and using the standard electrolyte concentration, the current efficacy increased steadily with decreasing current, from 3.9 cd A^{-1} for a current of 77 mA cm^{-2} to 9.8 cd A^{-1} for 7.7 mA cm^{-2} (Table 2.1a) and to 12.5 cd A^{-1} for 5 mA cm^{-2}.[33] Finally, for current densities below $\approx$2 mA cm^{-2} the device response became slow and the maximum performance was not reached after a measurement time of 40 h.

It could be interesting to conduct similar salt concentration versus LEC performance studies for related materials systems, using an optimized active film thickness at the same time. For example, the TMPE hydroxy end groups were replaced with methoxy (TMPE-OCH$_3$) groups.[32] Use of the TMPE-OCH$_3$ ion conductor in 100 nm thick LECs resulted in a faster turn-on to high luminance and increased peak (and average) values of 8.4 (7.5) cd A^{-1} for the current efficacy. In a follow-up study, a series of alkyl carbonate-capped TMPE derivatives was synthesized.[36] Again for 100 nm thick and a constant current driving of 7.7 mA cm^{-2}, the best of these ion conductors resulted in devices with peak (and average) values of 10.6 (10.3) cd A^{-1}. Comparison with data in Table 2.1f shows that these performance values are actually lower than what we measured for optimized TMPE LECs, hinting at an unexploited performance potential.

We finally mention that our experimental device optimization is only related to the peak current efficacy and power conversion efficacy as function of the salt amount and active layer thickness. A measurement time of 20 h was chosen to reach the maximum luminance level, whereas the long-term stability of SY:TMPE:Li$^+$CF$_3$SO$_3^-$ LECs during steady-state operation is several hundred hours.[28,30] For that reason we cannot comment on the influence of the salt content and film thickness on the device lifetime. Also a reasoning why the optimized salt concentration actually performs best is beyond the scope of this work. Due to excessive exciton quenching for too high salt concentrations and hindered carrier injection and conduction for too low salt concentrations, an optimum salt amount is indeed expected. A detailed explanation, however, should include intricate effects such as the extent of salt dissociation as function of the salt content and must consider that the film morphology and distribution of the electrolyte within the polymer matrix possibly change when the salt content is varied.

2.2.2 Optical Modelling

To analyse the strong dependence of the luminance on the active layer thickness, we consider the different factors contributing to the external quantum efficiency EQE = $\gamma \times \eta_{s,t} \times q_{eff} \times \eta_{out}$. The singlet/triplet factor $\eta_{s,t}$ does not depend on the device thickness because it is a materials property. The effective radiative quantum efficiency q_{eff} could change if quenching of excitons differs, for example, if the thickness and/or position of the charge recombination zone relative to the quenching doped zones strongly depend on the active layer thickness. Data of ref. [26], however, suggest a rather constant width of the intrinsic, low conductive region when varying the active layer thickness over a range from 100 to 380 nm; therefore, we assume here a constant intrinsic layer thickness and equal exciton and recombination profiles. From electrical simulations we also assume that the charge carrier balance factor γ does not depend on the active layer thickness. For a simple parameter set, simulated recombination currents for 70 and 110 nm thick devices were indeed the same and $\gamma = 1$ (Figure S2.3, Supporting Information). The simulation also reveals that the relative recombination position does not change with thickness; this point will be discussed further below.

As opposed to $\eta_{s,t}$, q_{eff}, and γ, which remain constant to a first approximation when changing the active layer thickness, the out-coupling factor η_{out} strongly depends on this thickness. First, the EL and absorption spectra of pristine, nondoped SY overlap slightly in the wavelength range 500-550 nm (Figure S2.4, Supporting Information). This means that a fraction of the emitted light on its way out of the device is reabsorbed by the polymer and that for a constant relative EP a larger fraction is reabsorbed when the layer thickness is increased. Second, p- and n-doping results in redshifted polaron absorption bands[29,37] that strongly overlap with the EL (Figure S2.4, Supporting Information); using the same arguments as for pristine SY, a higher fraction of emitted light is then reabsorbed by the doped polymer repeat units for thicker films. Finally, the emitting layer is sandwiched between a weakly (glass/ITO) and strongly (Al) reflecting interface, resulting in pronounced optical interference (weak microcavity) effects as function of the EP and the film thickness.[25,26,38] Microcavity effects depend strongly on the real part of the refractive indices of the materials, which notably change when the material is doped.

Expanding on previous studies, a comprehensive optical modelling study was performed that includes these effects. To achieve this, n- and k-values for pristine SY as well as for p- and n-doped layers were adopted from the literature (Figure S2.4, Supporting Information).[29] We assumed a constant thickness of 10 nm for the intrinsic zone and note that modelling results depend only slightly on this thickness and the Gaussian emitter width within reasonable variations (Figure S2.5, Supporting Information). Doping was only included for the standard salt concentration; the influence of doping on the optical model for lower and higher salt amounts is discussed in the Supporting Information. To incorporate the level of doping, we assumed that the added salt is fully dissociated and that all ions contribute to doping. For the standard concentration, this corresponds to an average doping concentration of 6.4% over the whole active layer thickness L_A. To account for the higher individual doping levels in the narrower p- and n-doped zones ($L_{p,n}$), the doping concentration was adjusted in both by 6.4 × ($L_A/L_{p,n}$). n- and k-values for these doping concentrations were interpolated from the measured literature values (Figure S2.6, Supporting Information). EPs were simulated in the range from 0.35 to 0.8. Outside this range, the

extrapolation from (calculated) doping concentrations to experimental data got less reliable (Figure S2.6, Supporting Information). We mention that our model does not include the short lifetime of emitter dipoles near the electrodes, justified by the simulated EP range. The model should be refined for EPs close to the electrodes to include quenching of the luminance.[39]

In the optical model *const. doping* it was assumed that the charge-compensating ions are evenly distributed over the doped zones, resulting in constant doping of these regions and an abrupt transition from the doped to the intrinsic region (**Figure 2.3**c). It has been shown, however, that in a more realistic scenario the doping level is largest close to the electrodes and gradually decreases toward the recombination zone.[10,40] We mimicked this situation by dividing the doped zones in three sections with different doping concentrations (model *graded doping*, Figure 2.3e). For comparison, optical modelling without doping was performed by using the intrinsic *n*- and *k*-values of SY throughout (model *no doping*, Figure 2.3a). For the simulation we adopted a current density of 7.7 mA cm^{-2}, $\eta_{s,t}$ = 0.25, q_{eff} = 68.3%[41] and γ = 1. Details and limitations of the optical model are further discussed in the Supporting Information.
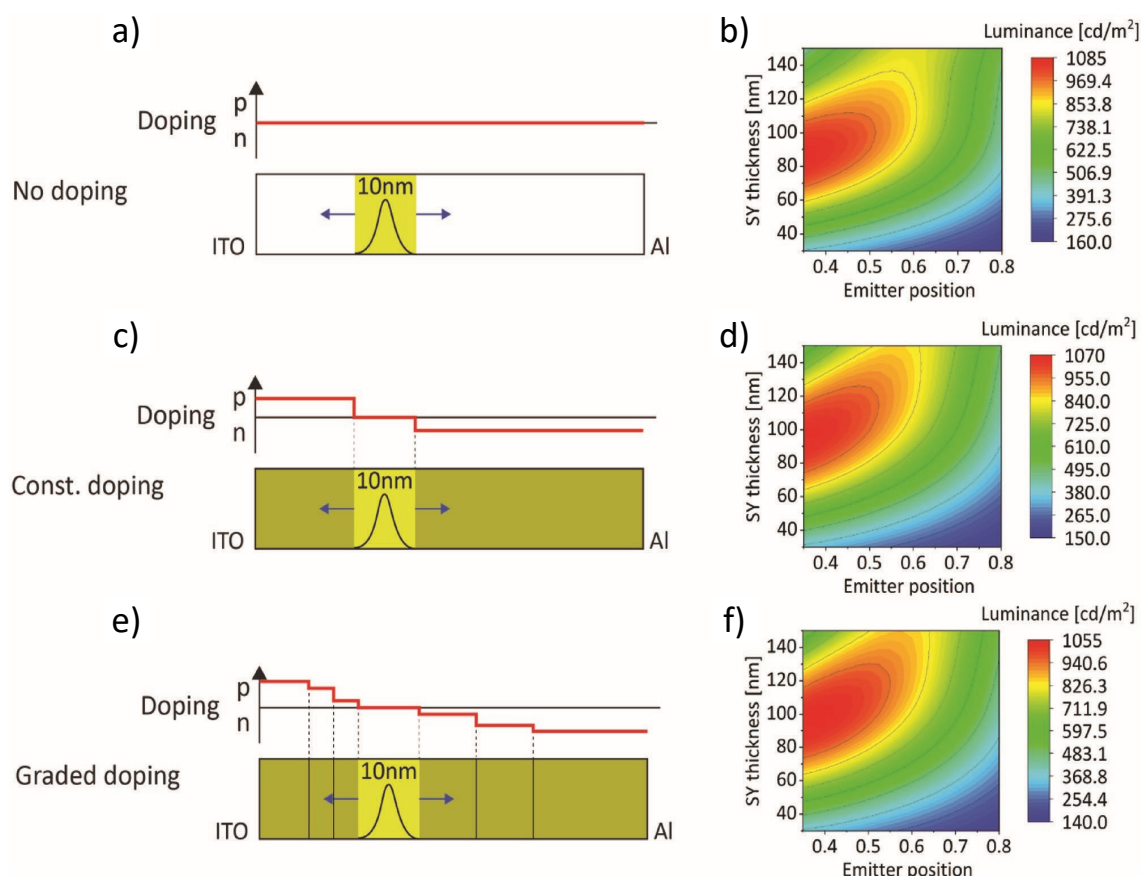
Figure 2.3. Schematics of the three different models no doping, const. doping, and graded doping and luminance for different emitter positions and active layer thicknesses. For all thicknesses, a constant intrinsic zone of 10 nm and a centred Gaussian emission profile with a width of 2.5 nm was assumed. Position 0 is at the ITO, 1 at the aluminium electrode.

Figure 2.3 displays plots of the luminance for different active layer thicknesses and EPs. The models *const. doping* (Figure 2.3d) and *graded doping* (Figure 2.3f) result in very similar emission shapes, and maximum values for the luminance (>1000 cd m^{-2}) are observed in a region of SY thicknesses ≈80-110 nm and EPs ≈0.35-0.45. This applies also to the model *no doping* (Figure 2.3b), but the calculated luminance decreases relatively for thicker layers. This confirms that changing refractive indices due to doping should be included in the simulation for higher accuracy. We note that the calculated optical dependence on the active layer thickness and the EP is largely determined by optical weak microcavity effects due to the reflecting Al top electrode. These can easily be demonstrated by replacing Al by air (Figure S2.7, Supporting Information). In this case, the pronounced region of strong luminance in Figure 2.3 disappears and the forward outcoupled luminance decreases strongly. Furthermore, when plotting data from Figure 2.3b as absolute distance from the Al electrode, it appears that the maximum luminance occurs for an EP situated 60 nm away from the cathode, independent of the active layer thickness (Figure S2.7, Supporting Information).

The effect of reabsorption can be separately studied in the optical model by setting *k*-values to zero. **Figure 2.4** shows the reabsorption losses for the three optical models and a layer thickness of 70 nm. When doping is omitted, the intrinsic self-absorption due to the emission-absorption overlap of SY amounts to 1-2%. Actually, this case would correspond to the reabsorption loss of an OLED and the value is in good agreement with a reported loss of 1% for a 100 nm thick device at the wavelength of 550 nm.[27] When doping is included, the reabsorption loss is up to ≈10%, depending on the EP. Reabsorption losses get substantial for thicker active layers, such as for 500 nm (loss ≈ 30%) or 1 μm (loss ≈ 55%) as shown in Figure S2.8 in the Supporting Information, where similar conclusions from literature are further discussed.
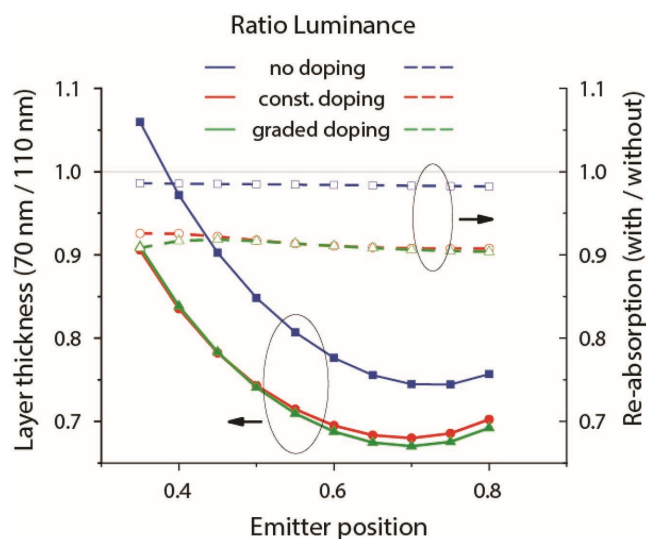
Figure 2.4. Quantitative data evaluation from contour plots shown in Figure 2.3. Dashed lines denote the ratio of the luminance when including and neglecting self-absorption for an active layer thickness of 70 nm. Solid lines denote the ratio of the luminance for an active layer thickness of 70 and 110 nm.

Figure 2.4 also includes the ratio between the calculated luminance values for layer thicknesses of 70 and 110 nm. These correspond to the experimental device thicknesses and we recall that the 70 nm thick LEC experimentally outperformed the 110 nm thick device (Table 2.1). In contrast to the experiment, the calculated luminance for the 110 nm thick device is higher than when using a 70 nm active layer in the EP range of 0.35-0.8 of our modelling study, but the luminance ratio trend indicates that the thinner device outperforms the thicker device for EPs < 0.35 (Figure S2.9, Supporting For the definite interpretation of these results the position of the EP as a function of the active layer thickness must be known. Recently, we have determined EPs for organic salt-based LECs by comparing experimental angle-dependent emission spectra with optical simulation.[8] The method uses a forward simulation based on dipole emission theory in an optical film cavity to fit the measured emission spectra with a superposition of local delta emitters. Unfortunately, a similar analysis is not possible in the present study because the (calculated) shape of the EL spectra depends only marginally on the position of the EP in SY LECs for thicknesses below ≈150 nm.

Therefore, it is unclear whether the relative EP is independent or dependent on the layer thickness and two scenarios are conceivable. When relative EPs are independent of the active film thickness, then agreement between experiment and modelling suggests EPs that are situated close to the ITO side. This would agree with results from SY OLEDs were the EP was found near the anode.[38] We note, however, that an EP near ITO disagrees with several reports on planar polymer LECs were the EP was found to be closer to the negative electrode.[7,14,21,42] Despite the view that results from planar polymer LECs cannot be directly transferred to sandwich devices with gaps thinner by several orders of magnitude and asymmetric contacts without reservation,[8,10] we also consider the possibility that the relative EP actually does depend on the active layer thickness. In this case, the EP would be at ≈0.55 for the 70 nm thick device and at EP ≈0.75 for the 110 nm device (from Figure 2.3d). Indeed, a thickness dependence of the relative recombination zone has been reported for other LEC material systems.[25,43] The pronounced EP shift for a relatively small thickness variation in our system, however, is intuitively not easy to understand and requires further studies. This includes a refinement of the electrical simulation, as for a simplified model assuming constant mobilities over space no relative shift of the EP is predicted when the layer thickness is changed. This assumption is in general not correct because electronic carrier mobilities are dependent on the electric field as well as the doping level and thus change continuously during the dynamic time-response of the device.[44] It must also be kept in mind that the film morphology and the distribution of the electrolyte throughout the active layer must not necessarily remain constant when the film thickness is changed.[33]

2.3   Conclusion

By optimizing the $(TMPE:Li^+CF_3SO_3^-)$-electrolyte loading and active layer thickness we observed that the efficiency of SY LECs can be substantially improved to values that agree with the performance of state-of-the art SY OLEDs. The optimum electrolyte concentration range for our material system is rather narrow and the strong performance decrease for higher electrolyte loadings indicates that the chosen salt concentration in many of the earlier works was too high. Very recently, efficient (13.8 cd A^{-1} at a luminance of 1060 cd m^{-2}) SY LECs have been presented

by replacing the oligoether TMPE with a carbonate based ion transporter.[45] For these devices, the chosen active layer thickness was 100 nm, the SY:Li$^+$CF$_3$SO$_3^-$ mass ratio was 1:0.03 and the molar ratio between the ion transporter and Li$^+$CF$_3$SO$_3^-$ was constant at 1. These parameters actually correspond to the established[28,32,36] but slightly suboptimal experimental conditions, and we anticipate that a fine-tuning of the electrolyte loading and active layer thickness can probably boost this record-high efficiency for a singlet-emitting LEC further. The same applies to new LEC materials systems introduced in the future.

The optical model aims to explain observations related to the thickness variation, and the effects of doping and reabsorption losses were only studied for the standard salt concentration. The model is useful to estimate the inherent efficiency potential of a materials system, to tune the optical cavity resonances and to predict the active layer thickness range for maximized outcoupling of light generated in the device. In our case, however, it is unclear whether the increased luminance for the thinner active layer thickness is due to a thickness-independent recombination zone that is situated close to the anode, or whether the recombination zone is thickness dependent and shifted toward the cathode for thicker layers. To address this open question, thicker active layers must be used in future work. Preliminary optical modelling studies and experimental results[26] indicate that for an active layer thickness beyond ≈150 nm the EP can indeed be determined by comparing experimental angle-dependent emission spectra with optical simulations.

2.4   Experimental Section

Dried (24 h, 0.1 mbar, 160 °C) Li$^+$CF$_3$SO$_3^-$ (Sigma-Aldrich), dried (24 h, 0.1 mbar, room temperature) TMPE (Sigma-Aldrich, average M_n 450), and dried (24 h, 0.1 mbar, 40 °C) SY (Merck) were separately dissolved in anhydrous tetrahydrofuran (Sigma-Aldrich) in concentrations of 10 mg mL^{-1} (salt, TMPE) and 5 mg mL^{-1} (SY). These precursor solutions were then stirred for 7 h at 60 °C inside a glove box (H$_2$O < 1 ppm, O$_2$ < 20 ppm). For the "standard" blend (labelled with the relative concentration "1"), the precursor solutions were mixed in mass ratios of 1:0.1:0.03 (SY:TMPE:Li+CF3SO3−) and were then stirred for at least 17 h at 60 °C. For blends with electrolyte concentrations between 0.5 and 2, relative to the standard concentration, the mass ratio SY:electrolyte was varied while keeping the molar ratio (=1) between TMPE and Li+CF3SO3− constant. Before spin coating, solutions were let to cool down for 20 min. Films from unfiltered solutions were spin coated at 2000 rpm (2000 rpm s^{-1}) for 1 min inside the glovebox onto cleaned ITO/glass substrates (Geomatec, ≈11 Ω square−1) and were then dried at 60 °C for 1 h. Finally, aluminium top electrodes (70 nm) were thermally evaporated through a shadow mask defining eight cells with an active area of 3.1 or 7.1 mm2 per sample. For the data presented, over 70 samples were fabricated and in most cases one cell per sample was measured. Layer thicknesses of ≈70 and ≈110 nm were measured with an Ambios XP1 profilometer (68 ± 3.5 nm; 110 ± 10 nm). For performance measurements, devices were placed in an airtight holder and were measured under nitrogen atmosphere outside the glove box at room temperature using two factory calibrated Konica Minolta LS-110 luminance meters with a close-up lens 110. The reflection of the top cover glass of the holder was not considered.

Transmission spectra were measured with a Varian Cary 50 UV−vis spectrometer. Optical transmission and luminance simulations were performed with SETFOS 4.6 (Fluxim AG, Switzerland). The refractive indices for the intrinsic and doped SY layers were taken from ref. [29] and confirmed by transmission spectra simulation. The photoluminescence spectrum was measured by fluorescence spectroscopy (Horiba Jobin Yvon Fluorolog). The refractive index of ITO was determined by spectroscopic ellipsometry (M2000-VI, J.A. Woollam Co.).

References

[1]   S. B. Meier, D. Tordera, A. Pertegás, C. Roldán-Carmona, E. Ortí, H. J. Bolink, *Mater. Today* **2014**, 17, 217.

[2]   A. Sandström, L. Edman, *Energy Technol*. **2015**, 3, 329.

[3]   E. Fresta, R. C. Costa, J. *Mater. Chem. C* **2017**, 5, 5643.

[4]   S. Tang, L. Edman, *Top. Curr. Chem*. **2016**, 374, 40.

[5]   S. Tang, A. Sandström, P. Lundberg, T. Lanz, C. Larsen, S. van Reenen, M. Kemerink, L. Edman, *Nat. Commun*. **2017**, 8, 1190.

[6]   S. van Reenen, P. Matyba, A. Dzwilewski, R. A. J. Janssen, L. Edman, M. Kemerink, *J. Am. Chem. Soc.* **2010**, 132, 13776.

[7]   J.-H. Shin, N. D. Robinson, S. Xiao, L. Edman, *Adv. Funct. Mater.* **2007**, 17, 1807.

[8]   S. Jenatsch, M. Regnat, R. Hany, M. Diethelm, F. Nüesch, B. Ruhstaller, *ACS Photonics* **2018**, 5, 1591.

[9]   M. Lenes, G. Garcia-Belmonte, D. Tordera, A. Pertegás, J. Bisquert, H. J. Bolink, *Adv. Funct. Mater.* **2011**, 21, 1581.

[10]   S. van Reenen, R. A. J. Janssen, M. Kemerink, *Adv. Funct. Mater.* **2012**, 22, 4547.

[11]   J. Gao, *ChemPlusChem* **2017**, 82, 1.

[12]   Q. Peng, G. Yu, C. Zhang, Y. Yang, A. J. Heeger, *Science* **1995**, 269, 1086.

[13]   L. Edman, D. Moses, A. J. Heeger, *Synth. Met.* **2003**, 138, 441.

[14]   Y. Hu, J. Gao, *Appl. Phys. Lett.* **2006**, 89, 253514.

[15]   J. Fang, Y. Yang, L. Edman, *Appl. Phys. Lett.* **2008**, 93, 063503.

[16]   S. van Reenen, P. Matyba, A. Dzwilewski, R. A. J. Janssen, L. Edman, M. Kemerink, *Adv. Funct. Mater.* **2011**, 21, 1795.

[17]   S. van Reenen, R. A. J. Janssen, M. Kemerink, *Adv. Funct. Mater.* **2015**, 25, 3066.

[18]   A. Sandström, P. Matyba, L. Edman, *Appl. Phys. Lett.* **2010**, 96, 053303.

[19]   J. Fang, P. Matyba, L. Edman, *Adv. Funct. Mater.* **2009**, 19, 2671.

[20]   J. Mindemark, L. Edman, *J. Mater. Chem. C* **2016**, 4, 420.

[21]   J. Fang, P. Matyba, N. D. Robinson, L. Edman, *J. Am. Chem. Soc.* **2008**, 130, 4562.

[22]   S. Tang, W.-Y. Tan, X.-H. Zhu, L. Edman, *Chem. Commun*. **2013**, 49, 4926.

[23]   S. Jenatsch, L. Wang, M. Bulloni, A. C. Véron, B. Ruhstaller, S. Altazin, F. Nüesch, R. Hany, *ACS Appl. Mater. Interfaces* **2016**, 8, 6554.

[24]   E. Bandiello, M. Sessolo, H. J. Bolink, J. *Mater. Chem. C* **2016**, 4, 10781.

[25]   H.-C. Su, *ChemPlusChem* **2018**, 83, 197.

[26]   E. M. Lindh, P. Lundberg, T. Lanz, J. Mindemark, L. Edman, *Sci. Rep.* **2018**, 8, 6970.

[27]   N. Kaihovirta, A. Asadpoordarvish, A. Sandström, L. Edman, *ACS Photonics* **2014**, 1, 182.

[28]   S. Tang, L. Edman, *J. Phys. Chem. Lett.* **2010**, 1, 2727.

[29]   T. Lanz, E. M. Lindh, L. Edman, J. *Mater. Chem. C* **2017**, 5, 4706.

[30]   A. Asadpoordarvish, A. Sandström, S. Tang, J. Granström, L. Edman, *Appl. Phys. Lett.* **2012**, 100, 193508.

[31]   N. Kaihovirta, C. Larsen, L. Edman, *ACS Appl. Mater. Interfaces* **2014**, 6, 2940.

[32]   S. Tang, J. Mindemark, C. M. G. Araujo, D. Brandell, L. Edman, *Chem. Mater.* **2014**, 26, 5083.

[33]   M. Kawecki, R. Hany, M. Diethelm, S. Jenatsch, Q. Grossmann, L. Bernard, H. J. Hug, *ACS Appl. Mater. Interfaces* **2018**, 10, 39100.

[34]   S. Burns, J. MacLeod, T. T. Do, P. Sonar, S. D. Yambem, *Sci. Rep.* **2017**, 7, 40805.

[35]   J. Huang, H. Nie, J. Zeng, Z. Zhuang, S. Gan, Y. Cai, J. Guo, S.-J. Su, Z. Zhao, B. Z. Tang, *Angew. Chem., Int. Ed.* **2017**, 56, 12971.

[36]   J. Mindemark, S. Tang, J. Wang, N. Kaihovirta, D. Brandell, L. Edman, *Chem. Mater.* **2016**, 28, 2618.

[37]   Q. Pei, Y. Yang, G. Yu, C. Zhang, A. J. Heeger, *J. Am. Chem. Soc.* **1996**, 118, 3922.

[38]   S. Höfle, T. Lutz, A. Egel, F. Nickel, S. W. Kettlitz, G. Gomard, U. Lemmer, A. Colsmann, *ACS Photonics* **2014**, 1, 968.

[39]   R. R. Chance, A. Prock, R. Silbey, in *Advances in Chemical Physics*, Vol. XXXVII (Eds: S. A. Rice, I. Prigogine), John Wiley & Sons, New York **1978**, Ch. 1.

[40]   Devižis, S. Jenatsch, M. Diethelm, V. Gulbinas, F. Nüesch, R. Hany, *ACS Photonics* **2018**, 5, 3124.

[41]   S. D. Yambem, M. Ullah, K. Tandy, P. L. Burn, E. B. Namdas, *Laser Photonics Rev.* **2014**, 8, 165.

[42]   D. Hohertz, J. Gao, *Adv. Mater.* **2008**, 20, 3298.

[43]   Y.-P. Jhang, H.-F. Chen, H.-B. Wu, Y.-S. Yeh, H.-C. Su, K.-T. Wong, *Org. Electron.* **2013**, 14, 2424.

[44]   V. I. Arkhipov, E. V. Emelianova, P. Heremans, H. Bässler, *Phys. Rev. B* **2005**, 72, 235202.

[45]   J. Mindemark, S. Tang, H. Li, L. Edman, *Adv. Funct. Mater.* **2018**, 28, 1801295.

Supporting Information
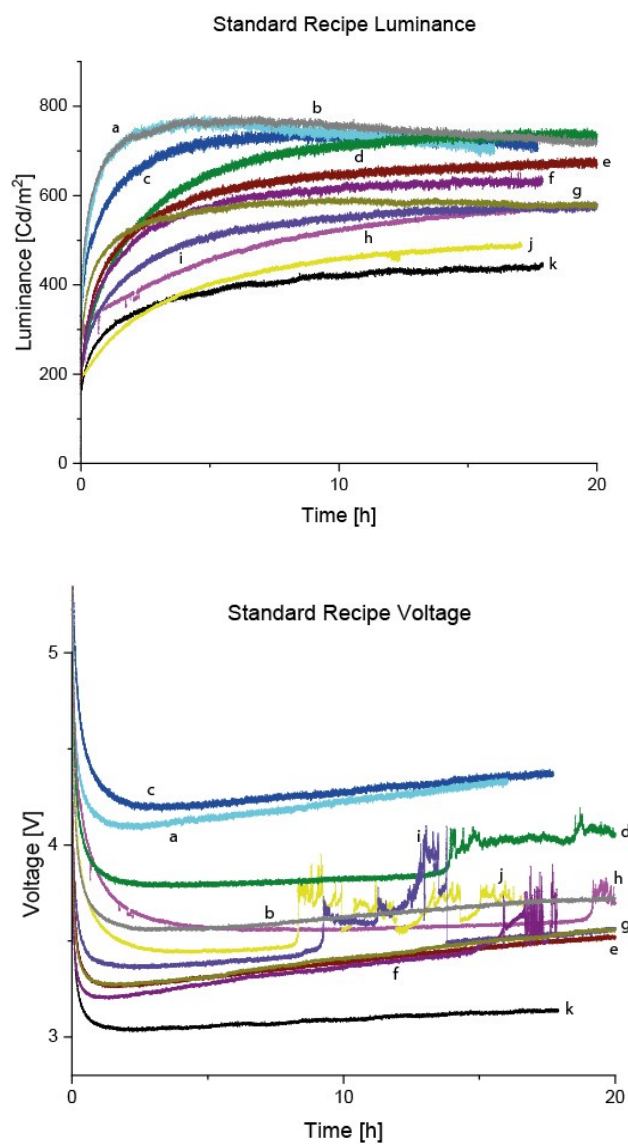
Figure S2.1. Luminance (top) and voltage (bottom) trends of 11 identical (ITO/SY+TMPE+ Li$^+$CF$_3$SO$_3^-$/Al) LECs. The mass ratio was SY:TMPE:Li$^+$CF$_3$SO$_3^-$ = 1:0.1:0.03 and the active layer thickness was 70 nm. Devices were driven at a constant current of 7.7 mA cm^{-2}.
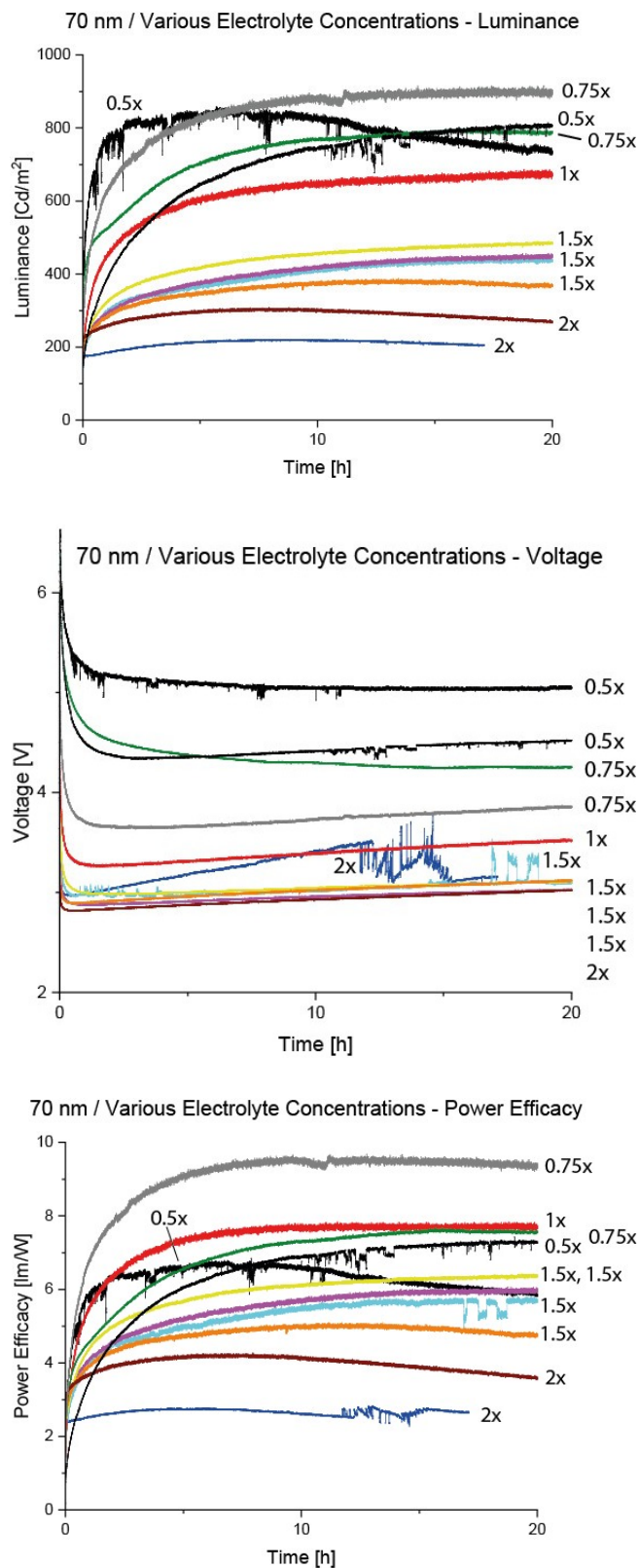
Figure S2.2. Luminance (top), voltage (middle) and power conversion efficiency (bottom) trends for (ITO/SY+TMPE+Li$^+$CF$_3$SO$_3^-$/Al) LECs with varying electrolyte concentrations. Devices were

driven at a constant current of 7.7 mA cm^{-2}. For the standard (1x) concentration, data for a typical average LEC from Figure S2.1 were included.

Electronic and optical model description

We used the software Setfos 4.6 from Fluxim.com for electronic and optical simulations.[S1]

The optical model is based on dipole emission.[S2] To simulate the electronic behaviour of the SY layer, a drift-diffusion simulation including mobile ionic charges was performed. The electrodes were modelled by assigning a work function only, which regulates the injection into the SY layer and thus acts as a Dirichlet boundary condition for electrons and holes in the drift-diffusion model. The anions and cations are modelled using a constant total concentration and zero current flux over the boundary. For simplicity exciton dynamics have not been included in the simulation. Relevant drift-diffusion parameters are summarized in Table S3.1. The difference of the electrode work function to experimental values is due to the fact that barrier lowering[S3] caused by the image potential of the injected charge carriers is not taken into account in the electrical model. The grid spacing of 4 points/nm was refined to 20 points/nm in a 10 nm range next to the electrode to cope with larger gradients of the electric field and ion charge concentrations near the interface. Steady state simulations were done where the voltage was adapted to a current density of 7.7 mA cm^{-2}.

Optically, all layers of the device stack were included in the simulation. Refractive indices n and extinction coefficients k were taken from the following sources: the glass substrate and ITO were measured by ellipsometry; data for aluminium were taken from the Setfos database; SY data were taken from ref. S4 (Figure S2.4). For all simulations, a current density of 7.7 mA cm^{-2}, an internal quantum efficiency of 68.3%,[S5] an exciton conversion efficiency of 25% and a charge carrier balance factor γ of 100% were assumed. The software Setfos was called by a script written in MATLAB R2018a.

In the following, the *graded doping* model (Figure 2.3e) is explained in detail. Using capacitance and Stark effect measurements on operated LECs we could show that there indeed exists a doping − and consequently ion − gradient towards the intrinsic zone.[S6] The intrinsic region was kept constant (10 nm) for all active layer thicknesses. The Gaussian emission was centred in the intrinsic region and had a width of 2.5 nm, such that the whole distribution fits into the intrinsic zone. It was expected that there is no emission from the doped regions due to exciton quenching. In the main text, doping was included for the standard salt concentration only. For the calculation of the doping density we considered that the salt is fully dissociated; based on our recent ToF-SIMS study[S7] we believe that this is indeed the case. In that work we could show that the ions are fully displaced towards the respective electrodes. With the assumption that all ions can contribute to doping, the concentration for n- and p- doping is 6.4% over the whole active layer. *Graded doping* was approximated by dividing the doped layer into three segments with different doping levels. The width of the first layer next to the electrode was chosen as half of the total width. The middle layer was one quarter wide, and its concentration was set to ¾ of the first layer. The third segment, next to the SY layer, was again one quarter and had ¼ of the concentration of the first layer. In this example, the average doping concentration is calculated via $\frac{28.4\%*10.5nm +21.3\%*5.25nm+ 7.1\%*5.25nm}{70nm} = 6.4\%$, as assumed.

To estimate n and k values for varying doping levels, data was interpolated from measured values.[S4] An example is shown in Figure S2.6. For very thin layers, the (calculated) doping concentrations exceeded experimental ones, such that extrapolation was necessary. For close data, such as the blue dashed line (calculated 21.3%, compared to (yellow) experimental 20%), the extrapolation was good. For higher concentrations such as 28.4%, black dashed line, the extrapolation got less reliable. This is the reason why we limited the optical model calculations with doping included (Figure 2.3) to a lower EP position of 0.35, because the highest experimental p-doping concentration data was only 20%.[S4]

Data in Figure 2.3 of the main text demonstrate that doping does influence the emission shape and luminance level. However, for the standard salt concentration the effects are relatively minor. Consequently, the influence of doping on the optical model would be even smaller for lower salt concentrations. The quantitative prediction of the influence of doping on the optical model for very high salt concentrations is difficult at the moment because experimental refractive indices and extinction coefficients for high n- and p-doping levels are not available. EPs were simulated in the range from 0.35 to 0.8 only, because outside this range the extrapolation of experimental data got less reliable (Figure S2.6). For higher salt amounts the calculated doping concentrations would increase and therefore the reliable EP range for optical modelling would shrink further.

Table S2.1. Electrical model

Parameter	Value	Source
Thickness SY	70 nm	Profilometry measurement
Electron mobility	4.1×10^{-7} cm^2/Vs	Ref. S8
Hole mobility	6.1×10^{-7} cm^2/Vs	
Radiative Recombination coefficient	1×10^{-9} cm^3/s	Guess
Effective density of states	1×10^{28} 1/m^3	Manual fit
LUMO SY	2.95 eV	Ref. S9
HOMO SY	5.45 eV	
Ohmic injection work function ITO	5.11 eV	Manual fit
Ohmic injection work function Al	3.29 eV	
Relative Permittivity SY	2.8	Calculated from capacitance measurement
Equilibrium density of mobile negative ions	1×10^{20} 1/cm^3	Estimation from used salt concentration with film density of 1 g cm^{-3} (ref. S4)
Equilibrium density of mobile positive ions	1×10^{20} 1/cm^3	
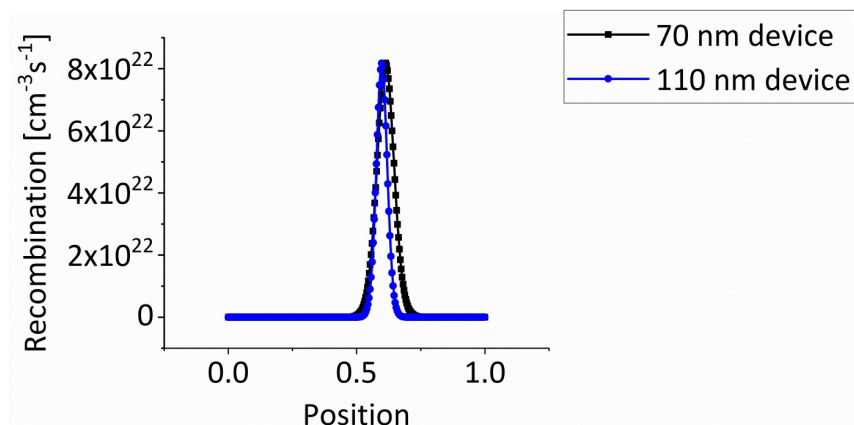
Figure S2.3. Electrical simulation of the recombination zone with parameters shown in Table S3.1. The relative peak position, recombination current and the width of the Gaussian-like peak is for both thicknesses the same; the 110 nm peak appears thinner because both x axes were scaled.
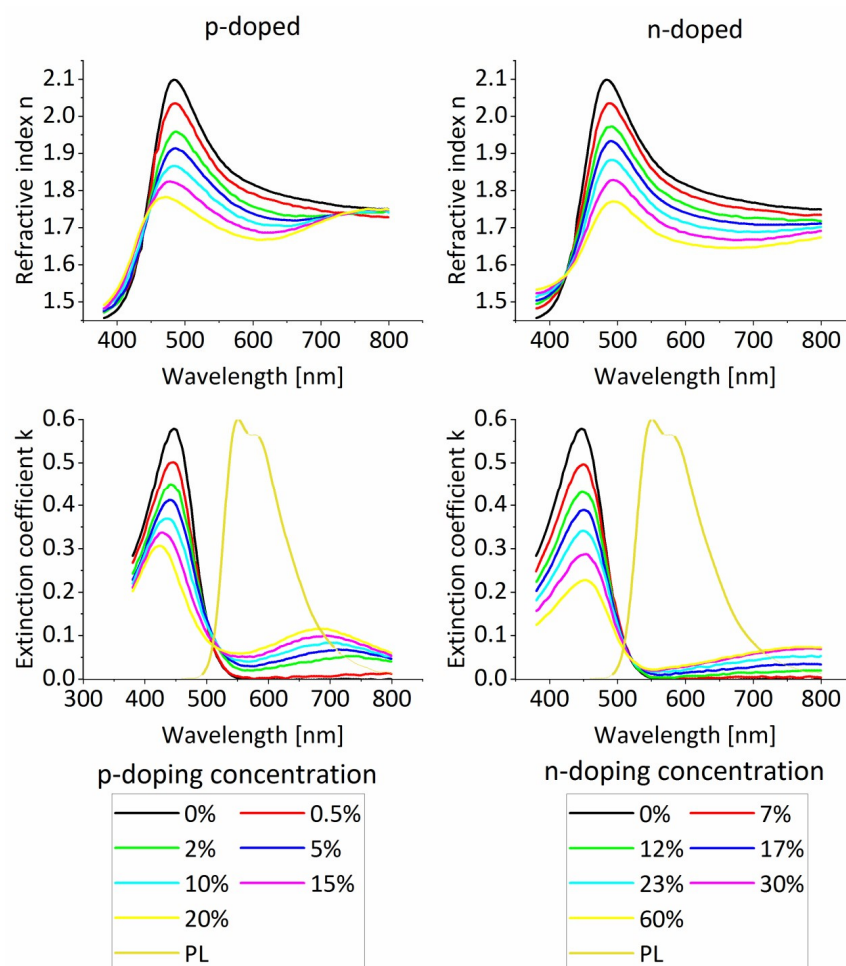
Figure S2.4. Refractive indices and extinction coefficients for different n- and p-doping levels extracted from ref. S4. Also shown is the in-house measured photoluminescence spectrum; the

overlap of the emission with the absorption of pristine and doped SY results in reabsorption of emitted light as shown in Figure 2.4 and Figure S2.8.
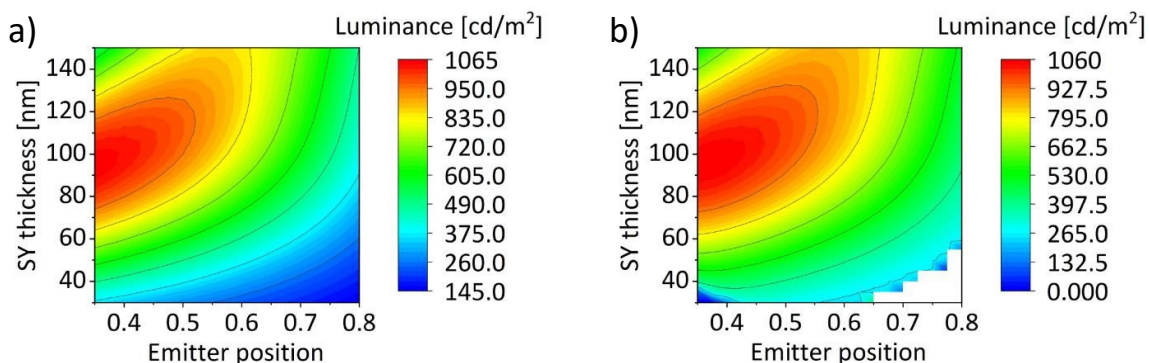
Figure S2.5. Constant doping model for a 5 nm a) and 20 nm b) intrinsic zone with a Gaussian emitter width of 25% of the intrinsic width. Results are very similar, and increasing the intrinsic zone further leads to the same result, although not all points can be simulated because of reasons explained in Figure S2.6.
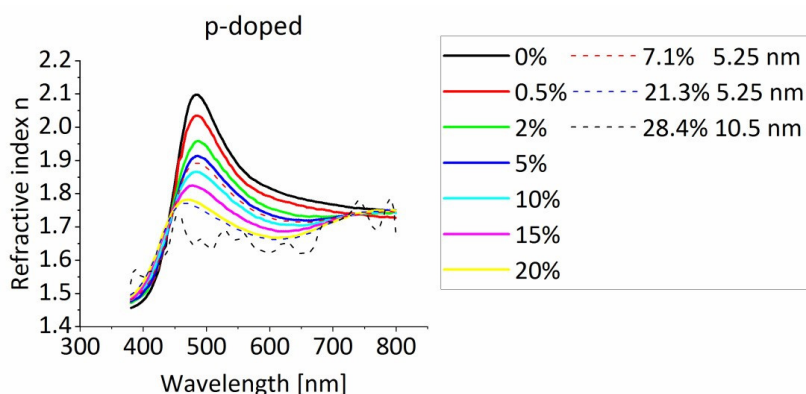
Figure S2.6. Interpolation and extrapolation of experimental n and k data. The dashed lines are examples of refractive indices of p-doped layers in a *graded doping* simulation of a 70 nm thick device, where the EP is situated at 0.35. For lower EPs and for EPs higher than 0.8, the extrapolation gets too unreliable.
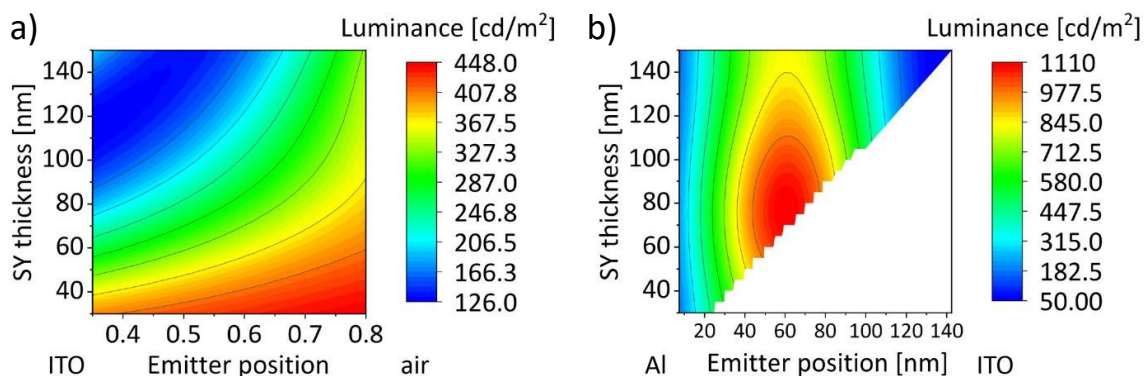
Figure S2.7. a) Simulated luminance for different emitter positions and active layer thicknesses when replacing the Al top electrode by air for the no doping model, showing the relevance of the cathode for the observed interference effect. b) When plotting the x-axis of a no doping simulation as in Figure 2.3b or Figure S2.9 in absolute values and as distance from the cathode, one can see that the maximum of the interference is ~60 nm away from the cathode, independent of the active layer thickness.
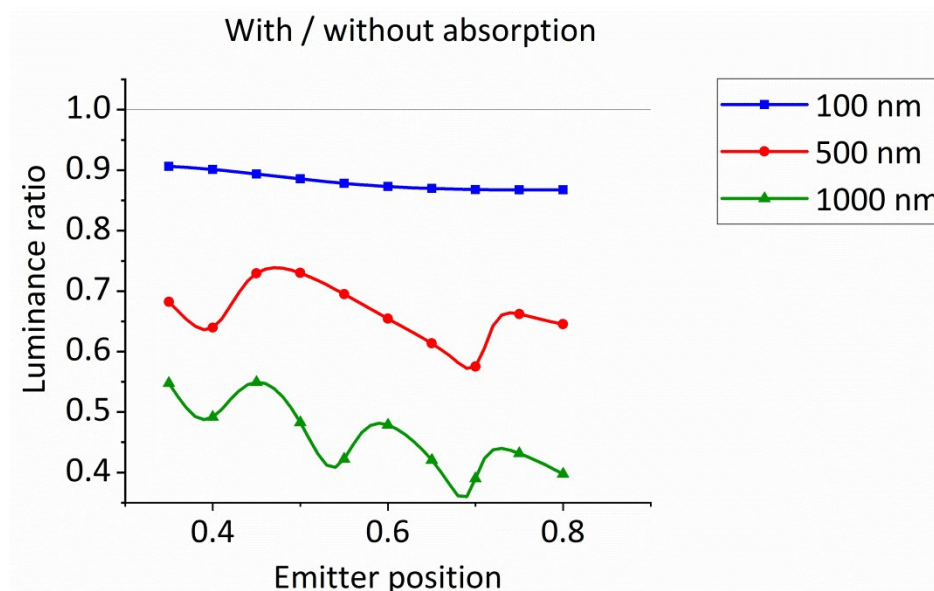
Figure S2.8. The model *const. doping* for a standard cell was simulated with and without self-absorption (k-values set to 0) and the ratio of the two lines at a thickness of 100 nm, 500 nm and 1000 nm are shown. The cavity effect leads to the wavy profile. The effect of doping induced self-absorption was already studied in ref. S10. The analysis involved several assumptions such as i) symmetric n- and p-doping and ii) that the emitted light passes the p-doped zone only once before being directly out-coupled – this implies no absorption by the n-doped layer and neglect of the weak microcavity effect. The self-absorption loss at steady state and at the EL peak wavelength 550 nm for a device thickness of 100 nm was reported to be 11%, for 500 nm the loss was 47% and for 1000 nm over 70%. Our analysis confirms the ~10% self-absorption loss for the 100 nm active layer and suggests that the actual loss is slightly lower for thicker layers.
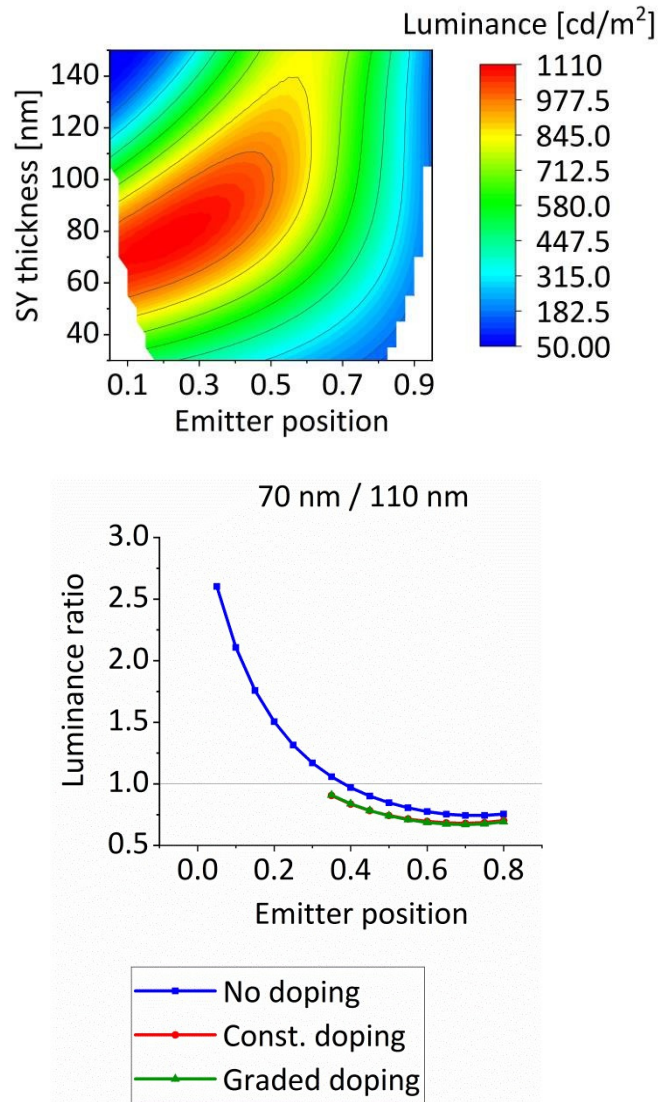
Figure S2.9. Luminance for different emitter positions and active layer thicknesses using the intrinsic n- and k-values of SY (top), and extended ratio between the luminance values for active layer thicknesses of 70 nm and 110 nm (bottom).
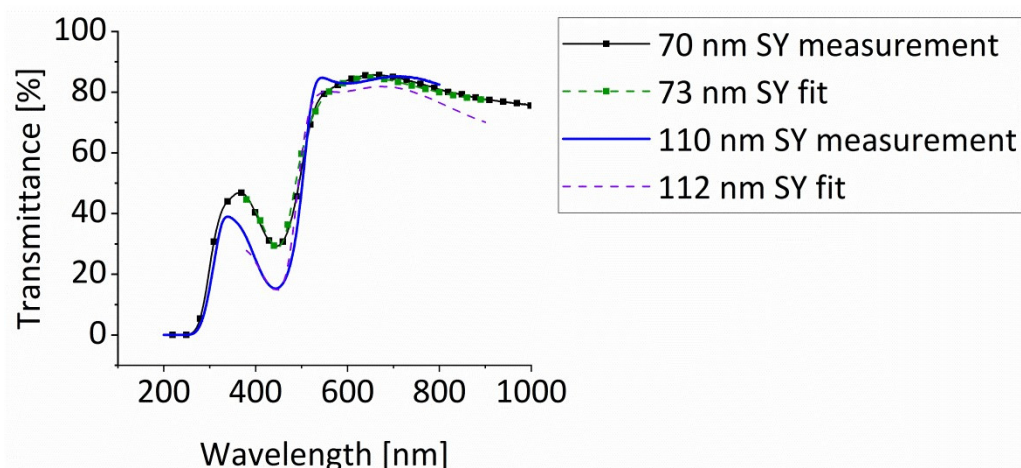
Figure S2.10. Transmittance measurements and simulations of standard cells with 70 nm and 110 nm thick active layers. For the simulations we used n- and k-values from pristine SY (Figure S2.4), viz. not from the blend. The good agreement in the visible wavelength range between experiment and simulation justifies this assumption and can be explained by the low electrolyte loading in the blend, not changing the optical constants significantly.

References

[S1]   B. Ruhstaller, T. Flatz, D. Rezzonico, M. Moos, N. Reinke, E. Huber, R. Haeusermann, B. Perucco, *Proceedings of SPIE* **2008**, *7051*, 70510J.

[S2]   R. R. Chance, A. Prock, R. Silbey, in *Advances in Chemical Physics*, Vol. XXXVII, edited by I. Prigogine, S. A. Rice, John Wiley and Sons, **1978**, chapter 1.

[S3]   P. R. Emtage, J. J. O'Dwyer, *Phys. Rev. Lett.* **1966**, *16*, 356.

[S4]   T. Lanz, E. M. Lindh, L. Edman, *J. Mater. Chem. C* **2017**, *5*, 4706.

[S5]   S. D. Yambem, M. Ullah, K. Tandy, P. L. Burn, E. B. Namdas, *Laser Photonics Rev.* **2014**, *8*, 165.

[S6]   A. Devižis, S. Jenatsch, M. Diethelm, V. Gulbinas, F. Nüesch, R. Hany, *ACS Photonics* **2018**, *5*, 3124.

[S7]   M. Kawecki, R. Hany, M. Diethelm, S. Jenatsch, Q. Grossmann, L. Bernard, H. J. Hug, *ACS Appl. Mater. Interfaces* **2018**, *10*, 39100.

[S8]   S. R. Tseng, Y. S. Chen, H. F. Meng, H. C. Lai, C. H. Yeh, S. F. Horng, H. H. Liao, C. S. Hsu, *Syn. Metals* **2009**, *159*, 137.

[S9]   S. Stolz, M. Petzoldt, S. Dück, M. Sendner, U. H. F Bunz, U. Lemmer, M. Hamburger, G. Hernandez-Sosa, *ACS Appl. Mater. Interfaces* **2016**, *8*, 12959.

[S10]   N. Kaihovirta, A. Asadpoordarvish, A. Sandström, L. Edman, *ACS Photonics* **2014**, *1*, 182.

Chapter 3   The Influence of Ionic Motion on the Electrical and Optical Performance of LECs

The Dynamic Emission Zone in Sandwich Polymer Light-Emitting Electrochemical Cells

Matthias Diethelm[1,2], Andreas Schiller[3,4], Maciej Kawecki[5,6], Andrius Devižis[7], Balthasar Blülle[4], Sandra Jenatsch[4], Evelyne Knapp[3], Quirin Grossmann[1], Beat Ruhstaller[3,4], Frank Nüesch[1,2], and Roland Hany[1]

[1]Empa, Swiss Federal Laboratories for Materials Science and Technology, Laboratory for Functional Polymers, 8600 Dübendorf, Switzerland
[2]EPFL, Institute of Materials Science and Engineering, Ecole Polytechnique Fédérale de Lausanne Station 12, 1015 Lausanne, Switzerland
[3]ZHAW, Zurich University of Applied Sciences, Institute of Computational Physics, Technikumstrasse 9, 8401 Winterthur, Switzerland
[4]Fluxim AG, Katharina-Sulzer-Platz 2, 8400 Winterthur, Switzerland
[5]Empa, Swiss Federal Laboratories for Materials Science and Technology, Nanoscale Materials Science, 8600 Dübendorf, Switzerland
[6]Department of Physics, University of Basel 4056 Basel, Switzerland
[7]FTMC, State Research Institute Center for Physical Sciences and Technology, Department of Molecular Compound Physics, Saulėtekio Avenue 3, LT-10257 Vilnius, Lithuania

Declaration of Contribution
M.D. contributed to and overviewed the device preparation and luminance characterisation, performed all impedance spectroscopy related measurement, did the optical and electrical simulation including all related input data measurements, analysed the data and prepared the manuscript.

Abstract

In light-emitting electrochemical cells (LECs), the position of the emission zone (EZ) is not predefined via a multilayer architecture design, but governed by a complex motion of electrical and ionic charges. As a result of the evolution of doped charge transport layers that enclose a dynamic intrinsic region until steady state is reached, the EZ is often dynamic during turn-on. For thick sandwich polymer LECs, a continuous change of the emission colour provides a direct visual

indication of a moving EZ. Results from an optical and electrical analysis indicate that the intrinsic zone is narrow at early times, but starts to widen during operation, notably well before the electrical device optimum is reached. Results from numerical simulations demonstrate that the only precondition for this event to occur is that the mobilities of anions (μ_a) and cations (μ_c) are not equal, and the direction of the EZ shift dictates $\mu_c > \mu_a$. Quantitative ion profiles reveal that the displacement of ions stops when the intrinsic zone stabilizes, confirming the relation between ion movement and EZ shift. Finally, simulations indicate that the experimental current peak for constant-voltage operation is intrinsic and the subsequent decay does not result from degradation, as commonly stated.

3.1   Introduction

The simultaneous occurrence of electronic and mobile ionic charge in organic materials has numerous applications in technologies ranging from organic electrochemical transistors to batteries, actuators, sensors and displays.[1–3] Arguably the best studied device application of the mixed electronic/ionic conduction in organic materials is the light-emitting electrochemical cell (LEC), and after 25 years of research the basic operation principles seem to have been firmly established.[4–10]

For a conjugated polymer LEC, a single solution-processed emissive polymer layer that contains an electrolyte is sandwiched between two electrodes. When a voltage is applied, the ions form electronic double layers (EDLs) at both electrodes that facilitate electronic charge injection. The reduced and oxidized polymer repeating units are electrostatically stabilized by opposite ionic charges, resulting in highly conductive n- and p-doped regions at the cathode and anode, respectively, which grow inside the film. Over time, a p-i-n junction develops where electrons and holes are injected from the electrodes into the active layer and travel along the doped regions to the intrinsic (i) zone where they recombine radiatively. Next to polymers, ionic transition metal complexes (iTMCs) and organic salts have been used as active LEC materials.[7,11–13] For these materials, the ionic and electronic transport occurs in the same material, but the device operation mechanism can be described by the same underlying processes.[14,15]

The developing p-i-n junction and the position of the zone where light is emitted (emission zone, EZ) can conveniently be followed by optical probing and photoluminescence experiments on so-called planar LECs that have a wide horizontal gap between the two electrodes.[6,15–24] The summary of numerous studies is that the EZ in many cases is off-centred. In addition, it has been observed that the EZ is dynamic and shifts across the device until steady state is reached.[15,21,25,26]

For sandwich-type LECs the active film thickness is below 1 µm and the dynamic formation of the p-i-n structure cannot be directly visualized with optical microscopy. For these devices, information about the EZ position could be obtained from a comparison of experimental emission spectra with optical simulations.[27–33] Just like for planar LECs, it was found that the EZ in sandwich LECs in many cases is off-centred and can move during operation.

As a complementary method, the p-i-n dynamics in sandwich LECs is often studied with impedance spectroscopy (IS). IS measurements yield simultaneous information about the dynamics of electronic and ionic charges, covering a wide frequency range from typically Hz to several MHz. Furthermore, the change in capacitance level at intermediate frequencies is commonly related to

the evolution of the intrinsic region with low conductivity.[11,34–40] Studies on poly(*para*phenylenevinylene)-type LECs combined IS measurement with equivalent circuit or drift-diffusion modelling, providing a solid understanding of the dynamic LEC junction.[34,36] One conclusion is that the width of the low-conductive region must not be equal to the width of the region with high recombination, i.e., the EZ.[36,38]

Despite these substantial achievements in the characterization and understanding of the dynamic p-i-n junction, it seems that a quantitative model that describes the often observed EZ shift in planar and sandwich LECs has not been presented so far. Off-centred EZs at equilibrium were explained by an asymmetry of electron and hole injection and transport.[41,42] For planar LECs, the moving p-n junction was explained with further doping of the partially doped polymer after the junction has formed.[23] EZ shifts were related to imbalances in carrier injection, conductivity, doping speed or a combination of these.[15] EZ shifts for short operation times were ascribed to incomplete formation of the doped zones and hence unbalanced carrier injection that balances later on.[28,29]

Here, we present a comprehensive experimental optical and electrical analysis of a moving EZ in polymer sandwich LECs that continued for more than 20 h and extended over more than 30% of the active layer thickness. For active layer thicknesses above ≈ 200 nm, the continuous change of the emission colour provided a direct visual indication of the moving EZ and the time-dependent EZ position was determined from angular emission measurements, observed for constant-voltage driven LECs also the current, and consequently the luminance, decreased after passing a maximum. We explained our observations of a moving EZ and a transient capacitance peak with results from numerical electrical drift-diffusion simulation and found that the sole precondition for these events to occur is that the mobilities of the anion and cation (μ_a, μ_c) are not equal. Time-of-flight secondary ion mass spectrometry (ToF-SIMS) ion profiles at different times during operation showed that the displacement of anions stopped when the capacitance levelled off, confirming the relation between ion movement and the observed EZ shift. As an important insight into the background science, simulation showed that the experimental current trend observed for constant-voltage driven devices is intrinsic to the LEC operation and does not result from (unspecified) device degradation, as commonly assumed. Device degradation mechanisms prevail only after the ionic movement has stopped.

3.2   Results

We investigated LECs with a phenyl-substituted poly(*para*phenylenevinylene) copolymer termed super yellow (SY) as emitting material, intermixed with an electrolyte consisting of the salt lithium trifluoromethanesulfonate ($Li^+CF_3SO_3^-$) and a hydroxyl-capped oligoether, trimethylolpropane ethoxylate (TMPE).[43] The chemical structures and the simple device architecture (glass/indium tin oxide (ITO)/active layer/Al or Ag top electrode) are shown in Figure S3.1 of the Supporting Information. In all following spatially resolved graphs and images, ITO is on the left and the metal electrode on the right side.

Previously, we optimized the efficiency (11.6 cd A^{-1}) of this device in terms of materials composition (SY:TMPE:$Li^+CF_3SO_3^-$ = 1:0.075:0.0225) and active layer thickness (70 nm).[44] Interestingly, a complex dynamic change in colour became apparent when studying devices with

much thicker active layers (**Figure 3.1**a). Pictures were taken with an optical microscope while the 430 nm thick device was biased with a constant current of +7.7 mA cm^{-2}, where the positive bias was applied to the ITO. The same trend is observed in Figure 3.1b as a valley in the luminance, and the minimum luminance value was at the same point in time when the colour shifted from red to green, where it appeared also the darkest. The effect seems to be more pronounced when the active layer thickness was increased. On the other hand, the voltages in Figure 3.1c did not change drastically over time, the only trend observable is a slight increase of the minimal voltage, which scaled roughly linear with thickness (Figure S3.2a, Supporting Information).
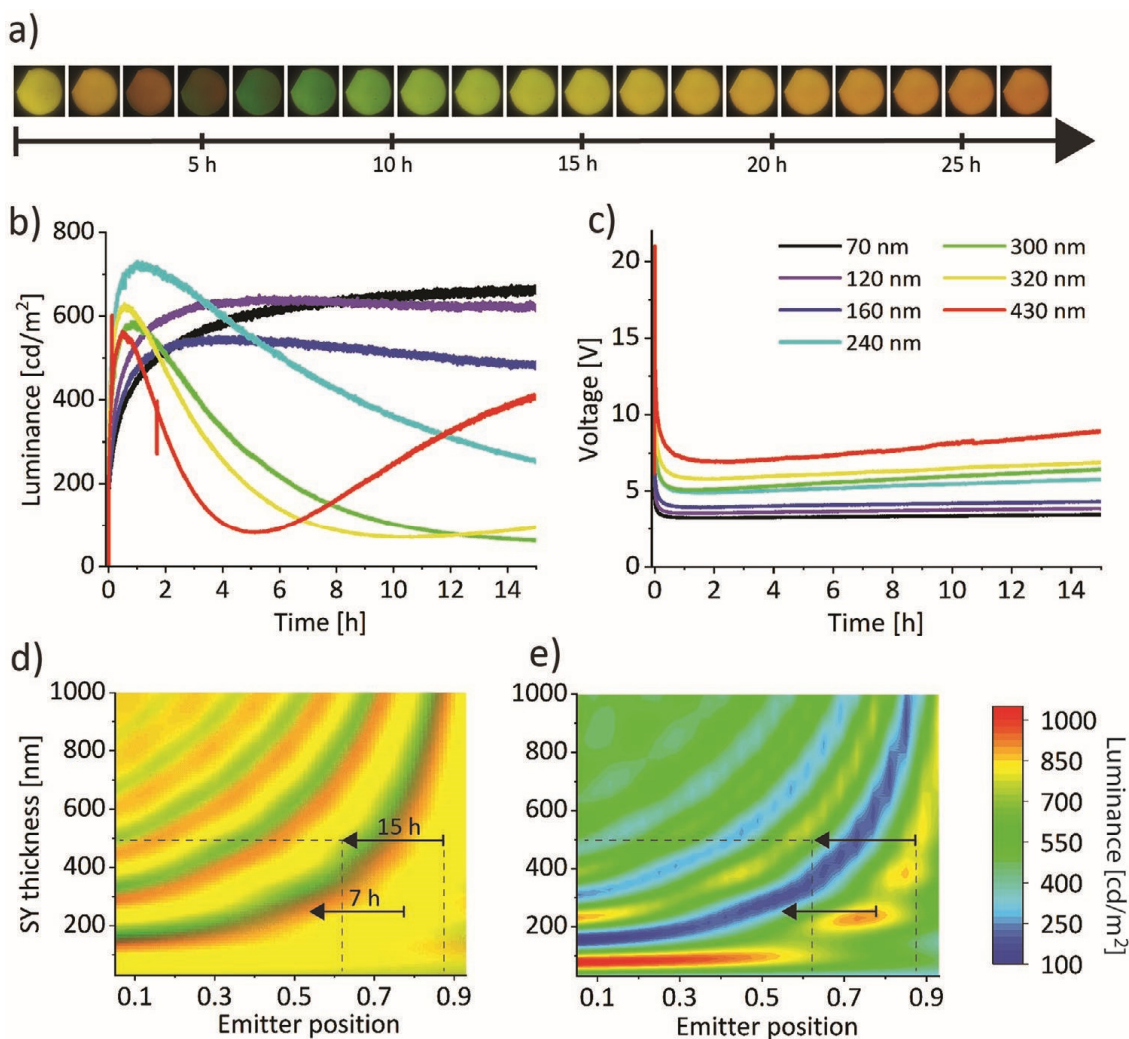
Figure 3.1. A change in colour over time is observed in a) for a constant-current driven LEC with an active layer thickness of 430 nm. b) Luminance transients and c) voltage transients for LECs with different active layer thicknesses. Optical simulations of the perceived colour d) and luminance e) at a 0° observer angle demonstrate the dependence on active layer thickness and emitter position. Experimental emitter position shifts from angular emission measurements are indicated by arrows in d) and e).

As observed before for that particular materials system,[44] it must be noted that the sample-to-sample variation was rather large, despite an apparent constant experimental device fabrication procedure. Data for the 430 nm thick device in Figure 3.1 show that the valley of the luminance was reached after 5 h and the corresponding voltage was 7.5 V. From a larger set of LECs (Figure S3.3, Supporting Information), we found that the average time when the luminance valley was reached was (7.5 ± 2.9) h, and the corresponding average voltage was (8.5 ± 1) V. Therefore, we unravel in the following the basic mechanisms responsible for the observed dynamic change in colour and identify trends rather than claim exact numbers. This will be especially important when comparing experimental data with results from optical and electrical simulations.

Data in Figure 3.1 suggest an optical phenomenon as the reason for the observed change in colour. As explained in previous work, LECs are heavily influenced by the microcavity effect.[31,32,44] Here, we expanded the optical simulations of ref. [44] to an active layer thickness of 1000 nm as shown in Figure 3.1d,e, where Figure 3.1d shows the perceived colour and Figure 3.1e the luminance observed perpendicular to the emitting surface. The position of a Gaussian profile emitter with a width at half maximum of 20 nm was swept from ITO at emitter position 0 to the metal electrode at a relative emitter position of 1. The resulting pattern appears as an interference effect due to the feedback of the emitted electromagnetic field of the dipole-like emitter that is reflected at the metal electrode.[45–47] When the same data are plotted as an absolute distance from the metal electrode (Figure S3.2b,c, Supporting Information), it is evident that the effect depends only on the distance of the emitter to the metal electrode. The luminance valleys (Figure 3.1e) overlap with the red/green colour bands (Figure 3.1d) because interference is suppressing parts of the spectra, such that it is perceived as another colour. The complete optical model is described in the Supporting Information.

By comparing the colour change over time in Figure 3.1a with the colour bands in Figure 3.1d, an immediate hypothesis is that the region where excitons recombine under emission of light shifted with biasing time over a large distance of more than 100 nm. Furthermore, the sequence of the change in colour is yellow-red-green-yellow, which dictates the movement to proceed from the metal electrode toward ITO. To quantify the EZ shift, we measured angular emission spectra from −85° to 85° in 5° steps while biasing a 430 nm and a 240 nm thick device with a constant current of 7.7 mA cm^{-2}. Data were fitted with the optical model (see above)[31,44] and the resulting emitter position over time is shown in Figure S3.2d (Supporting Information). These data were included as arrows into Figure 3.1d,e for clarity. Similar undulating luminance transients for SY LECs (using a different ion conductor and different materials composition) have recently been reported, but the optical analysis was restricted to steady state.[32,33]

For the 240 nm thick device after an operation time of 7 h, the EZ shifted very close to the centre of the active film, whereas for the 430 nm thick device and after an operation time of 15 h, the EZ was still slightly off-centred at a relative position of ≈0.6 (Figure 3.1d,e). From Figure 3.1a, however, it can be seen that the change in colour for longer operation times continued and the emitted colour after 25 h was red. When extrapolating the arrow in Figure 3.1d to the red colour band, it can be seen that the EZ for the 430 nm thick device after long operation time and close to steady state (see below) arrived also at a relative emitter position of ≈0.5. From this we conclude that in our LECs the steady-state EZ was in the centre, largely independent of the active layer thickness. A centred EZ implies similar electronic mobility values ($\mu_e \approx \mu_h$), or more precise a

balance in the combination between hole and electron mobilities in the doped and intrinsic regions as well as charge injection, as will be confirmed from numerical simulations results below. To investigate the emitter position and EZ shift, a number of experiments were carried out with 430 nm thick LECs. First, operated devices were short-circuited for at least 72 h, i.e., the metal contact and ITO were connected with a metal wire. After that, the device was operated for a second time and the original sequence of the change in colour was observed again (Figure S3.4, Supporting Information). This means that during the time of nonuse the p- and n-regions de-doped and complete ion relaxation occurred. When the device was short-circuited for only 24 h, the change in colour happened as well but started already from the colour red (emitter position ≈0.75; Figure 3.1d), indicating a partial ion relaxation.

Reverse driving, i.e., when the negative bias was applied at the ITO, resulted in fast device degradation when using an Al electrode due to electrochemical reactions at the SY/Al interface.[48] However, with a Ag electrode reverse biasing was possible. The surprising finding was that when the device turned on the emitted colour was green and the sequence of the change in colour was green-red-yellow, i.e., the opposite of the forward biased device (Figure S3.4, Supporting Information). We did not quantify from which position the emission started in that case, but from Figure 3.1d it gets clear that the EZ was now shifting from the ITO toward the Ag electrode. These observations demonstrate the dynamic LEC behaviour and show that the change in colour is not due to, for example, a trivial device degradation process.

Figure 3.2a shows the capacitance versus frequency dynamics, which was calculated from the imaginary part of the admittance from IS measurements taken from the pristine device and during constant-current operation. In the pristine, undoped device, the whole active layer is intrinsic and the extracted capacitance (4.8 nF cm^{-2}) at 10^7 Hz represents the geometrical capacitance. A slight increase of the capacitance to 7.1 nF cm^{-2} at 10 Hz occurred, which can be attributed to charges that penetrate further into the device.[36] During operation and after 1 h at lower frequencies, the capacitance has increased to a maximum value. This increase is related to the formation of the doped zones, resulting in a smaller intrinsic region, or more precisely to a shrinkage of the low conductivity part of the device.[36] The threshold frequency at roughly 10^3 Hz is the frequency where charges start to have enough time to reach the interface between the doped and intrinsic region, thus contributing to the capacitance. For longer measurement times up to 14 h the capacitance at low frequencies continuously decreased, indicating that the width of the intrinsic region increased again.
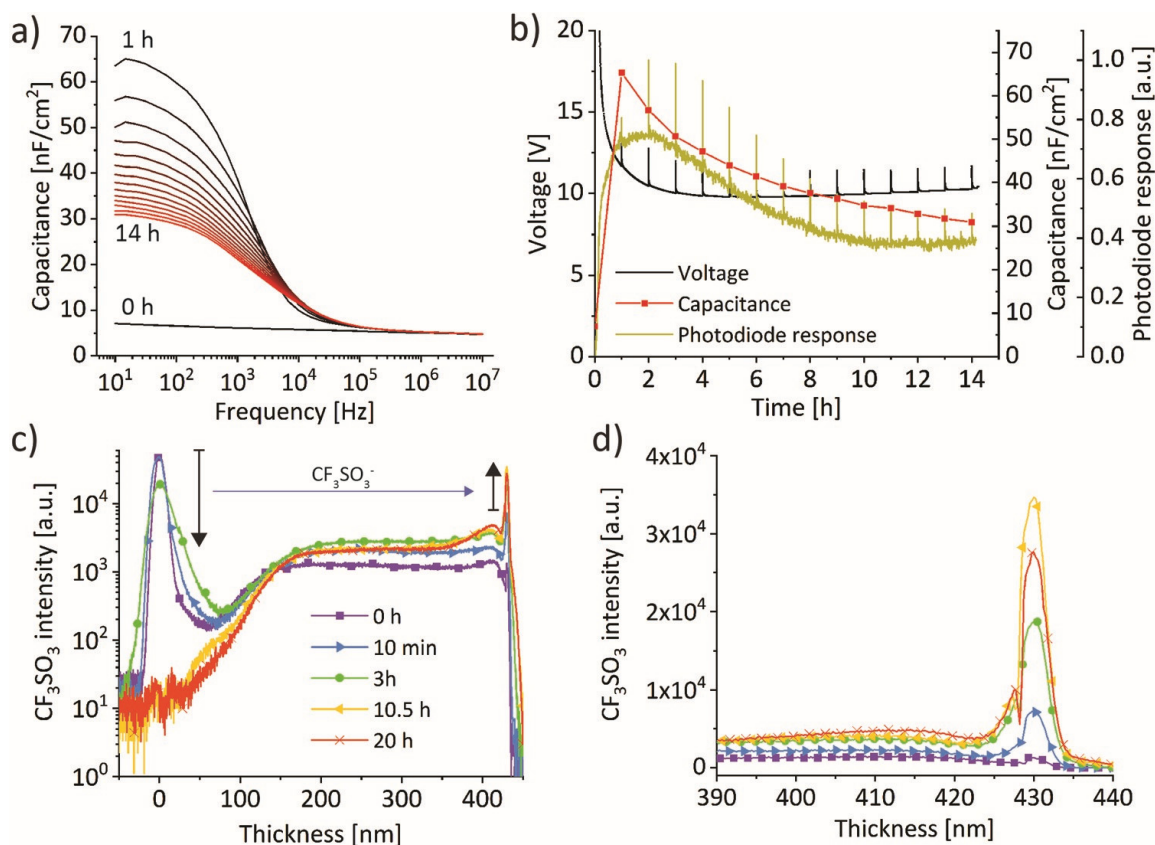
Figure 3.2. Capacitance, voltage, light intensity, and ToF-SIMS measurements on 430 nm thick devices. The capacitance versus frequency sweeps in a) were measured every hour on a device with an Al electrode, while a constant current of +7.7 mA cm^{-2} was applied at the ITO. The points at 10 Hz are plotted as transient in b) together with the measured voltage and light intensity. ToF-SIMS measurements c,d) were performed on a device with a Ag electrode and a reverse bias of -7.7 mA cm^{-2} applied at the ITO.

The simultaneously measured voltage, capacitance and light intensity transients are plotted in Figure 3.2b. The spikes in the voltage and photodiode response measurements are due to the 40 s breaks when the IS measurement was carried out at 0 V, and can be attributed to a slight device relaxation during that period. The origin of these spikes is discussed in the Supporting Information. The light intensity was measured with a photodiode. Because the temporal emission spectra are not precisely known, the exact conversion into a radiance (respectively luminance) transient is not possible. However, we detail in the Supporting Information (Figure S3.5, Supporting Information) that the trends are the same and that the difference between peak and valley values varies by ≈15% at most. The light intensity peaked at around 2 h, before the minimum of the voltage was reached at around 5 h. Such behaviour is usually explained by increased exciton quenching when the narrowing intrinsic region gets in close contact with the doped zones.[11] In our case, however, the observed light intensity decrease is due to interference effects while the EZ is shifting (Figure 3.1).

Surprisingly, and in contrast to the current understanding of the functioning of LECs, also the capacitance peaked (after 1 h) much before the minimum of the voltage was attained (Figure

3.2b). Generally, the transient voltage minimum is related to a device situation where the doped zones have fully developed, the intrinsic region is at its narrowest width and, consequently, the capacitance should be at the maximum. This observation was independent of the metal electrode (Al vs Ag), of the active layer thickness, and also recurred for operated devices after relaxation (Figure S3.6, Supporting Information).

As the evolution of our LECs took place over a period of many hours, we supposed that the dynamics is dictated by the slow movement of the ions through the device. We performed ToF-SIMS experiments on 430 nm thick devices to determine the $CF_3SO_3^-$ distribution throughout the film as function of the operation time. Recently, we operated LECs inside a ToF-SIMS spectrometer and cooled the sample to liquid nitrogen temperature before quantitative depth profiling was performed.[48] For 60 nm thick devices, we found that the initial anion distribution was inhomogeneous with a peak at the ITO.[48] The same result was measured here for devices that contained an Al or Ag top electrode and the anions accumulated during spin coating and film formation preferentially at the bottom electrode (Figure 3.2; Figure S3.7, Supporting Information). For this situation and when a positive bias is applied to the ITO, the anions would already be "at the right electrode" and their distribution would not change much during operation. Therefore, we studied the anion distribution for negative-biased (-7.7 mA cm^{-2} at ITO) LECs with a Ag electrode; as explained above, such devises are stable when operated under a reverse bias.

Already after 10 min, the $CF_3SO_3^-$ content at the ITO side has decreased and anions have started to pile up in a very narrow distribution at the Ag electrode. This can be interpreted as the start of the EDL formation. This ion displacement process continued for longer operation times and after around 10 h, the ITO side was completely depleted and the anions transferred to the Ag side. In the bulk of the film, the anion concentration remained low throughout, except of a small anion peak in the thickness range of $\approx$400-420 nm that grew over an operation time of 20 h.

We measured the voltage and capacitance trends for an ITO/SY(430 nm)/Ag LEC for reverse-biased operation conditions (Figure S3.7, Supporting Information), and observed similar transients as shown in Figure 3.2b for a forward-biased LEC containing an Al electrode. The capacitance increased in the beginning, passed through a maximum (after 2.2 h) and decreased afterward. Also, the capacitance peaked before the minimum of the voltage was reached (after 3.3 h). Interestingly, after around 10 h the capacitance levelled off and stayed almost constant during prolonged operation. From ToF-SIMS results, it can be seen that at this time also the final anion distribution has largely developed. This is a strong indication that the EZ shift indeed is dictated by the ionic displacement and that the overall device dynamics ends when the ionic distribution is in equilibrium.

Data presented so far were measured on constant-current driven devices. We performed measurements on constant voltage driven LECs to confirm that the essential device dynamics is independent of the operation mode. Results from capacitance versus frequency sweeps and from the current and light intensity trends of a 430 nm thick LEC operated at a constant voltage of 8 V are shown in **Figure 3.3**a,b. In Figure 3.3a, the threshold frequency during the first few hours changed from $\approx 10^3$ to $\approx 2 \times 10^4$ Hz because of a conductivity increase of the doped zones. As observed for constant-current driven devices (Figure 3.2), the capacitance passed through a maximum before the electrical device optimum, i.e., the maximum of the current, was reached. A similar observation was reported for a sandwich polymer LEC using a related materials system.[36]

Also the light intensity in Figure 3.3b showed the same variation in time and the change in colour could clearly be observed (data not shown). However, a straightforward interpretation of the change in colour for constant-voltage driven devices is more involved because the change of the light intensity due to the EZ shift is superimposed on the variation of the light intensity due to the continuously changing current. In Figure 3.3b, the light intensity decrease between ≈10 h and 25 h had a much smaller decreasing slope than the current, which is probably a sign of an increase of the light outcoupling efficiency due to the shift of the EZ during that period. After 25 h, the decrease of the light intensity followed exactly the current trend, which suggests that the EZ shift has stopped. Results from a further constant-voltage driven device where a clear luminance valley appeared are shown in Figure S3.8 (Supporting Information).
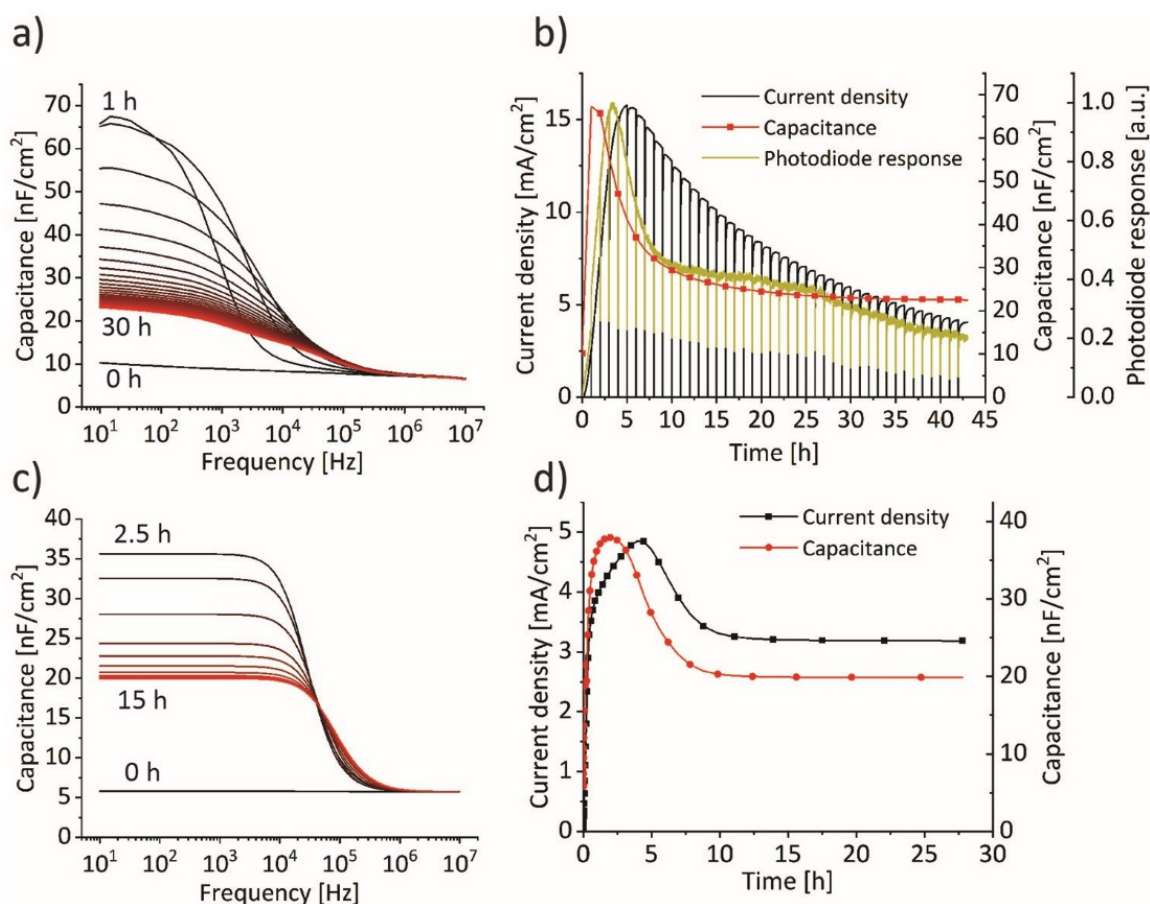
Figure 3.3. a) Capacitance versus frequency sweeps measured every hour and b) transients for the capacitance at 10 Hz, and current and light intensity for a 430 nm thick LEC driven at a constant 8 V bias. Results from drift-diffusion simulations on this device are shown in c) and d). For the simulation, $\mu_e = \mu_h$, equal injection barriers for electrons and holes, and $\mu_a = \mu_c/10$ was chosen, other parameters are compiled in Table S3.1 (Supporting Information).

3.3 Discussion

Due to the complex and simultaneous motion of ions and electronic charges during operation, an intuitive explanation for the observed EZ shift in LECs is difficult. Therefore, we resorted to an analysis of the device dynamics by numerical drift-diffusion modelling performed by applying a constant voltage. Results of the transient simulation are shown in Figure 3.3c,d. The good agreement with the measurement is apparent and the simulation could reproduce the essential experimental features. To obtain that level of agreement between experiment and modelling, the only but necessary simulation condition was to choose a different mobility parameter for the two ionic species, and the direction of the EZ shifts required a higher value for the cation mobility, μ_c > μ_a. Note that no device degradation effects were included in the model, meaning the experimentally observed current and associated light intensity decrease is intrinsic. The simulated current decay from the peak value is indeed substantial and on the order of 35%. This is a surprising result because a current decay in sandwich LECs for longer operation times so far has been mainly attributed to effects of—often unspecified—device degradation. The phenomenon seems not to be restricted to sandwich LECs, and similar current transients have been presented for planar LECs before.[6,17] Of course, this does not imply that no device degradation is occurring. For example, the experimental current in Figure 3.3b is continuously decreasing while the simulated current levels off after around 10 h of operation. As described above, we believe that after an experimental operation time of ≈25 h the EZ shift has ended, and we ascribe the further current and light intensity decrease to degradation.

Figure 3.4 shows the simulated device situation at different points of operation. The charge recombination profile (Figure 3.4a) is equivalent to the EZ and the current density is the area of the recombination profile, multiplied by the elementary charge q. For short operation times, the profile is narrow and situated close to the metal electrode. Over time, its width expands and shifts toward the ITO.
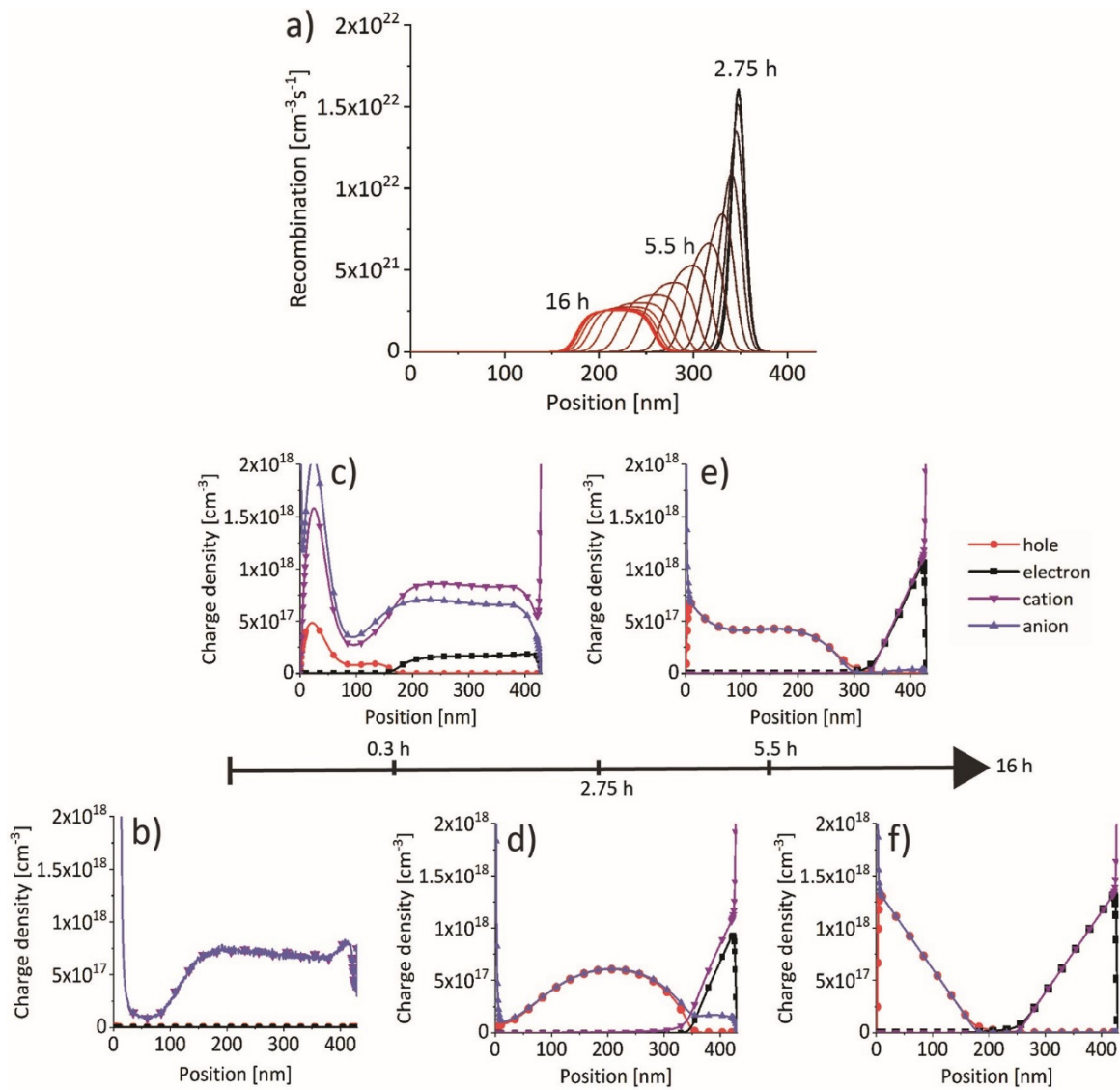
Figure 3.4. Simulation details for a 430 nm thick LEC. a) The charge recombination profile corresponds to the position of the EZ. b-f) Simulated charge distribution profiles for anions, cations, holes and electrons. For the simulation, $\mu_e = \mu_h$, equal injection barriers for electrons and holes, and $\mu_a = \mu_c/10$ was chosen. An equal mobility value for electrons and holes and a balanced injection results in a centred EZ at steady state f)—as observed experimentally—independent of the values for μ_a and μ_c.

The simulated charge distribution profiles are shown in Figure 3.4b-f. Figure 3.4b shows the experimental ToF-SIMS ion profile before operation, and very little electronic charge is present inside the device. Already after 0.3 h (Figure 3.4c), the EDLs at both electrodes are established and a small hole and electron current starts to develop. After 2.75 h (Figure 3.4d), the fast moving cations have completely displaced toward the metal electrode, while a fraction of the slow anions is still present in the bulk of the film. The charge recombination profile, which is proportional to the product of hole and electron density, is very narrow. This device situation corresponds to the

time where the capacitance is highest. For longer operation time (Figure 3.4e,f), the anions slowly drift toward the bottom electrode and the recombination zone gets wider. The recombination current peaks after an operation time of 5.5 h. The intrinsic thickness transient calculated from the simulated capacitance by the plate capacitor formula $C = \varepsilon_0 \varepsilon_r A/d$ correlates well with the recombination profile and the width defined by a certain electron and hole charge density, as explained in

Figure S3.9 (Supporting Information). The current peaks, however, when the area under the recombination profile curve is largest. The simulation confirms that the capacitance maximum must not coincide with the current maximum.

Details of the simulations and the parameter selection are described in the Supporting Information. In brief, the model solves the coupled continuity equations for the electronic and ionic charges and Poisson's equation as a function of time until steady state has been reached. For several time steps, the capacitance at 0 V is simulated by calculating the current response to a sinusoidal voltage. We summarize here the most important conclusions: i) The initial ion density profile has no fundamental influence on the simulation outcome. In the simulations presented in Figure 3.4 the initial ion distribution was chosen based on ToF-SIMS measurements. For a homogeneous initial ion distribution, the current dynamics is slower but the overall EZ shift direction is the same. Experimentally, this statement is confirmed from data shown in Figure S3.4 and Figure S3.10 (Supporting Information). ii) When $\mu_c > \mu_a$, the EZ shift direction is from the metal electrode toward ITO, for $\mu_a > \mu_c$ the shift direction is reversed. iii) For $\mu_c = \mu_a$ and our experimental initial ion profile the EZ shift occurs from the ITO toward the metal electrode. For $\mu_c = \mu_a$ and a constant ion profile, no EZ shift occurs. Statements (ii) and (iii) are valid for any value of μ_e and μ_h. iv) Imbalanced μ_e and μ_h or charge injection has an influence on the current level and the position of the EZ in steady state is off-centred, but the EZ shift direction is solely determined by μ_c and μ_a. More precise, our experimentally found centred EZ is the result of balanced charge mobility in combination with injection and, for example, an imbalance of μ_h and μ_e can be compensated by a reciprocal imbalance in charge injection. v) For a given average ion density, the steady state situation does not depend on the ion mobility values and the pristine ion profile.

Finally, we performed measurements and simulations for LECs with a 70 nm thick active layer thickness. Data in Figure 3.1d show that in such a case the emitted colour will always be yellow, independent of the EZ. Therefore, a shifting EZ does not result in a change of the emission colour.

Figure 3.5a,b shows the capacitance, current and light intensity trends for a constant +4 V driven LEC. Compared to the 430 nm thick device (Figure 3.3a), the capacitance in Figure 3.5a decreased at high frequencies because of a higher (geometrical) capacitance and an increase of the RC time constant. As observed for the 430 nm thick devices, the capacitance peaked before the current and levelled off for long operation times.
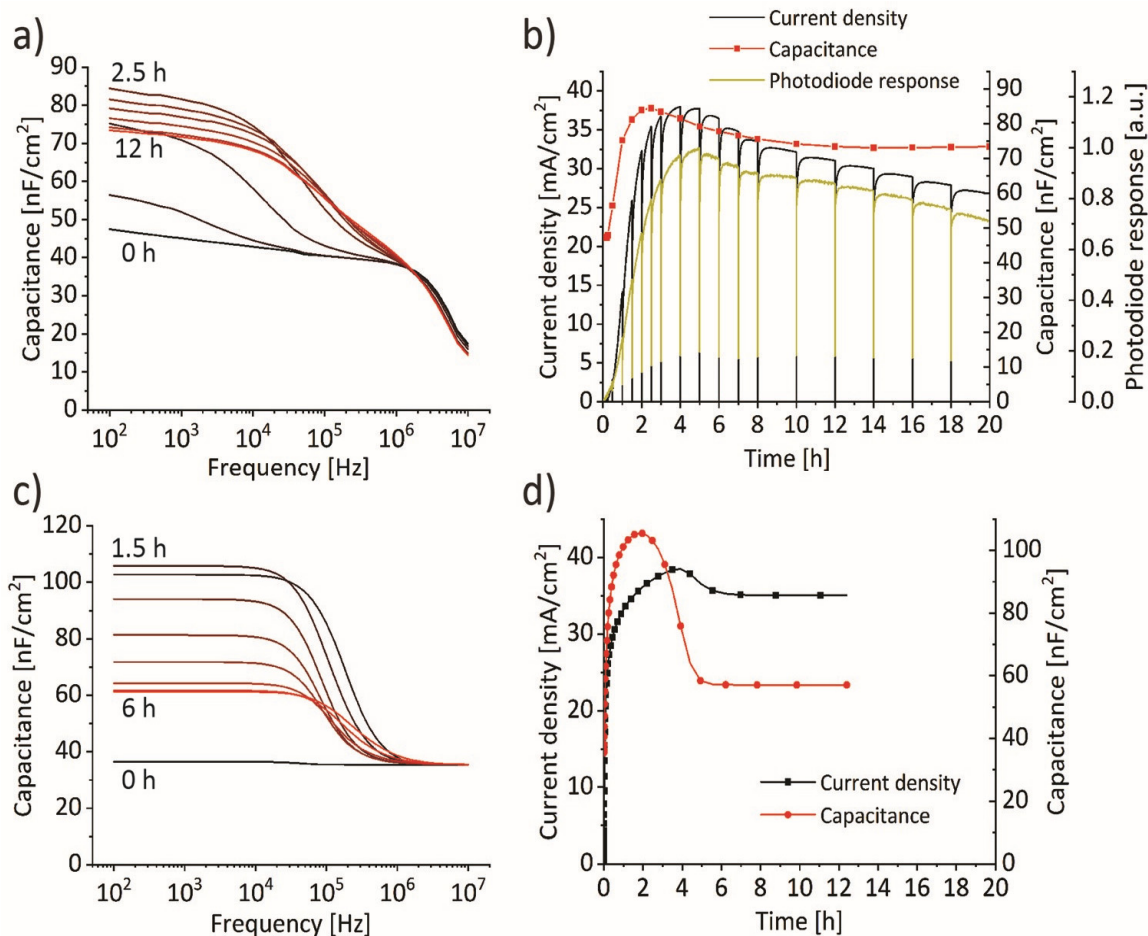
Figure 3.5. a) Capacitance versus frequency sweeps and b) transients for the capacitance at 10 Hz, and current and light intensity for a 70 nm thick LEC driven at a constant +4 V bias. Results from drift-diffusion simulations are shown in c) and d). For the simulation, $\mu_e = \mu_h$, equal injection barriers for electrons and holes, and $\mu_a = \mu_c/10$ was chosen, other parameters are compiled in Table S3.1 (Supporting Information).

These features were nicely reproduced by the simulation. In contrast to thick LECs, the light intensity maximum was now after the current peak.[44,49] We suggest this is a signature of the moving EZ that occurs also in thin-film devices. Figure 3.1e shows that for thicknesses below around 100 nm the luminance increases strongly when the EZ shifts from the metal electrode toward ITO. Therefore, for the thin device the maximum light intensity was measured after the current peak. Comparison between experiment and simulation suggests that also for thin-film LECs the measured current decrease before about 8 h ($\approx$10%) is intrinsic and only the succeeding decrease is due to device degradation.

Within the approximations of the model, we could thus demonstrate that a different mobility value for anions and cations is a sufficient requirement to explain the observed shift and widening of the EZ for our polymer LECs. However, simulations also showed that the transient and final EZ situation depends on the exact values chosen for the electronic mobilities and the charge injection. This means that a nonconstant mobility during operation can also result in a continuous

change of the EZ. Indeed, our assumption of constant μ_e and μ_h is in the general case not correct because mobilities may depend on the temperature, on the electric field as well as the doping level and thus possibly change continuously during operation.[36,50–53]

Time dependent EZ shifts in iTMC sandwich LECs were explained with imbalanced carrier injection and transport at early times that balanced during operation. Importantly, the EZ stabilized quickly while the current continuously increased for a much longer time.[29] This is different from our observations.

We also observed very similar luminance and voltage trends for LECs with an Al or Ag metal electrode over a measurement period of 16 h (Figure S3.15, Supporting Information). This finding points to different critical factors that determine the EZ dynamics in our LECs, because effects of injection barriers and imbalanced charge injection should become apparent during early operation times when the EDLs form and the doped regions start to grow. Furthermore, from simulation results (Figure S3.12 and Figure S3.14, Supporting Information), we find that while imbalanced electronic charge mobilities indeed result in an off-centred EZ, the influence on the calculated capacitance level is marginal.

For constant-current driven polymer LECs, Gao and coworkers reported that at elevated temperature, either due to internal or external heating, a p-n junction can relax into a p-i-n junction. A rapidly increasing voltage during operation indicated that the width of the resistive intrinsic zone increased, resulting in a strong increase of the luminance because in a wider intrinsic region less excitons are quenched by the nearby doped regions.[54–56]

In agreement with other reports,[57–59] we indeed also measured a considerable device temperature increase during operation (Figure S3.16, Supporting Information). However, we mention observations that indicate that in our case the temperature increase was probably not the reason for the observed widening of the EZ over time. The capacitance trends did not correlate with the heat generated from the electric power, which is the product of voltage and current. The capacitance peaked before the voltage minimum (Figure 3.2b), meaning that the intrinsic region width started to increase before the minimum of the generated heat was reached. Likewise, for constant-voltage operation (Figure 3.3b), the intrinsic region width continued to grow when the heat load decreased after the current peak. Furthermore, when applying a constant current, the capacitance decreases and thus the increase of the intrinsic region levelled off while the slope of the voltage drift was increasing; this is especially evident from Figure S3.6a (Supporting Information).

3.4   Conclusions

We used a combination of experiments and simulation to demonstrate that the observed EZ shift and the measured capacitance trend in polymer sandwich LECs is due to an imbalance between the cation and anion mobility. The experimental determination of the initial, inhomogeneous ion profile was an essential ingredient of this work. In most simulation studies reported so far, a homogeneous initial ion distribution and $\mu_c = \mu_a$ were chosen as modelling parameters. For these conditions, no simulated EZ shift occurs over time. Our findings indicate that for constant-voltage operation the current decay from the peak is intrinsic and not (exclusively) due to device degradation, which has implication for further studies. For example, a differentiation between an

intrinsic current decay and current decline due to device degradation can be made by operating a device twice, with a relaxation delay in between.

Our observations are not consistent with the hypothesis that the observed EZ shift over many hours is due to continuously changing electronic charge mobilities and injection barriers. However, we do not claim generality of our findings and other materials systems might behave differently. For example, iTMC LECs present a case where the large cation is essentially immobile.[15,40,60] This has the consequence that the EDL formation at the cathode is slow and imbalanced charge injection can potentially prevail very long.

For lighting applications, a fast turn-on and stable light source is desired. Experimentally, this can be achieved when $\mu_c = \mu_a$, since an imbalance in the ion mobility values is the main cause for a shifting EZ and thus changing luminance with time. Furthermore, the EZ should be positioned in a region with high light outcoupling efficiency. The EZ position can be tuned by adjusting the electronic mobility values or the charge injection ratio, respectively—the ionic mobility values have no influence on the EZ position in steady state.

3.5   Experimental Section

Dried (24 h, 0.1 mbar, 40 °C) SY (Merck) and dried (24 h, 0.1 mbar, 160 °C) $Li^+CF_3SO_3^-$ (Sigma-Aldrich) together with dried (24 h, 0.1 mbar, room temperature) TMPE (Sigma-Aldrich, average M_n 450) were separately dissolved in anhydrous tetrahydrofuran (THF, Sigma Aldrich). The concentrations for salt and TMPE were 10 mg mL^{-1}, SY is described below. Precursor solutions were stirred for 7 h at 60 °C inside a glove box (H_2O < 1 ppm, O_2 < 20 ppm). The precursor solutions were mixed in mass ratios of 1:0.1:0.03 (SY:TMPE:$Li^+CF_3SO_3^-$) and were then stirred for at least 17 h at 60 °C. Before spin coating, solutions were let to cool down for 20 min. The spin coating recipes for the film thicknesses 70, 110, 160, 240, 300, 320, and 430 nm were [(5, 2000), (6.5, 2000), (8, 2000), (10, 2000), (12, 2000), (10, 1000), (12, 1000)], in [(mg SY mL^{-1} THF, rpm)], the acceleration (in rpm s^{-1}) was equal to the speed in all cases, and the runtime was 60 s in all cases. Nonfiltered solutions were used for film coating. Layer thicknesses were measured with an Ambios XP1 profilometer. The indicated film thicknesses above 70-430 nm are average values from several measurements, but it was noted that for thicker films (above ≈200 nm) the thickness was not always constant over the sample film and thickness variations of around ±10% were found when measuring at different positions. Aluminium or silver top electrodes (70 nm) were thermally evaporated through a shadow mask defining eight cells with an active area of 3.1 or 7.1 mm^2 per substrate.

For luminance measurements, devices were placed in an airtight holder and were measured under nitrogen atmosphere outside the glove box at room temperature using a factory calibrated Konica Minolta LS-110 luminance meter with a close-up lens 110. The reflection of the top cover glass of the holder was not considered. The refractive indices for the intrinsic SY layer were taken from ref. [61] and were confirmed by simulation of experimental transmission spectra, measured with a Varian Cary 50 UV−vis spectrometer.[44] The photoluminescence spectrum was measured by fluorescence spectroscopy (Horiba Jobin Yvon Fluorolog).

The angular dependent EL measurement was performed with a prototype of the Phelos measurement system (Fluxim AG, Switzerland). Optical and electrical simulations were performed

with Setfos 5.0 (Fluxim AG, Switzerland). Simulation procedures and parameters are described in the Supporting Information. Impedance measurements at 0 V with an alternating 70 mV signal to determine the capacitance transients were performed on the Paios measurement system (Fluxim AG, Switzerland), as well as the corresponding current and light intensity transients. The light intensity was measured with a photodiode as photovoltage. The relation between the measured photovoltage and the corresponding radiance/ luminance is explained in the Supporting Information.

ToF-SIMS measurements were performed on a ToF-SIMS.5 instrument from IONTOF, Germany, operated in the spectral mode using a 25 keV Bi_3^+ primary ion beam with an ion current of 0.7 pA. For the ToF-SIMS measurements, LECs were operated in-situ and cooled down to liquid nitrogen temperature after a defined time in order to conduct dual beam depth profiling. For depth profiling, a 1 keV Cs^+ sputter beam with a current of 70 nA was used. The raster area of the sputter beam was 500 μm × 500 μm, and the mass-spectrometry was performed on an area of 100 μm × 100 μm in the centre of the sputter crater. During ToF-SIMS dual beam depth profiling a low-energy electron flood gun was used for charge compensation. The ToF-SIMS method was established in ref. [48].

References

[1]   *Iontronics, Ionic Carriers in Organic Electronic Materials and Devices* (Eds: J. Leger, M. Berggren, S. Carter), CRC Press, Boca Raton, FL **2011**.

[2]   E. W. H. Jager, O. Inganäs, I. Lundström, *Science* **2000**, *288*, 2335.

[3]   J. Rivnay, S. Inal, A. Salleo, R. M. Owens, M. Berggren, G. G. Malliaras, *Nat. Rev. Mater.* **2018**, *3*, 17086.

[4]   Q. Pei, G. Yu, C. Zhang, Y. Yang, A. J. Heeger, *Science* **1995**, *269*, 1086.

[5]   S. Tang, L. Edman, *Top. Curr. Chem.* **2016**, *374*, 40.

[6]   S. van Reenen, P. Matyba, A. Dzwilewski, R. A. J. Janssen, L. Edman, M. Kemerink, *J. Am. Chem. Soc.* **2010**, *132*, 13776.

[7]   R. D. Costa, E. Ortí, H. J. Bolink, F. Monti, G. Accorsi, N. Armaroli, *Angew. Chem., Int. Ed.* **2012**, *51*, 8178.

[8]   S. B. Meier, D. Tordera, A. Pertegás, C. Roldán-Carmona, E. Ortí, H. J. Bolink, *Mater. Today* **2014**, *17*, 217.

[9]   E. Fresta, R. D. Costa, *J. Mater. Chem. C* **2017**, *5*, 5643.

[10]   J. Gao, *ChemPlusChem* **2017**, *82*, 1.

[11]   S. Jenatsch, L. Wang, M. Bulloni, A. C. Véron, B. Ruhstaller, S. Altazin, F. Nüesch, R. Hany, *ACS Appl. Mater. Interfaces* **2016**, *8*, 6554.

[12] A. Pertegás, D. Tordera, J. J. Serrano-Pérez, E. Ortí, H. J. Bolink, *J. Am. Chem. Soc.* **2013**, *135*, 18008.

[13] S. Jenatsch, L. Wang, N. Leclaire, E. Hack, R. Steim, S. B. Anantharaman, J. Heier, B. Ruhstaller, L. Penninck, F. Nüesch, R. Hany, *Org. Electron.* **2017**, *48*, 77.

[14] S. van Reenen, T. Akatsuka, D. Tordera, M. Kemerink, H. J. Bolink, *J. Am. Chem. Soc.* **2013**, *135*, 886.

[15] S. B. Meier, S. van Reenen, B. Lefevre, D. Hartmann, H. J. Bolink, A. Winnacker, W. Sarfert, M. Kemerink, *Adv. Funct. Mater.* **2013**, *23*, 3531.

[16] J.-H. Shin, N. D. Robinson, S. Xiao, L. Edman, *Adv. Funct. Mater.* **2007**, *17*, 1807.

[17] S. van Reenen, P. Matyba, A. Dzwilewski, R. A. J. Janssen, L. Edman, M. Kemerink, *Adv. Funct. Mater.* **2011**, *21*, 1795.

[18] Y. Hu, J. Gao, *J. Am. Chem. Soc.* **2011**, *133*, 2227.

[19] F. AlTal, J. Gao, *Phys. Status Solidi RRL* **2015**, *9*, 77.

[20] P. Matyba, K. Maturova, M. Kemerink, N. D. Robinson, L. Edman, *Nat. Mater.* **2009**, *8*, 672.

[21] Y. Hu, J. Gao, *Appl. Phys. Lett.* **2006**, *89*, 253514.

[22] J. Fang, P. Matyba, N. D. Robinson, L. Edman, *J. Am. Chem. Soc.* **2008**, *130*, 4562.

[23] N. D. Robinson, J. Fang, P. Matyba, L. Edman, *Phys. Rev. B* **2008**, *78*, 245202.

[24] D. Hohertz, J. Gao, *Adv. Mater.* **2008**, *20*, 3298.

[25] Q. Pei, Y. Yang, G. Yu, C. Zhang, A. J. Heeger, *J. Am. Chem. Soc.* **1996**, *118*, 3922.

[26] T. Wågberg, P. R. Hania, N. D. Robinson, J.-H. Shin, P. Matyba, L. Edman, *Adv. Mater.* **2008**, *20*, 1744

[27] H.-C. Su, *ChemPlusChem* **2018**, *83*, 197.

[28] R. Sun, C.-T. Liao, H.-C. Su, *Org. Electron.* **2014**, *15*, 2885.

[29] T.-W. Wang, H.-C. Su, *Org. Electron.* **2013**, *14*, 2269.

[30] Y.-P. Jhang, H.-F. Chen, H.-B. Wu, Y.-S. Yeh, H.-C. Su, K.-T. Wong, *Org. Electron.* **2013**, *14*, 2424.

[31] S. Jenatsch, M. Regnat, R. Hany, M. Diethelm, F. Nüesch, B. Ruhstaller, *ACS Photonics* **2018**, *5*, 1591.

[32] E. M. Lindh, P. Lundberg, T. Lanz, J. Mindemark, L. Edman, *Sci. Rep.* **2018**, *8*, 6970.

[33] E. M. Lindh, P. Lundberg, T. Lanz, L. Edman, *Sci. Rep.* **2019**, *9*, 10433.

[34] A. Munar, A. Sandström, S. Tang, L. Edman, *Adv. Funct. Mater.* **2012**, *22*, 1511.

[35] Y. A. Davis, P. P. Crooker, N. M. Haegel, Y. Yoshioka, J. D. MacKenzie, *Appl. Phys. Lett.* **2011**, *99*, 233306.

[36] S. van Reenen, R. A. J. Janssen, M. Kemerink, *Adv. Funct. Mater.* **2012**, *22*, 4547.

[37] H. Campbell, D. L. Smith, C. J. Neef, J. P. Ferraris, *Appl. Phys. Lett.* **1998**, *72*, 2565.

[38] Devižis, S. Jenatsch, M. Diethelm, V. Gulbinas, F. Nüesch, R. Hany, *ACS Photonics* **2018**, *5*, 3124.

[39] S. B. Meier, D. Hartmann, A. Winnacker, W. Sarfert, *J. Appl. Phys.* **2014**, *116*, 104504.

[40] L. D. Bastatas, M. D. Moore, J. D. Slinker, *ChemPlusChem* **2018**, *83*, 266.

[41] Y. Yang, Q. Pei, *Appl. Phys. Lett.* **1996**, *68*, 2708.

[42] J. A. Manzanares, H. Reiss, A. J. Heeger, *J. Phys. Chem. B* **1998**, *102*, 4327.

[43] S. Tang, L. Edman, *J. Phys. Chem. Lett.* **2010**, *1*, 2727.

[44]   M. Diethelm, Q. Grossmann, A. Schiller, E. Knapp, S. Jenatsch, M. Kawecki, F. Nüesch, R. Hany, *Adv. Opt. Mater.* **2019**, *7*, 1801278.

[45]   H. Becker, S. E. Burns, R. H. Friend, *Phys. Rev. B* **1997**, *56*, 1893.

[46]   R. H. Friend, R. W. Gymer, A. B. Holmes, J. H. Burroughes, R. N. Marks, C. Taliani, D. D. C. Bradley, D. A. Dos Santos, J. L. Brédas, M. Löglund, W. R. Salaneck, *Nature* **1999**, *397*, 121.

[47]   S. Höfle, T. Lutz, A. Egel, F. Nickel, S. W. Kettlitz, G. Gomard, U. Lemmer, A. Colsmann, *ACS Photonics* **2014**, *1*, 968.

[48]   M. Kawecki, R. Hany, M. Diethelm, S. Jenatsch, Q. Grossmann, L. Bernard, H. J. Hug, *ACS Appl. Mater. Interfaces* **2018**, *10*, 39100.

[49]   K. Strassel, S. P. Ramanandan, S. Abdolhosseinzadeh, M. Diethelm, F. Nüesch, R. Hany, *ACS Appl. Mater. Interfaces* **2019**, *11*, 23428.

[50]   V. I. Arkhipov, E. V. Emelianova, P. Heremans, H. Bässler, *Phys. Rev. B* **2005**, *72*, 235202.

[51]   Y. Murat, G. Wantz, S. Fasquel, J.-Y. Laurent, T. Maindron, L. Hirsch, *Proc. SPIE* **2016**, *9941*, 994129.

[52]   S. R. Tseng, Y. S. Chen, H. F. Meng, H. C. Lai, C. H. Yeh, S. F. Horng, H. H. Liao, C. S. Hsu, *Synth. Met.* **2009**, *159*, 137.

[53]   S. van Reenen, R. A. J. Janssen, M. Kemerink, *Org. Electron.* **2011**, *12*, 1746.

[54]   Y. Zhang, Y. Hu, J. Gao, *Appl. Phys. Lett.* **2006**, *88*, 163507.

[55]   Y. Zhang, J. Gao, *J. Appl. Phys.* **2006**, *100*, 084501.

[56]   S. Hu, J. Gao, *Adv. Mater. Technol.* **2018**, *3*, 1800229.

[57]   L. Edman, M. Pauchard, B. Liu, G. Bazan, D. Moses, A. J. Heeger, *Appl. Phys. Lett.* **2003**, *82*, 3961.

[58]   L. Edman, *Electrochim. Acta* **2005**, *50*, 3878.

[59]   G. Yu, Y. Cao, M. Andersson, J. Gao, A. J. Heeger, *Adv. Mater.* **1998**, *10*, 385.

[60]   J. Mindemark, L. Edman, *J. Mater. Chem. C* **2016**, *4*, 420.

[61]   T. Lanz, E. M. Lindh, L. Edman, *J. Mater. Chem. C* **2017**, *5*, 4706.

Supporting Information
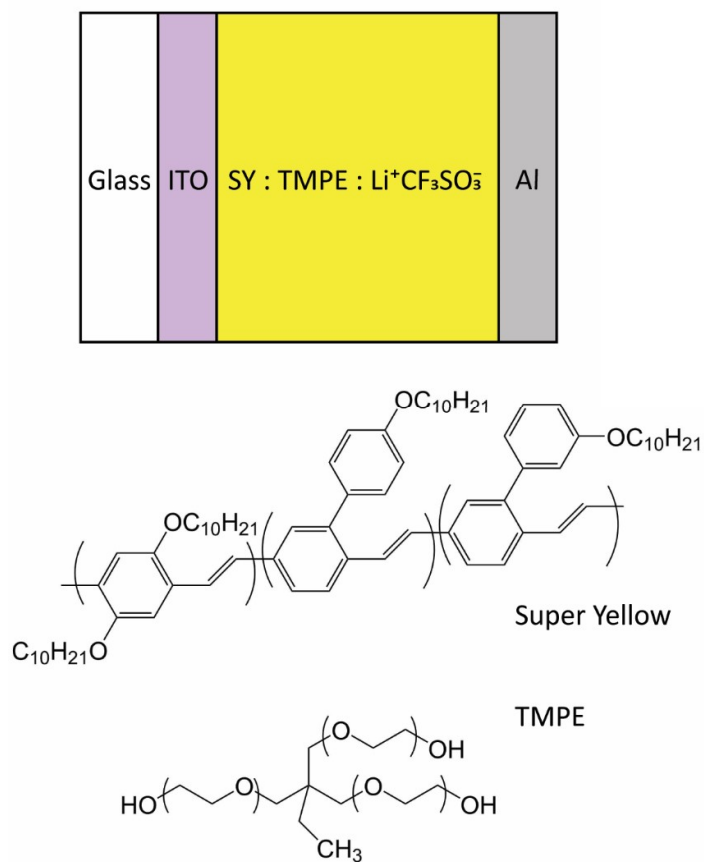
Figure S3.1. Device architecture and chemical structures of SY and TMPE. The thickness of ITO was (132 ± 2 nm), the active layer thickness was varied between 70 nm and 430 nm, and the Al electrode had a thickness of 70 nm.
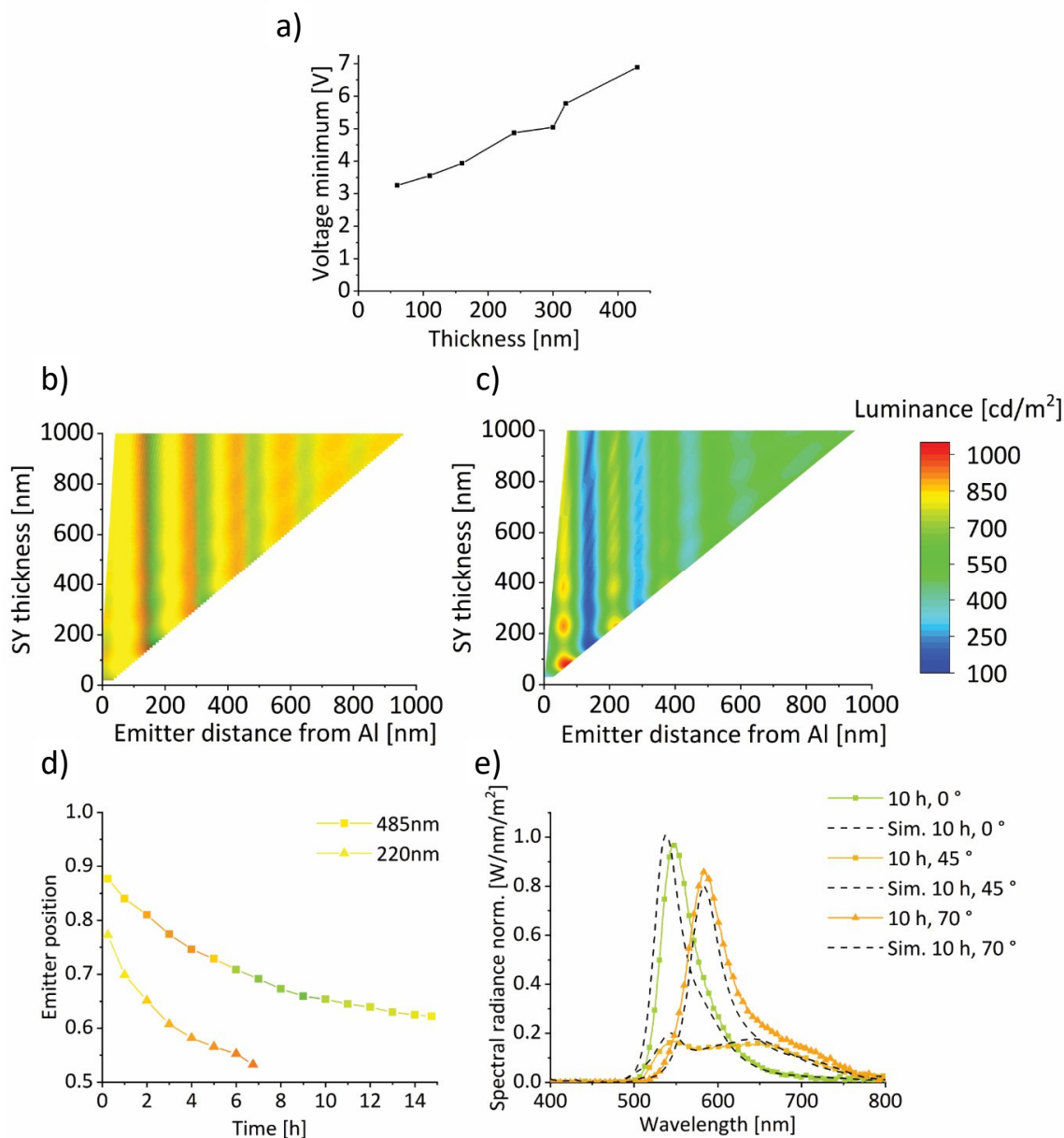
Figure S3.2. a) Voltage minima during 7.7 mA cm^{-2} constant-current biasing for devices with different active layer thicknesses. A linear voltage minimum trend with increasing active layer thickness is in accordance with literature.[S1]

When the perceived colour in b) and luminance in c) from a 0° observer angle are plotted as distance from the metal electrode, the patterns get independent of the thickness. This means that only the distance from the emitter position to the metal electrode is relevant, showing the effect of back coupling of the emitted electromagnetic field to the emitter itself. If a typical interference effect at the interfaces glass substrate/ITO, ITO/SY or SY/metal electrode would be the reason for the observed pattern, the effect would also depend on the SY active layer thickness.

The fitted emitter positions with time from angular emission measurements are displayed in d) for a nominal 430 nm and 240 nm thick device. The fitting errors were global minima, confirmed by starting the fitting procedure at several starting positions across the device. The active layer

thickness was a fitting parameter and the best fit was obtained for thicknesses of (485 ± 6) nm and (220 ± 3) nm, respectively. These values are within the deviations of the measured average film thicknesses. Point colours were computed from the measured spectra at 0°. We fitted the different points in time individually, so the resulting, mostly smooth curves give trust into the fit. A good fit after 10 h of biasing for three different angles is shown in e). The Gaussian width for the 430 nm thick device was (15 ± 7) nm, for the 240 nm device (1.9 ± 2.7) nm.

Note that the fit is not very sensitive to the specific Gaussian width in this thickness range.[S1]

The optical model includes the different layers of the device, where the n- and k-values of the 135 nm thick ITO were measured by spectroscopic ellipsometry, the SY data were taken from literature[S2] and the data for the 70 nm thick aluminium layer were taken from the Setfos software database, originally from J.A. Woollam. Exciton/polaron and electrode quenching, doping effects on refractive indices and losses through wave-guiding were not considered. The transmittance measurement of a 70 nm thick active layer was simulated to verify the refractive indices used in our previous work.[S3] The photoluminescence spectrum was measured on a Horiba Jobin Yvon Fluorolog spectrometer.
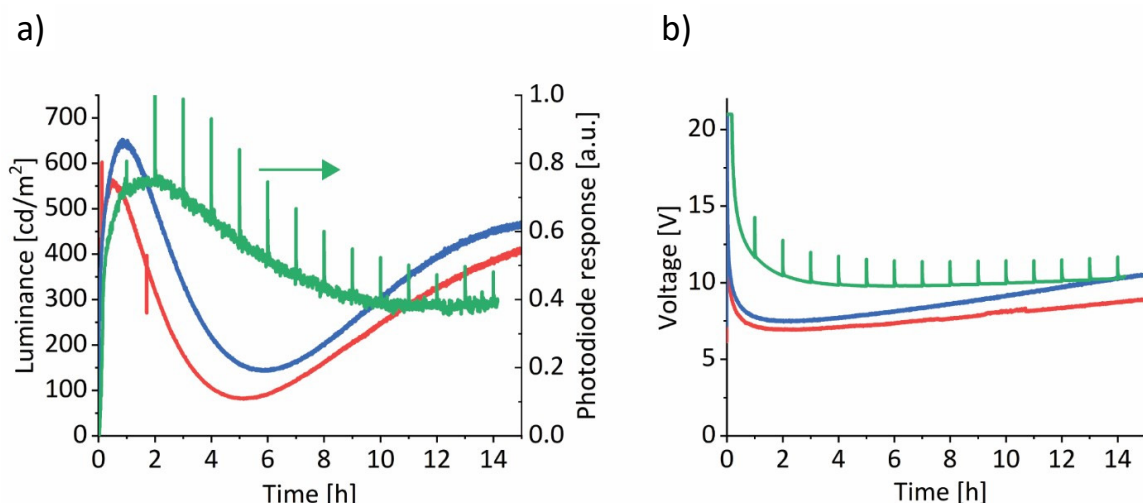
Figure S3.3. Variation of a) luminance and b) voltage transients for 430 nm thick LECs.
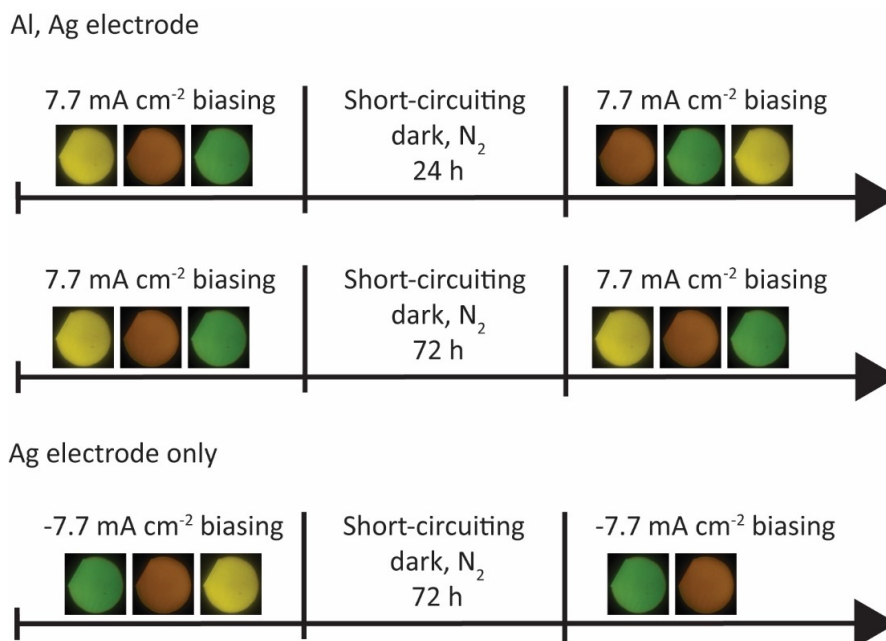
Figure S3.4. Investigation of change in colour on 430 nm thick devices. For forward biasing, identical results were observed for an Al or Ag top electrode. When the device was operated for the first time, the initial ion distribution changed and a change in colour occurred. During the idle time ions redistribute but certainly not back to the original, inhomogeneous distribution with a peak at the bottom ITO electrode. During the second operation, again a change in colour occurred. This confirms experimentally the simulation result that the initial ion distribution has no fundamental influence on the EZ shift.

Possible origin of the spikes in the voltage and photodiode response measurements of Figure 3.2b. It can be expected that during the 40 s break of the IS measurement a slight relaxation of the EDLs is taking place. This results in a worsened electronic charge injection and a higher voltage is required after the turn-on instant for a short time to establish the original situation. Due to the higher mobility of the cations, it is further reasonable to assume that the relaxation at the cathode is faster than at the anode. This results in an asymmetric charge injection barrier and after turn-on, hole injection will be favoured over electron injection. Simulation shows that asymmetric charge injection results in an EZ shift, for this situation it is towards the metal electrode. Therefore, the light intensity changes because of the EZ shift during the time of the voltage spike relaxation. Figure 3.1e shows that even a slight shift of the EZ can increase the luminance by ~25%.
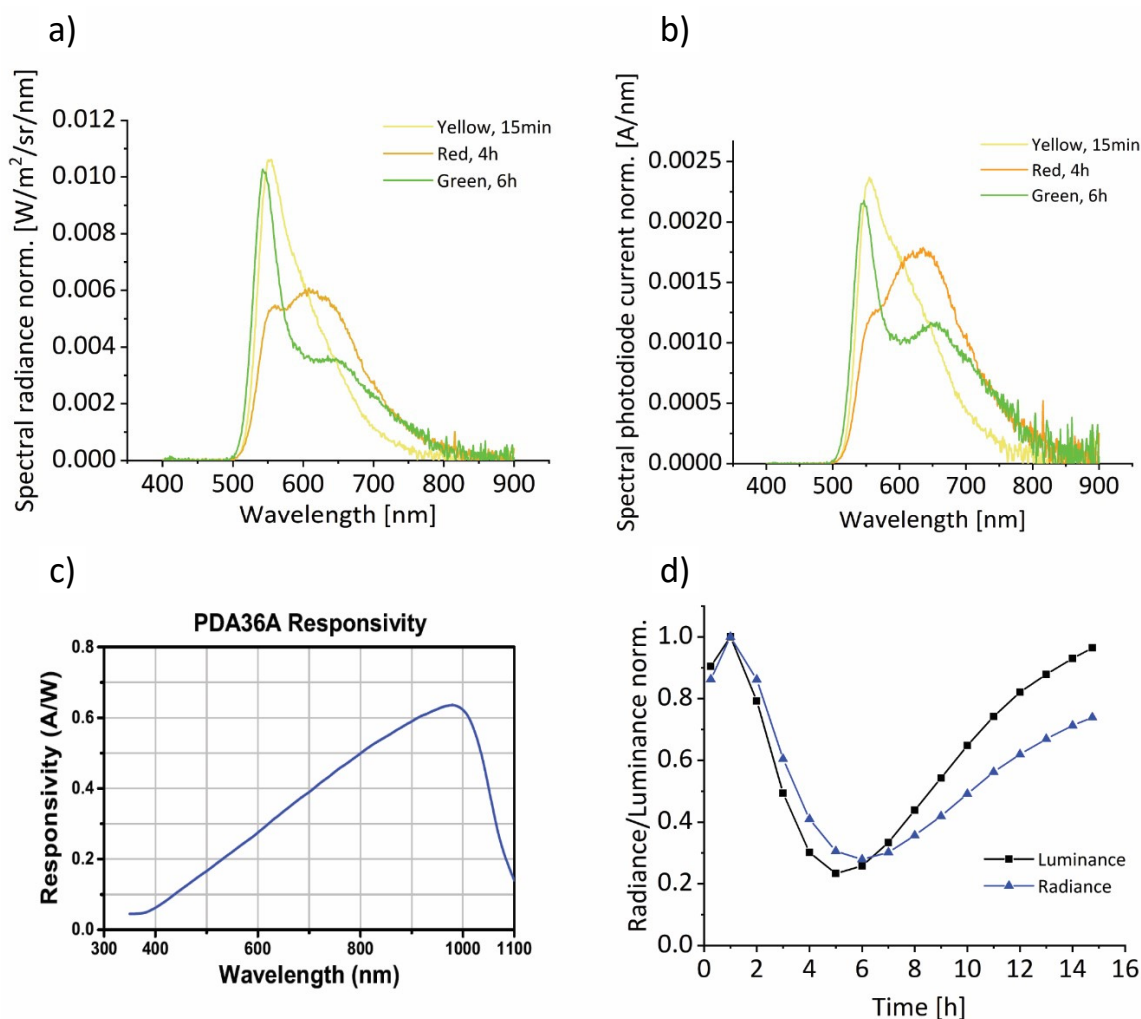
Figure S3.5. The light intensity transients in Figure 3.2b, Figure 3.3b and Figure 3.5b were measured with a photodiode as photovoltage. Because the temporal emission spectra are not precisely known, the exact conversion into a radiance/luminance transient is not possible. In a), a yellow (after 15 min), a red (after 4 h) and a green spectrum (after 6 h) from an observed 0° angle was chosen to represent the biggest discrepancy in spectral shape during the colour shift. The spectra were normalized in a) to have an integrated area of 1, which means the radiance is the same. Due to the photodiode responsivity c), the photocurrent spectra b) differ because higher wavelengths in radiance lead to higher currents (more photons for the same energy). Therefore, the integrated response is not the same anymore, which means that the photocurrent response is not directly proportional to the radiance of the different colours. In fact, the areas of the spectra change to yellow : green : red = 1 : 1.07 : 1.14. This means the photovoltage measurement (photovoltage to photocurrent conversion of the photodiode was 750 V/A) is over-estimating the radiance for red or green colour, such that the radiance valley after 12 h would in reality be lower compared to the peak at 2 h, but only by 15% at most. There is a further difference when comparing radiance to luminance data because of the photopic luminosity function. In d) the radiance and luminance is calculated from the spectral data of the EZ fit measurement in Figure 3.1, showing that the relevant trend is the same and is comparable.
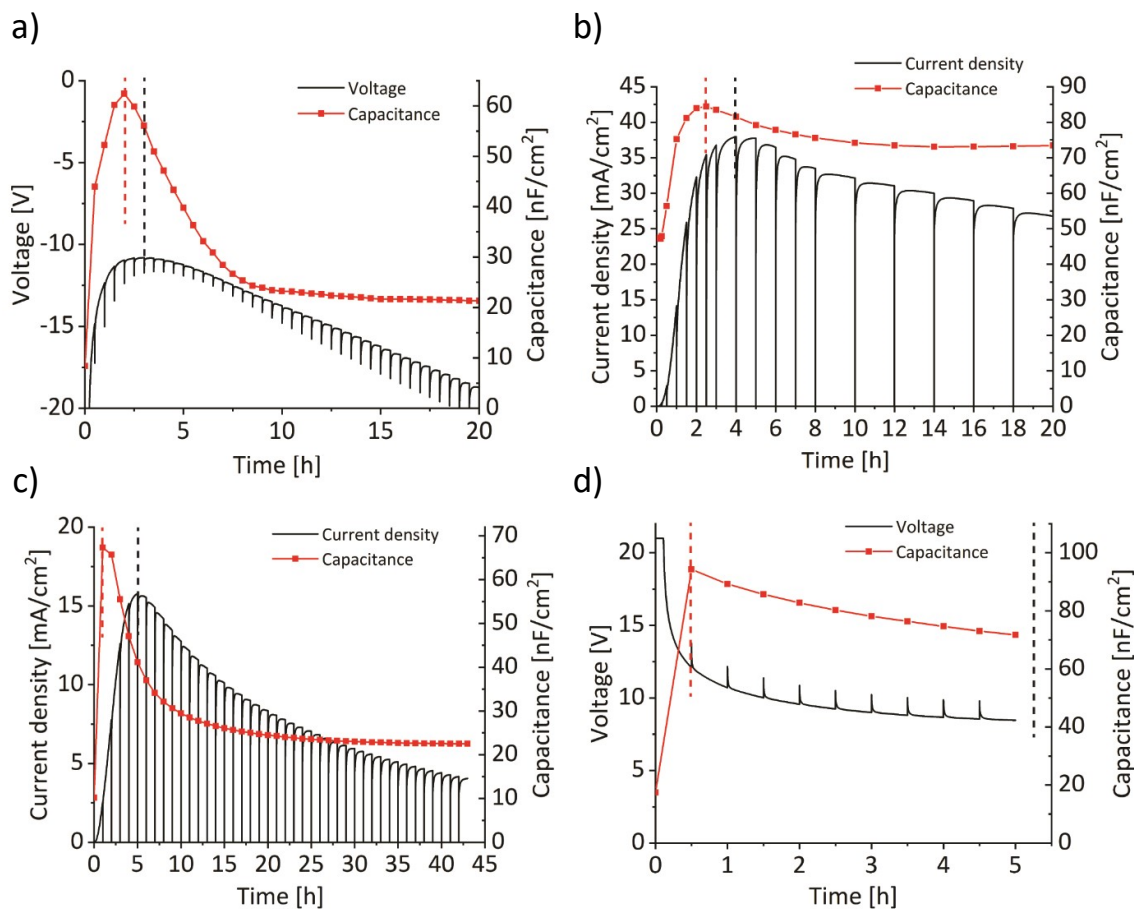
Figure S3.6. The capacitance peaks before the electrical device optimum (voltage minimum/current maximum) as shown for a device with a) a 430 nm thick active layer with a Ag electrode when biased in reverse, b) a 70 nm thick active layer with Al, c) a 430 nm thick active layer with Al and d) an operated device with a 430 nm thick active layer and an Al electrode after short-circuiting for six days.
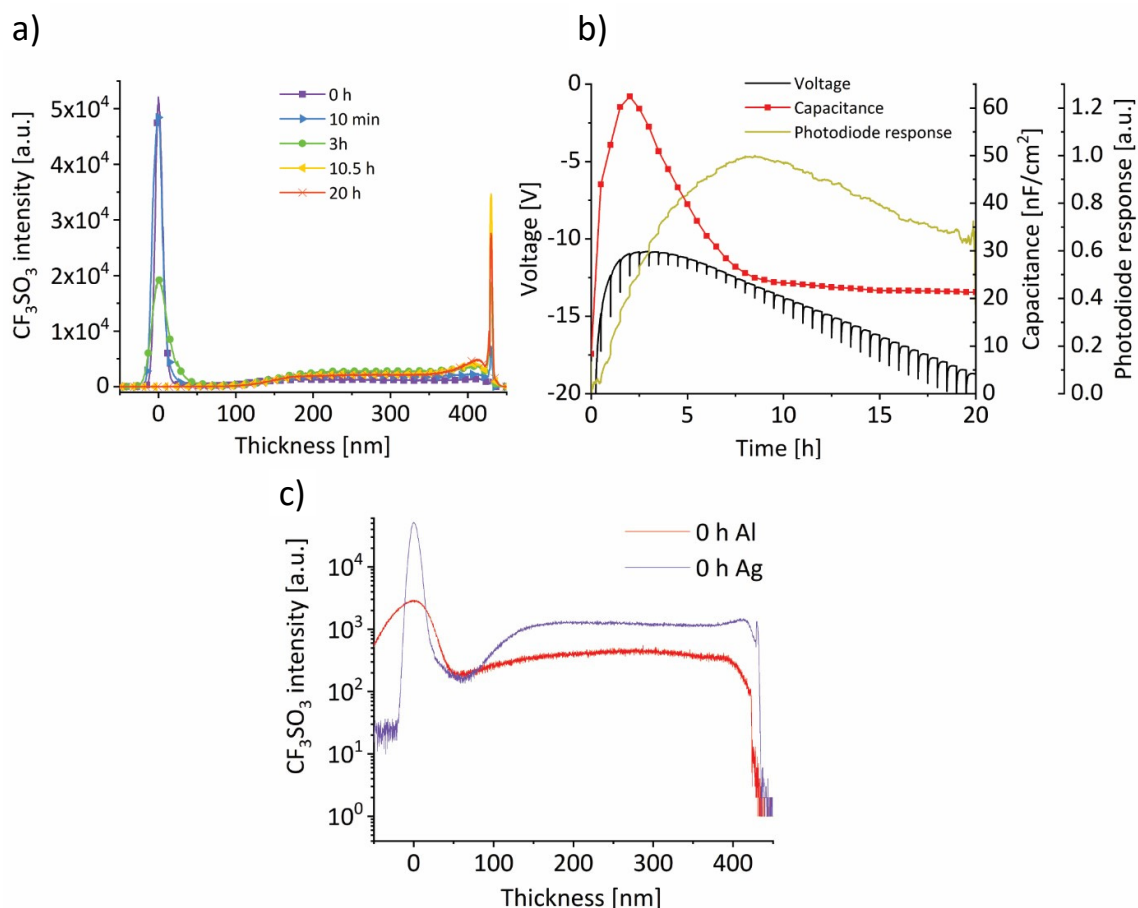
Figure S3.7. a) ToF-SIMS anion profiles as shown in Figure 3.2c, main text, with a linear yscale. b) Voltage, capacitance and light intensity transients for an ITO/SY(430 nm)/Ag device during operation at a reverse bias of 7.7 mA cm^{-2} applied at ITO. In contrast to the data shown in Figure 3.2b of the main text, the light intensity still increased after the minimum of the voltage was reached. This is because during reverse biasing, the emitted colour starts at green and the EZ moves away from the region where parts of the spectrum are suppressed due to interference (see Figure 3.1, main text). After an operation of ~10 h, the continuing voltage increase is a strong indication for device degradation. Therefore, we believe the light intensity decrease after 10 h must not necessarily come from an ongoing EZ shift, but is the result of a light intensity drop due to degradation. c) Comparison of pristine ToF-SIMS profiles for devices with an Al or an Ag top electrode.
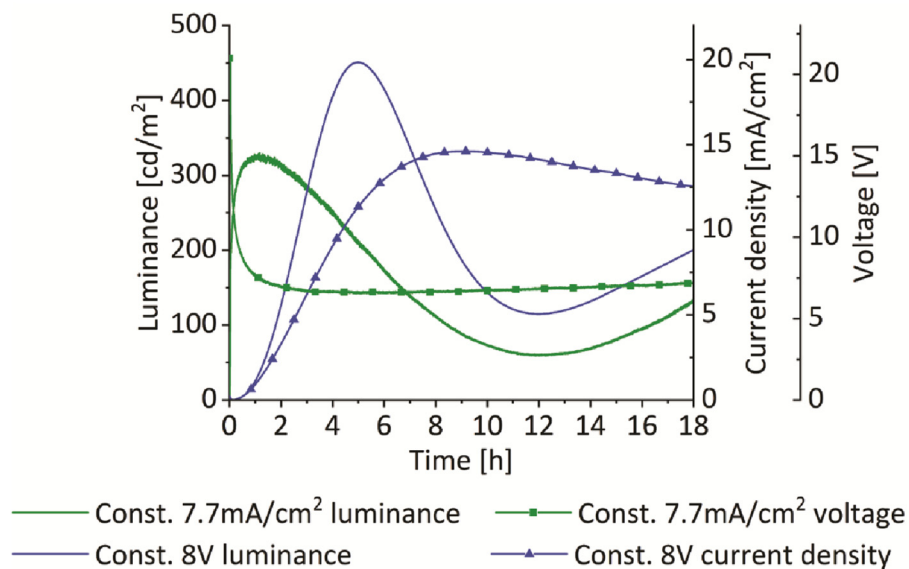
Figure S3.8. Luminance and voltage /current trends for 430 nm thick ITO/SY/Al LECs driven at a constant voltage or constant current. When applying a constant current the initial voltage is high, which results in a faster overall dynamics, a valley for the luminance appeared for both modes of operation.

Numerical electrical simulation

We simulated the device in constant-voltage mode, which is compatible with the Dirichlet potential boundary condition usually applied to drift-diffusion models.[S4,S5] Applying a constant-current boundary condition is in general possible. However, for transient simulations this requires very small time steps, since the equation is mathematically stiff.[S6] For devices with a large mobility difference between the charge carriers, e.g. mixed electronic/ionic devices as LECs, the number of time steps required leads to exceedingly long simulation runtimes. Constant-current simulations were thus omitted for this publication.

The five main conclusions (i-v) described in the main text were derived from the following simulations. For a simulation with the same parameters (Table S3.1) as used for Figure 3.3 but with a constant ion density profile at the beginning, the resulting current transient is slower as shown in Figure S3.10 but the overall EZ shift trend is the same. For early operation times the charge distributions strongly depend on the initial ion profile, but at the moments 2.75 h (Figure 3.4) and 7 h (Figure S3.11) the distributions almost match and the subsequent EZ shifts are similar. Data in Figure S3.4 confirm experimentally the simulation result that the initial inhomogeneous ion profile in our case is not the fundamental reason for the EZ shift. As a further confirmation, we measured luminance vs time trends for constant current and constant-voltage driven devices for more than 15 h, followed by a relaxation time and a second operation (Figure S3.10b). It can be expected that the ion distribution for a fully relaxed device is close to a homogeneous profile, and the second luminance trends indeed indicate that the EZ is again moving, but with different dynamics.

For a simulation with the experimental ion profile and $\mu_a = \mu_c$, the EZ shifts from the ITO to the metal electrode side. This is because in this case the anions are already close to the ITO and the EDL formation at the anode is fast, whereas the cations have to migrate through the active layer first. The only way, from a modelling perspective, to induce an EZ shift from the metal electrode towards the ITO is by setting $\mu_c \gg \mu_a$, thereby countering the effect of the inhomogeneous ion distribution. For the situation $\mu_c = 2 \times \mu_a$, no EZ shift takes place. Also no EZ shift occurs for a constant initial ion distribution and $\mu_c = \mu_a$: these are the modelling parameters chosen so far in literature.

The steady state solution of the drift-diffusion simulation does not depend on the cation and anion mobility due to the applied model. We calculate the diffusion constant by the Einstein relation ($D = \mu \frac{kT}{q}$). The continuity equation for the anions in steady state (no transient term, no generation/recombination) thus reads $\frac{\partial}{\partial x}\left(D_a \frac{\partial a}{\partial x} - \mu_a a \frac{\partial \psi}{\partial x}\right) = \frac{\partial}{\partial x}\left(\mu_a \frac{kT}{q}\frac{\partial a}{\partial x} - \mu_a a \frac{\partial \psi}{\partial x}\right) = 0$. We assume μ_a is constant over x. Thus it can be cancelled from the equation. The same is true for the continuity equation for cations. From a physical viewpoint, the equilibrium between drift and diffusion is established in steady state. Since both drift and diffusion depend on the mobility in the same way, changing the mobility does not affect the ion density distribution in steady state.

Further relevant parameters to discuss are $\mu_{e,h}$, the injection barriers and the ion density. Changing these parameters, but keeping μ_e/μ_h and μ_a/μ_c constant, does not change the transient behaviour qualitatively, the effects are a change in the current level and the width of the intrinsic zone, thus the capacitance level (Table S3.2). If only μ_e or the electron injection is increased, the transient behaviour remains but the EZ in steady state is shifted towards the hole injection side (Figure S3.12a). Accordingly, a higher μ_h or hole injection results in an off-centred EZ closer to the cathode (Figure S3.12b). Note that the timeline is the same for the simulations shown in Figure S3.4 and Figure S3.12; this is because μ_a, μ_c and the starting ion profile are the same. These findings suggest that the experimentally found centred EZ is the result of balanced charge mobility in combination with injection and, for example, an imbalance of μ_h and μ_e[S7,S8] can be compensated by a reciprocal imbalance in charge injection. Our intention was to reproduce the fundamental experimental features with the simplest model possible. Contrary to simulations of reference [S9], the injection barrier in our case is not dependent on the EDL voltage drop.

Figure **S3.13** shows the simulation extracted from Figure 3.5b in reference [S9] (blue colour) and our reproduction using the same parameters, without an EDL dependent injection but a constant injection barrier of 0.1 eV for electrons and holes (black colour). The good agreement indicates that the chosen injection model is probably not relevant for the time period after EDL formation, which is in our experiments on the order of a few minutes (Figure 3.2c and Figure 3.2d). The small mismatch in steady state current between the two simulations is probably due to a different recombination efficiency, since here Langevin recombination (direct electron-hole recombination) is used, while the reference uses an exciton model.

Furthermore, a binding energy between cations and anions was not included in the model as done in reference [S9] and [S12].

Figure **S3.13** shows the current transient reference [S9] with a binding energy between cations and anions (green colour). If our initial ToF-SIMS ion profile is used (without a binding energy), the

resulting transient has a similar appearance (red colour). This suggests that the binding energy has certainly an influence on the dynamics, but is not necessary to explain the fundamental trends we wanted to unravel in this work. Finally, we do not think that in our case the observed EZ shift is due to a continuous change of the electronic charge mobilities. Figure S3.14 shows steady-state simulations for different values of μ_e. The change in capacitance level simulated at 10 Hz is marginal – in contrast to the experimental capacitance trends - while the EZ peak shifted from 410 nm (EZ position 0.95) for μ_e = 1 x 10^{-6} cm^2/Vs to 125 nm (EZ position 0.29) for μ_e = 10 x 10^{-6} cm^2/Vs. Furthermore, with increasing temperature or increasing doping density, the charge mobility tends to increase.[S10,S11] The simulation in Figure S3.14b shows that an increase in mobility leads to an increase in current density, which does not agree with the experimentally observed decrease of the current.

Table S3.1. Input parameters for the simulations shown in Figure 3.3, Figure 3.4 and Figure 3.5, main text.

Parameter	430 nm device	70 nm device	Source
Thickness SY	430 nm	70 nm	Profilometry measurement
Electron mobility	5x10^{-6} cm^2/Vs	2.5x10^{-6} cm^2/Vs	Estimated from [S8]
Hole mobility	5x10^{-6} cm^2/Vs	2.5x10^{-6} cm^2/Vs	
Anion mobility	1x10^{-13} cm^2/Vs	1x10^{-14} cm^2/Vs	Estimated from calculation
Cation mobility	1x10^{-12} cm^2/Vs	1x10^{-13} cm^2/Vs	from conductivity measurement as done in [S12]: $\mu_a + \mu_c$ =5x10^{-12} cm^2/Vs
Radiative recombination coefficient	1x10^{-9} cm^3/s	1x10^{-9} cm^3/s	Manual fit
Effective density of states	1x10^{27} 1/m^3	1x10^{27} 1/m^3	Manual fit
LUMO SY	2.95 eV	2.95 eV	[S13]
HOMO SY	5.45 eV	5.45 eV	
Ohmic injection work function ITO	5.1 eV	5.16 eV	Chosen to have an equal barrier of 0.35 eV for both electrodes, leading to a charge carrier density at the electrode interface of 1x10^{15} cm^{-3}. For the 70 nm device, the barrier is 0.29 eV, or 1x10^{16} cm^{-3}
Ohmic injection work function Al	3.3 eV	3.24 eV	

Relative permittivity SY	2.8	2.8	Calculated from capacitance measurement
Equilibrium density of mobile negative ions on average	1×10^{18} 1/cm^3	1×10^{19} 1/cm^3	With the used salt concentration and a film density of 1 g cm^{-3} (ref. [S2]), the upper limit of the ion density is 1.17×10^{20} cm^{-3}
Equilibrium density of mobile positive ions on average	1×10^{18} 1/cm^3	1×10^{19} 1/cm^3	
Applied voltage	3 V	3 V	
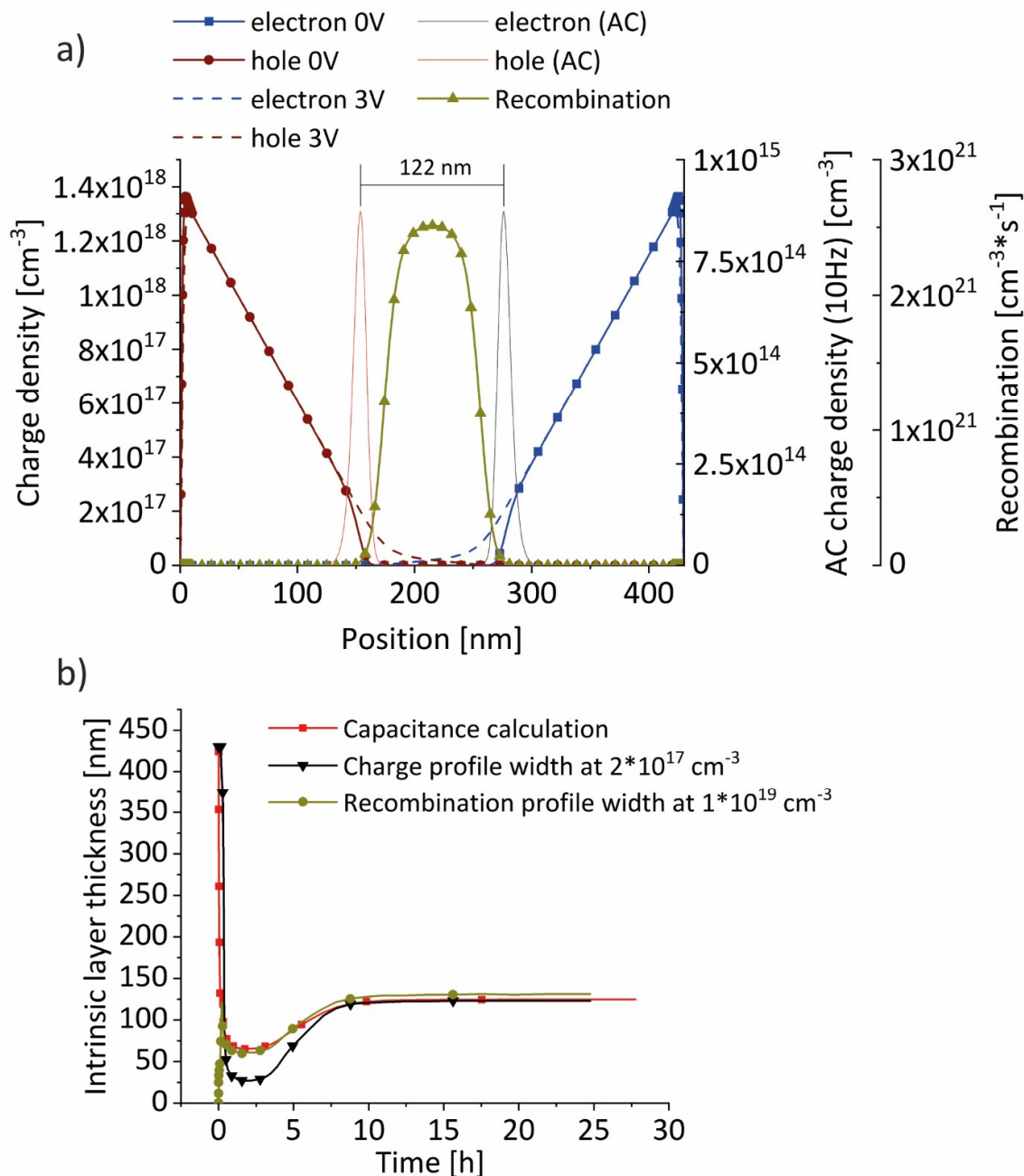
Figure S3.9. Capacitance simulation at steady state a) and during the transient simulation b). The capacitance is simulated as the measurement is carried out: A sinusoidal voltage is applied and the resulting change in current is measured, respectively calculated. Both for the measurement and simulation, the voltage amplitude is kept small such that a linear response can be assumed. This results in an output current which is also sinusoidal, and from the phase shift and amplitude the capacitance can be calculated, both for the measurement and simulation. The capacitance relates to a thickness where the injected charge resulting from the sinusoidal voltage piles up. This is where the conductivity gets very low, which is the intrinsic region.

Figure S3.9a shows the recombination profile in steady state after 16 h as shown in the main text, Figure 3.4a. The electron and hole profiles for the steady state at 3V are shown as dashed lines.

At 0 V for the given situation, the electron and hole profile (solid lines) change only in the region between 150 nm and 300 nm. We assume that during the 40 s interrupt for the impedance measurement (at 0 V) there is no change in the ion profiles relevant for the doping. Finally, the simulated 10 Hz AC charges (amplitude) that pile up are shown. The two peak positions relate to the plates of the capacitor in the simple model. This can be checked by calculating the thickness from the simulated capacitance in the steady state (19.9 nF/cm^2) as shown in Figure 3.3d. With the formula $C = \varepsilon_0 \varepsilon_r A/d$ and ε_r = 2.8 (Table S3.1), the resulting thickness is 124.7 nm, and the width between the two peaks is 122.2 nm. It seems that this thickness of around 122 nm corresponds to the width of the charge carrier profiles at a density of ~2*10^{17} cm^{-3} in the 3 V steady state, and to the width of the recombination profile at its base.

Figure S3.9b shows the transients of these three situations over the whole period. One can see that both the width of the charge carrier profiles and recombination width correlate with the thickness calculated from the capacitance.

a)   b)
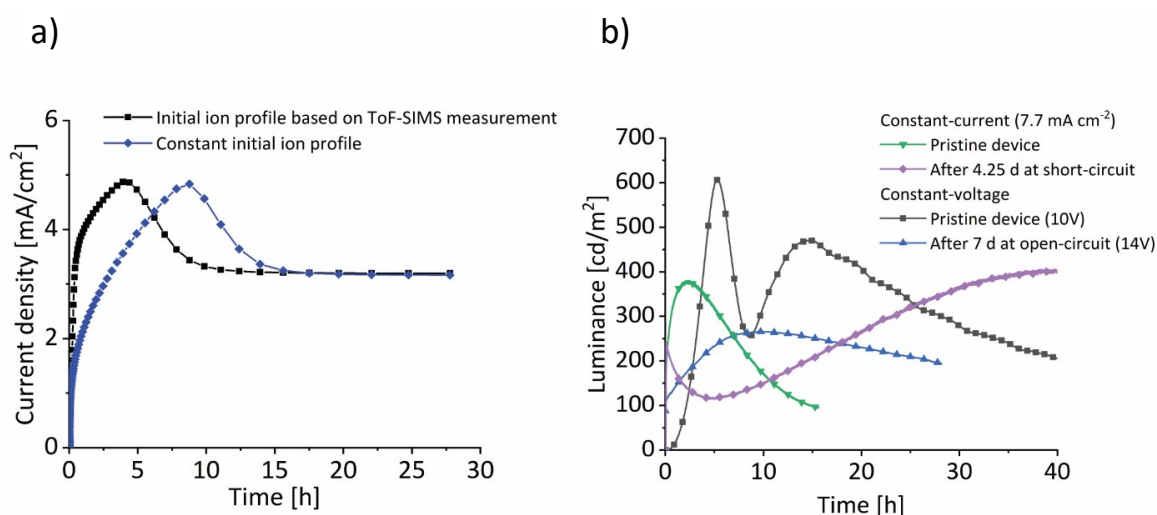
Figure S3.10. a) Comparison of simulated current transients starting with a constant initial ion profile and an initial ion profile based on ToF-SIMS measurements. Both simulations were performed with identical parameters listed in Table S3.1. For a homogeneous initial ion distribution, the EZ shift is slower but the fundamental trend is the same. b) Luminance of pristine devices and after relaxation over several days. All measurements show an EZ shift.
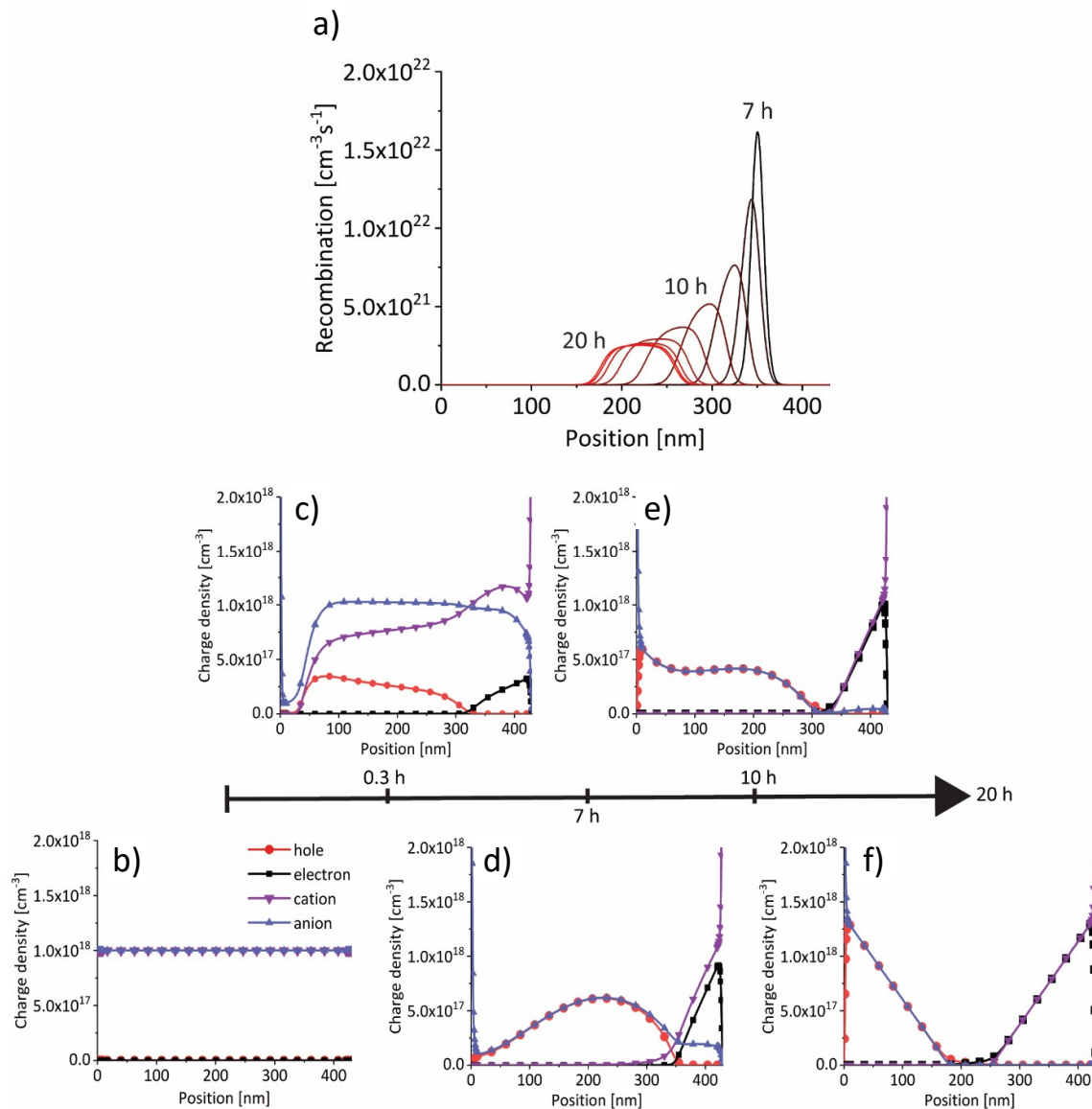
Figure S3.11. Simulations with parameters as used for Figure 3.3 (main text), but with an initial homogeneous ion distribution.

Table S3.2. Parameter influence on the EZ shift.

Parameter change	Influence
Increase of anion and cation mobilities by factor x (ratio stays the same)	Absolute values of the transient current and capacitance are maintained while the dynamics become faster by the factor x
Increase of electron and hole mobilities by factor x (ratio stays the same)	Mainly an increase of the current by a factor that non-linearly depends on x

Increase of electron and hole injection density by factor x (ratio stays the same)	Mainly an increase of the current by a factor that non-linearly depends on x
Increase of anion mobility while cation mobility is the same	Change in transient dynamics
Increase of electron mobility while hole mobility is the same	EZ in steady state is closer to the ITO electrode
Increase of electron injection density while hole injection density is the same	EZ in steady state is closer to the ITO electrode
Increase of ion density	The current increases, the intrinsic region gets narrower
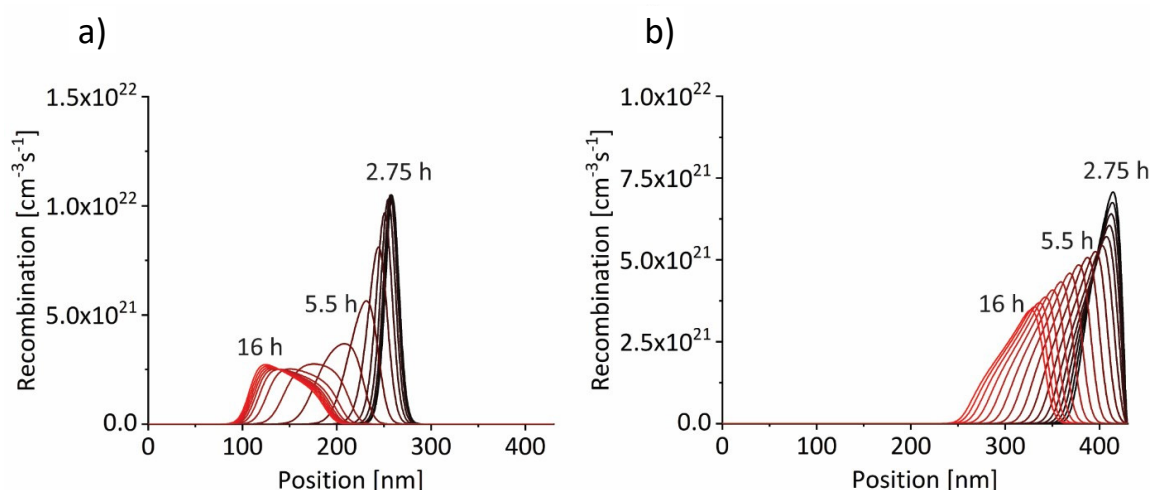
Figure S3.12. Recombination profiles of transient simulations when a) $\mu_e = 2 \times \mu_h$ ($\mu_e = 6.6 \times 10^{-6}$ cm^2/Vs, $\mu_h = 3.3 \times 10^{-6}$ cm^2/Vs) or b) $\mu_e = 1/2 \times \mu_h$ ($\mu_e = 3.3 \times 10^{-6}$ cm^2/Vs, $\mu_h = 6.6 \times 10^{-6}$ cm^2/Vs).
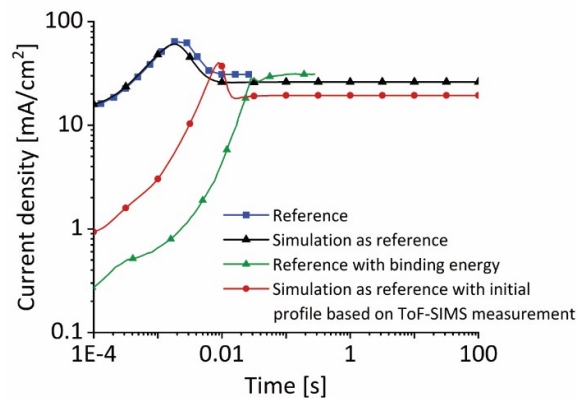
Figure S3.13. Re-simulation of current transients from reference [S9].
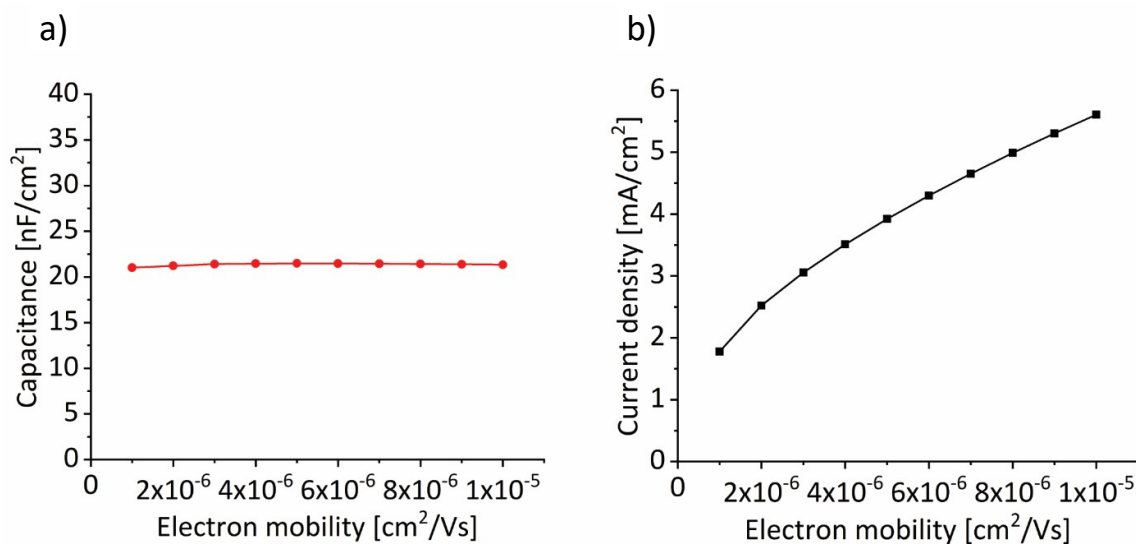
Figure S3.14. Influence of μ_e on a) the capacitance at 10 Hz and b) the current density in steady state. $\mu_h = 5 \times 10^{-6}$ cm^2/Vs was kept constant. The ion density was set to 8×10^{17} cm^{-3} to match the steady state of the transient 3 V simulation.
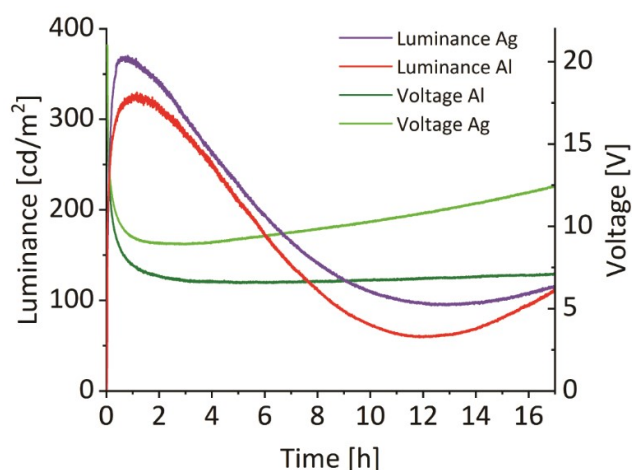
Figure S3.15. Comparison of 430 nm thick devices with an Ag or Al electrode.
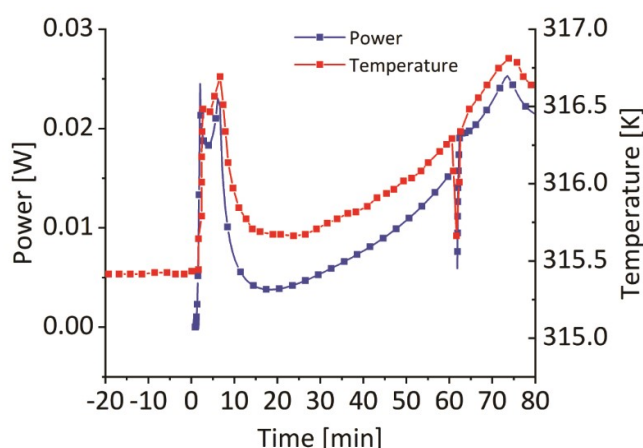
Figure S3.16. To estimate the temperature increase during operation, a 430 nm thick LEC was placed on a temperature-controlled plate at 320 K and a constant current of 5 x 7.7 mA cm^{-2} was applied. The temperature increase could hardly be measured for standard operation conditions, viz. room temperature and 7.7 mA cm^{-2}. The measured power profile (current x voltage) was in good agreement with the measured temperature, even a temperature decrease during the time when the capacitance was measured (electric power = 0) was registered. Because of the higher temperature and current during this experiment, the overall dynamics was much faster compared to room temperature. The temperature sensor was placed several millimetres away from the actual cell, and we estimate that the measured temperature increase of ~1 K corresponds to an actual cell temperature increase of several tens of degrees.

References

[S1]   E. M. Lindh, P. Lundberg, T. Lanz, L. Edman, *Sci. Rep.* **2019**, 9, 10433.

[S2]   T. Lanz, E. M. Lindh, L. Edman, J. *Mater. Chem. C* **2017**, 5, 4706.

[S3]   M. Diethelm, Q. Grossmann, A. Schiller, E. Knapp, S. Jenatsch, M. Kawecki, F. Nüesch, R. Hany, *Adv. Opt. Mater*. **2019**, 7, 1801278.

[S4]   S. van Reenen, P. Matyba, A. Dzwilewski, R. A. J. Janssen, L. Edman, M. Kemerink, *J. Am. Chem. Soc.* **2010**, 132, 13776.

[S5]   P. Calado, A. M. Telford, D. Bryant, X. Li, J. Nelson, B. C. O'Regan, P. R. F. Barnes, *Nat. Commun.* **2016**, 7, 13831.

[S6]   N. E. Courtier, G. Richardson, J. M. Foster, *Appl. Math. Modelling* **2018**, 63, 329.

[S7]   S. R. Tseng, Y. S. Chen, H. F. Meng, H. C. Lai, C. H. Yeh, S. F. Horng, H. H. Liao, C. S. Hsu, *Syn. Metals* **2009**, 159, 137.

[S8]   H. Najafov, I. Biaggio, T.-K. Chuang, M. K. Hatalis, *Phys. Rev. B* **2006**, 73, 125202.

[S9]   S. van Reenen, R. A. J. Janssen, M. Kemerink, *Adv. Funct. Mater.* **2015**, 25, 3066.

[S10]   V. I. Arkhipov, E. V. Emelianova, P. Heremans, H. Bässler, *Phys. Rev. B* **2005**, 72, 235202.

[S11]   Y. Murat, G. Wantz, S. Fasquel, J.-Y. Laurent, T. Maindron, L. Hirsch, *Proc. of SPIE* **2016**, 9941, 994129.

[S12]   S. van Reenen, R. A. J. Janssen, M. Kemerink, *Adv. Funct. Mater.* **2012**, 22, 4547.

[S13]   S. Stolz, M. Petzoldt, S. Dück, M. Sendner, U. H. F. Bunz, U. Lemmer, M. Hamburger, G. Hernandez-Sosa, *ACS Appl. Mater. Interfaces* **2016**, 8, 12959.

Chapter 4   Trap Induced Slow Transient Effects in Polymer LEDs

Electron Trap Dynamics in Polymer Light-Emitting Diodes

Matthias Diethelm[1,2], Michael Bauer[1], Wei-Hsu Hu[1,2], Camilla Vael[2,3], Sandra Jenatsch[3], Paul W. M. Blom[4], Frank Nüesch[1,2], and Roland Hany[1]

[1]Empa, Swiss Federal Laboratories for Materials Science and Technology, Laboratory for Functional Polymers, 8600 Dübendorf, Switzerland
[2]EPFL, Institute of Materials Science and Engineering, Ecole Polytechnique Fédérale de Lausanne, Station 12, 1015 Lausanne, Switzerland
[3]Fluxim AG, Katharina-Sulzer-Platz 2, 8400 Winterthur, Switzerland
[4]Max Planck Institute for Polymer Research, Ackermannweg 10, 55128 Mainz, Germany

Declaration of Contribution
M.D. fabricated devices, performed the optoelectronic measurements, did the optical and electrical simulation including all related input data measurements, analysed the data and prepared the manuscript.

Abstract

Semiconducting polymers are studied intensively for opto-electronic device applications, including solution-processed light-emitting diodes (PLEDs). Charge traps in polymers limit the charge transport and thus the PLED efficiency. It is firmly established that electron transport is hindered by the presence of an universal electron trap density, whereas hole trap formation governs the long-term degradation of PLEDs. Here, we study the response of PLEDs to electrical driving and breaks covering the timescale from microseconds to (a few) hours, thus focusing on electron traps. We identify three different traps with depths between ~0.4 eV and ~0.7 eV, and a total trap site density of ~2 x 10^{17} cm^{-3}. Surprisingly, filling of deep traps takes minutes to hours, at odds with the common notion that charge trapping is complete after a few hundred microseconds. We explain this unusual phenomenon with trap deactivation upon de-trapping and slow trap reactivation. Our results provide useful insight to pinpoint the chemical nature of the universal electron traps in semiconducting polymers.

4.1   Introduction

PLEDs are attractive electroluminescence devices for large-area display and lighting applications.[1,2] The presence of traps for electrons and holes in conjugated polymers, however, seriously limits the device efficiency and lifetime. It has been shown that there exists a universal electron trap site density, with a number of traps of 1-3 x 10^{17} cm^{-3}, centred at an energy of around

3.6 eV below the vacuum level.[2-6] For poly(para-phenylenvinylene) polymers, this translates into a trap depth in the range of E_t = 0.6 - 0.7 eV.[2,4,5] Electron traps are not limited to conjugated polymers, but occur also in vacuum-deposited small-molecular semiconductors.[6] They decrease the electron mobility and light emission via non-radiative recombination with free holes. In addition, when operating PLEDs at constant current over many tens of hours, the voltage continuously increases and the luminance decreases.[1] This is due to the formation of hole traps via the interaction of excitons with free holes. Hole traps grow over orders of magnitude with time and dictate the long-term stability of PLEDs.[1,5,7,8] It has been predicted[9] and experimentally confirmed[1,10] that by diluting the polymer with an insulating matrix, the effect of traps can be effectively eliminated, resulting in long-term stable PLEDs with a luminance efficacy (cd A^{-1}) that increases by almost a factor of two.

Here, we study the response of PLEDs to electrical stress pulses and breaks covering a time range of eight orders of magnitude. We test devices using as a reference polymer a phenyl-substituted poly(para-phenylenvinylene) copolymer termed super yellow, SY.[1,11,12] We identify first a fraction of shallow electron traps with a trap depth of ~0.4 eV. These traps are permanently present with a density in the range of 1 x 10^{17} cm^{-3}. We identify further electron traps with trap depths of ~0.5 eV and ~0.7 eV with a total concentration in the same range of 1 x 10^{17} cm^{-3}. By virtue of the trap depth and concentration, we assign these traps to the universal electron traps present in these materials. Deep traps de-trap slowly after switch-off, as expected. Surprisingly, however, also filling of these traps is very slow, as we infer from device recovery trends after rest that proceed over many minutes. We explain this finding with that the universal electron trap species effectively deactivate when the trap empties, either by thermal emission or after light excitation. Subsequently after switch-on, the probability that a deactivated trap species traps a passing charge is low, explaining the long trap filling time observed. We discuss that the scenario of trap deactivation upon de-trapping provides important information on the chemical nature of the universal electron traps in semiconducting polymers.

4.2   Results

Electron trap dynamics at short timescales. The cycle for electron traps when a PLED is switched on to drive and then back to rest can be readily understood. In a device at rest, electron traps are empty. When, for example, a voltage bias is then applied, the initial flow of mobile electron charge is high, as well as the radiative Langevin recombination between mobile electrons and holes. Over time, electron traps fill up and immobile charge replaces mobile charge. This results in a decrease of the current that is proportional to the number of filled traps. At the same time, non-radiative Shockley-Read-Hall (SRH) recombination between trapped electrons and free holes increases, thereby reducing the Langevin recombination. When the bias is switched off, free holes and electrons recombine rapidly. Subsequently, trapped electrons de-trap via thermal emission, and the de-trapping time is a measure of the trap depth. Thus, by measuring the current and light emission decay after switch-on and the de-trapping time after switch-off, we obtain information about the trap filling time and the trap concentration, as well as the trap depth. Similar considerations apply when driving a device at a constant current bias. The situation can be quantified with electrical and optical numerical simulations.

First, we applied a voltage pulse to a pristine PLED and measured the current and light response at short timescales (**Figure 4.1**). The current peak before ~2 µs is a displacement current due to the fast change of the electric field when the voltage bias is switched on within a few µs. In the measurement, the displacement current overlaps to some extent with a current peak at early times. Figure 4.1b and Figure 4.1c show simulations of the light and current transients. Simulation reproduces the displacement current qualitatively and identifies the current peak. The light peak at 20 µs and the initial current decline are due to electron trap filling, in an unaged device the hole trap site density is very low.[1] First, filled electron traps results in a trap space charge that displaces space charge from free charges (curve "electron density" in Figure 4.1c). This displacement happens because the electric field remains nearly constant during trap filling, which means the total space charge, coupled to the field by the Poisson equation, remains constant as well. Trapped charges do not contribute to the current in the device; thus, the current and the emitted light decrease. Secondly, SRH recombination increases with more trapped charge, reducing the emissive Langevin recombination. This explains why the decrease of light emission is stronger than the decrease of the current.
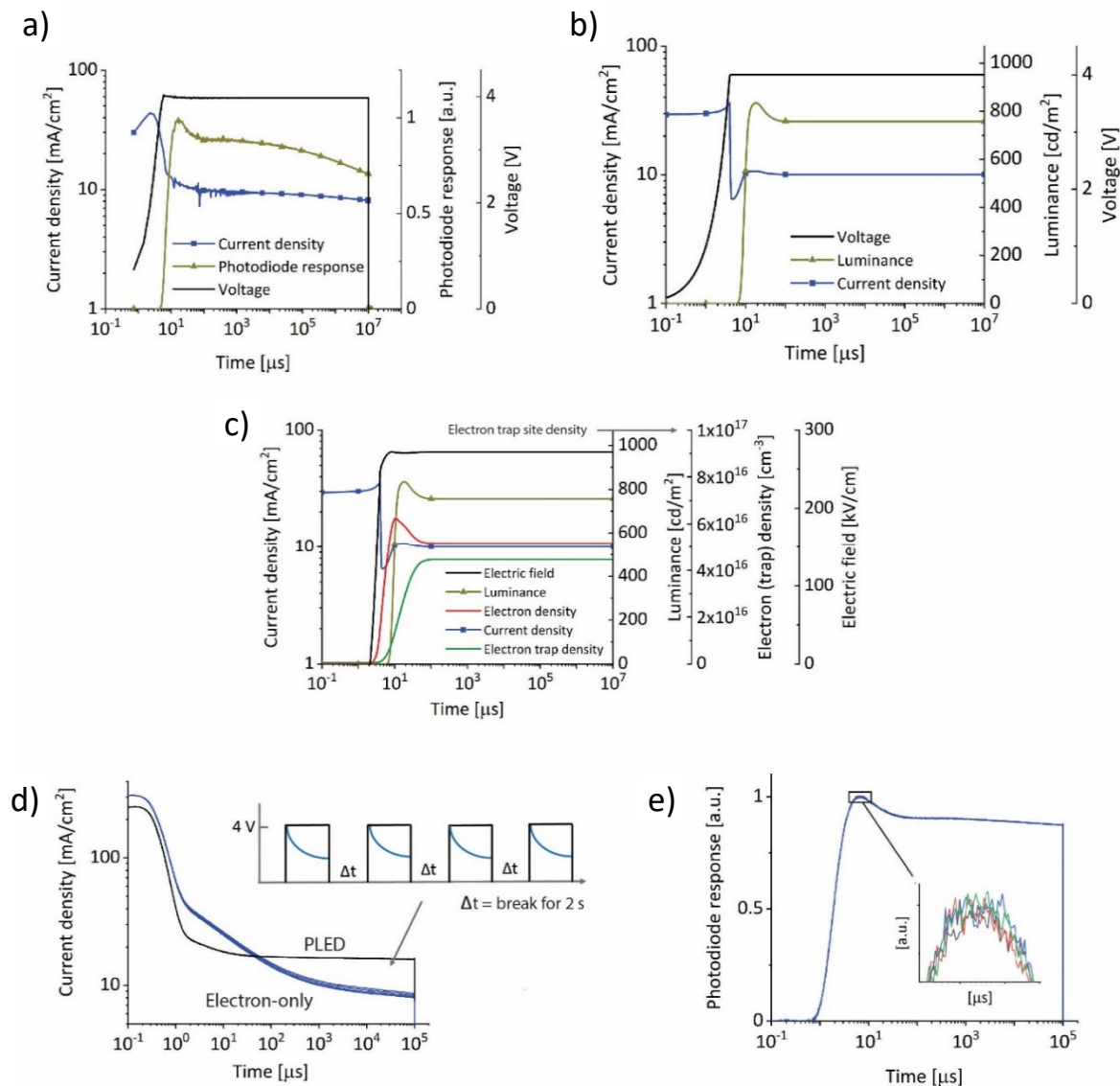
Figure 4.1. Transient response of pristine PLEDs at short timescales. a) Current and light transients measured when a voltage pulse is applied for 10 s. b) Transient drift-diffusion simulation with c) the corresponding simulated charge densities during the voltage pulse. A sequence of four short (0.1 s) voltage pulses with a break time of 2 s in between is applied to a pristine PLED and a pristine electron-only device, d) displays the current and e) the light measured during the pulses.

The transients in Figure 4.1a reach a steady state after ~ 200 µs, but after ~1 ms both the current and light start slowly to decline; we discuss this effect further below. For the simulation, the electron trap site density was set to 1×10^{17} cm^{-3} and the resulting trap filling time constant was 40 µs, other simulation parameters are discussed in the Supporting Information Note 1. The transient device response confirms the received opinion that charge trapping and recombination are fast processes, we discuss the trap density rate equation in the Supporting Information Note 2. When the device is switched off, the electroluminescence signal decays within less than 1 µs (Supporting Information Figure S4.1).

We applied a sequence of voltage pulses and rest periods to a pristine PLED and an electron-only device and measured the current and light response (Figure 4.1d and Figure 4.1e). The four current and light transients almost perfectly overlap (insert of Figure 4.1e). From this we conclude that complete electron de-trapping occurs during a break of 2 s; if there were trapped electrons still present after the break time, the current and light during a subsequent voltage pulse would start at a lower level. From a quantitative analysis (Figure 4.2e and related discussion, see below) we find that de-trapping related effects become visible after ~650 µs and traps fully de-trap within 100 ms. This period implies a trap depth of about 0.4 eV, resulting in a calculated de-trapping time constant of 10 ms (Supporting Information Note 2). Combining the findings from Figure 4.1, we identify in SY a shallow electron trap with a trap site density of ~1 x 10^{17} cm^{-3}. These traps are present in the pristine material already, charge trapping takes around 200 µs, and de-trapping is completed after ~100 ms.

The slow electron trap dynamics. We turn our attention to the observation from Figure 4.1a that after ~1 ms both the current and light start slowly to decline. **Figure 4.2**a shows the voltage and luminance trend of a PLED driven at a constant current bias of 7.7 mA cm^{-2} for 12 h, interrupted by breaks at specific moments. To check the consistent device response over the long measurement time, the current was interrupted after every 10 min for a short duration of 3.5 s. During some breaks, the device was rested at short circuit for longer times, ranging from 3 s (limited by the experimental setup) to 1.5 h. After every break, an intermediate increase in device performance is observed, both electrically (apparent via a decrease of the starting voltage) and optically (apparent via an increased starting photodiode response). Subsequently, the voltage and photodiode recovers back to the trend line before the break. This measurement protocol did not change the long-term behaviour of the PLED, as indicated by the dashed curve. The steady increase of voltage and decrease of light emission over many hours is attributed to the continuous formation of hole traps, in agreement with literature.[1] Data in Figure 4.2a were measured on a device with SY coated from THF, we observed similar long-term transients for devices coated from toluene (Supporting Information Note 3).
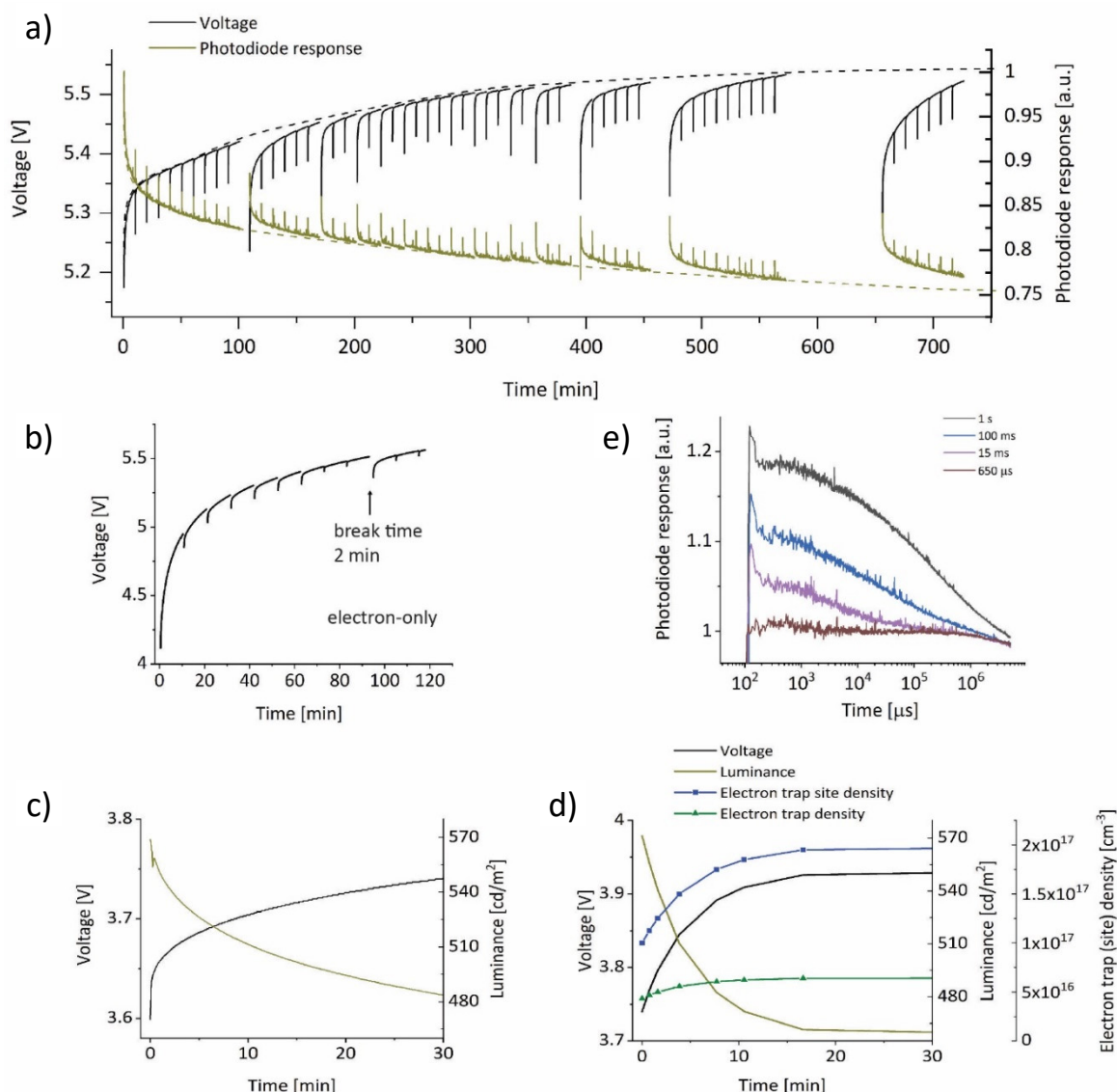
Figure 4.2. The slow electron trap dynamics. a) Voltage and light emission trend of a constant current-driven PLED (7.7 mA cm^{-2}). The current stress was interrupted at particular moments and the device rested at short circuit (0 V) for a certain time before switching to bias again. b) Voltage trend of a constant current-driven electron-only device. c) Experimental and d) simulated voltage and luminance trend at a constant current of 7.7 mA cm^{-2} during the first 30 min. e) The break time between two 5 s long voltage pulses (4 V) was varied from 10 μs to 1 s and light transients were measured during the second voltage pulse.

In a few cases, similar transients were reported for organic light-emitting diodes that continued for seconds to hours. This topic received little attention so far, and the effects were, suggestively, explained with temperature variations, reorientation of internal dipoles as well as redistribution of ionic impurities or trapped charge.[13-20] In the Supporting Information Note 3 we consider – and carefully exclude – that these effects explain the observed recovery trend in our case. We explain the observation by the presence of deep electron traps that de-trap slowly at rest – as expected –

and ascribe the slow recovery transients to the fact that de-trapping effectively deactivates the trap, followed by slow trap reactivation. In the following, we designate this phenomenon "trap deactivation".

The breaks at short circuit result in the slow emptying of electron traps (Supporting Information Figure S4.1), such that at switch-on both the electrical and optical performance improves until the traps fill up again. The fact that the voltage and light recovery takes a long time, however, is an unexpected observation, clearly in contrast to the general notion that trap filling occurs on a timescale of a few 100 μs or less, irrespective of the depth of the trap level.

We evaluate the magnitude of the relaxed voltage (undershoot) and photodiode response (overshoot) as well as the recovery times to the steady-state situation, which is the point where the measurement curve approaches the long-term transient, indicated by the dashed line. The trend is the same for all four quantities: the longer the break time, the larger is the voltage undershoot and recovery time, as well as the photodiode response overshoot and recovery time. The trends are summarized in the Supporting Information Figure S4.2, which show logarithmic behaviour with break time.

Three main observations emerge from these break experiments: i) The recovery time is in the range from minutes to hours. ii) The effect does not change over a drive time of 12 h, i.e. the same break duration at different points in time leads to similar light overshoots and voltage undershoots. iii) The initial increase of voltage and drop of photodiode response for a pristine device resembles the recovery after a break time of ~1000 s at a later time. Statements ii) and iii) indicate that the relaxation and recovery process does not involve the hole traps, because they form continuously and grow in number over time. We applied the measurement sequence from Figure 4.2a to an electron-only device (Figure 4.2b) and observed the same general trend, as expected when electron traps dictate the proceedings. Trap deactivation is slower for the electron-only device, which can be explained with the absence of hole traps that activate a small deactivation channel via electron-hole trap-trap recombination (Supporting Information Figure S4.3).

An assumed energetic trap depth of ~0.7 eV results in a de-trapping time constant at rest of 1000 s (Supporting Information Note 2), in good agreement with the measured relaxation timescale. We simulated the experimental voltage and luminance trend for a constant current-driven device over the first 30 minutes. Results in Figure 4.2 show that an electron trap site density of 1×10^{17} cm^{-3} develops over time, starting from a value of 1×10^{17} cm^{-3} at time zero that originates from the existing shallow traps that are filled immediately (Figure 4.1).

We studied the device response for break times shorter than 3 s. Therefore, we applied a sequence of two 5 s long voltage pulses to a pristine PLED. Pulses were separated by a variable break time (10 μs – 1 s) and the device response was measured during the second voltage pulse with a high time resolution. Figure 4.2e displays the light transients for that measurement sequence, we show the current transients in the Supporting Information Figure S4.2. A light peak during the first 200 μs of the measurement time gets noticeable for break times above ~650 μs; by comparing with data shown in Figure 4.1, we ascribe this feature to the filling of the shallow electron traps that empty during the break time. Complete de-trapping of the shallow electron traps takes around ~100 ms, because the magnitude of the short-term peak stays constant for longer break times.

It is interesting to note that data in Figure 4.2e clearly show that after a measurement time of ~200 μs a second dynamic feature evolves. The photodiode response level increases with increasing break time and relaxes over the measurement time of 5 s back to the steady state value. Again, we ascribe this trend to a trap filling process of traps that empty during the break. A de-trapping time of 1 s implies that the trap depth is close to 0.5 eV, clearly different from the shallow (0.4 eV) and deep (0.7 eV) trap levels we identified so far. We denote this trap as "intermediate". Both deep and intermediate traps share the common unusual feature that for a given de-trapping period at rest the recovery time is much longer. We explain this phenomenon with trap deactivation.

Again, we estimate the intermediate trap site density from simulation and for this note that the photodiode trends between 1 ms and 1 s from Figure 4.1a and Figure 4.2e closely match. In the simulation, we start from the steady-state situation in Figure 4.1b after 200 μs and add trap sites over time. For each portion, we simulate the resulting steady-state luminance. An added intermediate trap site density of 3×10^{16} cm^{-3} results in a simulated decrease of the photodiode response between 1 ms and 1 s of 12%, in agreement with the experiment.

The simulated trap site density from Figure 4.2d (1×10^{17} cm^{-3}) represents the total of the intermediate and deep traps. With the intermediate trap site density (3×10^{16} cm^{-3}) at hand, we thus find that the concentration of deep traps is slightly higher, on the order of 7×10^{16} cm^{-3}.

Electron de-trapping by light. We obtain further evidence for trap deactivation from illumination experiments. Therefore, devices were rested at short circuit and a constant voltage was then applied (**Figure 4.3**). Again, the initial device performance improved and a current overshoot occurred that recovered to the steady-state value. During the recovery time, we applied light pulses with a wavelength below the bandgap of SY. The first light pulse was applied directly at switch-on of the voltage, the second pulse during current recovery. From Figure 4.3 it can be seen that the current increases slowly during the duration of the second light pulse and recovers afterwards.
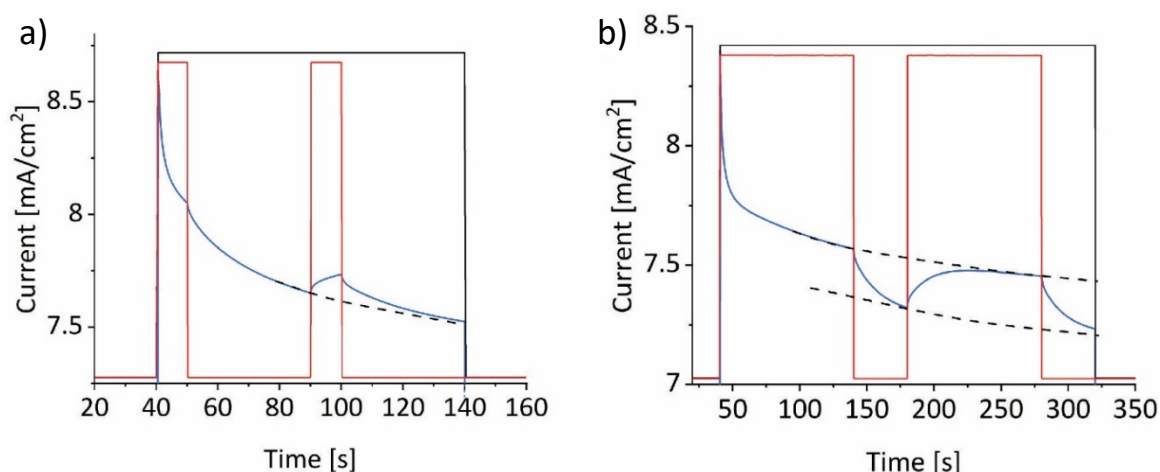
Figure 4.3. Electron de-trapping by light. A constant voltage of 5.3 V (black) was applied to a PLED after a break time of 40 s. At voltage switch-on, the current (blue) overshoots and recovers over

time to the steady-state value. In a), two LED pulses (red) with a wavelength of 656 nm were applied for 10 s during the measurement. In b), the LED pulses had a length of 100 s.

The overall current decrease during the voltage pulse is due to regeneration of intermediate and deep electron traps that deactivated at rest – at switch-on, the permanently present shallow traps fill up immediately and the current adjusts within 200 μs. Consequently, when light excites and empties a shallow trap, the trap fills up on the same fast timescale. Interestingly, during the second light pulse, the device response is much slower and it takes several tens of seconds until a new steady state is reached. We interpret this observation by that de-trapping induced by light immediately deactivates the intermediate and deep traps, followed by slow reactivation over time. Slow trap site activation competes with trap site deactivation, and a new steady state adjusts during the light pulse. If light-induced de-trapping would not result in trap deactivation, trap filling of deep traps would also occur within hundreds of μs, just like for the shallow traps, and the new steady state would adjust instantaneously on the timescale of the measurement. The timescale for the light experiment is the same as trap deactivation measured for breaks at short circuit, supporting that de-trapping by light deactivates the trap.

We summarize additional illumination experiments in the Supporting Information Note 4. Similar transients as shown in Figure 4.3 were observed for irradiation wavelengths ranging from 740 nm to 1020 nm. We used the same photon flux at each wavelength, indicating that the trap absorption profile is rather flat between around 650 to 1000m.

4.3   Discussion

By measuring the electrical and optical response of SY PLEDs to stress and rest periods ranging from microseconds to hours, we identify three electron trap levels and summarize the evaluated trap dynamics, energies of the trap levels and trap concentrations in **Figure 4.4**.

We define the trap depth with respect to the energy barrier a trapped electron has to overcome. In the picture of a Gaussian density of states (DOS) for the lowest unoccupied molecular orbital (LUMO),[2,3,21] this energy barrier is best described by the difference of the trap level to the energy level $E_0 - E_a$, which is formally equivalent to the conduction-band edge, with the centre of the Gaussian DOS E_0 minus the characteristic energy $E_a = \frac{\sigma^2}{2kT}$. E_a is around 0.2 eV for a typical variance $\sigma = 0.1$ eV of the Gaussian DOS.[2] For the calculation of the trap depths we considered only de-trapping by thermal emission and neglected hole trap formation during the first minutes of operation,[1] which opens presumably a small deactivation channel via electron-hole trap-trap recombination. Therefore, trap depths for intermediate and deep traps are actually slightly deeper than 0.5 eV and 0.7 eV. By virtue of the trap energies and their total concentration of around 1 x 10^{17} cm^{-3}, we identify these traps with the universal electron trap site density present in these materials.[3] It remains to be seen whether the shallow electron traps are specific to SY or whether they can be identified in other semiconducting polymers as well. These traps behave "normally" in the sense that trap filling is a fast process and completed within around 200 μs, as expected from the general notion of charge trapping in organic semiconducting materials.
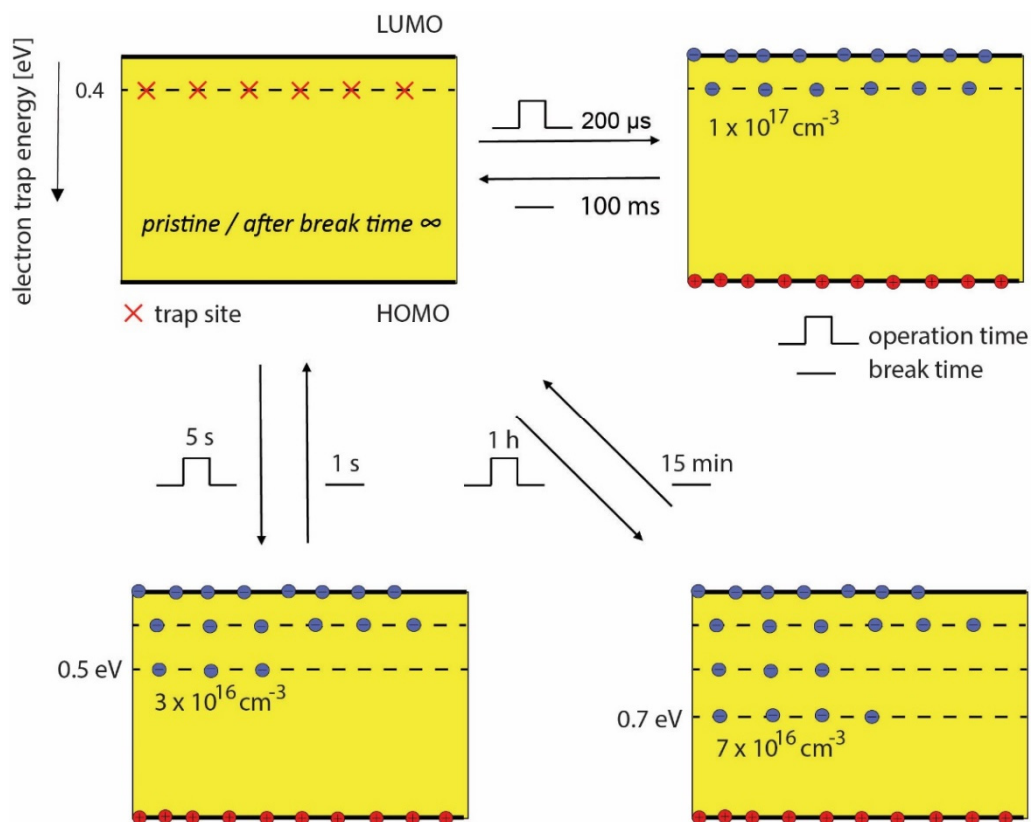
Figure 4.4. Schematic diagram summarizing the electron trap dynamics in SY PLEDs. Note that in the pristine device there are no (empty) trap sites present at trap levels of 0.5 eV and 0.7 eV, these traps deactivate upon de-trapping. Indicated times are experimental values for which we observe complete trapping and device relaxation; rate constants from simulations are slightly lower because they are defined differently (Supporting Information Note 2). Electron trap concentrations were evaluated via numerical simulation.

Two types of electron traps in PLEDs have been identified before.[10,22] The authors measured hysteresis effects in current-voltage scans using the polymer MEH-PPV, a poly(p-phenylene vinylene) derivative similar to SY. Results were interpreted that deep traps with a concentration of around 10^{16} cm^{-3} were responsible for hysteresis. By purification of the polymer, hysteresis free currents were obtained. We purified our SY material via a number of subsequent precipitations, as described for MEH-PPV,[22] but observed no difference in hysteresis between unpurified and purified material (Supporting Information Note 5). Therefore, our situation is different and the chemical nature of the different traps in SY does not originate from the presence of low-molecular weight polymer fractions in the material or from trivial impurities that are soluble in common organic solvents.

We discuss the long recovery trends after relaxation observed for the intermediate and deep traps that we designated as trap deactivation upon de-trapping. The origin of charge trapping in organic semiconductor materials is presently not well understood, primarily because of the small trap concentrations involved, which makes the chemical nature of traps difficult to characterize. Our presumption is that charge trapping is fast if a trap site is present and accessible at switch-on.

Furthermore, there is no reason to assume that the charge trapping time for active trap sites is related to the energetic depth of the trap.

One explanation for slow charge trapping relates to permanently present, but difficult-to-access traps that are located at remote sites in the bulk of the polymer. In this case, trapping and de-trapping is slow for morphological reasons. There are several arguments against such a scenario. First, if remote traps were permanently present in the material, it is not clear why de-trapping is much faster than trapping, as observed. Second, we calculated the trap depths of around 0.5 eV and 0.7 eV by assuming thermal emission out of the trap. For remote traps, the trap depth would in reality be much lower, because the measured de-trapping time is then determined by the probability that an isolated trap becomes accessible and de-trapping occurs. However, by systematically varying the electron affinity (EA) for a variety of polymers and by using chemical n-type doping,[2] it has clearly been shown that there exists a general impurity acting as the electron trap with an EA around 3.6 eV. For SY with an energy of the lowest unoccupied orbital level of 2.9 eV,[23] this indeed means that a trap with an actual trap depth of around 0.7 eV does exist.

Therefore, we speculate that de-trapping of the universal electron traps results in immediate trap deactivation. The chemical trap species remain present in the material and are accessible; however, the probability for trap reactivation and charge trapping at switch-on is low. This peculiar trap behaviour provides important information on the chemical nature of the deep electron traps. For example, it has been proposed that carbonyl containing end-groups in the polymer structure can be reduced electrochemically via reaction with the injected electrons and thus act as deep traps.[22] We argue that such a trap species would not show the phenomenon of deactivation upon de-trapping: if the electron de-traps from the carbonyl group at rest, it can immediately be reduced again at switch-on.

As a common origin for the omnipresent electron charge traps in conjugated polymers, hydrated oxygen complexes have been identified as likely candidates.[4,24] Not overselling the discussion, we mention findings in favour of the idea that hydrated oxygen complexes indeed act as charge traps, but that their probability of formation is effectively low. First, it has been reported that the neutral $H_2O \cdot O_2$ complex is very weakly bound, with a calculated binding energy of 0.016 eV[25] that is lower than the thermal energy. Therefore, oxygen and water (cluster) molecules are permanently present in the polymer, but usually not in the form of hydrated oxygen complexes that can immediately be reduced. The trap is stable once it has captured an electron, because the reduced $H_2O \cdot O_2^-$ species is an ion-dipole complex with a binding energy of 0.88 eV for dissociation to H_2O and O_2^-.[25] Support for a weakly bound complex comes from the observation that the trap reactivation time strongly depends on the break time. If the oxygen and water molecules were mostly in the unbound state but remain in close proximity, we expect that the probability that a passing charge encounters now and then a water oxygen complex does not depend on the break time. Rather, the trap recovery trend suggests that after de-trapping oxygen and water separate via diffusion, and the probability for an encounter and complex formation decreases with increasing time at rest. During device operation, trapped electrons recombine with free holes. This results also in trap deactivation, but the outcome is different from the situation at rest. Shortly after de-trapping, water and oxygen are still close and in a dynamic equilibrium with the complex, which can immediately capture a free electron and stabilize again.

4.4   Conclusion

We studied the dynamics of electron trap filling and de-trapping in SY PLEDs. For this, we measured the device response to electrical driving and breaks covering the timescale from microseconds to hours. By measuring the performance decay after switch-on and the de-trapping time after switch-off, we obtained information about the trap filling time and trap concentration, as well as the trap depth. From this analysis, we could identify the universal deep electron traps clearly. Surprisingly, trap filling of these deep traps proceeds over many minutes, clearly in contrast to the general notion that trap filling occurs on a timescale of a few hundreds of microseconds or less, irrespective of the depth of the trap level. Our observations are not consistent with the hypothesis that a permanently present and active chemical species in the material acts as the electron trap. Rather, it favours the proposed hydrated oxygen complex as the origin for the charge trap. Results suggest that the reduced complex is stable, but that after de-trapping oxygen and water separate via diffusion because the neutral complex is weakly bound. A slow diffusion process involved in the complex formation is in agreement with the slow trap filling observed. Our results on the surprisingly slow trap filling of the universal electron traps in semiconducting polymers are useful to pinpoint the chemical nature of the traps in further experimental and quantum-chemical studies.

4.5   Methods

Dried (24 h, 0.1 mbar, 40 °C) SY (Merck) was dissolved in a concentration of 5 mg mL^{-1} in anhydrous THF or toluene, respectively. Solutions were stirred for 24 h at 60 °C before coating. Patterned ITO substrates (~11 Ohms square^{-1}) were cleaned successively in acetone, ethanol, a 2 vol% aqueous solution of Hellmanex and deionized water using an ultrasonic bath. 40 nm thick PEDOT:PSS (HTL Solar, Ossila) films were spin coated (1000 rpm s^{-1}, 60 s at 3000 rpm) from filtered (pore size 0.45 µm) solution and were then dried for 20 min at 120 °C. SY films with a thickness of (80 ± 10 nm) were coated inside a glove box (H_2O < 1 ppm, O_2 < 20 ppm). Before spin coating, solutions were stirred at room temperature for 20 min. Films were coated from unfiltered solutions for 60 s at 2000 rpm and 2000 rpm/s, and were then dried at 60 °C for 1 h inside the glovebox. Calcium (10 nm) and aluminium (70 nm) were thermally evaporated through a shadow mask defining eight cells with an active area of 3.1 or 7.1 mm^2 per substrate. For the electron-only device, the PEDOT:PSS layer on ITO was replaced by a 20 nm thick aluminium layer.

For luminance measurements, devices were placed in an airtight holder and were measured under nitrogen atmosphere outside the glove box at room temperature using a factory calibrated Konica Minolta LS-110 luminance meter with a close-up lens 110. The reflection loss of the top cover glass of the holder was not considered. Hysteresis, current and light intensity transients were measured on the Paios measurement system (Fluxim AG, Switzerland). The light intensity was measured with a photodiode as photovoltage. The relation between the measured photovoltage and the corresponding radiance/luminance is explained in the Supporting Information of reference.[26] Impedance measurements were carried out at 0 V on a Metrohm Autolab.

Optical and electrical simulations were performed with Setfos 5.1 (Fluxim AG, Switzerland). Simulation procedures and parameters are described in the Supporting Information Note 1. Optical constants of SY were taken from reference [27] and were confirmed by simulation of

experimental transmission spectra measured previously.[28] Photoluminescence spectra were measured on a Horiba Jobin Yvon Fluorolog spectrometer.

References

[1]   Q. Niu, R. Rohloff, G.-J. A. H. Wetzelaer, P. W. M. Blom, N. I. Crǎciun, *Nat. Mater.* **2018**, *17*, 557.

[2]   M. Kuik, G.-J. A. H. Wetzelaer, H. T. Nicolai, N. I. Craciun, D. M. De Leeuw, P. W. M. Blom, *Adv. Mater.* **2014**, *26*, 512.

[3]   H. T. Nicolai, M. Kuik, G. A. H. Wetzelaer, B. de Boer, C. Campbell, C. Risko, J. L. Brédas, P. W. M. Blom, *Nat. Mater.* **2012**, *11*, 882.

[4]   D. Abbaszadeh, A. Kunz, N. B. Kotadiya, A. Mondal, D. Andrienko, J. J. Michels, G.-J. A. H. Wetzelaer, P. W. M. Blom, *Chem. Mater.* **2019**, *31*, 6380.

[5]   Q. Niu, G.-J. A. H. Wetzelaer, P. W. M. Blom, N. I. Crǎciun, *Adv. Electron. Mater.* **2016**, *2*, 1600103.

[6]   N. B. Kotadiya, A. Mondal, P. W. M. Blom, D. Andrienko, G.-J. H. A. Wetzelaer, *Nat. Mater.* **2019**, *18*, 1182.

[7]   Q. Niu, G.-J. A. H. Wetzelaer, P. W. M. Blom, N. I. Crǎciun, *Appl. Phys. Lett.* **2019**, *114*, 163301.

[8]   I. Rörich, Q. Niu, B. van der Zee, E. del Pino Rosendo, N. I. Crǎciun, C. Ramanan, P. W. M. Blom, *Adv. Electron. Mater.* **2020**,1700643.

[9]   M. Kuik, L. J. A. Koster, A. G. Dijkstra, G. A. H. Wetzelaer, P. W. M. Blom, *Org. Electronics* **2012**, *13*, 969.

[10] D. Abbaszadeh, A. Kunz, G. A. H. Wetzelaer, J. J. Michels, N. I. Crǎciun, K. Koynov, I. Lieberwirth, P. W. M. Blom, *Nat. Mater.* **2016**, *15*, 628.

[11] S. Burns, J. MacLeod, T. T. Do, P. Sonar, S. D. Yambem, *Sci. Rep.* **2017**, *7*, 40805.

[12] S. Tang, L. Edman, *J. Phys. Chem. Lett.* **2010**, *1*, 2727.

[13] T. Yamada, D. Zou, H. Jeong, Y. Akaki, T. Tsutsui, *Syn. Metals* **2000**, *111-112*, 237.

[14] Z. D. Popovic, H. Aziz, *IEEE J. selected topics quantum electronics* **2002**, *8*, 362.

[15] M. Yahiro, D. Zou, T. Tsutsui, *Syn. Metals* **2000**, *111-112*, 245.

[16] D. Zou, M. Yahiro, T. Tsutsui, *Jpn. J. Appl. Phys.* **1998**, *37*, L1406.

[17] D. Zou, M. Yahiro, T. Tsutsui, *Appl. Phys. Lett.* **1998**, *72*, 2484.

[18] A. J. A. B. Seeley, R. H. Friend, J.-S. Kim, J. H. Burroughes, *J. Appl. Phys.* **2004**, *96*, 7643.

[19] K. S. Rao, Y. N. Mohapatra, *J. Luminescence* **2014**, *145*, 793.

[20] L. Lepnev, A. Vaschenko, A. Vitukhnovsky, S. Eliseeva, O. Kotova, N. Kuzmina, *Syn. Metals* **2009**, *159*, 625.

[21] M. M. Mandoc, B. de Boer, G. Paasch, P. W. M. Blom, *Phys. Rev. B.* **2007**, *75*, 193202.

[22] N. I. Craciun, Y. Zhang, A. Palmaerts, H. T. Nicolai, M. Kuik, R. J. P. Kist, G. A. H. Wetzelaer, J. Wildeman, J. Vandenbergh, L. Lutsen, D. Vanderzande, P. W. M. Blom, *J. Appl. Phys.* **2010**, *107*, 124504.

[23]   J. Xu, A. Sandström, E. M. Lindh, W. Yang, S. Tang, L. Edman, *ACS Appl. Mater.* **2018**, *10*, 33380.

[24]   J.-M. Zhuo, L.-H. Zhao, R.-Q. Png, L.-Y. Wong, P.-J. Chia, J.-C. Tang, S. Sivaramakrishnan, M. Zhou, E. C.-W. Ou, S.-J. Chua, W.-S. Sim, L.-L. Chua, P. K.-H. Ho, *Adv. Mater.* **2009**, *21*, 4747.

[25]   A. J. Bell, T. G. Wright, *Phys. Chem. Chem. Phys.* **2004**, *6*, 4385.

[26]   M. Diethelm, A. Schiller, M. Kawecki, A. Devižis, B. Blülle, S. Jenatsch, E. Knapp, Q. Grossmann, B. Ruhstaller, F. Nüesch, R. Hany, *Adv. Funct. Mater.* **2020**, *30*, 1906803.

[27]   T. Lanz, E. M. Lindh, L. Edman, *J. Mater. Chem. C* **2017**, *5*, 4706.

[28]   M. Diethelm, Q. Grossmann, A. Schiller, E. Knapp, S. Jenatsch, M. Kawecki, F. Nüesch, R. Hany, *Adv. Opt. Mater.* **2019**, *7*, 1801278.

Supporting Information
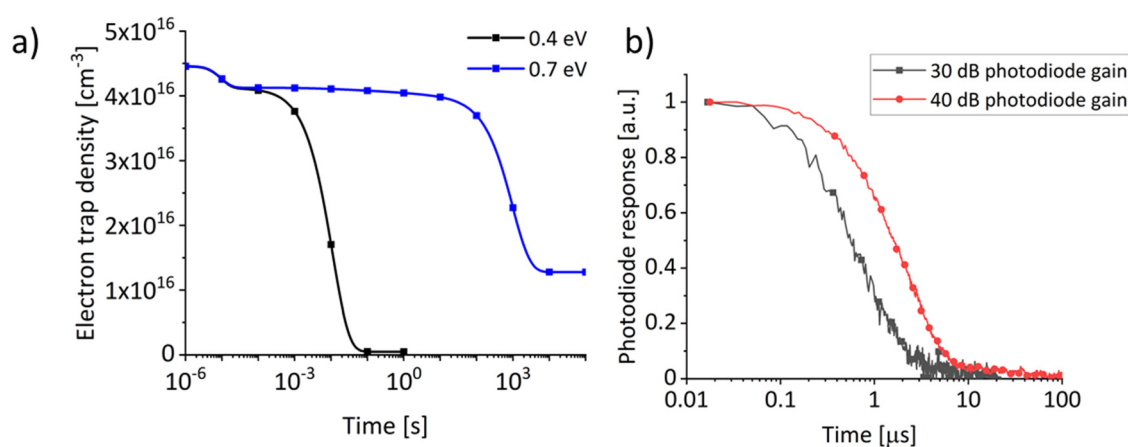
Figure S4.1. a) Transient simulation of the decay of the electron trap density in the PLED when the bias is set to 0 V after a 4 V steady state for different electron trap depths. b) Photodiode response decay of the PLED. A different electroluminescence decay time is measured when changing the photodiode gain, which means that the response speed of the photodiode determines the time resolution. The electroluminescence decays within below 1 µs.
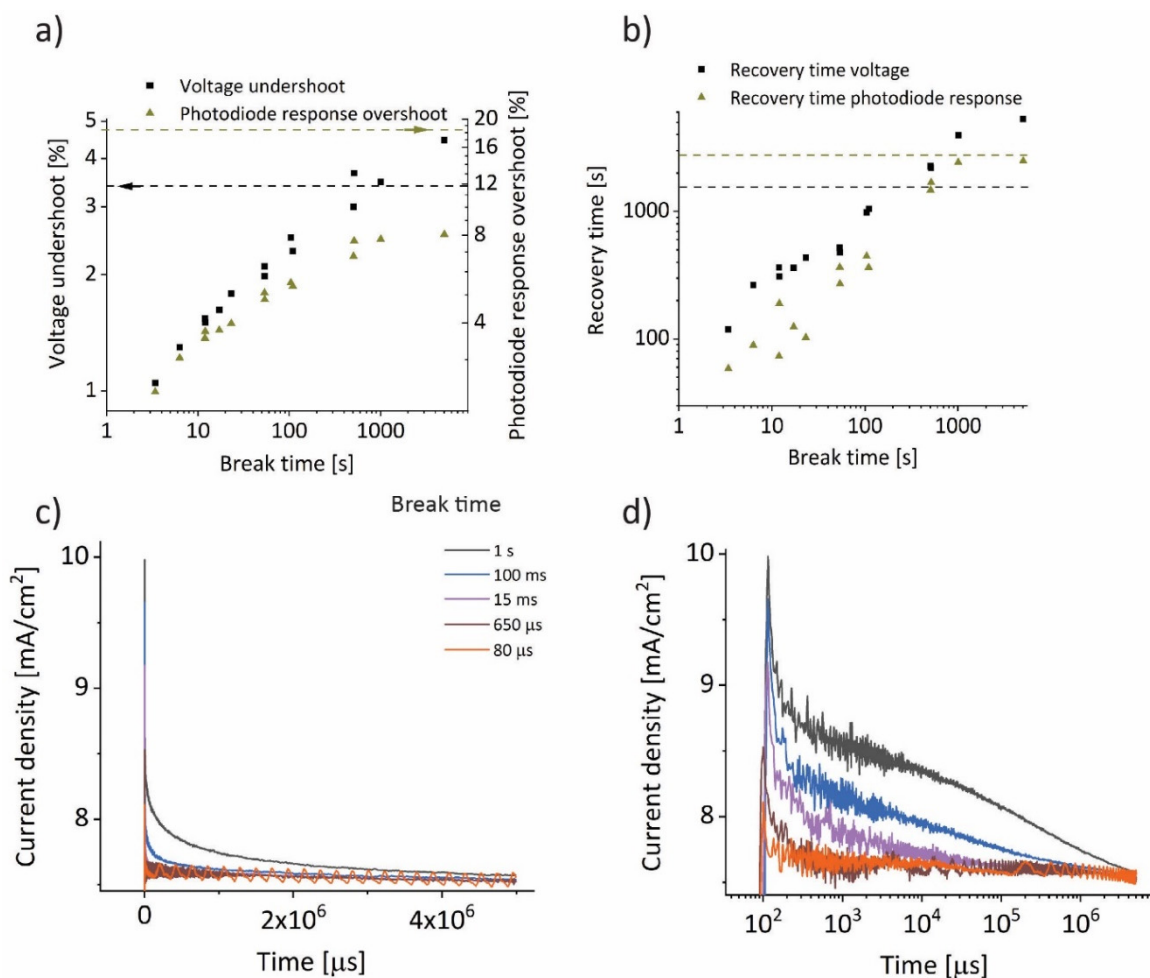
Figure S4.2. Long-term voltage undershoot and photodiode response overshoot vs. break time of PLEDs in a), and their recovery time vs. break time in b). The initial response is indicated by dashed lines. c) and d) show current recoveries during a constant (second) voltage pulse (4 V) of 5 s where the break time between two 5 s voltage pulses was varied from 10 μs to 1 s. In a linear scale in c), the current overshoot gets unnoticeable small below a break time of 100 ms. In the logarithmic plot d) there are still small overshoots visible for very short break times. From the current trends observed here we derive the same conclusions as discussed in the main text for the photodiode response trends (Figure 4.2).
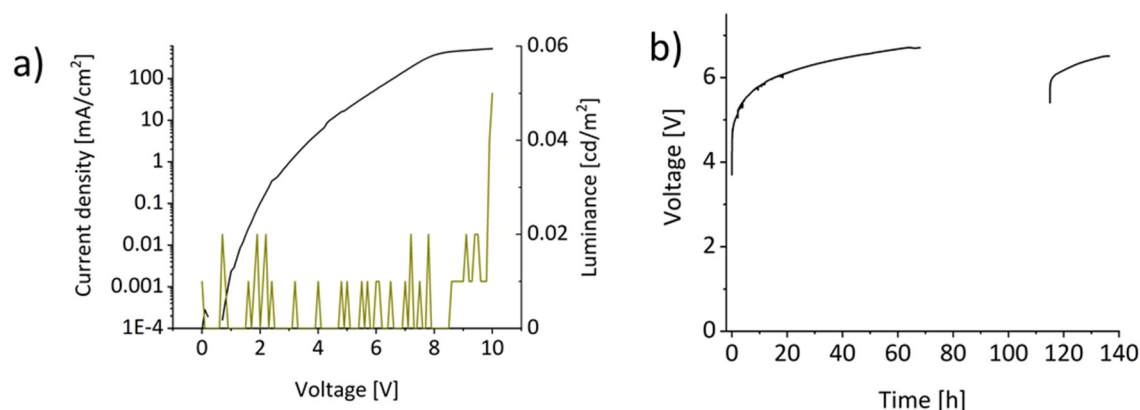
Figure S4.3. a) Current-voltage trend of an electron-only device. Beyond 10 V, the luminance starts to increase because of hole injection from the ITO/Al electrode into the SY HOMO. b) 48 h relaxation of an electron-only device at short-circuit after driving for 70 h at 7.7 mA/cm^2.

Supporting Information Note 1

Electrical model parameters

Electrical parameters were either directly taken, or were slightly adapted, from reference.[S1,S2] Some parameters were adopted from our previous work[S3], as described in table Table S4.1. For simplicity, the PEDOT:PSS layer in the PLED was not electrically simulated, instead a fixed number of injected holes was assumed at the SY/PEDOT:PSS interface.

Table S4.1. Electrical model parameters

Parameter	PLED	Source
Thickness SY	85 nm	Measured with a profilometer, fitted to current level
Electron mobility	3x10^{-6} cm^2/Vs	See below
Hole mobility	1x10^{-6} cm^2/Vs	
Radiative recombination coefficient	1x10^{-9} cm^3/s	Reference[S4]
Effective density of states	1x10^{27} 1/m^3	Reference[S1]
LUMO SY	2.95 eV	Reference[S5]
HOMO SY	5.45 eV	
Ohmic injection work function ITO / PEDOT:PSS	5.33 eV	Chosen to have an equal barrier of 0.12 eV, or 1x10^{19} cm^{-3} holes/electrons for the PLED
Ohmic injection work function Al / Ca/Al	3.07 eV	

Relative permittivity SY	2.8	Calculated from capacitance measurement[S3]
Applied voltage	4 V	Measurement voltage
Trap site density shallow electrons	1×10^{17} $1/cm^3$	
Added deep trap site density	1×10^{17} $1/cm^3$	Adopted from reference[S1]
Electron trap depth	0.4 eV	
Hole trap depth	0.6 eV	Adopted from reference[S2]
Hole trap density	1×10^{15} $1/cm3$	From reference[S4], pristine device at ~10 mA/cm^2
Capture coefficients	5×10^{-13} cm^3/s	Similar to reference[S1], factor 0.5 to match timescale of measurement

The chosen mobility of holes, $\mu_h = 1*10^{-6}$ cm^2/Vs, was calculated with the Extended Gaussian Disorder model (EGDM) mobility calculation from reference.[S2] With the EGDM mobility parameter of reference[2] and our simulation result with an average field of 270 kV/cm (Figure 4.1c) and an average hole density of $7.8*10^{16}$ cm^{-3} (not shown), the resulting hole mobility is $1.007*10^{-6}$ cm^2/Vs. The capture coefficient calculated with the formula[S2] $Cp = \left(\frac{q}{\varepsilon_0 \varepsilon_r}\right)\mu_p = \frac{1.602*10^{-19}C}{2.8* 8.854*10^{-12}\frac{F}{m}} * 1.007 * 10^{-10}\frac{m^2}{Vs} = 6.5 * 10^{-19}\frac{m^3}{s} = 6.5 * 10^{-13}\frac{cm^3}{s}$ is then in agreement with our fitted capture coefficients. Note that the hole capture coefficient has no impact via hole trapping since the hole trap influence is negligible for the pristine simulation, it does have a strong impact via SRH recombination of free holes with trapped electrons.

The calculated EGDM mobility with an average electron density of $5.2*10^{16}$ cm^{-3} (Figure 4.1c, main text) results in $\mu_e = 0.8*10^{-6}$ cm^2/Vs. A simulation as in Figure 4.1b, main text, with this mobility parameter results in no current drop and a much less pronounced emission peak. This is because in the simulation the free electron density for almost equal hole and electron mobility values is too low. Because of this, few electrons are trapped, and SRH recombination of free holes with trapped electrons decreases the number of trapped electrons further. For equal mobilities, the electron-hole profile is shifted towards the cathode. In this case, the SRH recombination has a peak of $1.6*10^{21}$ cm^{-3} s^{-1} at 65 nm with a full width half maximum (FWHM) of 45 nm (not shown). When choosing a higher electron mobility of $3*10^{-6}$ cm^2/Vs, the recombination profile peaks at 45 nm with a FWHM of 60 nm, and the peak reduces to $1.3*10^{21}$ cm^{-3} s^{-1} (Supporting Information Figure S4.4). Essentially, via a decreased SRH recombination the density of trapped electrons increases, which allows simulating the experimental transients from Figure 4.1a, main text.
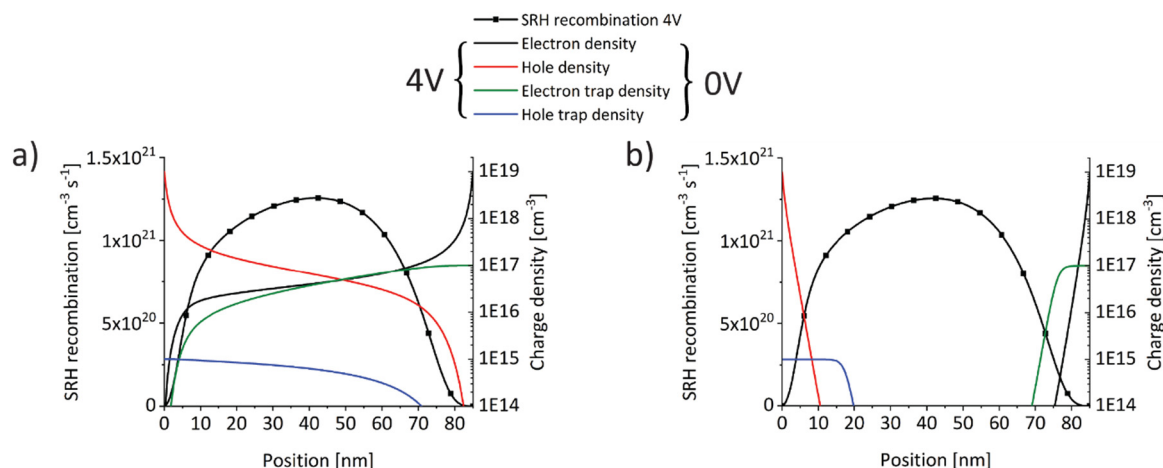
Figure S4.4. For all transients in Figure 4.1 and Figure 4.2 of the main text where a mean value was calculated across the active layer (electric field, trap density, electron density), the border regions 10 nm close to each electrode were not considered since they do not contribute to the essential physics of the charges that recombine within the device. This is apparent when looking at the SRH recombination close to the electrodes in a), which is low because the opposite charge density is negligibly low. While the traps that contribute to SRH recombination disappear mostly at 0 V, some traps remain within the device due to space charge at the interface and the non-existent amount of opposite charge, which leads to a filling of traps 10 nm next to the electrodes (b). As an example, if the whole layer would be taken to calculate the average of remaining electron traps in b), the fraction of remaining traps to the trap site density would be 10% instead of 0.5%, distorting the analysis to some extent.

Optical model parameters

For the optical simulations of PLEDs we used the n- and k-values of each layer. SY data were taken from reference[S6], data for aluminium, PEDOT:PSS and Ca were taken from the Setfos software database, originally from H.C. Starck, J.A. Woollam and unknown source, respectively. Additionally, a measured SY photoluminescence spectrum was used. For the simulations in Figure 4.1, main text, and Figure 4.2, main text, the electrically calculated recombination profile was coupled to the optical model including a triplet exciton loss of 75%. In addition to the triplet exciton loss, a PL quantum efficiency of 68.3% was taken into account.[S7] An anisotropy factor of 0.07 (nearly parallel emissive dipoles) was used as determined for SY.[S8] The emission was simulated for an observer angle of 0° (vertical emission) since the luminance setup also measures at a 0° angle.

Supporting Information Note 2

Trap density rate equation in the on state

The time dependence for the trapped electrons $\frac{dn_t}{dt}$ is given by the competition between trap filling and de-trapping processes, including emission and recombination. In equation S4.1, $R_{fill} = C_n * n(N_t - n_t)$ with the free electron density n that gets trapped with an electron capture coefficient C_n by the remaining free electron trap sites $(N_t - n_t)$. N_t is the trap site density and n_t the trapped electron density. The Shockley-Read-Hall (SRH) recombination is $R_{SRH} = C_p * p * n_t$, with the free hole density p recombining with the trapped electron density n_t with a hole capture coefficient C_p. In addition, the term for the emission of trapped electrons back to the conduction band is added. The emission coefficient e_n is small for trap depths of several 100 meV, but is relevant for shallow traps.

$$\frac{dn_t}{dt} = C_n * n(N_t - n_t) - e_n * n_t - C_p * p * n_t \qquad \text{(S4.1)}$$

By rearranging equation S4.1 to

$$\frac{dn_t}{dt} = C_n * n * N_t + n_t * \left(-C_n * n - e_n - C_p * p\right), \qquad \text{(S4.2)}$$

we get the form $\frac{dn_t}{dt} = a + n_t * (-b)$, where $a = C_n * n * N_t$ and $b = C_n * n + e_n + C_p * p$. The solution to this differential equation is

$$n_t(t) = \left(n_0 - \frac{a}{b}\right) * e^{-b*t} + \frac{a}{b} = \frac{a}{b} * (1 - e^{-b*t}), \qquad \text{(S4.3)}$$

where we used the condition $n_t(0) = n_0 = 0$, which means that traps are not filled at switch-on, i.e. all traps were emptied during the break at short circuit.
First we focus on the steady-state situation at $t \to \infty$,

$$n_t = \frac{C_n n * N_t}{C_n n + e_n + C_p p} \to \frac{n_t}{N_t} = \frac{C_n n}{C_n n + e_n + C_p p}. \qquad \text{(S4.4)}$$

It means that in equilibrium the ratio of trapped electrons to trapping sites n_t/N_t depends on the term $\frac{C_n n}{C_n n + e_n + C_p p}$. In the case of deep traps of several 100 meV, the emission coefficient e_n is very small and can be neglected due to its negative exponential dependency on the trap depth, such that the final equilibrated trap density depends only on the terms $C_p p$ from SRH recombination and $C_n n$ coming from trap filling. In the case $C_n n = C_p p$, equation S4.4 becomes $\frac{n_t}{N_t} = \frac{1}{2}$, which means half of the traps are filled in equilibrium. If $C_n n \gg C_p p$, which means SHR recombination is much slower than trap filling, equation S4.4 results in $\frac{n_t}{N_t} = 1$, since all traps will finally be filled.

On the other hand, $C_n n \ll C_p p$ leads to $\frac{n_t}{N_t} = 0$ because a very strong SRH recombination empties a trap instantly after filling. This analysis essentially means that the equilibrated amount of filled traps only depends on the relative strength of SHR recombination to trap filling, not on the absolute rates of these processes. The same conclusion is derived if we consider shallow traps where the emission coefficient is not negligible.

We evaluate the time until equilibrium is reached. If we consider again equation S4.3, we find the time constant to be $\frac{1}{b} = \frac{1}{C_n*n+e_n+C_p*p}$. At $t = \frac{1}{b}$, $n(t) = \frac{a}{b}(1 - e^{-1}) = 0.63 * \frac{a}{b}$, which means that at the time $\frac{1}{b}$, 63% of the traps of the steady-state ratio are already filled. It shows that the fastest process dominates the time constant. Capture coefficients are in the range from $10^{-12} \frac{cm^3}{s}$ [S3] to $10^{-14} \frac{cm^3}{s}$ [S1]. For a capture coefficient $5*10^{-13} \frac{cm^3}{s}$ and a free electron density of $5 * 10^{16} \, cm^{-3}$ as in the simulation, the time constant $\frac{1}{C_n*n}$ is 40 μs, and even smaller if the other processes ($e_n, C_p p$) are considered as well.

Trap density rate equation in the off state

A similar situation occurs for a PLED and an electron-only device at switch-off. In both cases there is no fast trap emptying process, because the free hole density p gets many orders of magnitude smaller at 0 V and SRH recombination is negligible. The same is true for the free electron density n, and the rate equation simplifies to

$$\frac{dn_t}{dt} = C_n * n(N_t - n_t) - e_n * n_t - C_p * p * n_t = -e_n * n_t \qquad (S4.5)$$

In this case, traps empty at the rate e_n, which depends on the electron capture rate C_n, the density of free electron states $N_{0,N}$ and the trap depth as

$$e_n = C_n * N_{0,N} * \exp(\frac{E_t - LUMO}{kT}) \qquad (S4.6)$$

$N_{0,N} = 1 * 10^{27} m^{-3}$, which is a result of one state per cubic nm[1], and the capture coefficient is $C_n = 5 * 10^{-13} \frac{cm^3}{s}$, which fits the time scale of the measurement as shown in Figure 4.1, main text. From Figure 4.2e, main text, we know that the shallow traps fully de-trap within 100 ms, and we know that de-trapping related effects become visible for break times of 650 μs or higher. This restrains the trap depth $E_t - LUMO$ to roughly 0.4 eV, which leads to a time constant of $\frac{1}{e_n} = 10 \, ms$ according to equation S4.6, such that $n_t(650\mu s) = N_0 e^{-\frac{650\mu s}{10ms}} = 0.94 * N_0$, i.e. de-trapping has just started, and $n_t(100 \, ms) = N_0 e^{-\frac{100ms}{10ms}} = 5 * 10^{-5} * N_0$, i.e. the traps are de-trapped to an unnoticeable level. Changing the trap depth by only 0.05 eV results in a time constant shift by a factor of 10, such that the resulting de-trapping dynamics does not agree with the established time range. At 0.45 eV, there are still 40% of the traps present after 100 ms, and

at 0.35 eV there are already 8% of the traps de-trapped after 80 μs, where we do not see any effect in the measurement.

Supporting Information Note 3

Effects of temperature, ionic impurities and dipole relaxation
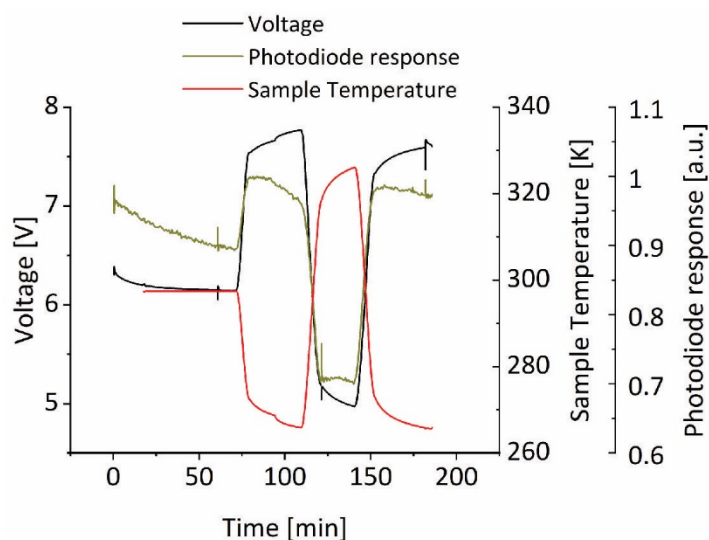
Figure S4.5. Investigation of temperature on transient device response. When the bias is switched off, the power is zero and the device temperature relaxes to room temperature. At switch-on, the electric power heats up the sample until steady state of heat loss and electric heating is reached. A changing temperature influences, for example, the charge mobility and the photoluminescence quantum efficiency. However, we exclude temperature as the cause for the transient overshoot effects for the following reasons.

The impact of a temperature change on the voltage and photodiode response was measured during biasing a PLED at 7.7 mA cm^{-2}. When decreasing the temperature after 70 minutes from 24 °C to -7 °C, the voltage and emitted light increase simultaneously. The increase of voltage can be explained by a decrease in charge mobility, an increase of emitted light at lower temperatures was related to a decreasing rate of exciton migration to non-emissive quenching sites.[S9] When the temperature was increased at minute 110 from -7 °C to 53 °C, the opposite effect occurred. While a decrease of emitted light would be consistent with an increase of temperature when switching on the device, the decrease of voltage is not. In the PLED, the voltage increased after switch-on.

It has also been shown for a similar device architecture that the absolute temperature increase for a current density of 10 mA cm^{-2} and at 3.5 V was only around 2 °C.[S10] The large temperature change of 60 °C in the Supporting Information Figure S4.5 resulted in a change of emission of roughly 30%. This indicates that an emission overshoot of 5 - 15% (Supporting Information Figure S4.2) can hardly be explained by a small temperature increase of only 2 °C.
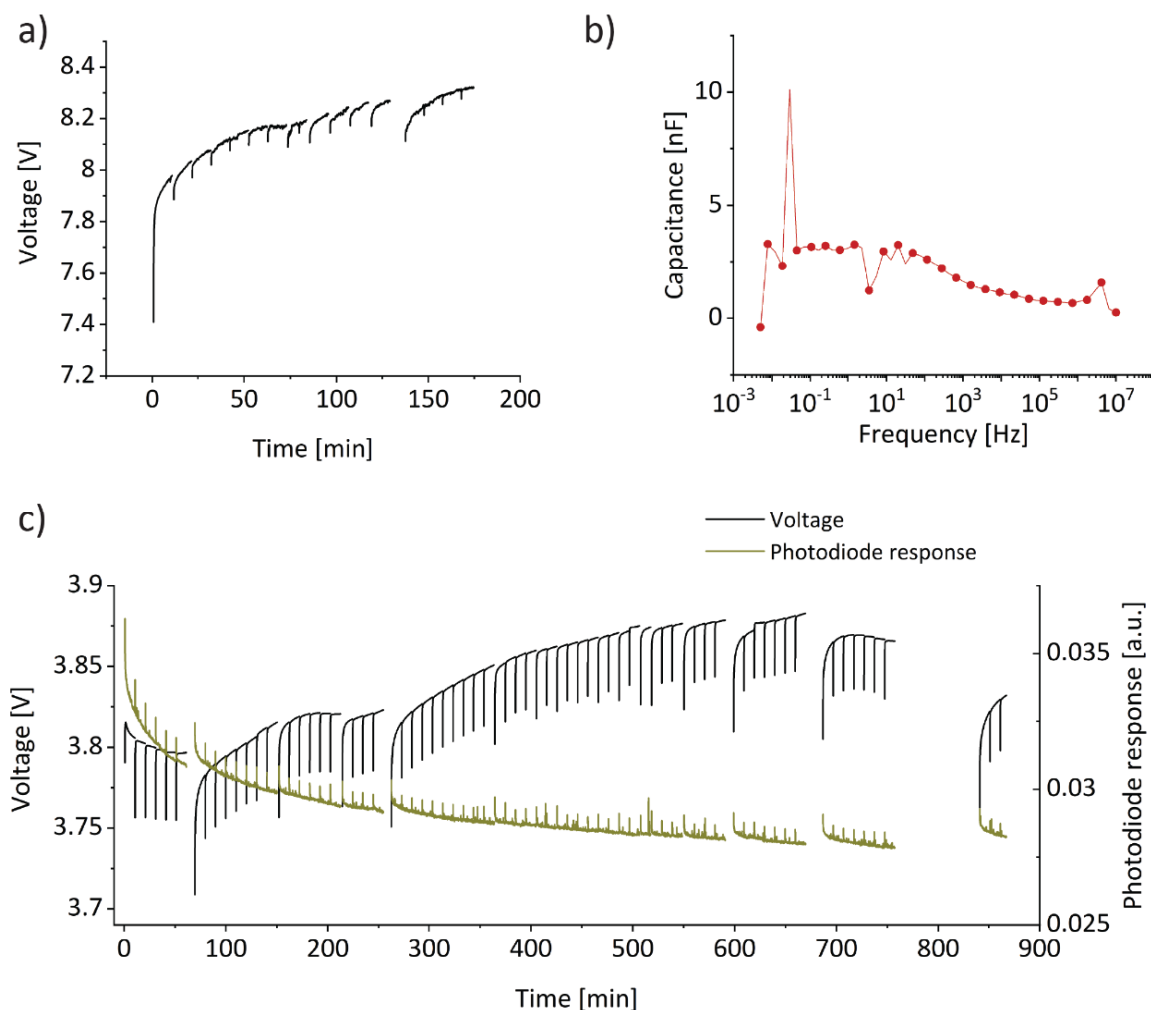
Figure S4.6. Discussion of effects of ionic impurities and dipole relaxation on transient device response. a) When replacing PEDOT:PSS with TPD in the PLED, similar voltage undershoots are observed. b) Electrochemical impedance measurement down to 5 mHz with the intention to detect ionic impurities via the formation of electronic double layers in the PLED. c) Transient voltage and light emission measurements on a PLED with SY coated from toluene. Trends are similar to devices with SY coated from THF.

It is known that PEDOT:PSS etches the ITO substrate and liberates indium ions.[S11] We exclude this source of ionic impurity because we observe similar voltage undershoots when PEDOT:PSS is replaced by N,N'-Bis(3-methylphenyl)-N,N'-diphenylbenzidine, TPD (a). From the impedance measurements on PLEDs shown in b), we do not observe a 100-1000 fold increase of the capacitance, as expected when electronic double layers would form due to ionic impurities. For SY light-emitting electrochemical cells (PLECs) – a device where ions are added intentionally – we observed that ion relaxation at short circuit results in a hindered charge injection at switch-on and the initial required voltage to drive a constant current is increased (SY-PLEC results will be presented in detail elsewhere). An ionic impurity in SY would result in a similar voltage overshoot in PLEDs, which we do not observe. Finally, to explain our voltage-light pulse results, ionic impurities must absorb light in the near-infrared wavelength region, which we do not expect.

We exclude effects due to dipolar reorientation[S12] of polymer repeating units when the electric field changes direction because of the small dipole moment of SY, the slow experimental recovery timescale and because measurements were carried out below the glass transition temperature of SY (T_g ~80 °C[S13]). In reference [S14], the polar solvent dimethylformamide was coated on the emissive layer of SY PLEDs, which resulted in a reduction of the electron-injection barrier. We fabricated PLEDs using the solvent toluene, which has a dipole moment that is around five times smaller than the dipole moment of THF. The drive voltage for toluene-based PLEDs is 30%[S15] lower but the observed overshoot effects are in a similar range for both solvents (c). Therefore, we exclude dipolar effects due to residual solvent in our case.

Supporting Information Note 4

Electron de-trapping by light

Additional illumination experiments are summarized in the Supporting Information Figure S4.7. Similar transients as shown in Figure 4.3 (main text) occur for irradiation wavelengths ranging from 740 nm to 1020 nm. We used the same photon flux at each wavelength, indicating that the trap absorption profile is rather flat between around 650 to 1000 nm. Finally, the luminance increased and the voltage decreased when a constant current-driven (77 mA cm^{-2}) PLED was simultaneously irradiated with light from a laser at 850 nm (data not shown).
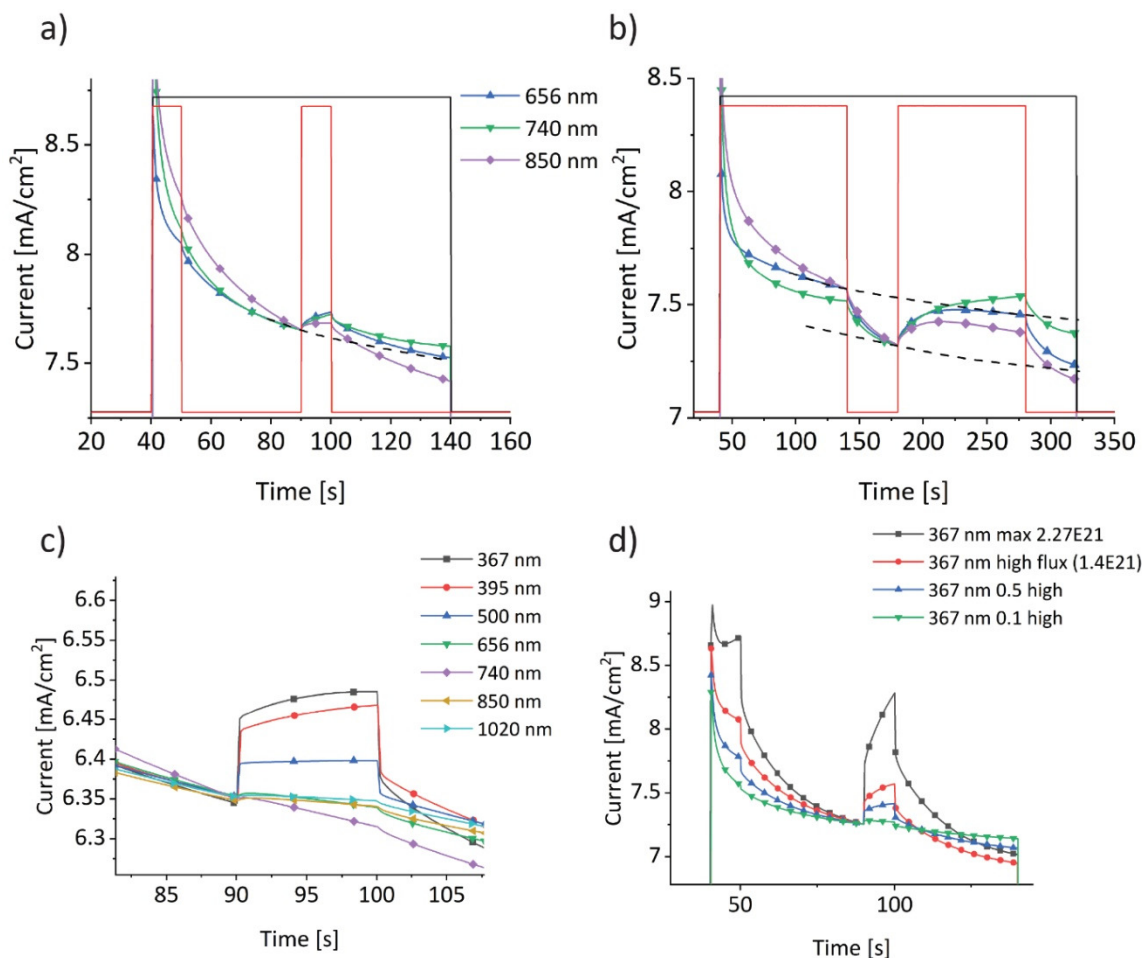
Figure S4.7. a) and b) show the same experiment as Figure 4.3 (main text), including additional measurements with LED wavelengths of 740 nm and 850 nm, all at a photon flux of $1.4 * 10^{21} \frac{1}{s*m2}$. c) shows measurements at a lower photon flux of $4.5 * 10^{20} \frac{1}{s*m2}$ to include weaker LEDs up to 1020 nm. d) shows measurements with different photon fluxes. Note that LEDs with wavelengths below 656 nm (367, 395 and 500 nm) irradiate in the absorption band of SY. The instant increase of current in these cases is likely due to a heating effect because of the absorbed light, resulting in a charge mobility increase. When reducing the light intensity at 367 nm sufficiently (d) the temperature increase is low and the prompt current increase disappears. There is also no prompt current increase observable for LED pulses with wavelengths beyond the SY absorption band, since the absorption is much smaller. We cannot decide whether light with wavelengths below 656 nm liberates trapped charge directly, or if the strong subsequent photoluminescence between around 500 nm and 700 nm is absorbed by the traps. We also note that the intrinsic PLED EL of, e.g. 500 cd m^{-2}, amounts to only ~2.5% of the LED photon flux in c) at 656 nm. Looking at the current trend for 656 nm irradiation in c), the current increase was ~0.9% only. Therefore, the intrinsic EL of an operated SY PLED results in a negligible current increase, on the order of 0.9% x 2.5% = 0.023%.
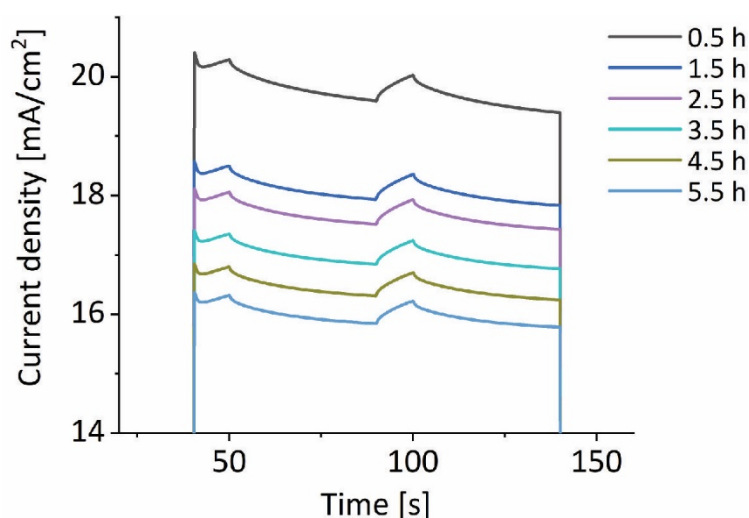
Figure S4.8. The same device response over 5.5 hours was observed for a constant current-driven device when applying the voltage-light pulse sequence described in Figure 4.3, main text, after every 30 minutes.

Supporting Information Note 5
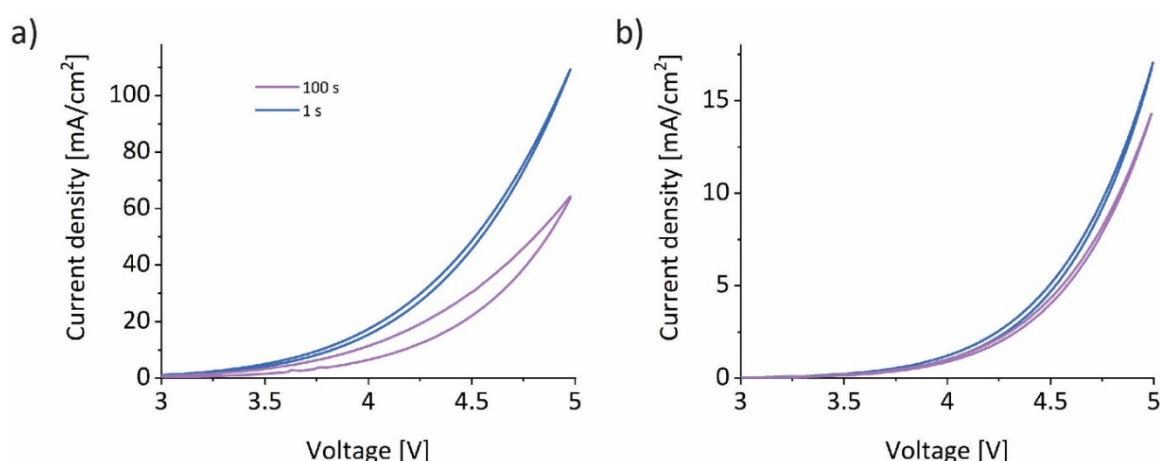
Figure S4.9. Current-voltage characteristics for a) a pristine electron-only device and b) after 30 minutes of operation. The voltage was scanned from 0 V to 5 V and back with a scan rate of 10 V s^{-1} and 0.1 V s^{-1}, respectively. The device was rested for ~2 s after 30 min operation before the voltage scan was applied.

Charge traps can also be characterized with hysteresis measurements, i.e. forward and backward current-voltage scans. The idea of the experiment is that if charge trapping is faster than de-trapping, traps fill up continuously during the scan. Therefore, the device situation for the two scan directions is not the same, resulting in a hysteresis.

We performed hysteresis measurements on a) a pristine electron-only device and b) after operation. After operation of 30 minutes, deep electron traps have largely developed, which explains why the overall current level is substantially lower. By varying the scan speed, we can

track the activation of intermediate and deep traps. During the scan time of 1 s intermediate traps are continuously activated. Therefore, more filled traps are present during the back-scan and the current is lower, explaining the hysteresis. The hysteresis is similar for the pristine and the aged device, because intermediate traps site deactivate partially during the rest period before the voltage scan.

We also performed voltage scans with a low scan rate of 0.1 V s^{-1}. For the pristine device, deep traps develop during the scan time of 100 s. Again, the amount of traps increases continuously and hysteresis occurs. However, after operation the hysteresis for the low scan rate almost disappears. This is because during operation, deep traps have developed completely and the system reaches equilibrium quickly when the scan starts.

Note that with hysteresis measurements as just described we cannot track the shallow traps. For these traps, trap filling is completed on a timescale of 200 μs. Therefore, when the scans starts and above the bandgap voltage, shallow traps fill up almost instantaneously and there is no difference in device situation during the up-scan and back-scan. Hysteresis induced by shallow traps would require a scan rate of 10^5 V s^{-1} or more.
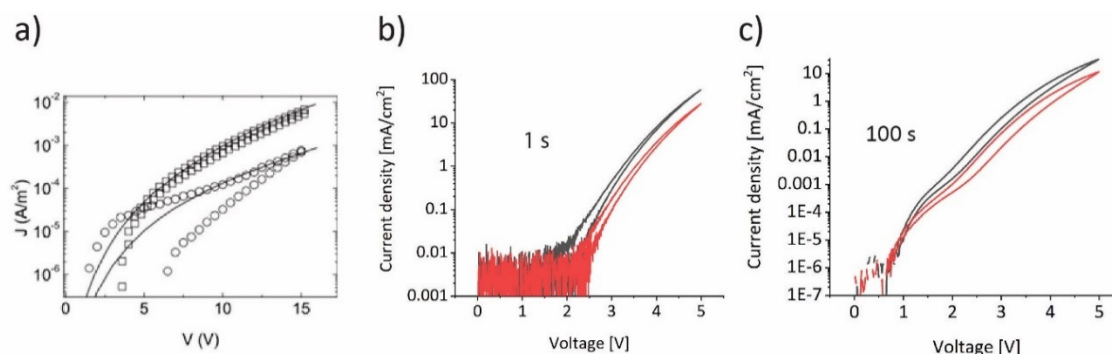
Figure S4.10. J-V hysteresis measurement of purified and unpurified polymer devices.

Figure S4.10a was taken from reference [S16]. Shown are J-V characteristics of an electron-only device of the purified MEH-PPV (a poly(p-phenylene vinylene) derivative similar to SY) with a thickness of 300 nm (squares) and an electron-only device not purified (circles). After purification the hysteresis has completely disappeared. Polymer purification in reference [S16] was carried out by subsequent precipitations. It was suggested that by removing the lower molecular weight polymers and oligomers, a large fraction of carbonyl containing end-groups is removed that can possibly act as deep electron-accepting traps. We adapted the method and purified SY as follows: 40 mg polymer were dissolved in 8 mL dry CHCl$_3$ and the solution was stirred at 60 °C for 3 days. The solution was filtered with a preheated glass frit and the precipitate was washed with 2 mL CHCl$_3$ at 60 °C. The filtrate was let to cool down and CHCl$_3$ was added to a total volume of 10 mL. 4 mL of dry methanol was added and the precipitate (fraction 1) was removed by centrifuging (8000 rpm, 20 min). To the remaining solution another 4 mL of dry methanol was added and the precipitate (fraction 2) was again centrifuged for 20 minutes. The precipitated fractions were dried in an argon stream, dispersed in acetone, filtered off and dried at 50 °C in high vacuum. GPC data of the high (1) and low (2) molecular fractions are shown in the Supporting Information Figure S4.11.

Electron-only devices coated from toluene were fabricated with the purified polymer fraction 2 and hysteresis measurements were carried out (Supporting Information Figure S4.10b and c). Hysteresis occurs, as explained in the Supporting Information Figure S4.9, but the effects are identical for the unpurified and purified material. Therefore, the chemical nature of the intermediate and deep traps in our SY does not originate from polymer carbonyl containing end groups or impurities that are soluble in chloroform. The current for the purified device is lower, which indicates that purification affects the charge transport to some extent. Indeed, the low molecular polymer fraction seems to affect the film morphology quite strongly, and we observed for electron-only devices with purified SY coated from THF two orders of magnitude smaller currents.
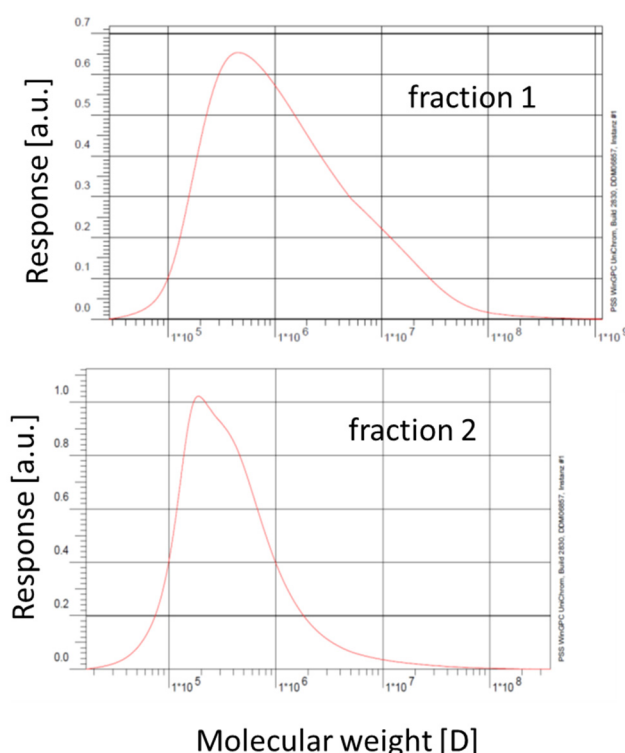
Figure S4.11. Gel permeation chromatograms of the high- and low-molecular soluble fractions of purified SY. Before precipitation to obtain fraction 1 and 2, an insoluble gel-like polymer fraction was removed by filtration.

References

[S1]   M. Kuik, G.-J. A. H. Wetzelaer, H. T. Nicolai, N. I. Craciun, D. M. De Leeuw, P. W. M. Blom, *Adv. Mater.* **2014**, 26, 512.

[S2]   Q. Niu, G.-J. A. H.Wetzelaer, P. W. M. Blom, N. I. Crăciun, *Adv. Electron. Mater.* **2016**, 2, 1600103.

[S3]   M. Diethelm, A. Schiller, M. Kawecki, A. Devižis, B. Blülle, S. Jenatsch, E. Knapp, Q. Grossmann, B. Ruhstaller, F. Nüesch, R. Hany, *Adv. Funct. Mater.* **2020**, *30*, 1906803.

[S4]   Q. Niu, R. Rohloff, G.-J. A. H. Wetzelaer, P. W. M. Blom, N. I. Crăciun, *Nat. Mater.* **2018**, 17, 557.

[S5]   S. Stolz, M. Petzoldt, S. Dück, M. Sendner, U. H. F. Bunz, U. Lemmer, M. Hamburger, G. Hernandez-Sosa. *ACS Appl. Mater. Interfaces* **2016**, 8, 12959.

[S6]   T. Lanz, E. M. Lindh, L. *J. Edman, Mater. Chem. C.* **2017**, 5, 4706.

[S7]   S. D. Yambem, M. Ullah, K. Tandy, P. L. Burn, E. B. Namdas, *Laser Photonics Rev.* **2014**, 8, 165.

[S8]   Y. Li, B. Van der Zee, G. A. H. Wetzelaer, P. W. M. Blom, *Adv. Electron. Mater.* **2021**, 7, 2100155.

[S9]   E. W. Snedden, L. A. Cury, K. N. Bourdakos, A. P. Monkman, *Chem. Phys. Lett.* **2010**, 490, 76.

[S10]   J. Ràfols-Ribé, N. D. Robinson, C. Larsen, S. Tang, M. Top, A. Sandström, L. Edman, *Adv. Funct. Mater.* **2020**, 30, 1908649.

[S11]   M. P. de Jong, L. J. van IJzendoorn, M. J. A. de Voigt, *Appl. Phys. Lett*. **2000**, 77, 2255.

[S12]   T. Yamada, D. Zou, H. Jeong, Y. Akaki, T. Tsutsui, *Synth. Met*. **2000**, 111–112, 237.

[S13]   S. Burns, J. MacLeod, T. Trang Do, P. Sonar, S. D. Yambem, *Sci. Rep.* **2017**, 7, 40805.

[S14]   Q. Niu, H. Wu, W. Huang, J. Tong, F. Ye, Y. Zhang, W. Zeng, R. Xia, Y. Min, *ACS Appl. Mater. Interfaces* **2017**, 9, 18399.

[S15]   K. Strassel, S. P. Ramanandan, S. Abdolhosseinzadeh, M. Diethelm, F. Nüesch, R. Hany, *ACS Appl. Mater. Interfaces* **2019**, 11, 23428.

[S16]   N. I. Craciun, Y. Zhang, A. Palmaerts, H. T. Nicolai, M. Kuik, R. J. P. Kist, G. A. H. Wetzelaer, J. Wildeman, J. Vandenbergh, L. Lutsen, D. Vanderzande, P. W. M. Blom, *J. Appl. Phys*. **2010**, 107, 124504.

Chapter 5 Unravelling Trap and Ion Dynamics in LECs

Identification of Electron and Hole Traps in Polymer Light-Emitting Electrochemical Cells

Matthias Diethelm[1,2], Andrius Devižis[3], Wei-Hsu Hu[1,2], Tao Zhang[1,2], Camilla Vael[2,5], Roman Furrer[4], Sandra Jenatsch[5], Frank Nüesch[1,2], and Roland Hany[1]

[1]Empa, Swiss Federal Laboratories for Materials Science and Technology, Laboratory for Functional Polymers, 8600 Dübendorf, Switzerland

[2]EPFL, Institute of Materials Science and Engineering, Ecole Polytechnique Fédérale de Lausanne, Station 12, 1015 Lausanne, Switzerland

[3]State Research Institute Center for Physical Sciences and Technology, Saulėtekio av. 3, LT-10257 Vilnius, Lithuania.

[4]Empa, Swiss Federal Laboratories for Materials Science and Technology, Transport at Nanoscale Interfaces, 8600 Dübendorf, Switzerland

[5]Fluxim AG, Katharina-Sulzer-Platz 2, 8400 Winterthur, Switzerland

Declaration of Contribution

M.D. fabricated devices, performed optoelectronic measurements, did the optical and electrical simulation including all related input data measurements, analysed the data and prepared the manuscript.

Abstract

Polymer light-emitting electrochemical cells (PLECs) and polymer light-emitting diodes (PLEDs) are receiving interest for large-area lighting and display applications. During operation of a PLEC, a p-i-n junction develops where electrons and holes are injected from the electrodes into the film and are transported along the n- and p-doped regions to the intrinsic (i) region, where they recombine and light is emitted. Conceptually, this resembles the device architecture of a PLED equipped with Ohmic charge-injection and transport layers. The similarity between the intrinsic region of the PLEC and the emissive layer of the PLED is obvious; however, implication of this has not been examined in detail so far. For example, for PLEDs it is well reputed that electron transport is seriously hindered by the presence of electron traps, and that hole trap formation dictates the long term device stability. Here, we study for PLECs the electrical and optical response to electrical driving and breaks, probe the current response to external light irradiation, and follow device degradation during operation with long term absorptions and capacitance measurements. We demonstrate the presence of electron traps in PLECs and find that hole trap formation limits the device lifetime, in the exact same manner as firmly established for PLEDs. Our conclusion is that

hole trap formation presents an important, but so far overlooked polymer-intrinsic degradation mechanism for PLECs.

5.1 Introduction

Polymer light-emitting electrochemical cells (PLECs) are one of the simplest electroluminescent devices and consist of a single solution-processed emissive polymer layer that contains an electrolyte, sandwiched between two air-stable electrodes.[1-7] When a bias is applied, the ions redistribute and the homogeneous polymer film divides into five sublayers with specific functions.[8] First, the ions form electronic double layers (EDLs) at both electrodes that facilitates charge injection. Subsequently, reduced and oxidized polymer repeating units are electrostatically stabilized by opposite ionic charges, resulting in conductive p- and n-doped regions at the anode and cathode, respectively, which grow inside the film. Over time, a p-i-n junction develops where holes and electrons are injected from the electrodes into the film and travel along the doped regions to the intrinsic (i) zone, where they recombine under the emission of light. The PLEC turn-on dynamics is dictated by the mobility of the ions,[8,9] and the time scale until ions are in equilibrium ranges from seconds to many hours.[3,9,10] A second timescale to consider is the relaxation time of the ions back to equilibrium when an operated PLEC in steady state is turned off. This time usually is even longer than the turn-on time and can reach up to several days.[9]

The "EDL-p-i-n-EDL" build-up of an operated PLEC strongly resembles the multilayer architecture of an organic light-emitting diode (OLED). For example, the functionality of charge-injection and –transport layers in the OLED are identified with the role the EDLs and doped regions play in the PLEC. Therefore, despite the different device architecture and dynamic turn-on behaviour, the mode of operation of PLEDs and PLECs – after steady state is reached - is quite comparable (Figure S5.1, Supporting Information).

We focus on the similarity between the emissive layers of a PLED and a PLEC, as the PLEC i-region is also void of ions and the place where excitons form and light emission occurs. We argue that a physical characteristic pertinent to the emissive polymer in a PLED can also be detected in a PLEC. Specifically, it is known that the efficiency and lifetime of PLEDs is seriously limited by the presence of traps for electrons and holes.[11] Trapped charges hinder the charge transport and increase the non-radiative Shockley-Read-Hall (SRH) recombination between trapped and free charge, thereby reducing the radiative Langevin recombination. In conjugated polymers, there exists a universal electron trap density of around $1-3 \times 10^{17}$ cm^{-3}, centred at an energy of ~3.6 eV below the vacuum level.[12-15] In addition, hole traps form continuously when operating PLEDs at constant current over many hours.[16-18] Hole trap growth dictates the long-term stability of PLEDs.[19]

Recently, we examined the dynamics of electron traps in PLEDs (chapter 4,[20]) We fabricated devices using a phenyl-substituted poly(para-phenylenvinylene) copolymer termed super yellow (SY) as emitting material (Figure S5.1, Supporting Information).[21-23] We studied the device response to electrical driving and breaks. In an operated PLED traps are filled and after turning-off, deep electron traps de-trap slowly via thermal emission over many minutes. After every break, we observed an intermediate increase in device performance, and the initial light emission was higher and a lower voltage was required to drive a constant current. Subsequently, the voltage and light emission recovered back to the trend line before the break. This is because electron traps fill up again. Surprisingly, we found that also filling of these traps is very slow and device recovery

trends proceed over many minutes. Because the electron trap density is constant, the light emission and voltage response to a break do not change over time, i.e. the same rest period at different moments leads to a similar initial performance improvement and recovery trends.

Here, we first identify the same electron trap filling and de-trapping mechanism in the i-region of SY PLECs. The analysis is more complicated than for a PLED, because relaxation and reconstruction of the EDLs occurs on a similar time scale as electron trap filling and de-trapping. Therefore, electronic and optical transients in PLECs have to be analysed as a superposition of effects due to a temporary imbalance in charge injection and electron trap filling. Based on the identified similarity between PLEDs and PLECs, we then argue that during long-term operation also hole traps form in a PLEC. We derive (indirect) evidence for hole trap formation by following the decrease of the p-polaron density with absorption measurements, and the observation that the i-region slowly expands over many hours after the ionic motion has stopped. We explain this observation with the specific hole trap formation mechanism, which is based on the interaction between excitons with free holes.[19] In a PLEC, there is no physical separation between the position of exciton generation and the doped zones. Therefore, part of the excitons are quenched due to the interaction with the radical anions and cations present in the doped zones. Exciton quenching via interaction with radical cations results in hole trap formation, explaining the erosion the the p-doped region. Our conclusion is that hole trap formation represent an important polymer-intrinsic device degradation mechanism that fundamentally limits the long-term stability of PLECs.

5.2   Results

For SY PLECs with the added electrolyte trimethylolpropane ethoxylate / $Li^+CF_3SO_3^-$, we discussed recently how the ionic rearrangement during device turn-on influences the light emission trend over many hours.[9,24] At early times, the emitter position (EP) is close to the Al electrode and moves during operation over more than 30% of the active layer thickness towards the centre. For an active layer thickness of below 150 nm, this EP shift results in a steady increase of the emitted light, while for thicknesses above 200 nm a valley of poor outcoupling efficiency is crossed. Directly after switch-on, the voltage decreases quickly due to the formation of electronic double layers (EDLs) and doped regions at both electrodes. Afterwards, the voltage stays almost constant for a thin device and increases slowly for thicker active layers.

The added salt constituents play an important role on the transient device response when a PLEC is switched to short circuit and then back on to drive. First, we find that the p- and n-doping is very persistent and the necessary hold time at short circuit to equilibrate an operated thick PLEC is on the order of several days (Figure S5.2, Supporting Information). The time scale of days implies that a break of seconds to minutes does not affect the p- and n-doped regions.

Steady-state simulations in **Figure 5.1** under bias and directly after switching to short circuit indicate why the doping relaxation is slow. In the doped regions the electric field is small because the counter ions screen the field of the polarons. Although there is a large number of polarons, the net charge density is low. The built-in voltage at 0 V drops across the intrinsic region rather than across the doped regions (Figure 5.1). Although there is a large negative field in the intrinsic region, there are no ions present in this region that could relax.

On the other hand, the EDLs are regions with high electric fields and large ion density gradients. The former lead to high ion drift currents, the later to strong ion diffusion currents. These currents are in opposite directions and cancel each other in steady state at 3 V. When switching to 0 V, the ionic charge density does not change instantaneously, which means the diffusion current remains the same. However, the potential drop is reversed due to the built-in field, which reduces the field in the EDLs. This leads to a net ion current as indicated in Figure 5.1a.

We simulated the EDL relaxation over time by integrating the first 2 nm of the ion density at both electrodes after switching to 0 V (Figure 5.1c). In order to explain the measured colour change of a thick PLEC over time, we reasoned previously that the mobility of the anions must be lower than the cation mobility.[9] Therefore, the cations at the Al electrode relax faster than the anions at the ITO electrode. This has the consequence that at switch-on the injection of electrons at the cathode is lower than the injection of holes at the anode. This results in a temporary shift of the EP towards the Al electrode, as indicated in the schematic of Figure 5.1c. When the EDLs recover, charge injection balances and the EP moves back in direction of the ITO electrode to the position where it was before the break.
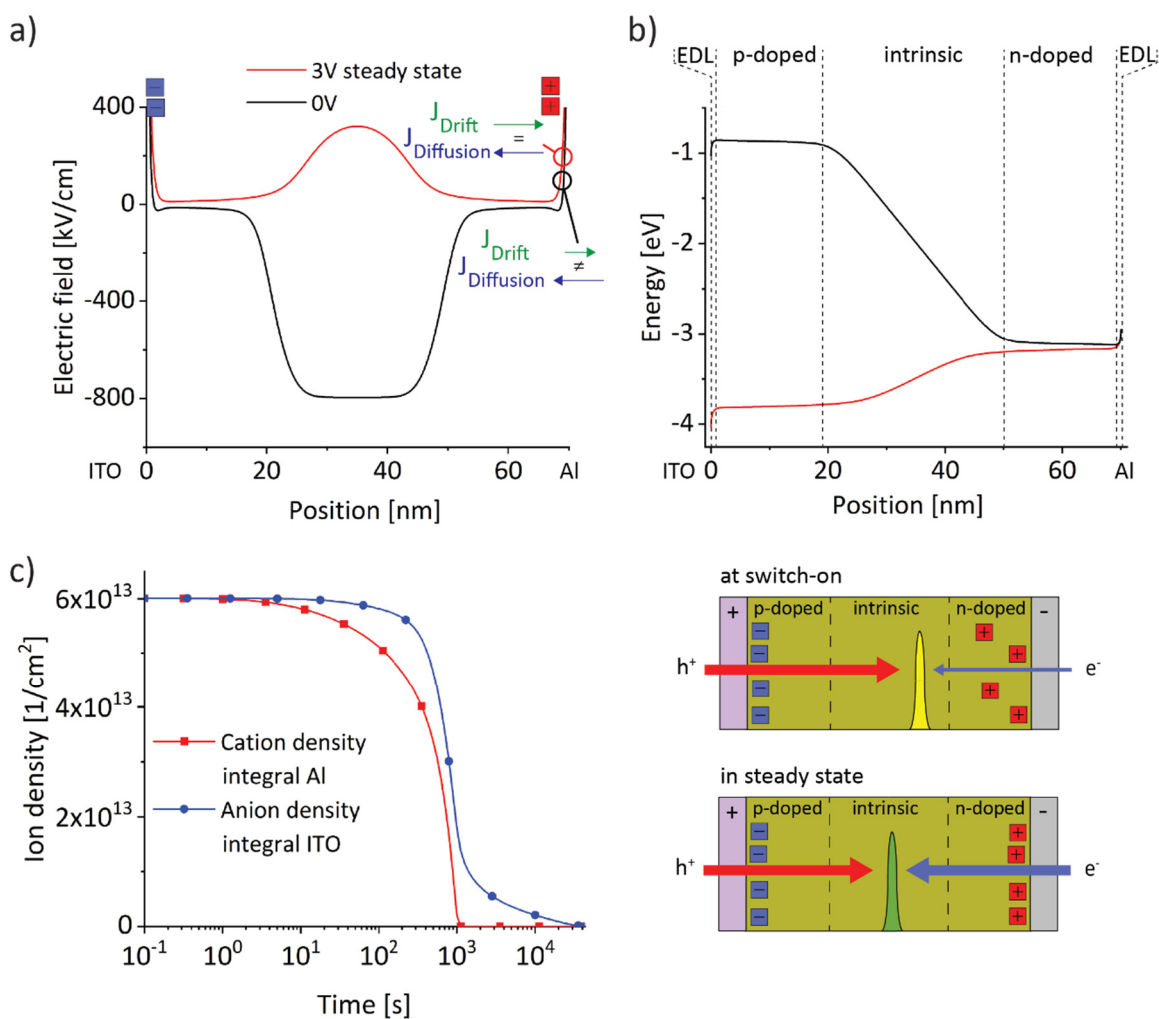
Figure 5.1. Drift-diffusion simulations on PLECs. a) Electric field and b) bending of the lowest unoccupied molecular orbital in the steady state for a biased device (red) and immediately after 0 V is applied (black). The dynamic evolution of the EDLs is shown in c) by integrating the first 2 nm near the electrodes at different points in time after switching to short circuit. Since the cations are more mobile than the anions, the relaxation at the Al electrode is faster. The schematic in c) illustrates that directly after switch-on the EP is situated closer to the cathode and shifts towards the anode when the EDLs recover. Simulation parameters were adapted from reference [9].
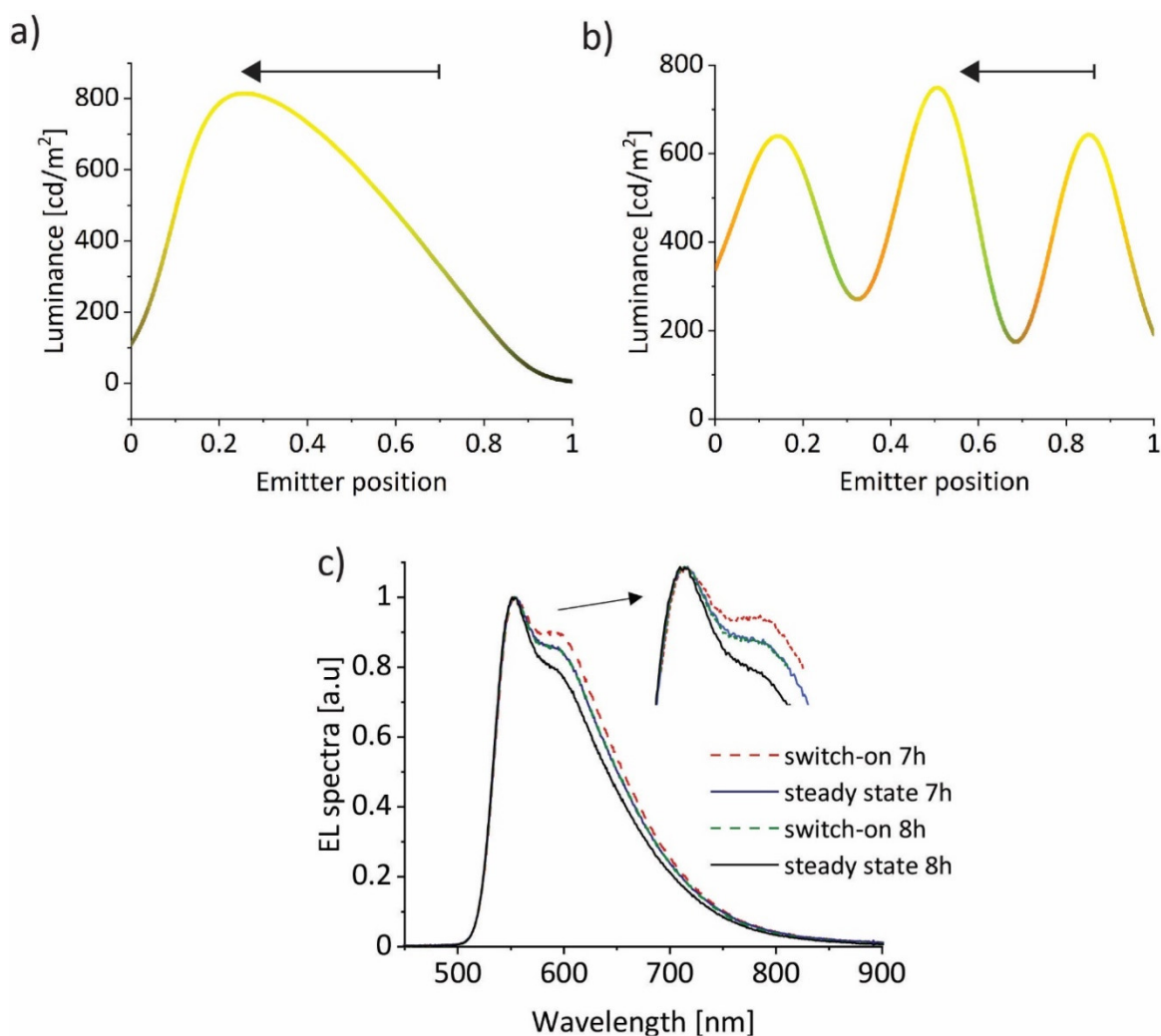
Figure 5.2. Optical simulations on PLECs. Luminance vs. emitter position for a) a 70 nm thick SY layer and b) a 430 nm thick SY layer. In both cases, a constant current of 7.7 mA cm^{-2} was assumed. Emitter position (EP) = 1 indicates the Al electrode, emitter position = 0 is the ITO electrode. The line colour represents the spectra at the given EP. Long term EP shifts during operation are indicated by arrows. c) Normalized electroluminescence (EL) spectra of a 430 nm thick PLEC directly after switch-on following a break at 0 V for 40 s, and 50 - 70 s later (close to steady state). Spectra at switch-on were more intense than the respective steady-state spectra by +12% at 7 h, and by +16% at 8 h. The actual colour of the emitted light after 7 h and 8 h operation was red.

A small shift of the EP can result in a large change of the outcoupling efficiency, i.e. that part of emitted photons that actually leave the device.[25,26] In **Figure 5.2**a, the luminance as function of the EP is simulated for a 70 nm thick device. Due to interference of the emitted with the reflected electromagnetic wave at the Al electrode, the luminance increases strongly when the EP shifts from the cathode to the anode with a peak luminance at around EP = 0.25.[27] The simulation in Figure 5.2b shows that an even more informative, undulating luminance pattern with changing emission colours occurs for the 430 nm thick device.

By fitting measured EL spectra to an optical model, it is possible to track the position of the EP.[9,25] Note that for thin devices the colour change is too small to determine the EP shift reliably. Figure 5.2c shows experimental EL spectra from a thick device taken after driving for 7 h and 8 h. After a break of 40 s, a first EL spectrum was measured immediately after switch-on, and a second spectrum when steady state was reached. The first spectrum after 8 h driving perfectly overlaps with the steady-state spectrum after 7 h. This means that during relaxation at 8 h the EP moved back to where it was in steady state after 7 h. We found before that 1 h of driving results in an EP shift of around 1% of the active layer thickness,[9] which translates into an emission intensity change of 15 – 20% (Figure 5.2b). Figure S5.3, Supporting Information, summarizes additional EL spectra for different driving times after relaxation and recovery. Data consistently confirm that the EP shifts from the Al electrode towards ITO after a break at 0 V.

Figure 5.3a and Figure 5.3b show long-term voltage and light emission trends for thick and thin PLECs, respectively. After every hour, the current bias was paused and the device switched to short circuit for 40 s. The voltage overshoots after every switch-on and recovers back to the trend line. We ascribe this to the relaxation of the EDLs during rest at short circuit, which deteriorates the initial charge injection and a higher voltage is required to drive a constant current until the EDLs have established again.

Also the light emission from the thick device (Figure 5.3a) overshoots at switch-on, but the magnitude is not constant over time, despite a steady break time. The light emission from the thin device (Figure 5.3b) starts first at lower values and changes to positive emission spikes shortly before steady state where the emitted light reaches a plateau.

Figure 5.3a and Figure 5.3b include magnifications of the transients after an operation time of 7 h. While for the thick device the light decay appears monotonic, the transient for the thin device shows an oscillatory behaviour, it starts below the trend line but then overshoots before approaching steady state. We interpret this behaviour is the result of superimposing effects due to EDL reconstruction and electron trap filling. Both effects influence the luminance at switch-on differently and have a slightly different time constant, which we disentangle in the following.

First, EDLs relax during the break at 0 V and this results in a shift of the initial EP at switch-on, as explained above. We kept the break time constant at 40 s over the whole measurement time and assume that also the EP shift is constant. However, a constant EP shift results in different emission spikes, depending on the actual EP (Figure 5.2). We illustrate this effect for the thick device at different points in time in Figure 5.3c. The simulated luminance trend assumes an EP shift with a constant speed of 0.01 h^{-1} from 0.85 to 0.55 over an operation time of 30 h (Figure 5.2b). For the relaxation during each break, we adopt the value of 0.01 EP, as discussed for the device situation after an operation time of 8 h (Figure 5.2c).

The simulated light emission trend in Figure 5.3c does not agree with the measurement, especially since the simulated emission spike is negative for EPs between 0.68 and 0.55. To replicate the experiment, we need to add a constant positive light overshoot of 25% of a particular light level to the emission after every break (Figure 5.3d). This overshoot is the result of electron de-trapping at rest (chapter 4,[20]). At switch-on, the light temporarily increases because non-radiative SRH recombination between trapped electrons and free holes is small. Trap filling during operation increases SRH recombination and the light recovers to the trend line before the break. We illustrate the light emission trend due to electron de-trapping at rest - followed by trap filling during operation - separately with a PLED, because a PLED contains no salt and EDL relaxation is not present (Figure S5.4, Supporting Information).

The combination of EDL relaxation and electron de-trapping at rest also explains the light emission trend of the thin device (Figure 5.3b). The effect of EDL relaxation alone results in a permanent light undershoot at turn-on (Figure 5.3e). When adding a constant positive emission spike, the experimental change of sign after 7 h is reproduced (Figure 5.3f). After rest, both PLECs show a positive voltage overshoot throughout. This indicates that the voltage undershoot due to charge de-trapping in the intrinsic region is masked by a stronger voltage increase due to EDL relaxation (Figure S5.4, Supporting Information).
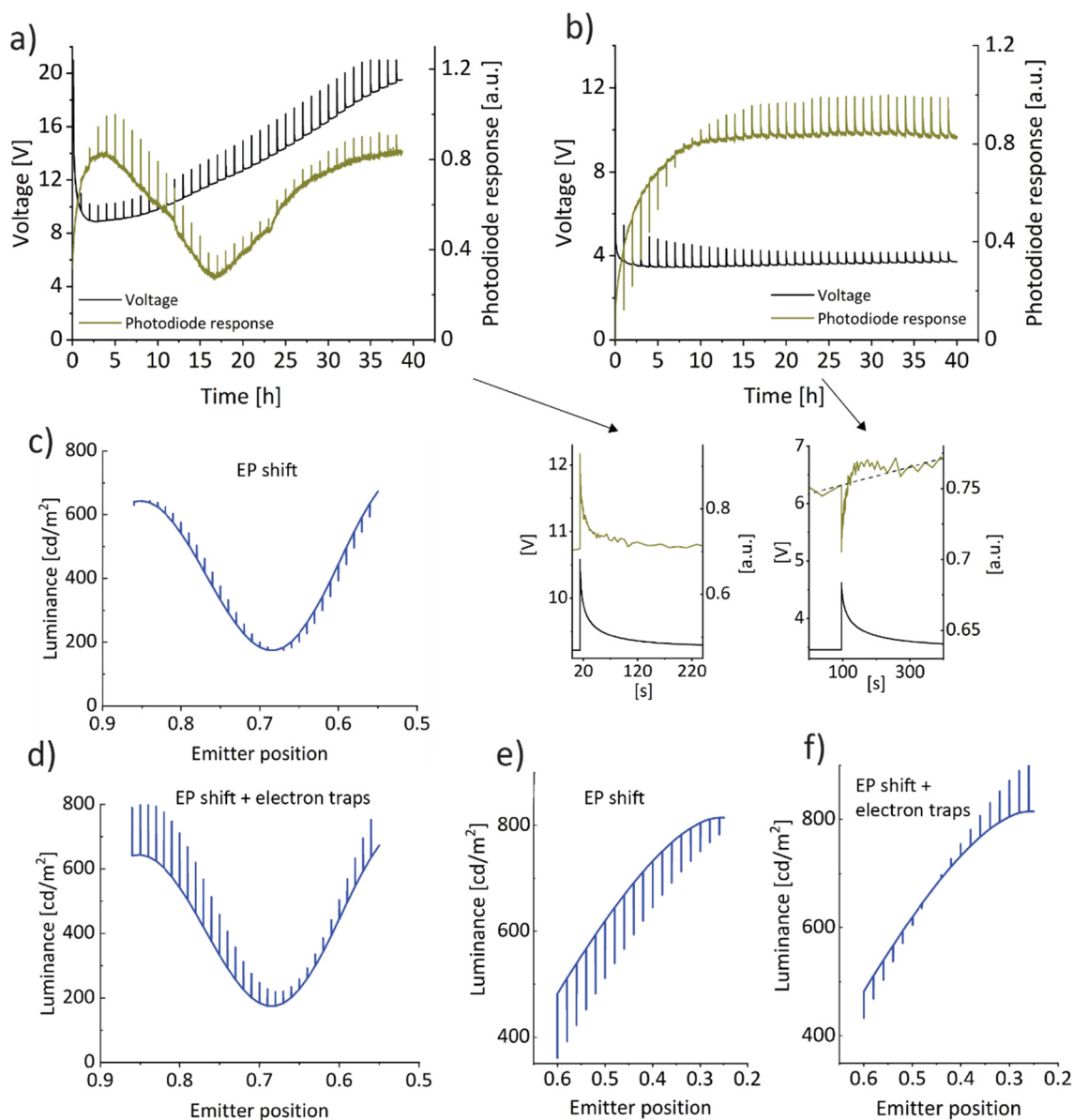
Figure 5.3. Long-term performance of PLECs. Voltage and light emission trends over 40 h for constant current-driven (7.7mA cm⁻²) PLECs with an active layer thickness of a) 430 nm and b) 70 nm. After every hour, the device was rested for 40 s at short circuit. Included are magnifications of a) and b) after 7 h driving. c-f) Simulated light emission characteristics for thick (c,d) and thin (e,f) PLECs.

We obtain further evidence for electron traps in the PLEC from illumination experiments with light at 656 nm, which is below the bandgap of SY.[28] Data in **Figure 5.4** show that the current increases during the light pulse and recovers afterwards to the trend line. Following the points made for PLEDs in chapter 4 [20] this trend indicates that light irradiation induces electron de-trapping, which results in a decrease of immobile trapped charge and an increase of the current. The evolving n- and p-polarons in the PLEC absorb light below the SY bandgap as well;[24,28] however, this does not affect the device performance. First, the current increase during the light pulse is independent of

the operation time (Figure 5.4b). This rules out the involvement of polarons, because the doped zones grow slowly over many hours. Furthermore, the current increase occurs even for a pristine device during light irradiation already after 50 s, when doped zones are not yet present (Figure 5.4c). The current decrease of the pristine device during the first 20 s in Figure 5.4c is due to electron trap filling, as observed for PLEDs (chapter 4,[20]).Afterwards, EDLs form and the overall current starts to increase.
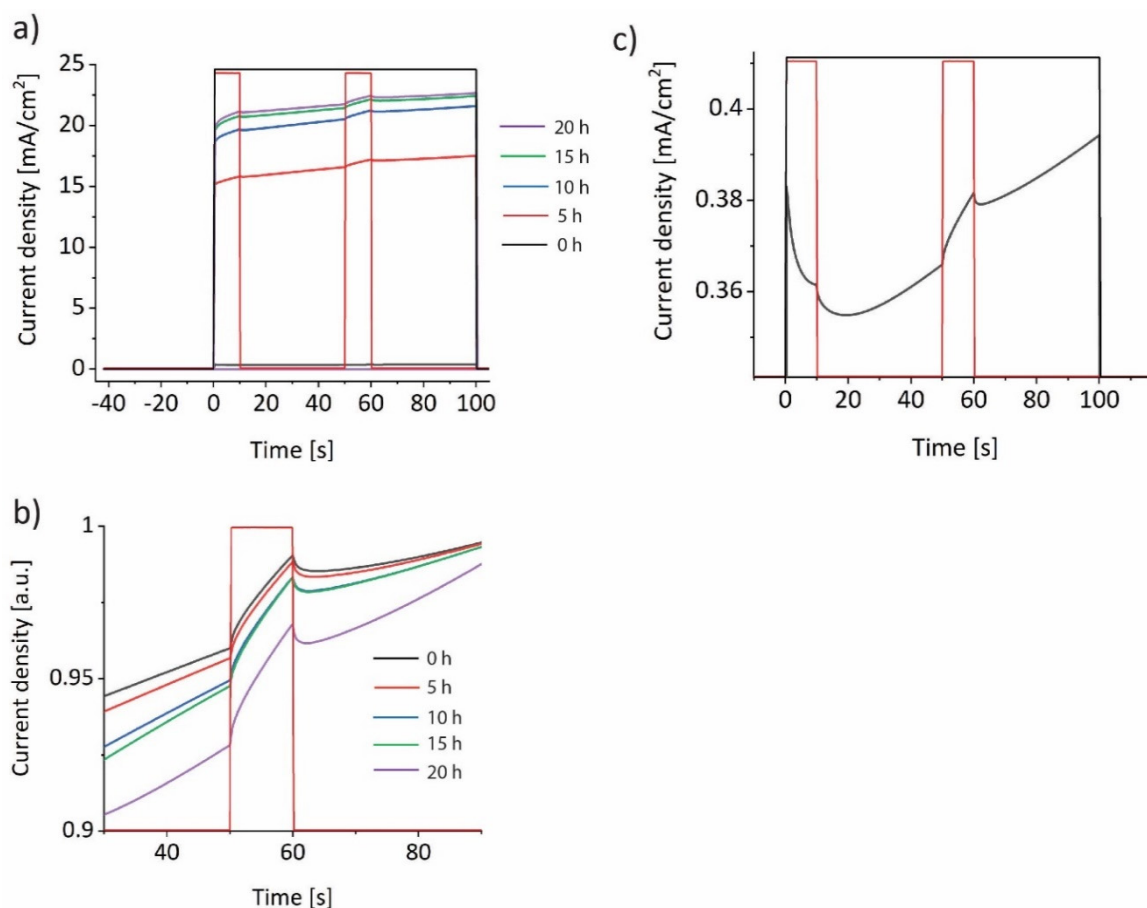
Figure 5.4. a) A PLEC was biased for 28 h at a constant current of 7.7 mA cm^{-2}. After every hour a break (40 s) at short circuit was applied, followed by a voltage pulse of 6 V for 100 s. The current level increases from ~0.4 mA cm^{-2} at 0 h, to above 20 mA cm^{-2} after 20 h driving; this increase is due to the formation of the EDLs and doped zones. Directly at switch-on and after 50 s, the device was irradiated for 10 s with light at 656 nm. b) Normalized current trends from a) to illustrate the constant influence of light on the current during the second irradiation. c) Current trend for a pristine device with light pulses applied.

To investigate the long-term device degradation, we turn to absorption measurements during biasing. Therefore, a device was operated at a constant voltage over more than 20 h. After every hour, the voltage bias was stopped and the absorption at different voltages was measured. **Figure 5.5**a displays the electroabsorption (EA) signal at 514 nm. At this wavelength, we probe the absorption of SY (Figure S5.5, Supporting Information). The signal is due to the Stark effect and

thus is a measure of the electric field in the device.[29] Because the field is strongest in the i-region (Figure 5.1a) and the voltage drop is constant across this region after EDL formation, the Stark signal is a measure for the thickness of the i-region. Specifically, the peak at 3 h in Figure 5.5a indicates that the electric field at this time is strongest, i.e. the i-region is the thinnest. The subsequent decrease of the signal indicates that the i-region expands over time. This finding agrees with results from our previous study, where we used capacitance measurement to track the thickness of the i-region.[9] The EA signal approaches a plateau after around 12 h, indicating the ion motion slows down. From sensitive capacitance measurements, however, we find that the width of the low conductivity part of the device still increases very slowly out to a measurement time of 35 h (Figure S5.6, Supporting Information).

Included in Figure 5.5a are the current density and EL signal. In contrast to the EA signal, the current and light transients decrease continuously during the measurement from 12 h to 20 h, which is a signature of device degradation. Note that the light and current decay show the same trend; this confirms that the shift of the EP has stopped after around 12 h.[9]
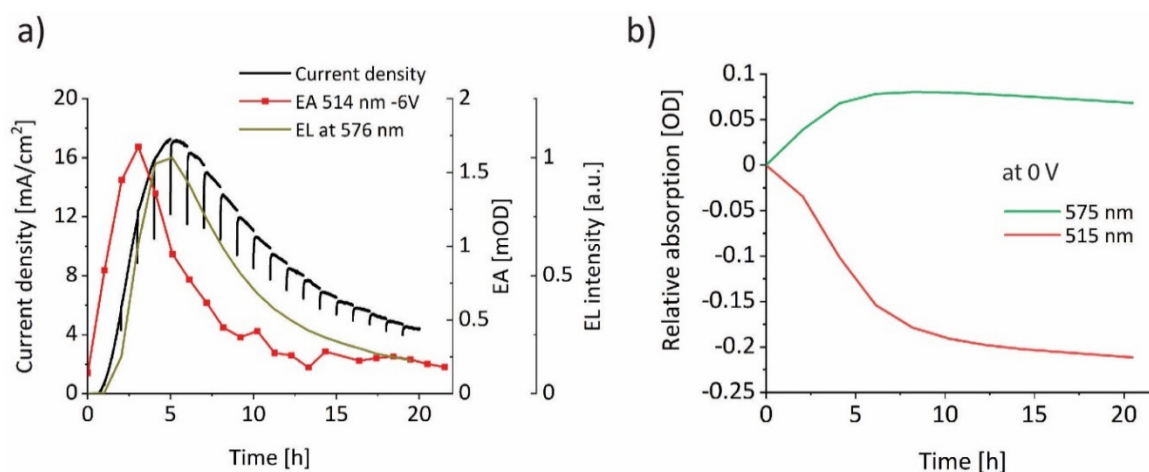
Figure 5.5. a) Current, light and absorption transients of a 430 nm thick constant voltage-driven PLEC (12 V). Shown is the absorption at 514 nm that was measured at -6 V, relative to the absorption at 0 V. b) Change of absorption over time of a 70 nm thick device relative to the absorption of the pristine device. The absorption of the pristine device was 0.74 OD at 515 nm, and 0.03 OD at 575 nm.

Figure 5.5b displays changes of absorptions at two wavelengths over time. At 515 nm we follow the absorption change of SY. We chose the wavelength 575 nm to detect changes in the p-polaron density, the absorption of the n-dopants at this wavelength is very small (Figure S5.5, Supporting Information).[28] The increase of the absorption at 575 nm during the first ~10 h is due to the growth of the doped zones. Radical cations and anions form from the parent SY, which explains the absorption decrease at 515 nm. For longer times, the absorptions at both wavelengths slightly decreases with a similar trend. Again, we ascribe this observation to device degradation.

5.3   Discussion

We detect electron traps in PLECs by measuring the device response to electrical driving and breaks. This measurement sequence involves a change in temperature. During break, the power is zero and the device temperature relaxes to room temperature. At switch-on, the electrical power heats up the sample until steady state between heat loss and electrical heating is reached. A changing temperature influences, for example, the charge mobility values and the photoluminescence quantum efficiency. This change in temperature, however, does not influence our measurements. We observed that the temperature adjusts in less than 10 s, which is much faster than the observed recovery times after switch-on (>200 s in Figure 5.3, and Figure S5.7 and Figure S5.8, Supporting Information).

Having identified the similarity of the emissive region in a PLED and a PLEC, an immediate educated guess is that also hole traps form during operation of a PLEC. In the PLED, long term device degradation is attributed to hole traps that continuously form via exciton – hole interactions.[19] The energy of the exciton is transferred to the hole, which is excited to higher energetic states. Subsequently, bonds breaking in some of these excited p-polarons can produce hole traps directly, or hole traps can form via further interactions with adjacent molecules.[18] The efficacy (cd A^{-1}) of a SY PLED and PLEC are comparable;[24] thus, the exciton densities are similar. In contrast, the stabilized polaron density (> 10^{18} cm^{-3}) in the doped regions of a PLEC is much higher than the free polaron density (a few times 10^{17} cm^{-3}) in the PLEC i-region and the PLED[16,19,20] (Figure S5.9, Supporting Information). Therefore, we can assume that next to hole trap formation in the PLEC i-region, hole traps form also at the border between the p-doped and the i-region. If the EP is not constant during turn-on, hole trap formation in PLECs spans a fraction of the total active layer thickness, but the majority of hole traps will form subsequently when the ionic motion has stopped and the system is in steady state. When a hole trap forms, the positive mobile charge of the stabilized p-dopant is replaced by the immobile positive charge of the hole trap. Thereby, the width of the i-region increases. This scenario is consistent with our long-term capacitance measurements that indicate that the width of the low conductivity part of the device slowly increases (Figure S5.6, Supporting Information). Interestingly, the long-term decay of the SY and p-polaron absorption show a similar trend (Figure 5.5b). This suggests a hole trap formation mechanism that consumes p-dopants and parent SY polymer repeating units at the same time.

Hole trap formation in a constant current-driven PLED results in a voltage increase and luminance decrease over time. For our constant current-driven PLECs, the voltage increase due to degradation during the first few hours is masked by the voltage drop when the EDLs and doped zones form (Figure 5.3). In addition, the decrease of the luminance due to degradation is covered by microcavity effects due to the moving EP, evident from the light emission trend shown for the thick PLEC shown in Figure 5.3a. For the thin PLEC (Figure 5.3b) the light emission after turn-on is constant. We interpret this trend that the decrease of light due to hole trap formation and the continuous increase of outcoupled light due to the moving EP (Figure 5.2a) effectively cancel each other out, by chance. For the thick PLEC (Figure 5.3a), an indicator for degradation and decrease of the emitted light over time is that the intensity of the second emission maxima after 40 h is smaller than the intensity of the first peak – the simulated optical model predicts the opposite (Figure 5.2b).

5.4   Conclusion

We have demonstrated the presence of electron traps and the formation of hole traps during operation in SY PLECs. The most important conclusion is that hole trap formation presents an important polymer-intrinsic degradation mechanism that limits the stability of PLECs. So far, experiments to increase the operational stability of PLECs were mostly targeted on optimizing the electrolyte concentration, stabilizing the p-i-n configuration, applying pulsed vs continuous driving schemes, or preventing electrochemical side reactions of the electrolyte.[1,4,30-33] Such attempts involved the variation of polymer-extrinsic parameters that can be varied, if necessary. Hole trap formation is a more fundamental degradation mechanism, as it concerns the light-emitting polymer directly.

5.5   Experimental Section

PLEDs and PLECs were fabricated as described recently.[9,20] The mass ratio between SY, the ion conductor TMPE and $Li^+CF_3SO_3^-$ was 1 : 0.1 : 0.03.[24] Electroluminescence spectra were measured with an integrating sphere on an Ocean Optics spectrometer QE Pro, calibrated before each measurement. Angular dependent EL measurements were performed with a prototype of the Phelos measurement system (Fluxim AG, Switzerland). Impedance measurements at 0 V with an alternating 70 mV signal to determine the capacitance transients were performed on the Paios measurement system (Fluxim AG, Switzerland), as well as the current and light intensity transients. The light intensity was measured with a photodiode as photovoltage. The relation between the measured photovoltage and the corresponding radiance/luminance is explained in the Supporting Information of reference [6].

Optical and electrical simulations were performed with Setfos 5.1 (Fluxim AG, Switzerland). Simulation procedures and parameters are described in the Supporting Information. The refractive indices for the intrinsic SY layer were confirmed by simulation of experimental transmission spectra measured previously.[24]

EA data were collected in a reflection configuration, where p-polarized light hits the device at 45 degrees angle of incidence from the transparent electrode side and is reflected outwards by the metallic electrode making two passes via the SY layer. Cree XP-E white-light LED powered by Mastech 3010D DC supply was utilized as a light source. Light propagation from the LED to the sample and further to the spectrometer Andor Shamrock 500i equipped with an Andor Newton DU970 CCD camera was directed in a simple optical scheme with the help of lenses. EA scans were performed during the interruptions of the constant voltage operation. At each scan, the ramp pulses of 150 ms period were applied to the sample by a Tektronix AFG 3101 function generator, the same used for DC biasing, with the amplitude starting at 12V (DC operation bias) reaching -6V and again increasing to 12V. The detecting camera, capturing 200 spectra per ramp period, was synchronized to the ramp sequence. Data were averaged from 375 pulses. Thus, certain spectra in the dataset corresponded to the certain voltage applied to the sample. The light intensity at 0 V was taken as reference and EA, i.e. changes of the light intensity vs voltage, was calculated in OD units. Variation of the absolute intensity of the detected light was used as a measure for the change in sample absorption during device operation. The same spectrometer and camera were

used to record electroluminescence spectra of the operating sample while blocking the light from the LED by computer-controlled shutter.

References

[1]   S. Tang, L. Edman, *Top. Curr. Chem.* **2016**, 374, 40.

[2]   S. B. Meier, D. Tordera, A. Pertegás, C. Roldán-Carmona, E. Ortí, H. J. Bolink, *Mater. Today* **2014**, *17*, 217.

[3]   J. Mindemark, S. Tang, H. Li, L. Edman, *Adv. Funct. Mater.* **2018**, *28*, 1801295.

[4]   J. Gao, *ChemPlusChem* **2018**, *83*, 183.

[5]   K. Youssef, Y. Li, S. O'Keeffe, L. Li, Q. Pei, *Adv. Funct. Mater.* **2020**, *30*, 1909102.

[6]   J. Ràfols-Ribé, N. D. Robinson, C. Larsen, S. Tang, M. Top, A. Sandström, L. Edman, *Adv. Funct. Mater.* **2020**, *30*, 1908649.

[7]   E. Fresta, R. D. Costa, *Adv. Funct. Mater.* **2020**, *30*, 1908176.

[8]   S. van Reenen, R. A. J. Janssen, M. Kemerink, *Adv. Funct. Mater.* **2012**, *22*, 4547.

[9]   M. Diethelm, A. Schiller, M. Kawecki, A. Devižis, B. Blülle, S. Jenatsch, E. Knapp, Q. Grossmann, B. Ruhstaller, F. Nüesch, R. Hany, *Adv. Funct. Mater.* **2020**, *30*, 1906803.

[10]   S. Tang, J. Mindemark, C. M. G. Araujo, D. Brandell, L. Edman, *Chem. Mater.* **2014**, *26*, 5083.

[11]   N. B. Kotadiya, A. Mondal, P. W. M. Blom, D. Andrienko, G.-J. A. H. Wetzelaer, *Nat. Mater.* **2019**, *18*, 1182.

[12]   M. Kuik, G.-J. A. H. Wetzelaer, H. T. Niolai, N. I. Craciun, D. M. De Leeuw, P. W. M. Blom*, Adv. Mater.* **2014**, *26*, 512.

[13]   H. T. Nicolai, M. Kuik, G. A. H. Wetzelaer, B. de Boer, C. Campell, C. Risko, J. L. Brédas, P. W. M. Blom, *Nat. Mater.* **2012**, *11*, 882.

[14]   D. Abbaszadeh, A. Kunz, N. B. Kotadiya, A. Mondal, D. Andrienko, J. J. Michels, G.-J. A. H. Wetzelaer, P. W. M. Blom, *Chem. Mater.* **2019**, *31*, 6380.

[15]   D. Abbaszadeh, A. Kunz, G. A. H. Wetzelaer, J. J. Michels, N. I. Crăciun, K. Koynov, I. Lieberwirth, P. W. M. Blom, *Nat. Mater.* **2016**, *15*, 628.

[16]   Q. Niu, G.-J. A. H. Wetzelaer, P. W. M. Blom, N. I Crăciun, *Adv. Electron. Mater.* **2016**, *2*, 1600103.

[17]   Q. Niu, G.-J. A. H. Wetzelaer, P. W. M. Blom, N. I Crăciun, *Appl. Phys. Lett.* **2019**, *114*, 163301.

[18]   I. Rörich, Q. Niu, B. van der Zee, E. del P. Rosendo, N. I. Crăciun, C. Ramanan, P. W. M. Blom, *Adv. Electron. Mater.* **2020**, 1700643.

[19]   Q. Niu, R. Rohloff, G.-J. A. H. Wetzelaer, P. W. M. Blom, N. I. Crăciun, *Nat. Mater.* **2018**, *17*, 557.

[20]   M. Diethelm, M. Bauer, W.-H. Hu, C. Vael, S. Jenatsch, P. W. M. Blom, F. Nüesch, R. Hany, Electron trap dynamics in polymer light-emitting diodes, **unpublished results**.

[21]   S. Burns, J. MacLeod, T. T. Do, P. Sonar, S. D. Yambem, *Sci. Rep.* **2017**, *7*, 40805.

[22]   S. Tang, L. Edman, *J. Phys. Chem. Lett.* **2010**, *1*, 2727.

[23] M. Kawecki, R. Hany, M. Diethelm, S. Jenatsch, Q. Grossmann, L. Bernard, H. J. Hug, *ACS Appl. Mater. Interfaces* **2018**, *10*, 39100.

[24] M. Diethelm, Q. Grossmann, A. Schiller, E. Knapp, S. Jenatsch, M. Kawecki, F. Nüesch, R. Hany, *Adv. Opt. Mater.* **2019**, *7*, 1801278.

[25] S. Jenatsch, M. Regnat, R. Hany, M. Diethelm, F. Nüesch, B. Ruhstaller, *ACS Photonics* **2018**, *5*, 1591.

[26] E. M. Lindh, P. Lundberg, T. Lanz, L. Edman, *Sci. Rep.* **2019**, *9*, 10433.

[27] H. Becker, S. E. Burns, R. H. Friend, *Phys. Rev. B* **1997**, *56*, 1893.

[28] T. Lanz, E. M. Lindh, L. Edman, *J. Mater. Chem. C* **2017**, *5*, 4706.

[29] A. Devižis, A. Gelzinis, J. Chmeliov, M. Diethelm, L. Endriukaitis, D. Padula, R. Hany, *Adv. Funct. Mater.* **2021**, 2102000.

[30] J. Fang, P. Matyba, L. Edman, *Adv. Funct. Mater.* **2009**, *19*, 2671.

[31] J. Gao, G. Yu, A. J. Heeger, *Appl. Phys. Lett.* **1997**, *71*, 1293.

[32] J. M. Leger, D. B. Rodovsky, G. P. Bartholomew, *Adv. Mater.* **2006**, *18*, 3130.

[33] D. Tordera, S. Meier, M. Lenes, R. D. Costa, E. Ortí, W. Sarfert, J. J. Bolink, Adv. *Mater.* **2012**, *24*, 897.

Supporting Information
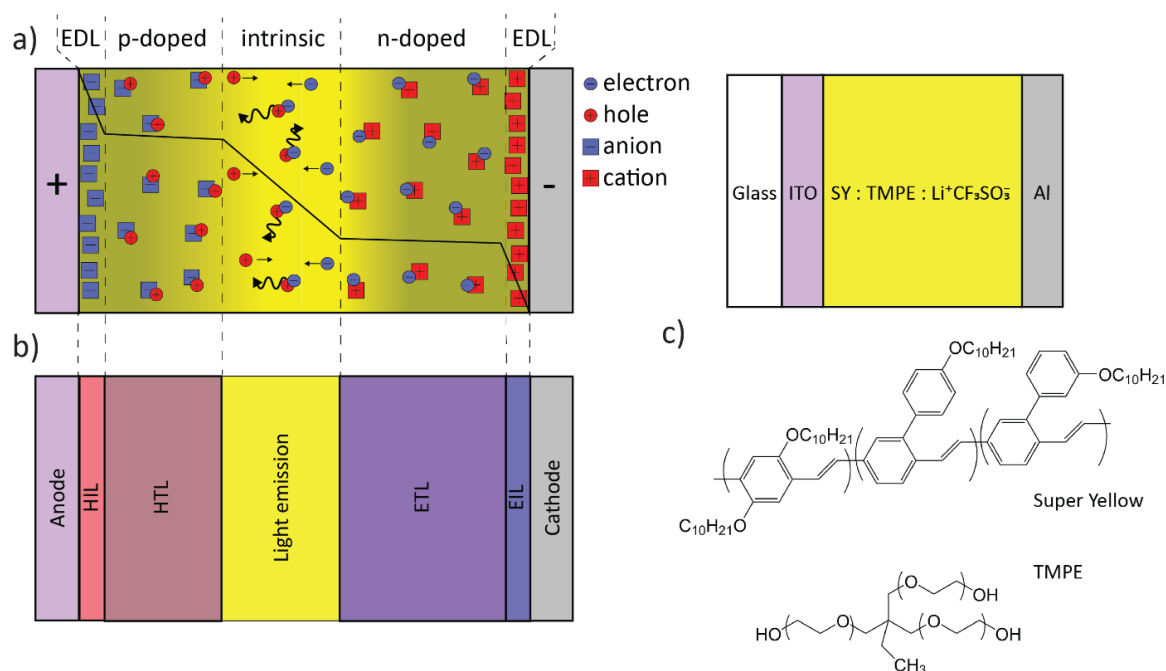
Figure S5.1. a) Schematic comparison of a light-emitting electrochemical cell in steady state and b) of an organic light-emitting diode (HIL, EIL: hole- and electron-injection layer; HTL, ETL: hole- and electron-transport layer). c) Device architecture of the PLEC used in this work and the chemical structures of SY and TMPE. The thickness of ITO was 132 ± 2 nm, the active layer thickness was 70 nm or 430 nm, and the Al electrode had a thickness of 70 nm.

When a bias is applied to a PLEC, ions drift to their respective electrode interface and form electric double layers (EDLs). This facilitates the injection of electrical charges and, descriptively, the EDL effectively takes over the task of the injection layer in a PLED. Also, no transport layers are needed in a PLEC because the injected charges and mobile ions produce p- and n-doped regions at the anode and cathode. In these regions, ions screen the field of the doped polymer repeating units, resulting in a high polaron charge density. This electrochemical doping process increases the conductivity of the doped regions. An operated PLEC consists of a p-i-n structure, where electron-hole recombination and light emission takes place in the intrinsic (i) region. The intrinsic region of a PLEC plays the role of the active layer in a PLED.
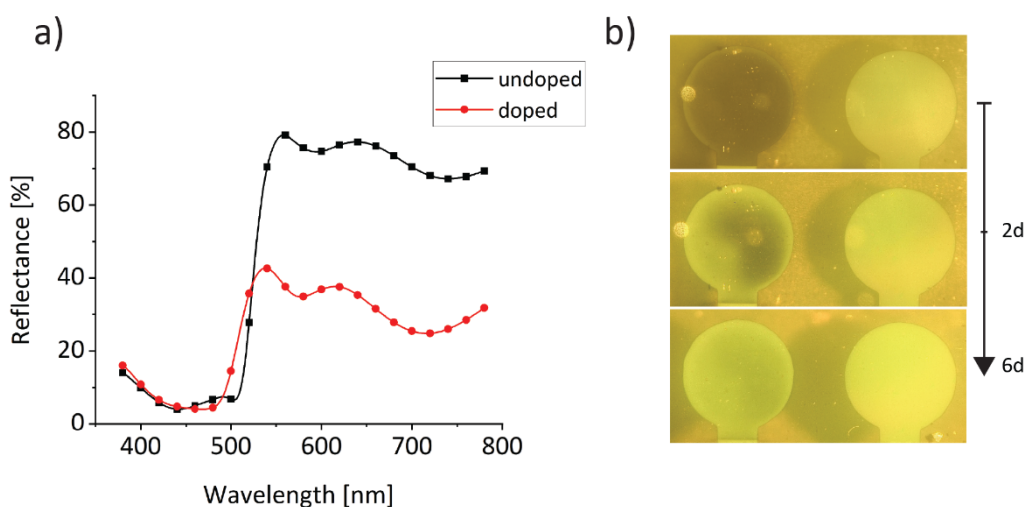
Figure S5.2. a) Reflectance simulation of a SY PLEC with and without doping. The simulations correspond to the left device in b) directly after biasing and after rest for 6 days, respectively. The right device in b) is shown as a reference.

A simple visual method to estimate the time of ion relaxation can be used for thin PLECs. The reflected room light from the aluminium electrode appears yellowish because SY absorbs the light below 550 nm as simulated in Figure S5.2a (undoped). The polaron species absorb beyond 550 nm and the reflectance in this region is lower, such that the device appears darker (doped).[S1] Figure S5.2b shows pictures of a unbiased control cell (right) over time, and of a cell (left) that was biased at 7.7 mA cm^{-2} for 5 h, and that was then stored at short circuit. Over time, the reflectance increased, which indicates that the doped species slowly disappear.
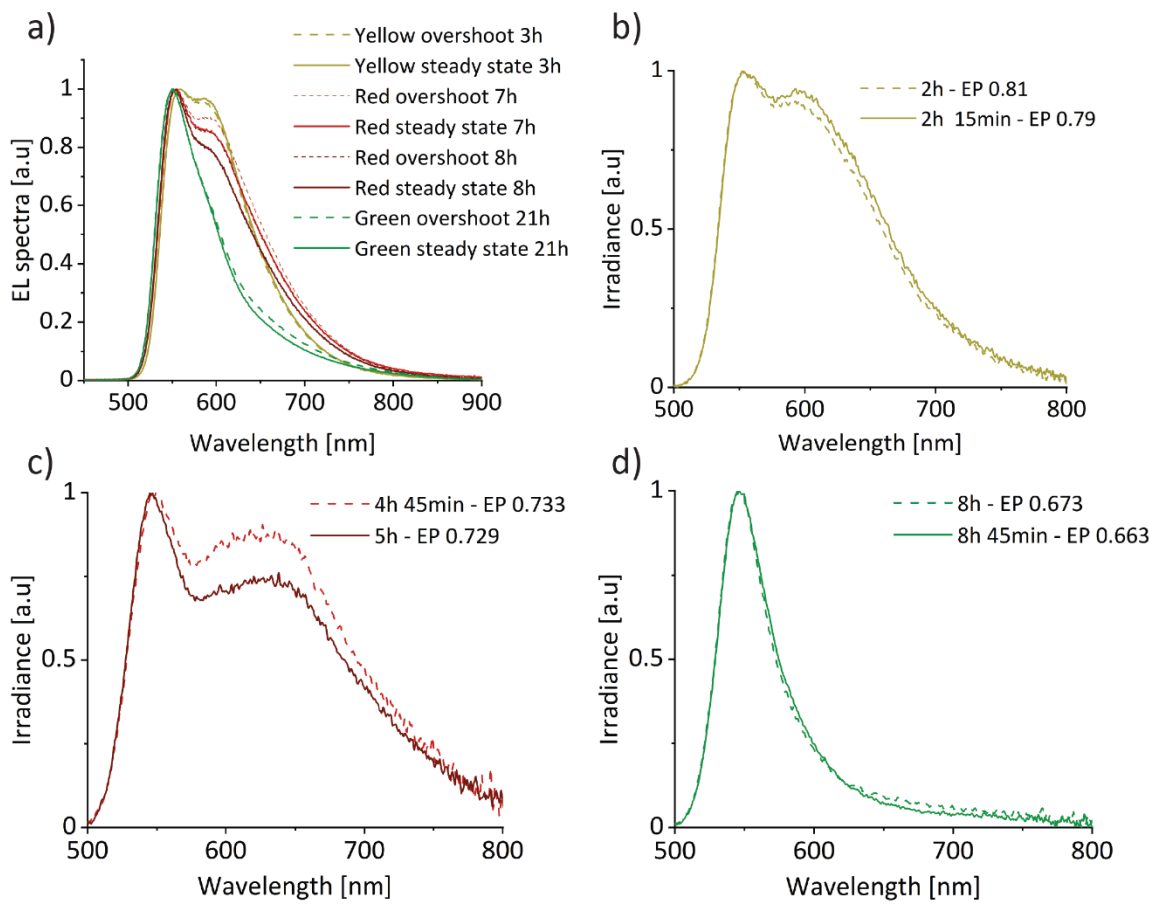
Figure S5.3. Transient EL spectra of PLECs. a) Normalized EL spectra of a 430 nm thick LEC directly after switch-on following a break at 0 V for 40 s (overshoot), and 50 - 70 s later (close to steady state). The overshoot spectra are more intense than the respective steady-state spectra by +23% at 3 h, +12% at 7 h, +16% at 8 h and by +12% at 21 h. Recently, we fitted the spectra during biasing to an optical model in order to track the emitter position (EP).[S2] b)-d) show how the spectrum changes when the EP moves from the Al electrode (EP = 1) towards the ITO electrode (EP = 0). Comparison of the different overshoot and steady-state spectra in a) with EL spectra in b)-d) indicates a back shift of the EP towards the Al electrode during the break at 0 V. Spectra in a) were measured in an integrating sphere, which is an average over all angles, while b)-d) were measured at a certain angle (b: -15° c: 0° d: -5°, where 0° is perpendicular). The angle was chosen to match the spectra in a) the best.
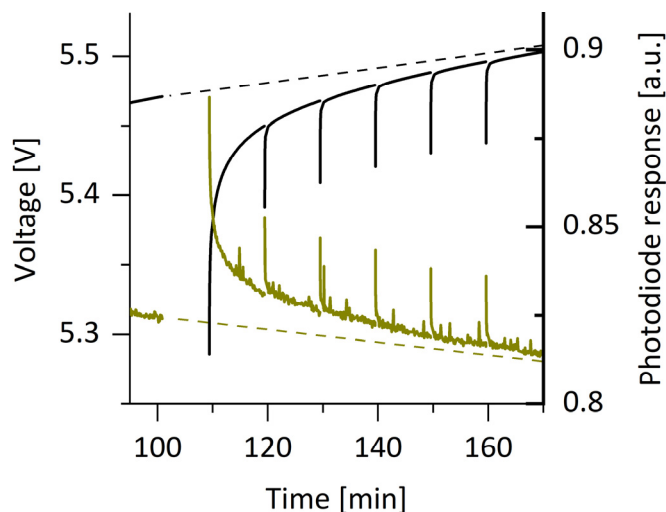
Figure S5.4. Voltage and light emission trend of a constant current-driven SY PLED (7.7 mA cm^{-2}). After 100 min, the device was rested at short circuit for 10 min, shorter breaks of 40 s were applied during the operation time 110 min to 170 min. After every break, an intermediate increase in device performance is observable, as it needs a lower voltage to drive a constant current, and the light emission is higher. Subsequently, the voltage and photodiode response recovers to the trend line before the break. This behaviour is explained with the presence of deep electron traps in the polymer.[S3] At rest, trapped electrons de-trap slowly via thermal emission, as expected. However, also filling of these traps is very slow, as inferred from the device recovery trend after rest that proceeds over many minutes. Generation of electron traps increases the amount of immobile charge in the device, and it needs a higher voltage to drive a constant current. In addition, non-radiative Shockley-Read-Hall (SRH) recombination increases with more trapped charge, reducing the emissive Langevin recombination. The effect of electron de-trapping and trap filling does not depend on the drive time, i.e. the same break duration at different points in time leads to similar light overshoots and voltage undershoots. Therefore, in Figure 5.3 of the main text, a time-independent and constant luminance overshoot due to electron de-trapping was added to replicate the PLEC luminance trend.
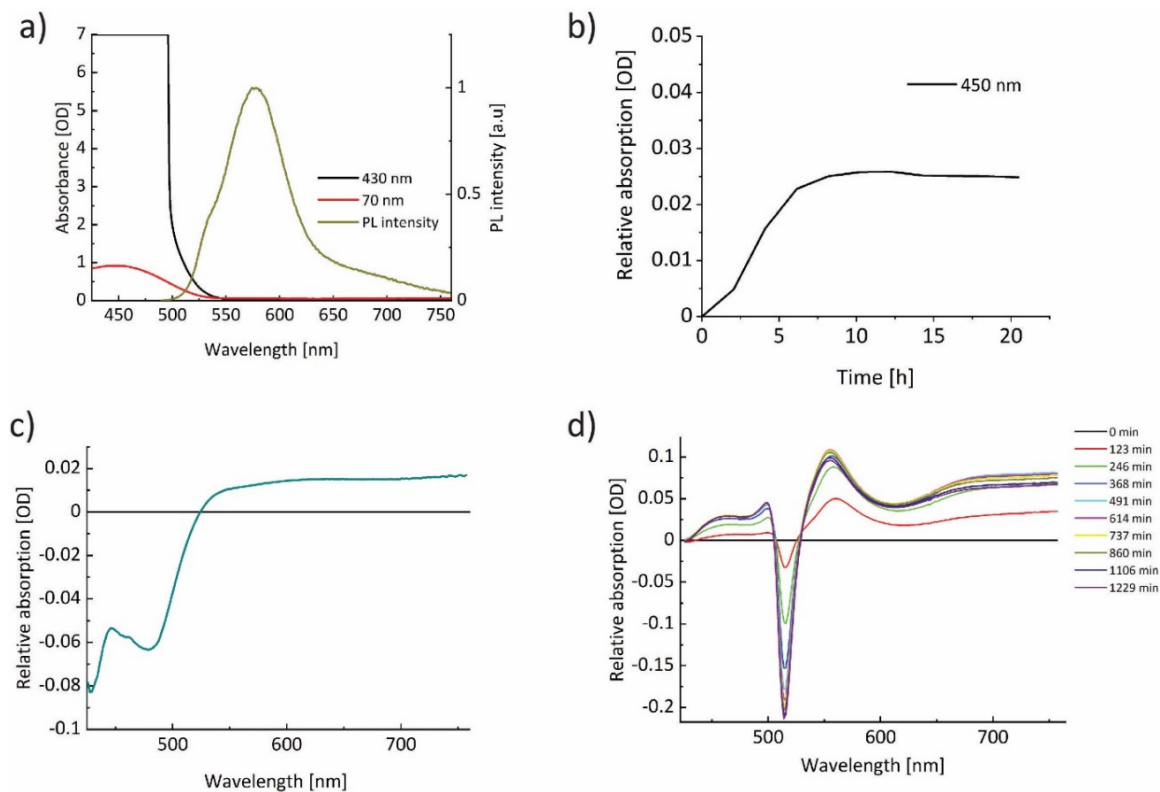
Figure S5.5. a) Absorption spectra of a 70 nm and a 430 nm thick SY layer. Included is the SY photoluminescence spectrum. b) Absorption change over time at 450 nm for a 430 nm thick PLEC. At this wavelength, the absorption of the SY layer is above 7 OD, which does not allow to detect a small change in absorption over time. We measured the intensity from the reflected light, thus the measured signal reflects changes of the reflection at the ITO/SY interface. The signal increase during the first 10 h might be due to the evolving EDL at the ITO electrode due the slow rearrangement of the anions on that timescale, as we have shown recently with the help of ToF-SIMS measurements.[S4] During the measurement time of 10 h to 20 h, the signal stays constant. This indicates that the light source and detector were stable over this time scale. From this we conclude that the measured small absorption changes at 515 nm and 575 nm during 12 h and 20 h in Figure 5.5b (main text) are real, and do not come from a long-term stability drift of the measurement setup. c) Absorption of a 70 nm thick PLEC after an operation time of 700 min, relative to the absorption at time zero. From optical absorption simulations, we found that the absorption above ~540 nm is mainly due to the formation of p-dopants and the simulated absorption profile is almost constant, as experimentally observed. d) change of absorption at 12 V over time of a 430 nm thick device. At this scale, absorptions at 12 V and 0 V are almost equal, as the electroabsorption signal strength is only a few mOD. Due to the higher thickness of the active layer, the polaron absorption in d) is around 5 times higher compared to c). To understand the undulating absorption trends above ~540 nm in d), we performed optical absorption simulations for a symmetric p(160 nm)-i(70 nm)-n(160 nm) device situation with a constant doping concentration. Due to interference effects in the thick device, the simulated absorption appeared indeed wavelike, in agreement with the measurement. During operation of the PLEC, the EP

moves and the doping profile changes continuously; thus, we did not attempt to simulate the absorption trend quantitatively.
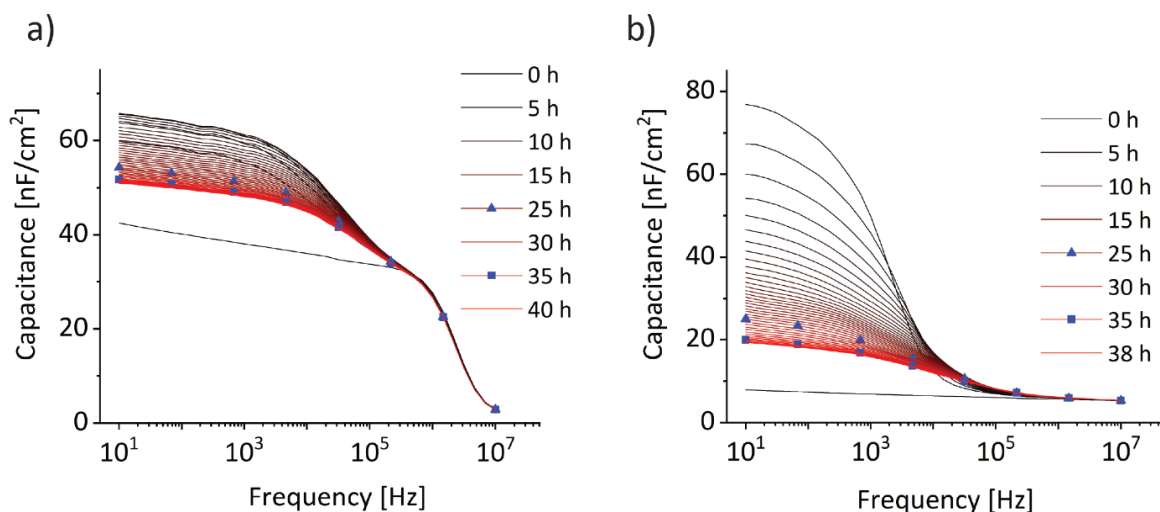
Figure S5.6. Impedance measurements on a) a 70 nm thick PLEC and b) a 430 nm thick PLEC demonstrate that the width of low conductivity part of the device still increases slightly during 25 h and 35 h. The ions have reached steady state before.
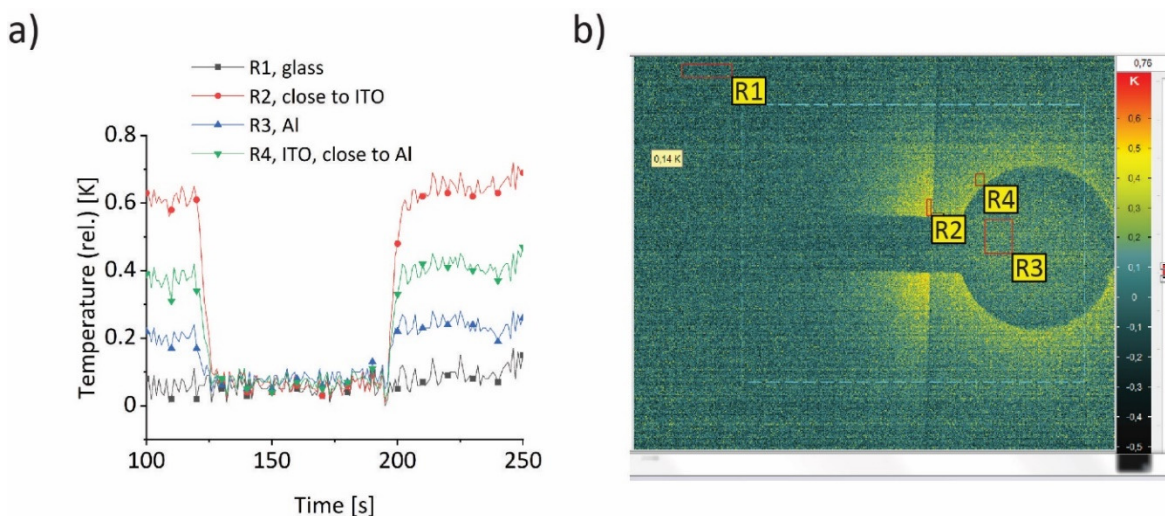
Figure S5.7. Investigation of temperature on transient device response. a) shows infrared imaging measurements during short-circuit breaks of 80 s on a 430 nm thick PLEC that was operated for several hours at 7.7 mA cm^{-2} before. Several spots (R1-R4) on and around the cell were measured as labelled in b).

Different materials emit radiation differently, such that the signal intensity varies and the signal directly on the cell (R3, Al) is not the strongest. The camera was not calibrated for absolute values, the real temperature increase might be slightly different. However, for our purpose only the relative change is relevant, which is the same for all signals. Temperature trends show that it takes less than 10 s until a steady-state temperature is reached, both when turning the bias off and after

switch-on. The transient relaxation and recovery effects, however, increase in intensity and relaxation time for break times larger than 20 s (Figure S5.4). Furthermore, recovery times are longer than 20 s (>200 s in Figure 5.3 (main text), Figure S5.8).
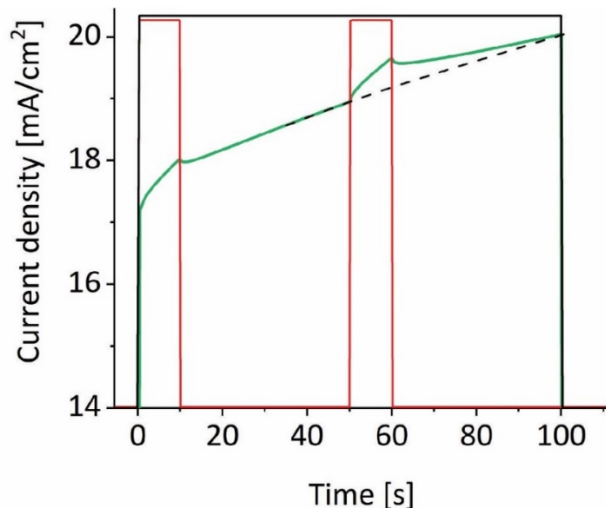
Figure S5.8. A PLEC was operated at a constant current of 7.7 mA cm^{-2} for 7 h, followed by a break of 40 s and a subsequent 100 s long voltage pulse (6 V) during which light pulses at 656 nm were applied. The dashed black line indicates the current recovery trend in the absence of light. After switching off the light, current relaxation takes 40 s.
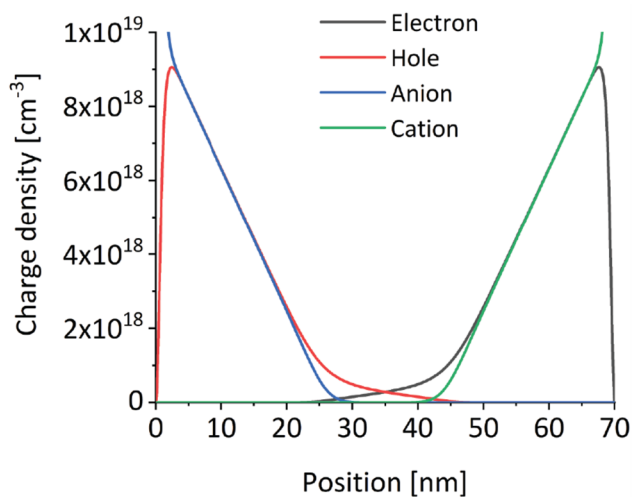
Figure S5.9. Charge density profiles at 3V steady state.

Electrical model parameters

Table S5.1. Electrical model parameters were taken from our previous work, reference [S2].

Parameter	PLEC	Source
Thickness SY	70 nm	Profilometry measurement
Electron mobility	2.5×10^{-6} cm^2/Vs	Estimated from [S5]
Hole mobility	2.5×10^{-6} cm^2/Vs	
Anion mobility	1×10^{-14} cm^2/Vs	Estimated from calculation from conductivity measurement as done in [S6]:
Cation mobility	1×10^{-13} cm^2/Vs	$\mu_a + \mu_c =5 \times 10^{-12}$ cm^2/Vs
Radiative recombination coefficient	1×10^{-9} cm^3/s	Manual fit
Effective density of states	1×10^{27} 1/m^3	Manual fit
LUMO SY	2.95 eV	Ref.[S7]
HOMO SY	5.45 eV	
Ohmic injection work function ITO / PEDOT:PSS	5.16 eV	Chosen to have an equal barrier of 0.29 eV for both electrodes of the PLEC, leading to a charge carrier density at the electrode interface of 1×10^{16} cm^{-3} electrons.
Ohmic injection work function Al / Ca/Al	3.24 eV	
Relative permittivity SY	2.8	Calculated from capacitance measurement
Equilibrium density of mobile negative ions	1×10^{19} 1/cm^3	With the used salt concentration and a film density of 1 g cm^{-3} (ref. [S1]), the upper limit of the ion density is 1.17×10^{20} cm^{-3}
Equilibrium density of mobile positive ions	1×10^{19} 1/cm^3	
Applied voltage	3 V	

Optical model parameters

For the optical simulations of PLECs we used the n- and k-values of each layer. Values for the 135 nm thick ITO layer were measured by spectroscopic ellipsometry, SY data were taken from reference [S1]. Data for the 70 nm thick aluminium layer was taken from the Setfos software database, originally from H.C. Starck. Additionally, a measured SY photoluminescence spectrum was used. The optical simulations in Figure 5.2, main text, were performed by assuming a constant current of 7.7 mA cm^{-2} and a Gaussian emission profile, where the Gaussian width (50 nm for the 430 nm thick PLEC, 8 nm for the 70 nm PLEC) was chosen such that it represents an intermediate width of the recombination zone during the electrically simulated shift.[S2] In addition to the triplet exciton loss, a PL quantum efficiency of 68.3% was taken into account.[S8] The refractive indices for

the intrinsic and doped SY layers were calculated[S1,S9,S10] from parameters of the Tauc-Lorentz model taken from reference [S11].

References

[S1]   T. Lanz, E. M. Lindh, L. Edman, *J. Mater. Chem. C* **2017**, *5*, 4706.

[S2]   M. Diethelm, A. Schiller, M. Kawecki, A. Devižis, B. Blülle, S. Jenatsch, E. Knapp, Q. Grossmann, B. Ruhstaller, F. Nüesch, R. Hany, *Adv. Funct. Mater.* **2020**, *30*, 1906803.

[S3]   M. Kuik, G. J. A. H. Wetzelaer, H. T. Nicolai, N. I. Craciun, D. M. De Leeuw, P. W. M. Blom, *Adv. Mater.* **2014**, *26*, 512.

[S4]   M. Kawecki, R. Hany, M. Diethelm, S. Jenatsch, Q. Grossmann, L. Bernard, H. J. Hug, *ACS Appl. Mater. Interfaces* **2018**, *10*, 39100.

[S5]   H. Najafov, I. Biaggio, T.-K. Chuang, M. K. Hatalis, *Phys. Rev. B* **2006**, *73*, 125202.

[S6]   S. Van Reenen, R. A. J. Janssen, M. Kemerink, *Adv. Funct. Mater.* **2012**, *22*, 4547.

[S7]   S. Stolz, M. Petzoldt, S. Dück, M. Sendner, U. H. F. Bunz, U. Lemmer, M. Hamburger, G. Hernandez-Sosa, *ACS Appl. Mater. Interfaces* **2016**, *8*, 12959.

[S8]   S. D. Yambem, M. Ullah, K. Tandy, P. L. Burn, E. B. Namdas, *Laser Photonics Rev.* **2014**, *8*, 165.

[S9]   G. E. Jellison, F. A. Modine, *Appl. Phys. Lett.* **1996**, *69*, 371.

[S10]   G. E. Jellison, F. A. Modine, *Appl. Phys. Lett.* **1996**, *69*, 2137.

[S11]   E. M. Lindh, P. Lundberg, T. Lanz, L. Edman, *Sci. Rep.* **2019**, *9*, 10433.

Chapter 6   Ion- and Trap-Mediated Slow Processes in Perovskite Optoelectronic Devices

Matthias Diethelm[1,2], Jessica Girard[1], Frank Nüesch[1,2], and Roland Hany[1]

[1]Empa, Swiss Federal Laboratories for Materials Science and Technology, Laboratory for Functional Polymers, 8600 Dübendorf, Switzerland
[2]EPFL, Institute of Materials Science and Engineering, Ecole Polytechnique Fédérale de Lausanne, Station 12, 1015 Lausanne, Switzerland

Declaration of Contribution
M.D. contributed to and overviewed device fabrication, performed optoelectronic measurements, did the optical and electrical simulation including all related input data measurements, did the SEM measurements, analysed the data and prepared the manuscript.

Abstract

After an extraordinary rise in power conversion efficiency, perovskite thin film technology is reaching the performance of silicon photovoltaics, and tandem applications such as perovskite-on-silicon are promising candidates to go well beyond 30% efficiency. Recently, perovskite light-emitting diodes (PeLEDs) also reached more than 20% external quantum efficiency. Regarding commercialization of both technologies, however, understanding of dynamic processes due to mobile ions and electrical charges, and possible degradation mechanisms is mandatory. Ionic point defects - mobilised by high temperature, irradiation and external electric fields - contribute to the intrinsic device instability. Recent research indicates a lack of in-depth understanding of the actual defect passivation effect, and calls for suitable characterization methods. Dynamic processes due to mobile ions and trap development within the perovskite layer are well studied individually, but their interplay has still to be further unravelled. Here, such interplays are discussed. Due to the mobility of defects, many more processes compared to an organic LED/LEC system are identified. Furthermore, the potential to apply the optical model based on the microcavity effect to the perovskite LED system is discussed. Experimental thickness variation of the evaporated TPBi transport layer of a $CsPbBr_3$ based PeLED indicates the validity of the optical model. A transient voltage pulse reveals an emission feature within the time range of ionic mobility. Transient drift-diffusion simulation is able to describe the observed emission increase as a result of ionic movement. The subsequent emission drop is not reproduced by the simulation, and the missing model part is discussed.

6.1   Introduction

Perovskite photovoltaic (PV) single junction technology is almost on a par with silicon PV in terms of certified power conversion efficiency both for lab devices and modules.[1] Therefore, the future of perovskite PV commercialization does not rely on a further efficiency increase, but rather on the increase of device stability. There are only a few but very promising results with initial efficiencies above 20% and a slight degradation of 5% (T_{95}) when stressed for more than 1000 h under full-spectrum sunlight and accelerating high temperature.[2–4] While the lifetime of 1000 h has been defined as benchmark by the perovskite community [5], there is still a long way to go to reach the stability offered by silicon PV industry, i.e. < 10% degradation after 10 years and < 20% after 25 years.[6] Two years after a perovskite solar cell with an efficiency of 11% was reported [7], a perovskite LED (PeLED) made its first appearance in 2014 with an EQE of 0.8% [8]. Since then the field has been growing rapidly, and an external quantum efficiency (EQE) of 23% has been reached for green PeLED.[9] Red and near-infrared PeLEDs also reached 20% EQE, and blue and white PeLEDs reached more than 10% EQE.[10] It is this colour-tunability with narrow-band emission that makes this technology especially interesting. However, the stability of PeLEDs is rather low with minutes to hours until the efficiency drops below 50% of its maximum.[9,11,12] Besides external issues like moisture and oxygen, the intrinsic stability of both perovskite solar cells and PeLEDs is problematic because of ionic point defects that are mobilised by high temperature, light irradiation and strong external electric fields. The majority of these point defects, either vacancies, interstitials or substitutions, lead to shallow traps and only a few result in deep traps that enable dark Shockley-Read-Hall (SRH) recombination.[13,14] The influence of shallow and deep trap defects has been studied; mobile shallow traps indirectly influence the performance by changing the electric field distribution or by local doping. Deep traps and the resulting SRH recombination reduce the device performance in the form of a smaller open circuit voltage (V_{OC}).[15] In addition to point defects, deep traps also originate from defects at grain boundaries or interfaces.[16] Several strategies are used to deactivate and suppress the movement of defects. Addition of large cations splits up the crystalline 3D into a 2D structure, which prevents ionic movement to some extent. However, 2D materials might have fundamentally lower electric charge mobility that limits the efficiency. Furthermore, deep trap defects are thereby not passivated. A further notable strategy is strain control of the perovskite film, leading to an increase in stability due to increased activation energy of ion mobility.[17] A promising solution are also ionic additives which suppress the motion of intrinsic defects and passivate them at the same time. This lead to the aforementioned stability records in solar cells and also to major improvements in perovskite LEDs.[18,19] In solar cells, additives seem to result in a trade-off between efficiency and stability, as the most efficient devices are not the most stable ones and do not use additives.[20] There are reports of solar cells using additives with intermediate high stability and efficiency.[21] The reason for this current trade-off might be that the influence of additives on the crystallization process requires a re-optimization of the many parameters that influence the film formation. In PeLEDs, there seems to be a trend that increased efficiency correlates with better stability [22], but there are also exceptions, where the efficiency increases but the stability decreases.[19]

As pointed out by many recent reviews on the stability issue, there is a lack of understanding of the actual defect passivation effect of additives, and the need for suitable characterization

methods is identified.[16,23–27] First of all, this refers to the experimental methodology used to study dynamic processes. One prominent example is the occurrence of a hysteresis in the current-voltage curve. The debate on the origin went on for years until ions got commonly accepted as culprit, but it took more time until the full picture of the ion-interface deep trap relation evolved.[28] Further examples are impedance spectroscopy where the interpretation of a negative capacitance was solved only recently [29,30], or intensity-modulated photocurrent spectroscopy where the interpretation is still unclear [31]. Conventional characterization methods are increasingly used to probe dynamic processes, such as transient Kelvin probe force microscopy (KPFM) to reveal charge accumulation and recombination processes on the time scale of seconds [32], as well as photoluminescence measurements to track halide segregation within minutes to hours [33]. Many effects are well studied on their own [27], however, the great complexity during operation of a device originates from their interplay. In addition, many studies are conducted laterally on films or very thick active layer devices due to the resolution limit of an individual experimental method, and results might not be directly transferable to thin operated device.

This work transfers the gained knowledge on trap and ion induced dynamics in super yellow polymer LEDs and LECs from chapter 2 to chapter 5 to PeLEDs. Potential dynamic processes are discussed in detail first before a $CsPbBr_3$ system is investigated. No passivating additives are added to the perovskite layer to pinpoint ionic effects to intrinsic ions, which would not be straightforward otherwise as additives often introduce mobile ionic species.

Dynamic processes in perovskite devices

Figure 6.1 displays dynamic processes in a PeLED in comparison to an organic LED/LEC as discussed in section 1.3.3. Electronic processes faster than ns, such as phonon interactions [34,35] or transitions like exciton dissociation[36] and formation[37] are not investigated in this chapter. Photoluminescence decay in a PeLED can also be in the order of a few ns as in an OLED [38,39] but is up to μs for passivated films of different lead based $APbX_3$ structures[18,22,40]. In contrast, electroluminescence decay is faster than in an OLED as the electronic charge carrier mobility is much higher and is thus below μs.[41] Both the displacement current and RC time are higher because the relative permittivity ε_r for perovskite materials is much larger. Typically, ε_r is around 30 [42–44], while reported values range from 6 to over 100 [45]. Optoelectrical processes faster than the RC time can be masked due to the charging and discharging time of the electrodes, as investigated for transient photovoltage measurement on perovskite solar cells.[46] Capacitive currents are also visible in a current-voltage hysteresis measurement at low currents.[47] Charge carrier mobilities are generally higher than in an OLED. Again, a large variation is found in literature as a result of different measurement techniques and material systems, ranging from $10^{-6}\ cm^2/Vs$ up to $1\ cm^2/Vs$.[45] According to the few literature works existing on trap capture dynamics in perovskite devices [38,48], the capture coefficients of free electrons and free holes can be as high as 10^{-10} cm³ s⁻¹. For a free charge carrier density in the order of 10^{17} cm⁻³ [49], 63% of the traps of the steady state ratio are already filled after $\frac{1}{C_n * n} = \frac{1}{10^{-10}\frac{cm^3}{s} * 10^{17}\ cm^{-3}} = 0.1\ \mu s$ [50,51].

However, the studies above used PL as method to characterize the non-radiative decay. It might be possible that effective capture rates are different in an electrically operated device. Ion dynamics in perovskite system are faster than in organic LEC systems with reported ion mobilities

from $10^{-9} \, cm^2/Vs$ up to $10^{-7} \, cm^2/Vs$.[52,53], leading to effects in the ms time range. There are, however, also ionic effects observed on the timescale of seconds and larger.[54,55]

Displacement current
RC time
Trap filling
e⁻/h⁺ movement
Ion movement ————|
————— PL decay
EL decay

ns | μs | ms | s
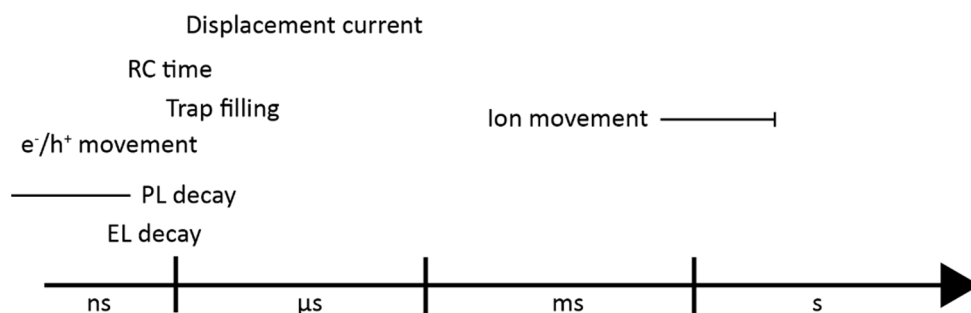
Figure 6.1. Time range of different dynamic effects in perovskite systems

The influence of ions

After the identification of the time range on which the ions move (ms to s), the possible effects they have during their movement is discussed. According to theoretical and experimental results, ion migration happens already at electric fields of $3 \, kV/cm$ and smaller.[56] The main process, as soon as an electric field is applied, is the movement of the ions to their respective interface – cations towards the negative cathode, here the $CsPbBr_3$/TPBi interface, and anions drift toward the positive anode, here the PEDOT:PSS/$CsPbBr_3$ interface. After fabrication, the devices remain in open circuit condition before the first measurement. It is not very important to know the initial distribution of holes and electrons for the simulation and interpretation of a measurement, as the focus is on slower dynamic responses, but it is relevant to know the initial ionic distribution. Often discussed is how the ion distribution looks in open circuit. Since a metal is connected to a semiconductor, there is a charge drop at the interface, in our case TPBi/Al(LiF) and ITO/PEDOT:PSS, such that there is an electric field in the vicinity of these interfaces. However, the perovskite layer is then expected to be field free. Although it is often done for simplicity, assuming and starting the simulation from a 0 V situation is not accurate, as it introduces negative fields such that ions pile up at the opposite interface.[42] However, this assumption does not introduce a major error, as the steady state situation is the same in the end, but can lead to differences during the transient simulation as shown and explained in the electrical model section of the Supporting Information. The pileup of ions at the interface introduces many effects in theory. The strong electric field within the electronic double layer screens the electric field. Firstly, this can lead to an increase of charge injection if the potential drop is high enough within a few nm next to the interface, as observed in light-emitting electrochemical cells (see section 1.2). The equivalent effect for solar cells is changes in charge extraction, which has implications for the solar cell functioning as well.[57] Secondly, the electric field within the perovskite layer is reduced, which alters the space charge distribution in the bulk.[42,45] According to a theoretical drift-diffusion analysis, this is only an issue when the bulk recombination is strong and/or the electronic charge mobility low.[28] A further effect of the ionic charge accumulation is a change of interface recombination, which has been identified as the cause for hysteresis.[58,59] There are, however, more recent reports that attribute the hysteresis to the bulk field screening effect.[45,60]

There are many claims of p-i-n or pn junction formation in the perovskite layer as a result of ion movement, as it is observed in an LEC (see section 1.2). There are about 20 perovskite publications claiming an LEC behaviour, some of them added additional Li-salt. However, the claim of junction formation relies solely on the interpretation of different current increase behaviour during a constant voltage bias.[61–65] Perovskite literature claims of p-i-n junction formation often rely on KPFM due to the possibility to measure changes in Fermi levels as a result of doping. However, band-bending due to simple charge accumulation of ions can lead to a similar effects [66], a point that is often not considered. As summarized in a recent review, intrinsic doping is theoretically (DFT) and experimentally (mostly Hall effect measurements) verified and varied by changing the stoichiometry and thus defect densities. While p-n junction have been reported, their stability due to the defect migration remains uncertain.[67] Considering additionally the reports claiming that intrinsic ions are able to screen the electric field completely in the bulk[45,60], a p-i-n junction from an LEC perspective as in the electrochemical doping model (ECD, explained in section 1.2) with an electric field drop across the intrinsic junction is unlikely. If any, then the electrodynamic (ED) model[68,69] might apply, where, however, the inability to form doped zones is not a result of poor injection as described in the ED model, but might be due to a general inability to form doped regions in a perovskite film.

While the ionic movement of the added salt in the SY LEC systems is decoupled from the optically active polymer material, the ions are part of the emissive perovskite crystal. Therefore, their movement also means essentially a change of the structural composition and therefore the band structure. This can lead to changes of the emission spectra and phase segregation.[56,70] These effects occur on timescales of seconds to minutes, which is an indication for different ionic species than the ones that are responsible for fast effects below seconds.

Trapping behaviour

Chapter 4 explains the dynamics of uncharged trap sites during filling. Besides an increase of SRH recombination during trap filling, trapped charges can also affect the space charge if the density gets high enough. There are two potential processes that are fundamentally different in perovskite systems. The first one are mobile defects in contrast to static trap sites. Many mobile defects are said to be shallow and as such do not trap many charges and do not introduce SRH recombination.[13,14,16] It is not clear, however, if deep traps are also mobile. Several studies have linked SRH recombination to halide segregation, but the trapping is seen as the cause for segregation and it is not clear whether the trap site also moves.[15,70] The consequence of moving deep traps to the interface would be similar to moving ions that create Pb-related deep traps at the interface.[71] In both situations the trap site only appears at the interface after movement of the ions. This means the time scale of the dynamic response is slow, dictated by the ionic movement, but the effect is characterized by trap filling, i.e. increase of SRH recombination and changes in space charge. The second process that would lead to a substantially different trapping dynamics is if the deep trap site density was charged beforehand, as it is the case for mainly halide and lead antisite occupations.[16,72] When an electric charge gets trapped by such a charged defect the trap site as a whole gets neutral and does in turn only deteriorate the optical performance by the introduced SRH recombination. In principle, the trapping dynamics of such charged defects would in turn lead to an increase of free space charge and thus increase of the current.

Optical model

It is very relevant to answer the question whether the outcoupling efficiency in PeLEDs also strongly depends on the emitter position as shown for organic emitters.[73–75] If so, then essentially every process that alters the space charge distribution, like ion movement or trapping, can have additionally a dynamic component on the emission characteristic due to the movement of the emission zone (EZ). EZ position dependence is rarely reported in literature, also when loss modes are discussed.[76] One study explains increasing efficiency of thinner PeLEDs with the optical model based on the oscillating dipole model as used in this thesis and as such also shows a dependence of EZ position.[77] In another work the EZ position is modified by tuning the thickness of the PEDOT:PSS transport layer. The authors hypothesised that the thinner PEDOT:PSS layer shifts the EZ closer to the TPBi electrode, which improves the EQE because they observed a higher density of quasi-2D perovskite crystals closer to the TPBi electrode.[78] There is also a report of a white PeLED that claims to have no cavity effect.[79] As explained in section 1.4.2 the Purcell effect leads to such a strong EZ position dependence. The Purcell effect has a quantum mechanical origin, where, according to Fermi's golden rule, the spontaneous emission probability depends on the optical field surrounding the excited state.[80] There is therefore no fundamental reason why it should not happen in perovskite systems. The Purcell effect was shown for a methylammonium lead iodide film by time resolved PL measurement [81], and also for lower dimensional or nanostructured perovskite films [82,83].

6.2   Results

Figure 6.2 shows the electrical and morphological characterization of an ITO/PEDOT:PSS/$CsPbBr_3$/TPBi/LiF/Al PeLED. The average efficiency of this device structure is 0.4 cd/A, the maximum efficiency reached is 1.2 cd/A. This is in accordance with literature results with the same structure and without additives, with most reported efficiencies around 1 cd/A.[84–87]
The shunt resistance is very high and around 19 MΩ (Supporting Information Figure S6.1a and Figure S6.1b. This seems surprising as the SEM image in Figure 6.2b shows many pinholes, where the evaporated TPBi directly connects to the PEDOT:PSS layer. It can be explained by the very well blocking diode of ITO/PEDOT:PSS /TPBi/LiF/Al as shown in the Supporting Information Figure S6.1c.

a)

b)

c)

70 nm Al
40 nm TPBi
~70-100 nm CsPbBr$_3$
40 nm PEDOT:PSS
135 nm ITO

Glass substrate
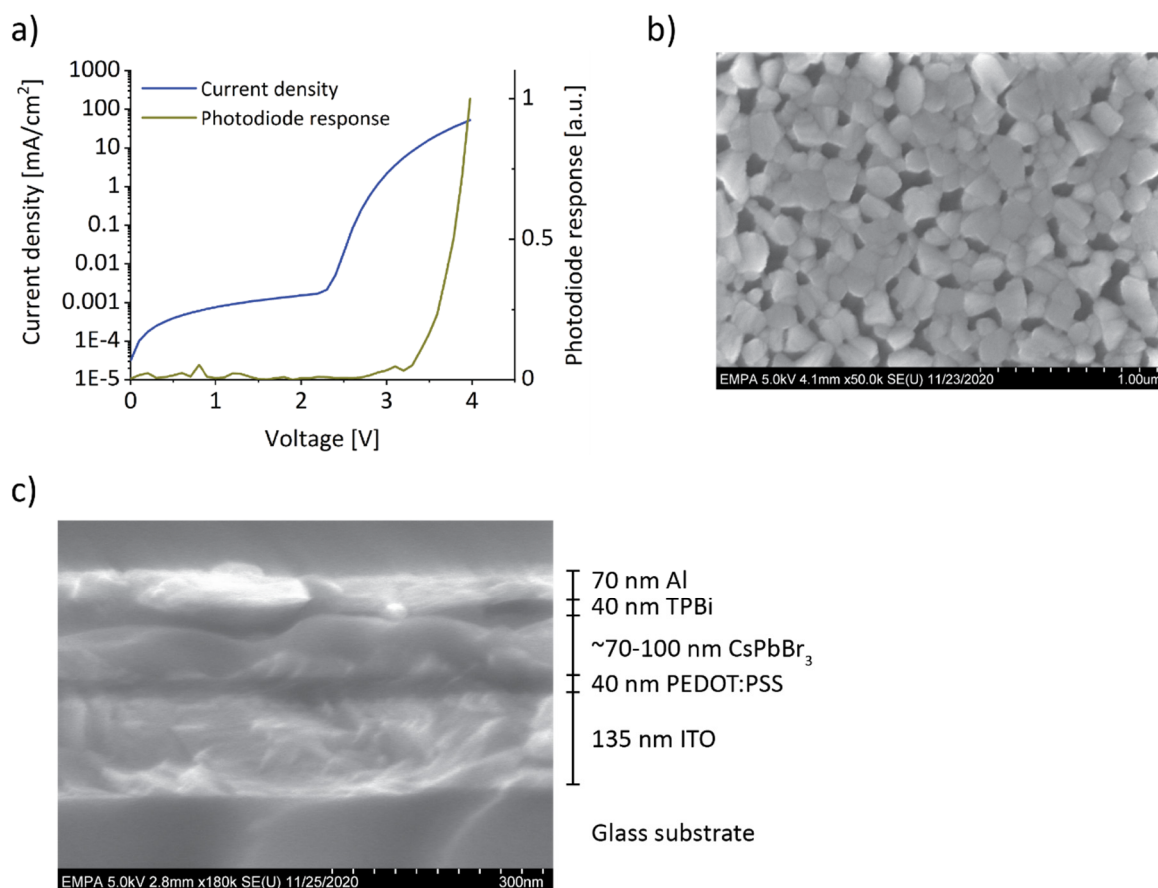
Figure 6.2. a) JV measurement of an ITO/PEDOT:PSS/CsPbBr$_3$/TPBi/LiF/Al PeLED. b) shows the top view SEM image and c) the cross section.

Figure 6.3a shows the microcavity/Purcell effect in an optical-only simulation (for an assumed constant current of 7.7 mA/cm2) of a CsPbBr$_3$ PeLED (for structure see Supporting Information Figure S6.2b) for different perovskite layer thicknesses and EZ positions. While Figure 6.3a is the result when assuming a delta emitter, the effect of a potential wide recombination zone is tested in Figure 6.3b. In this case, the spatial broad emission averages out the effects to some extent, which is especially evident for thicknesses below 70 nm where the emission covers the whole layer. Even in this extreme case the outcoupled efficiency varies by up to a factor 5 in the thickness range 70 to 130 nm. A simple optical model proof as shown in chapter 3 by processing devices with thick active layers is not possible, since the emission is too narrow for relative spectral changes. The electroluminescence (EL) spectra of CsPbBr$_3$ has a full width at half maximum (FWHM) of 20 nm, while the FWHM of super yellow (SY) is 110 nm. The perceived colour remains therefore the same also for very thick active layers as shown in Figure 6.3d and by the largest spectral change in the Supporting Information Figure S6.3a. However, since the distance to the metal electrode is essential, the thickness of the evaporated TPBi layer substantially alters the landscape as shown in Figure 6.3c for a 60 nm thick TPBi layer instead of 40 nm of a ITO/PEDOT:PSS/CsPbBr$_3$/TPBi/LiF/Al PeLED (see Supporting Information Figure S6.3b for a direct comparison between the two layer thicknesses). As the perovskite layer below is not altered, the only further difference of the two devices is the higher resistivity of a thicker TPBi layer that has

to be taken into account. Figure 6.3e shows current-voltage (JV) measurements of a PeLED with a TPBi layer thickness of 40 nm and 60 nm. The current density of the latter is slightly lower for higher voltages, presumably due to the higher resistance of the thicker TPBi layer and the resulting higher potential drop for current densities higher than 30 mA/cm^2 at about 3.7 V. Below, the current densities are very similar as a result of simultaneous processing of all layers despite the evaporated TPBi layer. It means essentially all relevant processes such as bulk and interface recombination, ion densities such as charge mobilities are similar, and therefore we assume that the emitter position is equal as well. Yet the emission and thus current efficacy is substantially higher, which is only explainable by an optical effect as discussed above.
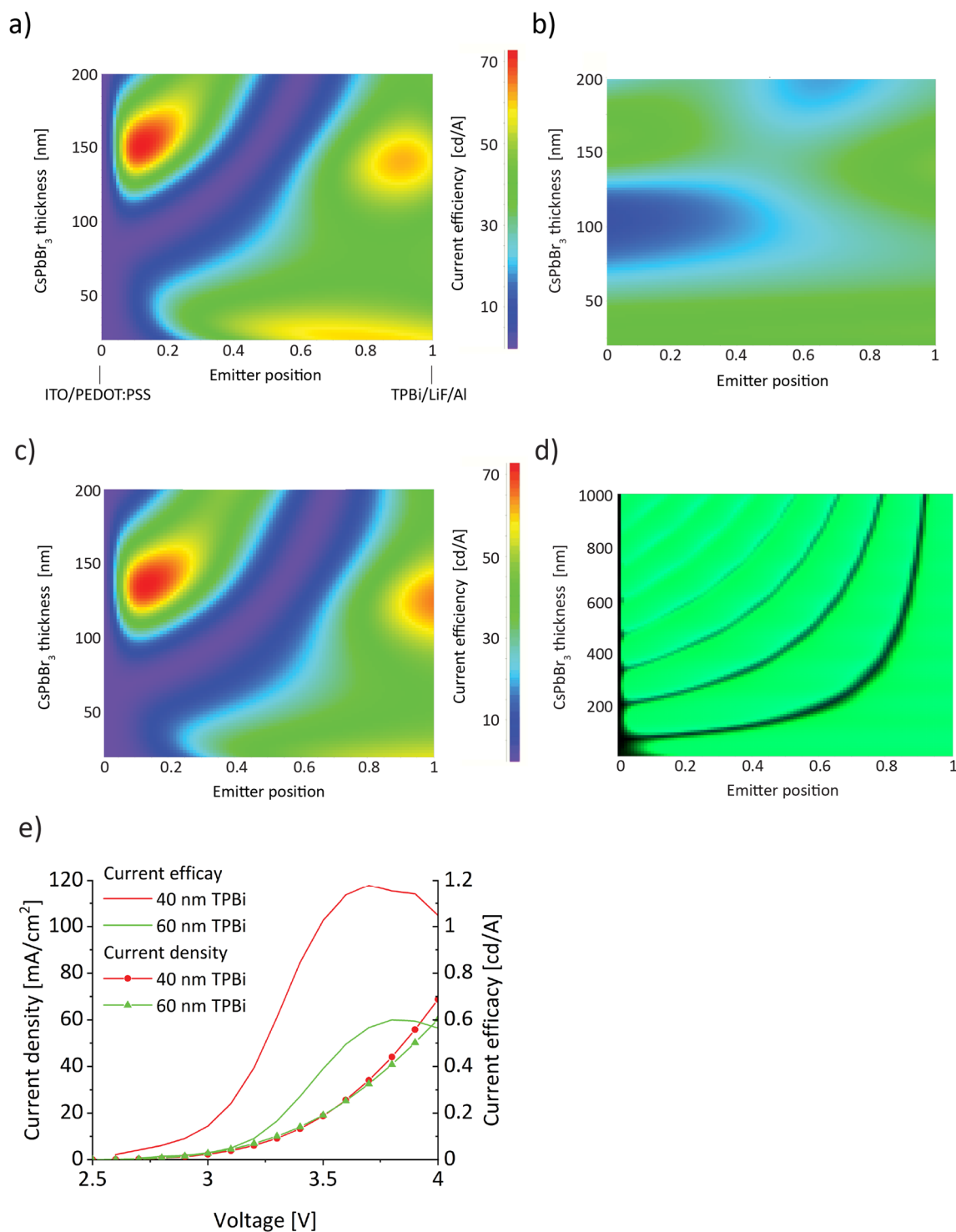
Figure 6.3. Optical simulations of the current efficiency at a 0° observer angle for a perovskite LED. The dependence of out-coupled emission on active layer thickness and emitter position is shown for a constant recombination current. The emission profile in a) is a delta peak, in b) a wide Gaussian distribution with a FWHM of 100 nm, essentially covering the whole layer such that the interference effect is less pronounced. The simulation in a) and b) is with a 40 nm TPBi layer, c)

with a 60 nm TPBi layer. d) Perceived colour up to a perovskite thickness of 1000 nm. e) JV measurement of PeLEDs with a 40 nm and 60 nm thick TPBi layer.

In the PeLED literature dynamic electrical processes are still moderately investigated. The investigation of the device stability lead to inclusion of transient optoelectrical measurements in the timescale of seconds to hours.[12] A recurring reported feature is an initial increase of the EQE before the performance degrades continuously, which is often uncommented and not investigated further.[11,19,88] It has been shown that suppression of ion mobility by 2D structuring also suppresses said feature, where the ion accumulation at the interface is assumed to influence the injection.[89] We observe a similar feature with an ITO/PEDOT:PSS/CsPbBr$_3$/TPBi/LiF/Al PeLED . The response to a 10 s voltage pulse with a high time resolution down to µs as in chapter 4 is shown in **Figure 6.4**a. The first 1000 µs look similar as for the SY PLED system with a decrease of the current. The subsequent dynamics is, however, very peculiar, especially for the emission. Impedance spectroscopy shows an increase of capacitance at the same timescale, which indicates ionic movement to the interface (see Supporting Information Figure S6.4a). As the time scale of this effect is indeed in the range of faster mobile ion species as explained in section 6.1, we investigate here the effect with drift-diffusion simulation and hypothesise the same effect as discovered in solar cells. There, hysteresis measurement was explained by ion movement to the interface where they influence the interface recombination. The potential to accurately describe the processes governed within the perovskite layer has been shown for solar cells [42,45,90], but also hole only Au/MAPbI3/Au devices [91]. Note that equations than can be derived from the drift-diffusion formalism using certain simplifications are often used in literature to evaluate data, as for example the bipolar space charge limited current (Mott-Gurney) equation [44,92], open circuit voltage calculations [15,93] or the classical Shockley diode equation [94]. A model is setup with deep trap sites at the interface and in the bulk, and ionic mobilities of $10^{-8} \, cm^2/Vs$ to match the timescale of the emission peak, in agreement with literature as discussed in section 6.1. The PEDOT:PSS and TPBi layer are also electronically simulated, the injection of electronic charge carriers comes from the ITO and LiF/Al layer. The simulation result of the voltage pulse is shown in Figure 6.4b. The features of current and emission are qualitatively reproduced until 1000 µs with a first increase of the emission to a plateau, which is the time the space charge needs to form as a result of the electron and hole movement from the electrodes. While the electronic charges can cross the perovskite layer below µs, the limiting factor here is the transit time across the organic transport layers. For an average electron mobility of $5 * 10^{-5} \frac{cm^2}{Vs}$ and electric field of $100 \frac{kV}{cm}$ across the 40 nm thick TPBi layer it takes $\frac{40 \, nm}{5*10^{-5}\frac{cm^2}{Vs} * 100\frac{kV}{cm}} = 8$ µs for electrons to cross the layer, in agreement with the timescale in the measurement when the emission starts to increase. The first emission plateau (of slight increase) is reached when the space charge is built up within the perovskite layer. There is no decrease of luminance observable as for the PLED in chapter 4 due to trap filling because here, the trap sites fill too fast with respect to the build-up of space charge.

From 1 ms onwards in the model, the ions start to pile up at the respective interfaces. With a time and space-averaged electric field of roughly 25 kV/cm (result of the simulation) a drift velocity of $v = \mu * E = 1 * 10^{-8} \frac{cm^2}{Vs} * 25 \frac{kV}{cm} = 2.5 * 10^{-4} \frac{cm}{s}$ results such that it takes 30 ms for ions to

cross the 70 nm layer to the other side. Since the ion mobility was chosen to fit the dynamic of the measurement feature from Figure 6.4a, the calculated time of 30 ms agrees with the peak of the emission. As a result, a strong rise in luminance is shown in the model, as it is also observed in the measurement. Interestingly, there is no change afterwards anymore in the simulation, while the emission in the experiment decreases again. Since the exact same measurement on the same cell 30 min later results in the same feature (see Supporting Information Figure S6.4b), it is not just an effect due to permanent degradation, but an effect apparently not covered by the model.
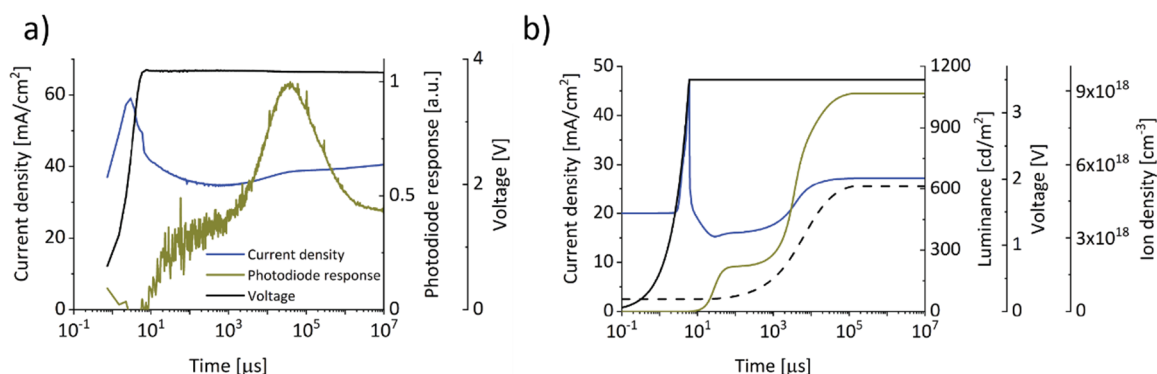
Figure 6.4. Current and light transient measurements a) and drift-diffusion simulation b) when a voltage pulse is applied for 10 s. The dashed black line in b) is the simulated anion accumulation within 2 nm from the PEDOT:PSS/CsPbBr$_3$ interface and shows the correlation of current density and luminance increase with ion movement.

6.3 Discussion

To be able to identify the missing part of the model that describes the reproducible decay of the emission, the exact cause for the emission increase in the simulation is investigated. The strong increase in the simulation is clearly a feature of ionic movement. Without ions, the emission stays on the low level of the plateau as shown in **Figure 6.5**a. As discussed, hysteresis measurement in solar cells were explained by the influence of ions on traps, specifically on interface traps.[58,59] The simulation in Figure 6.4b also shows a change of trap level during the ion movement (not shown here). Therefore, a simulation is done without any traps (Figure 6.5b), and one with only a strong interface trap density (Figure 6.5c, $10^{18} cm^{-3}$ trap density 5 nm next to both transport layers instead of the $10^{17} cm^{-3}$ bulk trap density). Both changes do have an influence on both current and emission transients, but since the emission increase from 1 ms onwards is still present, traps are not the main reason. As such, it can only be a space charge redistribution of electrons and holes as a result of the ionic charge. Initially, before the ion movement, the electrons and holes are piled up at the PEDOT:PSS and TPBi interface, respectively. This is because they have a relative high charge mobility such that they travel across the thin perovskite layer without being fully recombined by either emissive Langevin or SRH recombination. There, they cannot be extracted due to the high PEDOT:PSS LUMO and low TPBi HOMO (see Supporting Information Figure S6.2a). Essentially, the anions that move to the PEDOT:PSS interface lead to a reduction of the piled up electronic charge and thus equalize the system (the same happens for cations and holes) such that the Langevin recombination gets more efficient and the emission increases.

a)

b)

c)
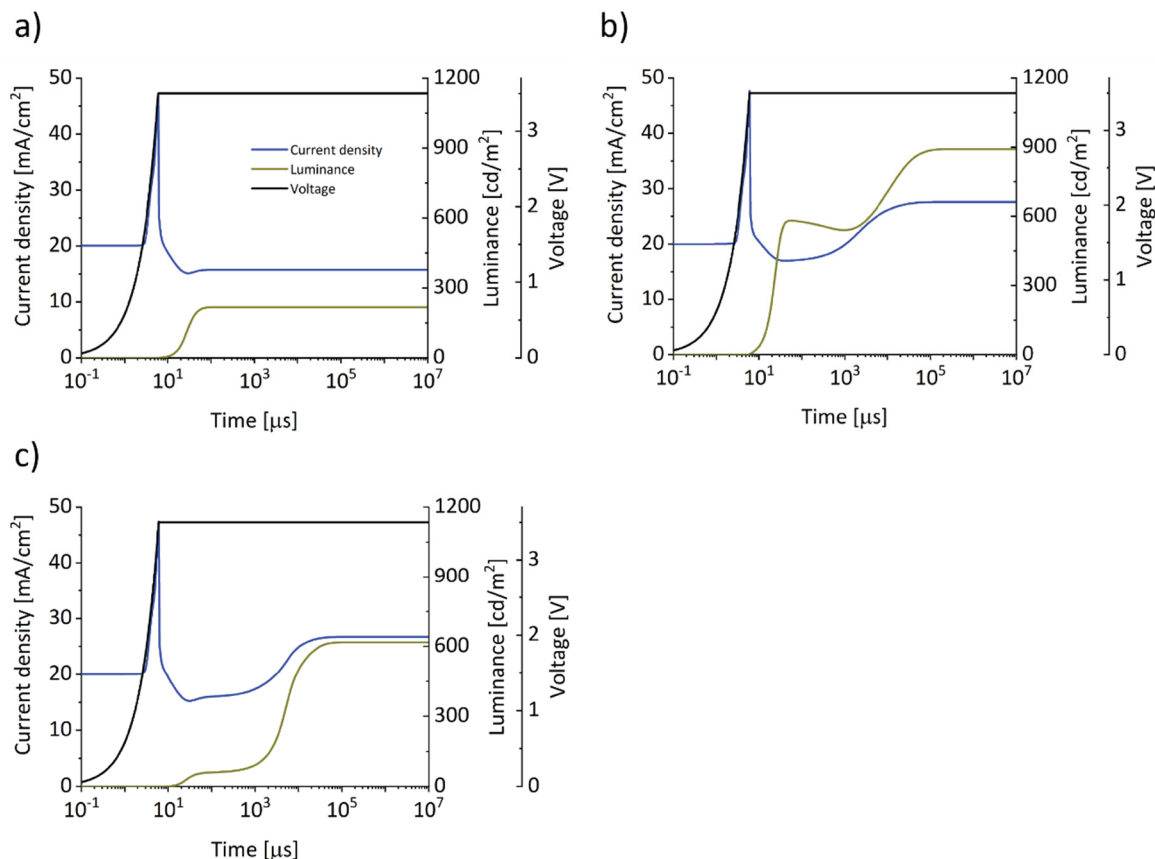
Figure 6.5. Different simulations to unravel the observed increase of the luminance after 1 ms with respect to the simulation in Figure 6.4b. a) shows the simulation without ions, where secondary emission increase is not observed. Without interface traps in b) the initial luminance increase is much higher as there is no SRH recombination and a strong interface recombination in c) decreases the luminance overall compared to Figure 6.4b, but the same features are observed.

The question is now what needs to be added to the model in order to explain the emission decrease, while the current still increases as observed in the measurement in Figure 6.4a. It cannot be a permanent effect as it is repeatable as shown in Supporting Information Figure S6.4b. A possible option is charge trapping, because an increase of trap sites can decrease the optical performance via SRH recombination without decreasing the current. **Figure 6.6** shows four simulations starting from the situation at 100 ms in Figure 6.4b and increases the interface trap level from $10^{17} cm^{-3}$ to $10^{19} cm^{-3}$ at the PEDOT:PSS and TPBi level, for hole and electron traps. While an increase of electron trap density at the PEDOT:PSS interface results in a slight current increase and strong drop of luminance, there are further possibilities not implemented in the model, as for example charged trap sites that get neutral upon trapping an electric charge [95], or emission zone shift due to changes in charge injection. Further clarification requires additional measurements and experiments, for example fabrication of electron or hole only devices to isolate certain effects.[45] An experimental difficulty is the fast rate of this effect and the fast degradation in PeLEDs in general, which limits the choice of measurement during the transient measurement as done in chapter 2 to chapter 5 for SY PLEDs and LECs, where the ion and trap dynamics changed

over hours. Similar investigation are simpler in perovskite solar cells as the processes are slower, presumably due to a lower operation voltage and thus lower electric field, and passivating additives seem to decrease the degradation rate much stronger compared to PeLED passivation.[2–4,12]
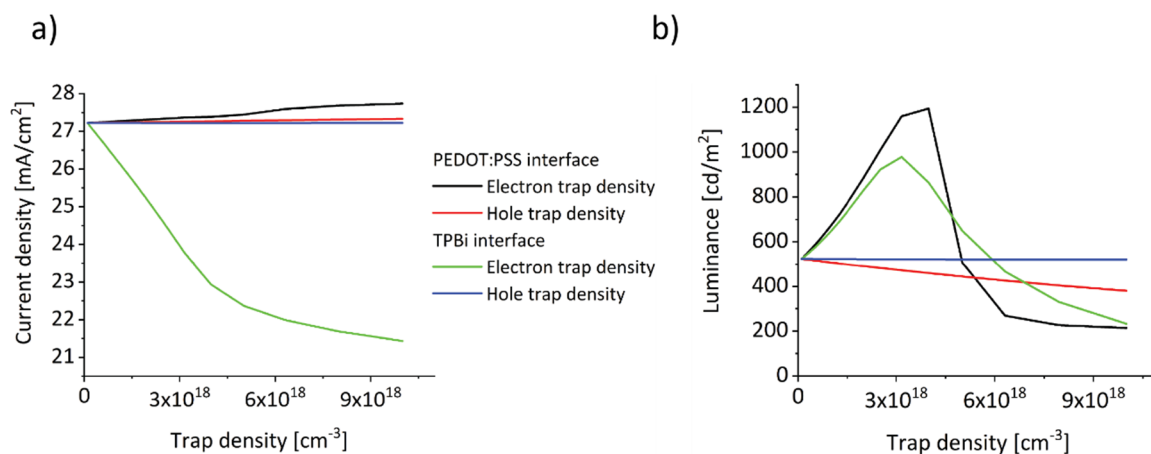
Figure 6.6. Starting from the situation at 100 ms in Figure 6.4b, the interface recombination (5 nm next to the transport layer) is increased from $10^{17} cm^{-3}$ to $10^{19} cm^{-3}$ at the PEDOT:PSS and TPBi interface for hole and electron traps. This is done individually for each of the situations and the influence on current density in a) and luminance in b) are shown.

6.4   Conclusion

Potential dynamic effects of perovskite defects are discussed with respect to their ionic character and trapping behaviour of deep trap defects. Due to the mobility of defects, many more processes compared to an organic LED/LEC system are identified. The adaption of the optical model based on the microcavity effect to the perovskite system is discussed, and experimental variation of the TPBi transport layer thickness of CsPbBr$_3$ based PeLED gives strong indication towards the validity of the optical model. A transient voltage pulse reveals an emission feature within the time range of ionic mobility. Transient drift-diffusion simulation is partially able to describe the observed emission peak by ionic movement, and missing model parts are discussed.

6.5   Experimental Section

ITO substrates were purchased from Geomatec ($\approx$11 Ω square^{-1}). Poly(3,4-ethylenedioxythiophene):poly(styrenesulfonate) (PEDOT:PSS, Clevios PVP AI 4083) was purchased from Heraeus. Lead(II) bromide (PbBr2, 99.999%) and caesium bromide (CsBr, 99.999%) were purchased from Sigma-Aldrich, as well as dimethyl sulfoxide anhydrous (DMSO, $\geq$ 99.9%). 2,2',2"-(1,3,5-Benzinetriyl)-tris(1-phenyl-1-H-benzimidazole) powder (TPBi, $\geq$ 99.8%) and lithium fluoride precipitated (LiF, $\geq$ 99.99%) were purchased from Lumtec. Aluminium pellets were purchased from Kurt J.Lesker.

CsBr and PbBr2 were dissolved in DMSO (0.5M) at a molar ratio of 1:1.7 inside the glovebox (N$_2$) and stirred at 60°C overnight.

The patterned ITO substrates were cleaned by ultrasonication in acetone (5 minutes sonication), ethanol (5 minutes sonication), in a 2% (v/v) Hellmanex III (HelmaAnalytics) before being cleaned in deionized water (3x5 min) and dried with a nitrogen gun. The substrates were then treated in oxygen plasma for 5 minutes.

PEDOT:PSS at room temperature was filtered with a 0.45 µm pore size hydrophilic filter (PTFE, Perkin Elmer) and 0.2 ml of the solution was spin coated onto the ITO-glass (60s, 4000 rpm, 400 rpm/s). The substrates were annealed at 150°C for 10 minutes in ambient atmosphere followed by an additional 10 minutes at 120°C inside the glovebox. 0.2 ml filtered (0.45 µm PTFE, VWR) perovskite precursor solution was spin-coated (60s, 4000 rpm, 1000 rpm/s) and annealed at 80°C for 10 minutes, where a yellowish film is formed after a few seconds. 40 nm of TPBi was thermally evaporated at 0.2 Å/s for 20 nm and subsequently 0.4 Å/s for 20 nm, followed by 1 nm of LiF at 0.1 Å/s. Then 70 nm of Al was evaporated at 0.2 Å/s for 10 nm and 0.4 Å/s for 60 nm with a shadow masks to create round electrodes of the size 0.031 cm2 and 0.071 cm2.

Scanning electron microscope images were measured on a Hitachi-S-4800.

Optical and electrical simulations were performed with Setfos 5.1 (Fluxim AG, Switzerland). Simulation procedures and parameters are described in the Supporting Information.

References

[1]   The National Renewable Energy Laboratory, Best Research-Cell Efficiency Chart, Champion Photovoltaic Module Efficiency Chart **2021**.

[2]   S. Wang, B. Yang, J. Han, Z. He, T. Li, Q. Cao, J. Yang, J. Suo, X. Li, Z. Liu, S. (Frank) Liu, C. Tang, A. Hagfeldt, *Energy Environ. Sci.* **2020**, *13*, 5068.

[3]   Y.-H. Lin, N. Sakai, P. Da, J. Wu, H. C. Sansom, A. J. Ramadan, S. Mahesh, J. Liu, R. D. J. Oliver, J. Lim, L. Aspitarte, K. Sharma, P. K. Madhu, A. B. Morales-Vilches, P. K. Nayak, S. Bai, F. Gao, C. R. M. Grovenor, M. B. Johnston, J. G. Labram, J. R. Durrant, J. M. Ball, B. Wenger, B. Stannowski, H. J. Snaith, *Science* **2020**, *369*, 96.

[4]   S. Bai, P. Da, C. Li, Z. Wang, Z. Yuan, F. Fu, M. Kawecki, X. Liu, N. Sakai, J. T.-W. Wang, S. Huettner, S. Buecheler, M. Fahlman, F. Gao, H. J. Snaith, *Nature* **2019**, *571*, 245.

[5]   M. V. Khenkin, E. A. Katz, A. Abate, G. Bardizza, J. J. Berry, C. Brabec, F. Brunetti, V. Bulović, Q. Burlingame, A. Di Carlo, R. Cheacharoen, Y.-B. Cheng, A. Colsmann, S. Cros, K. Domanski, M. Dusza, C. J. Fell, S. R. Forrest, Y. Galagan, D. Di Girolamo, M. Grätzel, A. Hagfeldt, E. von Hauff, H. Hoppe, J. Kettle, H. Köbler, M. S. Leite, S. Liu, Y.-L. Loo, J. M. Luther, C.-Q. Ma, M. Madsen, M. Manceau, M. Matheron, M. McGehee, R. Meitzner, M. K. Nazeeruddin, A. F. Nogueira, Ç. Odabaşı, A. Osherov, N.-G. Park, M. O. Reese, F. De Rossi, M. Saliba, U. S. Schubert, H. J. Snaith, S. D. Stranks, W. Tress, P. A. Troshin, V. Turkovic, S. Veenstra, I. Visoly-Fisher, A. Walsh, T. Watson, H. Xie, R. Yıldırım, S. M. Zakeeruddin, K. Zhu, M. Lira-Cantu, *Nat. Energy* **2020**, *5*, 35.

[6]   M. Vázquez, I. Rey-Stolle, *Prog. Photovoltaics Res. Appl.* **2008**, *16*, 419.

[7]   M. M. Lee, J. Teuscher, T. Miyasaka, T. N. Murakami, H. J. Snaith, *Science* **2012**, *338*, 643.

[8]   Z.-K. Tan, R. S. Moghaddam, M. L. Lai, P. Docampo, R. Higler, F. Deschler, M. Price, A. Sadhanala, L. M. Pazos, D. Credgington, F. Hanusch, T. Bein, H. J. Snaith, R. H. Friend, *Nat. Nanotechnol.* **2014**, *9*, 687.

[9]   Y.-H. Kim, S. Kim, A. Kakekhani, J. Park, J. Park, Y.-H. Lee, H. Xu, S. Nagane, R. B. Wexler, D.-

H. Kim, S. H. Jo, L. Martínez-Sarti, P. Tan, A. Sadhanala, G.-S. Park, Y.-W. Kim, B. Hu, H. J. Bolink, S. Yoo, R. H. Friend, A. M. Rappe, T.-W. Lee, *Nat. Photonics* **2021**, *15*, 148.

[10] Z. Chen, Z. Li, T. R. Hopper, A. A. Bakulin, H.-L. Yip, *Reports Prog. Phys.* **2021**, *84*, 046401.

[11] X.-K. Liu, W. Xu, S. Bai, Y. Jin, J. Wang, R. H. Friend, F. Gao, *Nat. Mater.* **2021**, *20*, 10.

[12] G. Li, K. Chen, Y. Cui, Y. Zhang, Y. Tian, B. Tian, Y. Hao, Y. Wu, H. Zhang, *Adv. Opt. Mater.* **2020**, *8*, 1902012.

[13] Y. Chen, H. Zhou, *J. Appl. Phys.* **2020**, *128*, 060903.

[14] D. Meggiolaro, F. De Angelis, *ACS Energy Lett.* **2018**, *3*, 2206.

[15] S. Mahesh, J. M. Ball, R. D. J. Oliver, D. P. McMeekin, P. K. Nayak, M. B. Johnston, H. J. Snaith, *Energy Environ. Sci.* **2020**, *13*, 258.

[16] L. Fu, H. Li, L. Wang, R. Yin, B. Li, L. Yin, *Energy Environ. Sci.* **2020**, *13*, 4017.

[17] D.-J. Xue, Y. Hou, S.-C. Liu, M. Wei, B. Chen, Z. Huang, Z. Li, B. Sun, A. H. Proppe, Y. Dong, M. I. Saidaminov, S. O. Kelley, J.-S. Hu, E. H. Sargent, *Nat. Commun.* **2020**, *11*, 1514.

[18] M. Abdi-Jalebi, Z. Andaji-Garmaroudi, S. Cacovich, C. Stavrakas, B. Philippe, J. M. Richter, M. Alsari, E. P. Booker, E. M. Hutter, A. J. Pearson, S. Lilliu, T. J. Savenije, H. Rensmo, G. Divitini, C. Ducati, R. H. Friend, S. D. Stranks, *Nature* **2018**, *555*, 497.

[19] J. H. Warby, B. Wenger, A. J. Ramadan, R. D. J. Oliver, H. C. Sansom, A. R. Marshall, H. J. Snaith, *ACS Nano* **2020**, *14*, 8855.

[20] E. H. Jung, N. J. Jeon, E. Y. Park, C. S. Moon, T. J. Shin, T.-Y. Yang, J. H. Noh, J. Seo, *Nature* **2019**, *567*, 511.

[21] X. Zheng, Y. Hou, C. Bao, J. Yin, F. Yuan, Z. Huang, K. Song, J. Liu, J. Troughton, N. Gasparini, C. Zhou, Y. Lin, D.-J. Xue, B. Chen, A. K. Johnston, N. Wei, M. N. Hedhili, M. Wei, A. Y. Alsalloum, P. Maity, B. Turedi, C. Yang, D. Baran, T. D. Anthopoulos, Y. Han, Z.-H. Lu, O. F. Mohammed, F. Gao, E. H. Sargent, O. M. Bakr, *Nat. Energy* **2020**, *5*, 131.

[22] W. Xu, Q. Hu, S. Bai, C. Bao, Y. Miao, Z. Yuan, T. Borzda, A. J. Barker, E. Tyukalova, Z. Hu, M. Kawecki, H. Wang, Z. Yan, X. Liu, X. Shi, K. Uvdal, M. Fahlman, W. Zhang, M. Duchamp, J.-M. Liu, A. Petrozza, J. Wang, L.-M. Liu, W. Huang, F. Gao, *Nat. Photonics* **2019**, *13*, 418.

[23] F. Zhang, K. Zhu, *Adv. Energy Mater.* **2020**, *10*, 1902579.

[24] X. Deng, L. Xie, S. Wang, C. Li, A. Wang, Y. Yuan, Z. Cao, T. Li, L. Ding, F. Hao, *Chem. Eng. J.* **2020**, *398*, 125594.

[25] S. Singh, Laxmi, D. Kabra, *J. Phys. D. Appl. Phys.* **2020**, *53*, 503003.

[26] S. Akin, N. Arora, S. M. Zakeeruddin, M. Grätzel, R. H. Friend, M. I. Dar, *Adv. Energy Mater.* **2020**, *10*, 1903090.

[27] M. Kim, S. Ham, D. Cheng, T. A. Wynn, H. S. Jung, Y. S. Meng, *Adv. Energy Mater.* **2020**, *2001753*, 2001753.

[28] N. Wu, D. Walter, A. Fell, Y. Wu, K. Weber, *J. Phys. Chem. C* **2020**, *124*, 219.

[29] H. Wang, A. Guerrero, A. Bou, A. M. Al-Mayouf, J. Bisquert, *Energy Environ. Sci.* **2019**, *12*, 2054.

[30] F. Ebadi, N. Taghavinia, R. Mohammadpour, A. Hagfeldt, W. Tress, *Nat. Commun.* **2019**, *10*, 1574.

[31] D. Cardenas-Morcoso, A. Bou, S. Ravishankar, M. García-Tecedor, S. Gimenez, J. Bisquert, *ACS Energy Lett.* **2020**, *5*, 187.

[32] D. Toth, B. Hailegnaw, F. Richheimer, F. A. Castro, F. Kienberger, M. C. Scharber, S. Wood,

G. Gramse, *ACS Appl. Mater. Interfaces* **2020**, *12*, 48057.

[33]   A. J. Knight, J. B. Patel, H. J. Snaith, M. B. Johnston, L. M. Herz, *Adv. Energy Mater.* **2020**, *10*, 1903488.

[34]   T. Debnath, D. Sarker, H. Huang, Z. Han, A. Dey, L. Polavarapu, S. V Levchenko, J. Feldmann, *Nat. Commun.* **2021**, *12*, 2629.

[35]   C. C. S. Chan, K. Fan, H. Wang, Z. Huang, D. Novko, K. Yan, J. Xu, W. C. H. Choy, I. Lončarić, K. S. Wong, *Adv. Energy Mater.* **2021**, *11*, 2003071.

[36]   N. L. Tran, M. H. Elkins, D. P. McMeekin, H. J. Snaith, G. D. Scholes, *J. Phys. Chem. Lett.* **2020**, *11*, 10081.

[37]   D. Meggiolaro, F. Ambrosio, E. Mosconi, A. Mahata, F. De Angelis, *Adv. Energy Mater.* **2020**, *10*, 1902748.

[38]   I. Karimata, K. Ohta, Y. Kobori, T. Tachikawa, *ACS Appl. Mater. Interfaces* **2018**, *10*, 37057.

[39]   M. A. Becker, R. Vaxenburg, G. Nedelcu, P. C. Sercel, A. Shabaev, M. J. Mehl, J. G. Michopoulos, S. G. Lambrakos, N. Bernstein, J. L. Lyons, T. Stöferle, R. F. Mahrt, M. V. Kovalenko, D. J. Norris, G. Rainò, A. L. Efros, *Nature* **2018**, *553*, 189.

[40]   C.-H. Gao, F.-X. Yu, Z.-Y. Xiong, Y.-J. Dong, X.-J. Ma, Y. Zhang, Y.-L. Jia, R. Wang, P. Chen, D.-Y. Zhou, Z.-H. Xiong, *Org. Electron.* **2019**, *70*, 264.

[41]   M. Xu, Q. Peng, W. Zou, L. Gu, L. Xu, L. Cheng, Y. He, M. Yang, N. Wang, W. Huang, J. Wang, *Appl. Phys. Lett.* **2019**, *115*, 041102.

[42]   M. T. Neukom, A. Schiller, S. Züfle, E. Knapp, J. Ávila, D. Pérez-del-Rey, C. Dreessen, K. P. S. Zanoni, M. Sessolo, H. J. Bolink, B. Ruhstaller, *ACS Appl. Mater. Interfaces* **2019**, *11*, 23320.

[43]   N. E. Courtier, J. M. Cave, J. M. Foster, A. B. Walker, G. Richardson, *Energy Environ. Sci.* **2019**, *12*, 396.

[44]   E. A. Duijnstee, J. M. Ball, V. M. Le Corre, L. J. A. Koster, H. J. Snaith, J. Lim, *ACS Energy Lett.* **2020**, *5*, 376.

[45]   M. Sajedi Alvar, P. W. M. Blom, G.-J. A. H. Wetzelaer, *Nat. Commun.* **2020**, *11*, 4023.

[46]   Z. S. Wang, F. Ebadi, B. Carlsen, W. C. H. Choy, W. Tress, *Small Methods* **2020**, *4*, 2000290.

[47]   G. Garcia-Belmonte, J. Bisquert, *ACS Energy Lett.* **2016**, *1*, 683.

[48]   X. Fu, K. J. Weber, T. P. White, *J. Appl. Phys.* **2018**, *124*, 073102.

[49]   N. Tessler, Y. Vaynzof, *ACS Energy Lett.* **2020**, *5*, 1260.

[50]   M. Diethelm, M. Bauer, W.-H. Hu, C. Vael, S. Jenatsch, P. W. M. Blom, F. Nüesch, R. Hany, *To be Submitt. soon* **2021**.

[51]   W. Shockley, W. T. Read, *Phys. Rev.* **1952**, *87*, 835.

[52]   J. Zhang, C. Li, M. Chen, K. Huang, *J. Phys. D. Appl. Phys.* **2021**, *54*, 044002.

[53]   A. R. Bowring, L. Bertoluzzi, B. C. O'Regan, M. D. McGehee, *Adv. Energy Mater.* **2018**, *8*, 1702365.

[54]   Y. Liu, A. V Ievlev, N. Borodinov, M. Lorenz, K. Xiao, M. Ahmadi, B. Hu, S. V Kalinin, O. S. Ovchinnikova, *Adv. Funct. Mater.* **2021**, *31*, 2008777.

[55]   W. Chen, Z. Gan, M. A. Green, B. Jia, X. Wen, *Small Methods* **2021**, *5*, 2000731.

[56]   W. Zhou, J. Gu, Z. Yang, M. Wang, Q. Zhao, *J. Phys. D. Appl. Phys.* **2021**, *54*, 063001.

[57]   A. Abudulimu, L. Liu, G. Liu, N. Aimaiti, B. Rezek, Q. Chen, *J. Energy Chem.* **2020**, *47*, 132.

[58]   M. T. Neukom, S. Züfle, E. Knapp, M. Makha, R. Hany, B. Ruhstaller, *Sol. Energy Mater. Sol. Cells* **2017**, *169*, 159.

[59]   P. Calado, A. M. Telford, D. Bryant, X. Li, J. Nelson, B. C. O'Regan, P. R. F. Barnes, *Nat. Commun.* **2016**, *7*, 13831.

[60]   T. Zhang, C. Hu, S. Yang, *Small Methods* **2019**, *1900552*, 1.

[61]   A. Mishra, M. Alahbakhshi, R. Haroldson, L. D. Bastatas, Q. Gu, A. A. Zakhidov, J. D. Slinker, *Adv. Opt. Mater.* **2020**, *8*, 2000226.

[62]   D. Gets, M. Alahbakhshi, A. Mishra, R. Haroldson, A. Papadimitratos, A. Ishteev, D. Saranin, S. Anoshkin, A. Pushkarev, E. Danilovskiy, S. Makarov, J. D. Slinker, A. A. Zakhidov, *Adv. Opt. Mater.* **2021**, *9*, 2001715.

[63]   M. F. Aygüler, M. D. Weber, B. M. D. Puscher, D. D. Medina, P. Docampo, R. D. Costa, *J. Phys. Chem. C* **2015**, *119*, 12047.

[64]   B. M. D. Puscher, M. F. Aygüler, P. Docampo, R. D. Costa, *Adv. Energy Mater.* **2017**, *7*, 1.

[65]   P. Andričević, X. Mettan, M. Kollár, B. Náfrádi, A. Sienkiewicz, T. Garma, L. Rossi, L. Forró, E. Horváth, *ACS Photonics* **2019**, *6*, 967.

[66]   S. Sadewasser, N. Nicoara, S. D. Solares, *Beilstein J. Nanotechnol.* **2018**, *9*, 1272.

[67]   J. Euvrard, Y. Yan, D. B. Mitzi, *Nat. Rev. Mater.* **2021**, *6*, 531.

[68]   K. Schlingman, Y. Chen, R. S. Carmichael, T. B. Carmichael, *Adv. Mater.* **2021**, *2006863*, 2006863.

[69]   E. Fresta, R. D. Costa, *Adv. Funct. Mater.* **2020**, *30*, 1908176.

[70]   A. J. Knight, L. M. Herz, *Energy Environ. Sci.* **2020**, *13*, 2024.

[71]   S. T. Birkhold, J. T. Precht, H. Liu, R. Giridharagopal, G. E. Eperon, L. Schmidt-Mende, X. Li, D. S. Ginger, *ACS Energy Lett.* **2018**, *3*, 1279.

[72]   Y. Chen, T. Shi, P. Liu, W. Xie, K. Chen, X. Xu, L. Shui, C. Shang, Z. Chen, H.-L. Yip, G. Zhou, X. Wang, *J. Mater. Chem. A* **2019**, *7*, 20201.

[73]   R. . Chance, A. Prock, R. Silbey, *Advances in Chemical Physics*; Prigogine, I.; Rice, S. A., Eds.; Advances in Chemical Physics; John Wiley & Sons, Inc.: Hoboken, NJ, USA, 1978; Vol. 162.

[74]   M. Furno, R. Meerheim, S. Hofmann, B. Lüssem, K. Leo, *Phys. Rev. B* **2012**, *85*, 115205.

[75]   L. Penninck, S. Mladenowski, K. Neyts, *J. Opt.* **2010**, *12*.

[76]   A. Liu, C. Bi, R. Guo, M. Zhang, X. Qu, J. Tian, *Adv. Opt. Mater.* **2021**, *2002167*, 2002167.

[77]   L. Zhao, K. M. Lee, K. Roh, S. U. Z. Khan, B. P. Rand, *Adv. Mater.* **2019**, *31*, 1805836.

[78]   Z. Li, Z. Chen, Y. Yang, Q. Xue, H.-L. Yip, Y. Cao, *Nat. Commun.* **2019**, *10*, 1027.

[79]   Z. Chen, Z. Li, Z. Chen, R. Xia, G. Zou, L. Chu, S.-J. Su, J. Peng, H.-L. Yip, Y. Cao, *Joule* **2021**, *5*, 456.

[80]   W. L. Barnes, *J. Mod. Opt.* **1998**, *45*, 661.

[81]   J. Wang, R. Cao, P. Da, Y. Wang, T. Hu, L. Wu, J. Lu, X. Shen, F. Xu, G. Zheng, Z. Chen, *Appl. Phys. Lett.* **2016**, *108*, 022103.

[82]   B. Gholipour, G. Adamo, D. Cortecchia, H. N. S. Krishnamoorthy, M. D. Birowosuto, N. I. Zheludev, C. Soci, *Adv. Mater.* **2017**, *29*, 1604268.

[83]   T. Abir, R. Shechter, T. Ellenbogen, Y. Bekenstein, *ACS Photonics* **2020**, *7*, 2329.

[84]   X. Liu, X. Guo, Y. Lv, Y. Hu, Y. Fan, J. Lin, X. Liu, X. Liu, *Adv. Opt. Mater.* **2018**, *6*, 1.

[85]   A. Kanwat, N. Yantara, Y. F. Ng, Y. F. Ng, T. J. N. Hooper, P. J. S. Rana, B. Febriansyah, P. C. Harikesh, T. Salim, P. Vashishtha, S. G. Mhaisalkar, S. G. Mhaisalkar, N. Mathews, N. Mathews, *ACS Energy Lett.* **2020**, *5*, 1804.

[86]   H. Wang, X. Zhang, Q. Wu, F. Cao, D. Yang, Y. Shang, Z. Ning, W. Zhang, W. Zheng, Y. Yan,

S. V. Kershaw, L. Zhang, A. L. Rogach, X. Yang, *Nat. Commun.* **2019**, *10.*

[87]   L. Song, X. Guo, Y. Hu, Y. Lv, J. Lin, Z. Liu, Y. Fan, X. Liu, *J. Phys. Chem. Lett.* **2017**, *8*, 4148.

[88]   K. Lin, J. Xing, L. N. Quan, F. P. G. de Arquer, X. Gong, J. Lu, L. Xie, W. Zhao, D. Zhang, C. Yan, W. Li, X. Liu, Y. Lu, J. Kirman, E. H. Sargent, Q. Xiong, Z. Wei, *Nature* **2018**, *562*, 245.

[89]   H. Kim, J. S. Kim, J.-M. Heo, M. Pei, I.-H. Park, Z. Liu, H. J. Yun, M.-H. Park, S.-H. Jeong, Y.-H. Kim, J.-W. Park, E. Oveisi, S. Nagane, A. Sadhanala, L. Zhang, J. J. Kweon, S. K. Lee, H. Yang, H. M. Jang, R. H. Friend, K. P. Loh, M. K. Nazeeruddin, N.-G. Park, T.-W. Lee, *Nat. Commun.* **2020**, *11*, 3378.

[90]   A. Riquelme, L. J. Bennett, N. E. Courtier, M. J. Wolf, L. Contreras-Bernal, A. B. Walker, G. Richardson, J. A. Anta, *Nanoscale* **2020**, *12*, 17385.

[91]   M. Sajedi Alvar, P. W. M. Blom, G. A. H. Wetzelaer, *Adv. Electron. Mater.* **2020**, *6*, 1900935.

[92]   T. Matsushima, F. Bencheikh, T. Komino, M. R. Leyden, A. S. D. Sandanayaka, C. Qin, C. Adachi, *Nature* **2019**, *572*, 502.

[93]   W. Tress, M. Yavari, K. Domanski, P. Yadav, B. Niesen, J. P. Correa Baena, A. Hagfeldt, M. Graetzel, *Energy Environ. Sci.* **2018**, *11*, 151.

[94]   P. Caprioglio, M. Stolterfoht, C. M. Wolff, T. Unold, B. Rech, S. Albrecht, D. Neher, *Adv. Energy Mater.* **2019**, *9*, 1901631.

[95]   T. S. Sherkar, C. Momblona, L. Gil-Escrig, J. Ávila, M. Sessolo, H. J. Bolink, L. J. A. Koster, *ACS Energy Lett.* **2017**, 2, 1214.

Supporting Information

a)

b)

c)
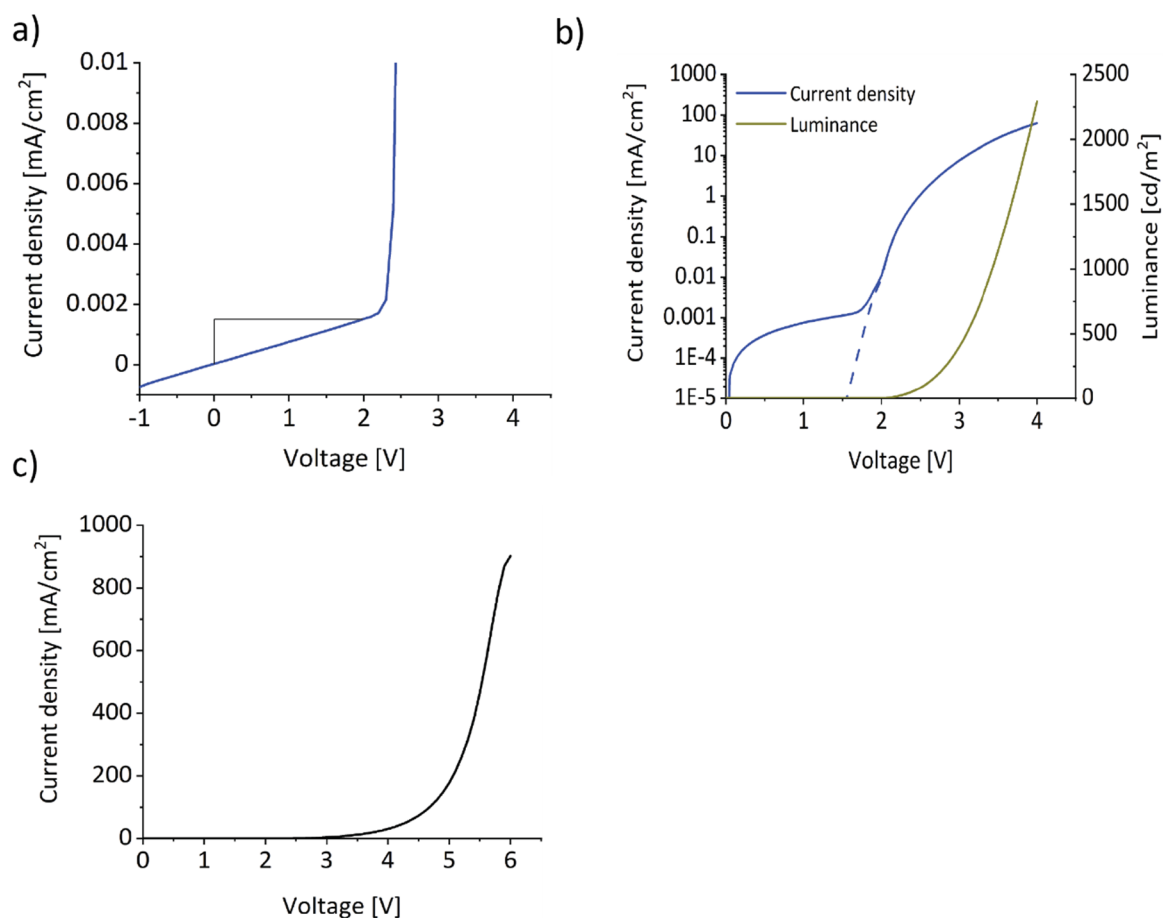
Figure S6.1. a) The linear increase at low voltages is due to a shunt resistance of $\frac{2V}{0.0015mA/cm^2 * 0.0707cm^2} = 18.86\ M\Omega$. b) JV simulation of the PeLED with a parallel resistance of $18.86\ M\Omega$ and without (dashed). For a logarithmic JV simulation it is necessary to include, but irrelevant of the current density is observed on a linear scale as in the transient measurements. c) ITO/PEDOT:PSS/TPBi/LiF/Al that shows a diode behaviour.
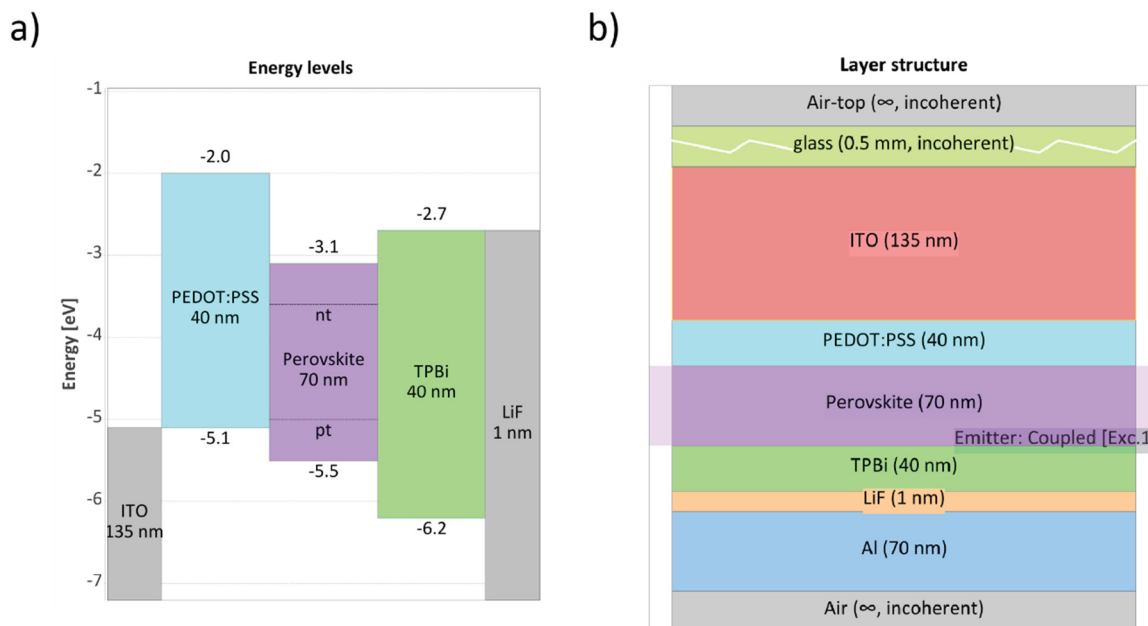
Figure S6.2. a) Energy level for the electrical simulation and b) layer structure for the coupled optical simulation
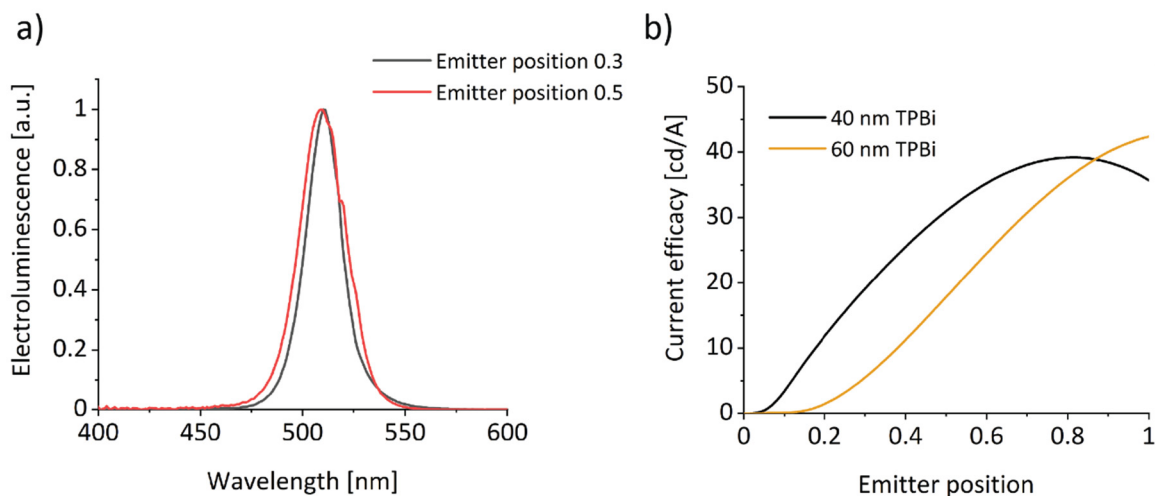
Figure S6.3. a) Outcoupled electroluminescence spectra of a PeLED with a 200 nm thick perovskite layer at a relative emitter position of 0.3 and 0.5. Spectra were normalized by a factor 0.426 W/m^{2}sr (for EP = 0.3) and 0.1 W/m^{2}sr (for EP = 0.5). b) Optical simulation of a PeLED where the TPBi thickness was changed. Shown are line plots of Figure 6.3a and Figure 6.3c at a CsPbBr3 thickness of 70 nm according to the thickness in the SEM crossection (Figure 6.2c).
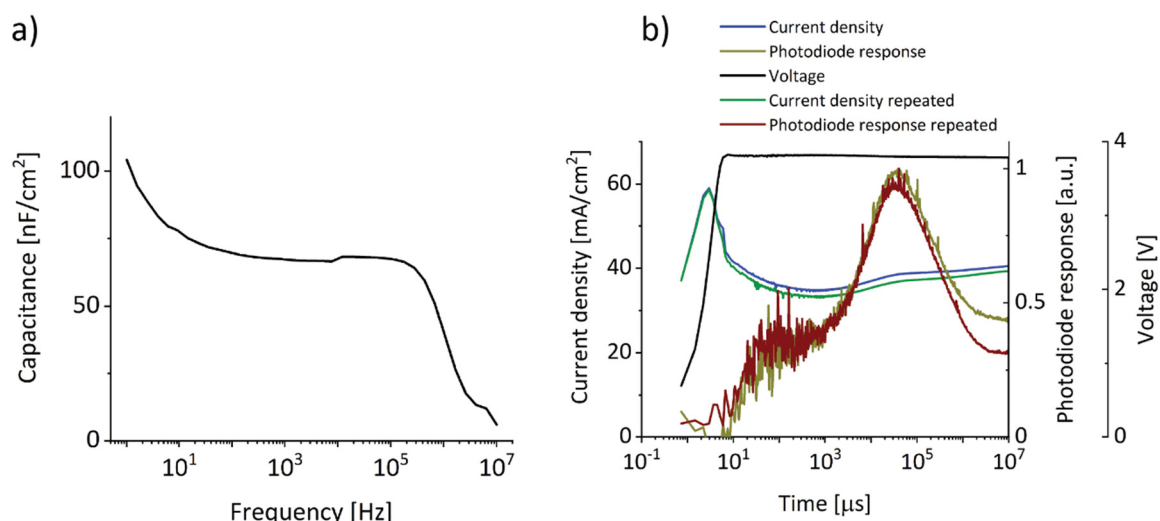
Figure S6.4. a) Impedance spectroscopy of the PeLED showing an increase of capacitance below 100-1000 Hz. This timescale matches the increase of current density between 1-10 ms. b) Repetition of the voltage pulse 30 min later results in a very similar measurement with a slightly lower current and emission showing the emission feature is not a result of permanent degradation.

Optical model

Refractive indices n and extinction coefficients k were used for each layer. Data for the 135 nm thick ITO layer were measured by spectroscopic ellipsometry. PEDOT:PSS data was taken from the Setfos database, which are labelled as Baytron P AL 4083 with reference H.C. Starck, www.hcstarck.com. $CsPbBr_3$ data was extracted from reference.[S1] TPBi data was taken from the Setfos database with reference.[S2] LiF data was as well from the Setfos database with a reference to the SOPRA n&k database. Data for the aluminium layer was taken from the Setfos software database with a reference to Woollam. Additionally, a measured $CsPbBr_3$ electroluminescence spectrum was used. The optical simulations in Figure 6.3 (besides b), main text, were performed by assuming a constant current of 7.7 mA cm^{-2} and a delta emitter (i.e. all charge carriers recombine at one position). No triplet exciton loss and an internal quantum efficiency of 100% is assumed. For all transient simulations, the recombination profile is dictated by the exciton recombination profile. It is a result of the electrical simulation, as well as the current density and internal quantum efficiency.

Electrical model

In Table S6.1 the parameters for simulation in Figure 6.4 are shown with their source. Figure S6.5 discusses the difference of a homogeneous to a 0 V preconditioned ion distribution as a starting situation for the transient simulation.

Table S6.1. Electrical model parameters

Parameter	Value	Source
Electron mobility perovskite	1×10^{-2} cm^2/Vs	reference[S3]
Hole mobility perovskite	1×10^{-2} cm^2/Vs	
PEDOT:PSS hole mobility	8×10^{-4} cm^2/Vs	Setfos material database. Reported values are usually in the order of 1×10^{-2} cm^2/Vs.[S4] The used PEDOT:PSS formulation AL4083 (Ossila) has much higher resistivity, however (of 500-5000 Ω.cm compared to other formulations with resistivities below 10 Ω.cm)
TPBi electron mobility (field dependent)	8.53×10^{-7} cm^2/Vs E0: 1390 kV/m	Setfos material database. Resulting mobilities in the electric field of the simulation vary between 5×10^{-5} cm^2/Vs and 1×10^{-4} cm^2/Vs and are in agreement with literature.[S4]
Radiative recombination coefficient	1×10^{-9} cm^3/s	
Effective density of states	1×10^{27} 1/m^3	
LUMO perovskite	3.1 eV	Bandgap agrees with measured EL peak at 2.4 eV, and Homo taken from reference.[S5]
HOMO perovskite	5.5 eV	
Ohmic hole injection from the ITO electrode	6.3×10^{15} cm^{-3}	This injection density is equal to a injection barrier into the transport levels of 0.3 eV
Ohmic electron injection from the LiF/Al electrode	6.3×10^{15} cm^{-3}	
Relative permittivity perovskite	24	reference[S6]
Applied voltage	3.5 V	Close to measurement voltage (3.8V)
Trap site density of electrons and holes	1×10^{17} 1/cm^3	
Electron trap depth	0.5 eV	
Hole trap depth	0.5 eV	
Capture coefficients	1×10^{-10} cm^3/s	references[S7,S8]
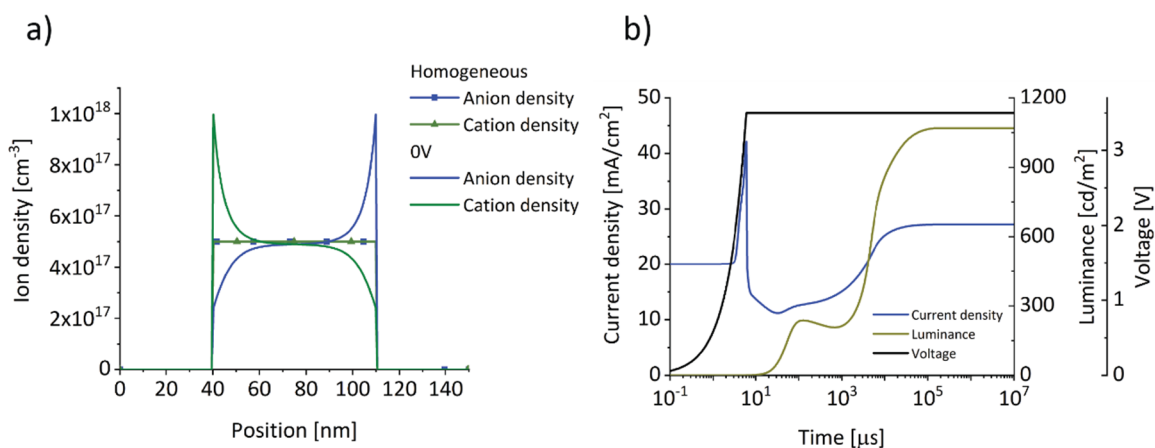
Figure S6.5. a) Initial homogenous ion distribution and an initial ion distribution at 0 V, where the ions are situated at the opposite electrode due to the internal electric field at 0 V with respect to their position at the biased steady state. As a consequence, their initial movement away towards the other electrode leads to a decrease of luminance as a result of higher SRH recombination as shown in b) from 100 μs to 1ms, which was suppressed due to the ions at the interface beforehand.

References

[S1]   W. Yan, L. Mao, P. Zhao, A. Mertens, S. Dottermusch, H. Hu, Z. Jin, B. S. Richards, *Opt. Express* **2020**, *28*, 15706.

[S2]   A. Salehi, Y. Chen, X. Fu, C. Peng, F. So, *ACS Appl. Mater. Interfaces* **2018**, *10*, 9595.

[S3]   M. Sajedi Alvar, P. W. M. Blom, G.-J. A. H. Wetzelaer, *Nat. Commun.* **2020**, *11*, 4023.

[S4]   Z. Chen, Z. Li, T. R. Hopper, A. A. Bakulin, H.-L. Yip, *Reports Prog. Phys.* **2021**, *84*, 046401.

[S5]   A. Kanwat, N. Yantara, Y. F. Ng, Y. F. Ng, T. J. N. Hooper, P. J. S. Rana, B. Febriansyah, P. C. Harikesh, T. Salim, P. Vashishtha, S. G. Mhaisalkar, S. G. Mhaisalkar, N. Mathews, N. Mathews, *ACS Energy Lett.* **2020**, *5*, 1804.

[S6]   N. E. Courtier, J. M. Cave, J. M. Foster, A. B. Walker, G. Richardson, *Energy Environ. Sci.* **2019**, *12*, 396.

[S7]   X. Fu, K. J. Weber, T. P. White, *J. Appl. Phys.* **2018**, *124*, 073102.

[S8]   I. Karimata, K. Ohta, Y. Kobori, T. Tachikawa, *ACS Appl. Mater. Interfaces* **2018**, *10*, 37057.

Conclusion and Outlook

The basic operation principles of the light-emitting electrochemical cell (LEC) have been firmly established after 25 years of research. The mixed electronic/ionic conduction has as well been the focus of extensive research in perovskite LEDs (PeLEDs) and solar cells, as the relevance of ionic movement for their operational performance has been recognized. Yet, this work reveals a large gap in the understanding of operational processes in those systems, because of the high complexity the combination of ionic and electronic charges brings about.

By investigating the ion concentration and active layer thickness in a super yellow (SY) polymer LEC (PLEC) it was observed that the efficiency of SY LECs can be improved to values that agree with the performance of state-of-the art SY polymer LEDs (PLEDs). While the influence of the electrolyte concentration is explained by the electrochemical doping model, the thickness variation implies unexplored optical effects. An optical model including the microcavity/Purcell effect was introduced that shows the strong dependence of the outcoupling efficiency on the emitter position (EP) within the SY layer. Effects of doping and reabsorption losses were studied. For thin SY layers, however, it is not simple to pinpoint the location of the emitter.

Thicker active layers were used such that the EP could be determined by comparing experimental angle dependent emission spectra with optical simulations. A continuous change of the emission colour of the thick LEC under operation provided a direct visual indication of a moving EP. A combination of experiments and electrical drift-diffusion simulation demonstrated that the observed EZ shift and the measured capacitance trend in PLECs are due to an imbalance between cation and anion mobility, and are therefore effects of ionic redistribution. The findings indicate that the initial current decay during operation is intrinsic and not due to device degradation, and that for a homogeneous initial ion distribution and similar ionic mobilities no EP shift occurs over time. Although no EP shift occurs, the model still predicts a widening of the intrinsic region. Investigation of this prediction by experimental changes of the cation to anion mobility ratio would give an indication about the generality of the developed drift-diffusion model. Such changes have been done in literature, for example by altering the end-group of the ion transporter TMPE used in this work.

The analysis suggested so far unexplored electrical effects in the LEC during operation. Therefore, the dynamics of electron trap filling and de-trapping in SY PLEDs were studied by measuring the device response to electrical driving and breaks covering the timescale from microseconds to hours. From this analysis, the universal deep electron trap in semiconducting polymers could be identified, but with a surprisingly slow trap filling rate. The analysis favours the proposed hydrated oxygen complex as the origin for the charge trap, with a slow diffusion process involved in the complex formation. The results provide useful insight to pinpoint the chemical nature of the universal electron traps in future studies. The slow complex formation time can be utilized to observe differences in an in-situ driven material characterization measurement that detects the complex directly, for example by infrared spectroscopy. The trap recovery trend suggests that after de-trapping oxygen and water separate via diffusion, and the probability for complex formation decreases with increasing time at rest. During device operation, trapped electrons recombine with free holes as part of the Shockley-Read-Hall (SRH) process. This results also in trap

deactivation, but the outcome is different from the situation at rest. Shortly after de-trapping, water and oxygen are still close and in a dynamic equilibrium with the complex, which can immediately capture a free electron and stabilize again. As such, the equilibrated density of complex trap sites should depend on the free electron density. This hypothesis can be investigated by doing the same characterization at lower current densities, where the free electron density is lower as well. The complex should then have more time to separate and diffuse after de-trapping, such that the equilibrated density of complex trap sites is smaller, and in turn also the SRH recombination. However, this analysis is difficult because the fraction of trap sites that are filled i.e. the trapped charge density depends as well on the free charge and thus current density.

The same electron charge trap features have been identified in the SY LEC. Further investigation by electroabsorption measurement indicated the formation of hole traps as well. This presents an important polymer-intrinsic degradation mechanism that limits the stability of PLECs, which has not been addressed so far. Further work should thus focus on similar strategies as used in the PLED field to decrease long-term degradation, for example by diluting the polymer with a large-bandgap semiconductor, which eliminates the effect of traps and thereby increases the device lifetime. Hole trap formation in polymers occurs via the interaction of excitons with free holes. To prevent hole trap formation, a SY host-emitting guest approach can be tested as well, because in this case the exciton and free hole are located on different materials.

The developed methodology on the interplay of electronic charges, ions and trapping is applied to perovskite PeLEDs. Many more dynamic effects compared to the PLEC/PLED system are identified, e.g. due to the mobility of charged trapping defects. The adaption of the optical model based on the microcavity effect to the perovskite system is discussed and indications towards the validity of the optical model has been found in a $CsPbBr_3$ PeLED. A peculiar emission feature revealed by a transient voltage pulse measurement in the milliseconds is within the time range of the ionic mobility. Transient drift-diffusion simulation is partially able to describe the observed emission peak by ionic movement, and missing model parts are discussed. Further clarification requires additional measurements and experiments, for example fabrication of electron- or hole-only devices, such that effects from electron and hole trap species can be investigated separately. Another method consists of repeated fast measurements during the dynamic change of interest (i.e. ionic or trap redistribution) that do not alter the dynamic process itself. Examples are impedance spectroscopy at low frequencies as a measure of ionic EDL formation, or fast voltage pulses to track the first emission increase as a measure for trapping. However, the fast timescale of this dynamic feature and the fast degradation in PeLEDs complicates such an analysis, as the requirement of not altering the ionic or trap distribution is likely not fulfilled. These investigations are simpler in perovskite solar cells as the processes are slower, presumably due to the lower applied electric field. With a set of complementary measurements at hand that are able to identify individual trap- or ion-related processes, a second step then can be to understand the effect of additives on deep and shallow point defects. There are many open questions that needs to be answered in more detail in my opinion, such as how deep trap states are related to ion migration and what their relevance for changes in performance is, how the dynamics of trap filling and de-trapping are related to ion migration and their stabilization, what the role of mobile defects and deep traps are in device degradation or what the fundamental effect of passivation by ionic additives is. Without a clearer understanding, it might a tedious work to improve the stability from

days to years. For example, accelerated testing metrics to predict the stability of perovskite solar cells require understanding whether a testing protocol properly reflects the intrinsic stability or introduces additional degradation paths.

Curriculum Vitae

Matthias Diethelm

Empa - Swiss Federal Laboratories for Materials Science and Technology
Laboratory for Functional Polymers
Überlandstrasse 129 - 8600 Dübendorf, Switzerland
matthias.diethelm@empa.ch

Personal information

Date of birth	27 December 1989
Nationality	Swiss
OrcID	orcid.org/0000-0002-8899-1755
Scopus author ID	56725496000

Education

06.2017 - present
Defence: 08.2021

PhD Student in Materials Science and Engineering, *EPF Lausanne*, Laboratory for Functional Polymers, externally at EMPA Dübendorf.

- PhD thesis: Ion Induced Dynamic Phenomena in Salt Semiconductor Devices
  Thesis director: Prof. Dr. Frank Nüesch
  Thesis co-director: Dr. Roland Hany

09.2013 - 08.2015

Master of Science in Electrical Engineering and Information Technology, *ETH Zürich*.
Focus in Micro- and Optoelectronics/ Photovoltaics
Thesis Grade: 5.75/6 Final Grade: 5.5/6, mean: 5.32 (107 students, Std Dev: 0.27)

- Master thesis: Potassium Treatment of Solution-Processed Kesterite Solar Cells
  Supervisors: Prof. Dr. Ayodhya N. Tiwari, Dr. Yaroslav Romanyuk, Dr. Stefan Haass

07.2014 - 12.2014

Master's exchange semester at the School of Photovoltaic and Renewable Energy Engineering, *University of New South Wales*, Sydney, Australia.

- Received High Distinction (best grade) in photovoltaics and renewable energy courses

09.2009 - 02.2013

Bachelor of Science in Electrical Engineering and Information Technology, *ETH Zürich.*
Focus in Micro- and Optoelectronics
Final Grade: 5.25/6, mean: 4.8 (114 students, Std Dev: 0.38)

Employment history

09.2016 - 05.2017 **R&D Engineer/ Research Assistant,** *Fluxim AG/ ZHAW*, Institute of Computational Physics.
R&D projects in the field of organic lighting and photovoltaics.

- Developing hardware and software for organic LED and solar cell measurement system "Paios" (steady state, impedance, transient and spectral measurements)
- Using OLED&PV device simulation tool "Setfos" and large area semiconductor device simulation software "Laoss" for research projects as part of the Organic Electronics and Photovoltaics group
  Advisors: Dr. Martin Neukom, Prof. Dr. Beat Ruhstaller

08.2015 - 12.2015 **Solar Technology Internship (Civilian Service)**, *Institute for Solar Technology SPF*, Hochschule für Technik Rapperswil.
Technical and manual projects in the field of solar technology. Advisors: Prof. Christof Biba, Prof. Matthias Rommel

04.2013 - 09.2013 **Research and Development Internship,** *ABB*, Baden**.**
Optical investigation of switching arcs in high-voltage circuit breaker with laser technology. Advisor: Dr. Patrick Stoller

Institutional responsibilities

01.2020 - present **Sustainability Grassroot Group,** *Empa Dübendorf*, Founded at Empa St.Gallen as a result of the Empa CO2 neutrality strategy until 2030.
Clean-Up-Day 2020, Projects on biodiversity, slow traffic

Supervision of junior researchers

09.2020 - 02.2021 **Master thesis,** *Empa Dübendorf*, Laboratory for Functional Polymers, Jessica Girard.
Title: "Influence of grain boundary passivation and ion migration on the performance and stability of CsPbBr3 light-emitting diodes". Influence of intermixed KTFA on morphology and efficiency.

11.2017 - 04.2018 **Civilian service,** *Empa Dübendorf*, Laboratory for Functional Polymers, Quirin Grossmann.
Fabrication and variation of super yellow polymer light-emitting electrochemical cells leading toco-authorship of three of my papers.

Teaching activities

03.2011 - 06.2011 **Teaching Assistant at Department D-MATH,** *ETH Zürich*, 3 months.
Lecture Complex Analysis, 40 students

Active memberships in scientific societies

2015 - present **Alumni,** *ETH Zürich.*

2012 - present **Swiss Engineering STV,** *section electronics and IT, Basel and Zurich.*

Individual scientific reviewing activities

2019 - present **Journals**
Scientific report (2 times), Solar energy (2 times), Science and Technology of Advanced Materials (2 times)

Prizes, awards, fellowships

2021 **SNSF Postdoc.Mobility grant**
Title: "Dynamics of Ionic Additive Passivation in Perovskite Solar Cells" in the Photovoltaic and Optoelectronic Device Group of Prof. Henry Snaith, University of Oxford

2020 **Poster Award at EU PVSEC**
Title: "Novel Electro-Thermal Modelling Approach for DC and AC Solar Cell Characterizaton" in the thematic area of "New Materials and Concepts for Photovoltaic Devices"

2019 **The Paper of the Year 2019 in the Korean Journal of Information Display.**
For the publication "Quantitative analysis of pixel crosstalk in AMOLED displays" (800 US Dollars)

2019 **Scholarship for International Summer School "Materials 4.0" at the TU Dresden,** *Covering travel cost, accommodation and participation fee.*
Presented work: "Relevance of Numerical Drift-Diffusion Simulation for Unravelling the Functioning of Light-Emitting Electrochemical Cells"

Language skills

German Mother tongue
English Business fluent
French Intermediate
Spanish Basic

Digital competences

Programming Python, Matlab and Origin LabTalk mainly for data analysis, Labview, C++, Java

Tools Origin, Adobe Illustrator and Photoshop, LATEX, GIMP, Zemax, PV-SYST, SketchUp (OpenStudio), Mathematica

Research output list

━━━━━━━━ Publications in peer-reviewed scientific journals

A. Devižis, A. Gelzinis, J. Chmeliov, M. Diethelm, L. Endriukaitis, D. Padula, and R. Hany, "Carrier Tunneling from Charge Transfer States in Organic Photovoltaic Cells," *Advanced Functional Materials*, vol. 2102000, p. 2 102 000, **2021**. DOI: doi.org/10.1002/adfm.202102000.

M. Diethelm, A. Schiller, M. Kawecki, A. Devižis, B. Blülle, S. Jenatsch, E. Knapp, Q. Grossmann, B. Ruhstaller, F. Nüesch, and R. Hany, The Dynamic Emission Zone in Sandwich Polymer Light-Emitting Electrochemical Cells, *Advanced Functional Materials*, vol. 30, no. 33, p. 1 906 803, **2020**. DOI: doi.org/10.1002/adfm.201906803.

M. Diethelm, L. Penninck, M. Regnat, T. Offermans, B. Zimmermann, C. Kirsch, R. Hiestand, S. Altazin, and B. Ruhstaller, Finite element modelling for analysis of electroluminescence and infrared images of thin-film solar cells, *Solar Energy*, vol. 209, no. May, pp. 186–193, **2020**. DOI: doi.org/10.1016/j.solener.2020.08.058.

K. Strassel, S. P. Ramanandan, S. Abdolhosseinzadeh, M. Diethelm, F. Nüesch, and R. Hany, "Solution-Processed Organic Optical Upconversion Device," *ACS Applied Materials & Interfaces*, vol. 11, no. 26, pp. 23 428–23 435, **2019**. DOI: doi.org/10.1021/acsami.9b06732.

R. Aderne, K. Strassel, S. Jenatsch, M. Diethelm, R. Hany, F. Nüesch, R. d. S. Carvalho, C. Legnani, and M. Cremona, "Near-infrared absorbing cyanine dyes for all-organic optical upconversion devices," *Organic Electronics*, vol. 74, no. July, pp. 96–102, **2019**. DOI: doi.org/10.1016/j.orgel.2019.07.002.

S. B. Anantharaman, K. Strassel, M. Diethelm, A. Gubicza, E. Hack, R. Hany, F. A. Nüesch, and J. Heier, "Exploiting supramolecular assemblies for filterless ultra-narrowband organic photodetectors with inkjet fabrication capability," *Journal of Materials Chemistry C*, vol. 7, no. 46, pp. 14 639–14 650, **2019**. DOI: doi.org/10.1039/C9TC04773E.

M. Diethelm, Q. Grossmann, A. Schiller, E. Knapp, S. Jenatsch, M. Kawecki, F. Nüesch, and R. Hany, Optimized Elec- trolyte Loading and Active Film Thickness for Sandwich Polymer Light-Emitting Electrochemical Cells, *Advanced Optical Materials*, vol. 7, no. 3, p. 1 801 278, **2019**. DOI: doi.org/10.1002/adom.201801278.

M. Diethelm, L. Penninck, S. Altazin, R. Hiestand, C. Kirsch, and B. Ruhstaller, Quantitative analysis of pixel crosstalk in AMOLED displays, *Journal of Information Display*, vol. 19, no. 2, pp. 61–69, **2018**. DOI: doi.org/10.1080/15980316. 2018.1428232.

M. Kawecki, R. Hany, M. Diethelm, S. Jenatsch, Q. Grossmann, L. Bernard, and H. J. Hug, "Direct Measurement of Ion Redistribution and Resulting Modification of Chemical Equilibria in Polymer Thin Film Light-Emitting Electrochemical Cells," *ACS Applied Materials & Interfaces*, vol. 10, no. 45, pp. 39 100–39 106, **2018**. DOI: doi.org/10.1021/acsami. 8b14198.

S. Jenatsch, M. Regnat, R. Hany, <u>M. Diethelm</u>, F. Nüesch, and B. Ruhstaller, "Time-Dependent p-i-n Structure and Emission Zone in Sandwich-Type Light-Emitting Electrochemical Cells," *ACS Photonics*, vol. 5, no. 4, pp. 1591–1598, **2018**. DOI: doi.org/10.1021/acsphotonics.8b00047.

L. Penninck, <u>M. Diethelm</u>, S. Altazin, R. Hiestand, C. Kirsch, and B. Ruhstaller, "Modelling crosstalk through common semiconductor layers in AMOLED displays," *Journal of the Society for Information Display*, vol. 26, no. 9, pp. 546– 554, **2018**. DOI: doi.org/10.1002/jsid.671.

K. Strassel, A. Kaiser, S. Jenatsch, A. C. Véron, S. B. Anantharaman, E. Hack, <u>M. Diethelm</u>, F. Nüesch, R. Aderne, C. Legnani, S. Yakunin, M. Cremona, and R. Hany, "Squaraine Dye for a Visibly Transparent All-Organic Optical Upconversion Device with Sensitivity at 1000 nm," *ACS Applied Materials & Interfaces*, vol. 10, no. 13, pp. 11 063– 11 069, **2018**. DOI: doi.org/10.1021/acsami.8b00047.

A. Devižis, S. Jenatsch, <u>M. Diethelm</u>, V. Gulbinas, F. Nüesch, and R. Hany, "Dynamics of Charge Distribution in Sandwich-Type Light-Emitting Electrochemical Cells Probed by the Stark Effect," *ACS Photonics*, vol. 5, no. 8, pp. 3124–3131, 2018. DOI: doi.org/10.1021/acsphotonics.8b00358.

S. Haass, M. Diethelm, C. Andres, Y. Romanyuk, and A. Tiwari, "Potassium post deposition treatment of solution- processed kesterite solar cells," *Thin Solid Films*, vol. 633, pp. 131–134, **2017**. DOI: doi.org/10.1016/j.tsf.2016.11. 012.

S. G. Haass, <u>M. Diethelm</u>, M. Werner, B. Bissig, Y. E. Romanyuk, and A. N. Tiwari, 11.2% Efficient Solution Processed Kesterite Solar Cell with a Low Voltage Deficit, *Advanced Energy Materials*, vol. 5, no. 18, p. 1 500 712, **2015**. DOI: doi.org/10.1002/aenm.201500712.

<p style="text-align:center; color:#3b7dc4">Peer-reviewed conference proceedings</p>

D. Braga, S. Jenatsch, L. Penninck, R. Hiestand, <u>M. Diethelm</u>, S. Altazin, C. Kirsch, and B. Ruhstaller, "67-4: Modelling Electrical and Optical Cross-Talk between Adjacent Pixels in Organic Light-Emitting Diode Displays", *SID Symposium Digest of Technical Papers*, vol. 50, no. 1, pp. 953–956, **2019**. DOI: doi.org/10.1002/sdtp.13083.

<p style="text-align:center; color:#3b7dc4">Contributions to conferences</p>

2020 **EUPVSEC, online,** *European PV Solar Energy Conference*, Poster presentation, Poster Award in the thematic area of New Materials and Concepts for Photovoltaic Devices.
Novel Electro-Thermal Modelling Approach for DC and AC Solar Cell Characterization

2020 **SimOEP, online**, *International Conference on Simulation of Organic Electronics and Photovoltaics*, Oral presentation.
The Dynamic Emission Zone in Sandwich Polymer Light-Emitting Electrochemical Cells

2019 **EDMX Research Day, EPF Lausanne, Switzerland**, *Internal conference of the EDMX doctoral program*, Poster and oral presentation.
The Dynamic Emission Zone in Sandwich Polymer Light Emitting Electrochemical Cells

2019 **PhD Symposium, Empa St.Gallen, Switzerland,** *Internal conference of the Empa Dübendorf, St.Gallen and Thun*, Poster presentation.
The Dynamic Emission Zone in Sandwich Polymer Light Emitting Electrochemical Cells

2019 **DCMS Materials 4.0 - Deep Mechanics, Dresden, Germany,** *Dresden Center for Computational Materials Science International Summer School*, Poster presentation, Chosen for scholarship covering travel cost, accommodation and participation fee.
Relevance of Numerical Drift-Diffusion Simulation for Unravelling the Functioning of Light-Emitting Electrochemical Cells

2019 **INFORM, Valencia, Spain,** *International Conference on Interfaces in Organic and Hybrid Thin-Film Optoelectronics*, Poster presentation.
Unravelling the Dynamic Evolution of the Emission Zone in Sandwich Polymer Light-Emitting Electrochemical Cells

2018 **EDMX Research Day, EPF Lausanne, Switzerland,** *Internal conference of the EDMX doctoral program*, Poster presentation.
Optimized Electrolyte Loading and Active Film Thickness for Sandwich Polymer Light-Emitting Electrochemical Cells

2018 **PhD Symposium, Empa Dübendorf, Switzerland,** *Internal conference of the Empa Dübendorf*, St.Gallen and Thun, Oral presentation.
Optimized Electrolyte Loading and Active Film Thickness for Sandwich Polymer Light-Emitting Electrochemical Cells

2018 **SimOEP, Winterthur, Switzerland,** *International Conference on Simulation of Organic Electronics and Photovoltaics*, Oral presentation.
Optimized Electrolyte Loading and Active Film Thickness for Sandwich Polymer Light-Emitting Electrochemical Cells

2018 **ICOE, Bordeaux, France,** International Conference on Organic Electronics, Poster presentation.
Revisiting the Super Yellow Light Emitting Electrochemical Cell - Enhanced Efficiency and Lifetime

2017 **HOPV, EPF Lausanne, Switzerland,** *International Conference on Hybrid and Organic Photovoltaics at EPF Lausanne*, Poster presentation.
Simulation-Based Investigation of Non-Uniformities for Large Area Organic and Perovskite Solar Cells

Outreach activities

2019 - present **Part of the PhD Council,** *Empa and Eawag Dübendorf.*
Organization of entertaining events for PhDs of the two neighbouring institutes with the intention to bring together the PhDs and provide a networking platform

Unpublished/submitted work

<u>M. Diethelm</u>, M. Bauer, W.-H. Hu, C. Vael, S. Jenatsch, P. W. M. Blom, F. Nüesch, R. Hany, "Electron Trap Dynamics in Polymer Light-Emitting Diodes", submitted. **2021**.

<u>M. Diethelm</u>, A. Devižis W.-H. Hu, T. Zhang, C. Vael, R. Furrer, S. Jenatsch, F. Nüesch, R. Hany, "Identification of Electron and Hole Traps in Polymer Light-Emitting Electrochemical Cells", To be submitted soon. **2021**.

<u>M. Diethelm</u>, J. Girard, F. Nüesch, R. Hany, "Ion- and Trap-Mediated Slow Processes in Perovskite Optoelectronic Devices", To be submitted soon. **2021**.